PRACA DOKTORSKA

Institute of Physical Chemistry
Polish Academy of Sciences
Kasprzaka 44/52
01-224 Warsaw

Ph.D. Dissertation

Thin films of functional redox materials
for solar energy conversion, electrocatalysis, and energy storage

Ievgen Obraztsov

The dissertation completed at the Institute of Physical Chemistry

of the Polish Academy of Sciences within the International Doctoral Studies

Supervisor:

Prof. Wlodzimierz Kutner, Ph.D., D.Sc.

NASCENT

Nanomaterials for Application in Sensors,
Catalysis and Emerging Technologies

MARIE CURIE ACTIONS

NARODOWE
CENTRUM
NAUKI

NanoBiom

Warsaw, February 2015

Dedicated to my family.

Acknowledgments

First of all, I thank to my parents, Vladimir and Tatiana Obraztsov, and to my brother, Aleksei, for their love, for guiding me through the life meanders, and for being an unwearying source of inspirations. I thank to my wife, Valya, for being the basis of my life, home and flowers in windows. Without their constant support, nothing positive would have happened.

I would like to acknowledge gratefully my supervisor, Professor Włodzimierz Kutner, for directing my research, valuable discussions, criticism, and patience. I acknowledge strategic contribution of Professor Francis D'Souza, discussions of ideas and providing the synthesized compounds.

I am grateful to all our group members for a great team spirit, support, and making my socialization in Poland easier. I acknowledge contribution of all my co-authors to this work.

Besides, I am thankful to:

- Dr. K. Noworyta for passing his knowledge and experience, helpful discussions, DFT calculations, and FTIR measurements.

- Dr. P. Pięta, Dr. A. Pietrzyk-Le, and Dr. P. S. Sharma for passing their knowledge and helpful discussions.

- S. Gadde, C. A. Wijesinghe, S. K. Das, and B. KC Chandra (Chemistry Department of the Wichita State University, Wichita, U.S.A.) for syntheses of the monomers and other compounds used herein.

- Prof. M. Resmini (The School of Biological and Chemical Sciences, Queen Mary University of London, London, United Kingdom) for coordination of the NASCENT consortium, which made the present work possible, and for guiding me through ethics in science.

- Dr. J. W. Sobczak for the XPS measurements and the resulting spectra interpretation.

- Prof. J. Waluk for helpful discussion on the donor-acceptor dyads.

- Dr. G. Z. Zukowska (Chemistry Department of the Warsaw University of Technology) for the Raman spectroscopy measurements of the $(Ph_3N)_4ZnP$ polymer films.

- Prof. J. Augustynski and Dr. P. Barczuk (Centre of New Technologies, University of Warsaw, Warsaw, Poland) for help with photoelectrochemical experiments.

- Dr. V. Horvath (Inorganic and Analytical Chemistry Department of the Budapest University of Technology and Economics, Budapest, Hungary) for hosting my research visit.

- Dr. R. Nowakowski and M.Sc. T. Jaroch for the AFM imaging of the Langmuir-Blodgett films of $C_{60}ur : (2-AP)$ and the STM imaging of the Langmuir-Blodgett films of $C_{60}im$-Zn(TPPE).

The results presented in the thesis were partially published in the following papers and patents

A. Publications

A.1 **Obraztsov, I.**; Noworyta, K.; Kutner, W.; Gadde, S.; D'Souza, F., *Phys. Status Solidi B*, **2007**, *244*, 3861-3867, "Nanostructuring of Watson-Crick type base-paired (C_{60}-uracil):(2-aminopurine) conjugates in Langmuir films".

A.2 Subbaiyyan, N. K.; **Obraztsov, I.**; Wijesinghe, C. A.; Tran, K.; Kutner, W.; D'Souza, F. *J. Phys. Chem. C,* **2009**, *113*, 8982-8989, "Supramolecular donor-acceptor hybrid of electropolymerized zinc porphyrin with axially coordinated fullerene: formation, characterization, and photoelectrochemical properties".

A.3 Pieta, P.; **Obraztsov, I.**; Sobczak, J. W.; Chernyayeva, O.; Das, S. K.; D'Souza F.; Kutner, W. *J. Phys. Chem. C* **2013**, *117*, 1995-2007, "A Versatile Material for a Symmetrical Electric Energy Storage Device: A Composite of the Polymer of the Ferrocene Adduct of C_{60} and Single-Wall Carbon Nanotubes Exhibiting Redox Conductivity at Both Positive and Negative Potentials".

A.4 **Obraztsov, I.**; Noworyta, K.; Hart, A.; Gobeze, H. B.; Chandra, B. KC; Kutner, W.; D'Souza F. *ACS Appl. Mater. Interfaces* **2014**, *6*, 8688-8701, "Langmuir-Blodgett films of self-assembled (alkylether derivatized Zn phthalocyanine)-(C_{60} imidazole adduct) dyad with controlled intermolecular distance for photoelectrochemical studies".

B. Patent applications

B.1 Pieta, P., **Obraztsov, I.**, Sobczak, J., Winkler, K., Balch, A. L., Das, S., D'Souza, F. Kutner, W., Polish Pat. Appl. No. P-393956, 18 February 2011, „Materiał kompozytowy, zwłaszcza do budowy kondensatorów elektrochemicznych i kondensator elektrochemiczny" ("Composite Material, Especially for Constructing Electrochemical Capacitors and Electrochemical Capacitor").

C. Review papers

C.1 Pieta, P.; **Obraztsov, I**.; D'Souza, F.; Kutner, W. *ECS J. Solid State Sci. Technol.* **2013**, 2, 10, M3120-M3134. "Conducting Polymers and Various Carbon Nanostructures for Electrochemical Supercapacitors".

D. Publications in preparation

D.1 **Obraztsov, I.**; Noworyta, K.; Wijesinghe, C. A.; Kutner, W.; D'Souza F., **2015**, in preparation, "Structure-reactivity effects in electrocatalytic dioxygen reduction in aqueous solutions at electrodes coated by electrochemically synthesized molecularly imprinted polymers of a cobalt porphyrin tetra-diphenylamine derivative".

The results described in the thesis were partially presented at conferences and international scientific meetings

(S) - short communication
(P) - poster presentation
(L) - lecture

2-9 March 2013	The XXVIIth International Winterschool on Electronic Properties of Novel Materials, (Kirchberg in Tyrol, Austria). **Obraztsov, I**., Hart, A., Chandra B. KC, D'Souza, F., and Kutner, W., "Langmuir and Langmuir-Blodgett films of the electron donor-acceptor dyad of Zn phthalocyanine bearing peripheral alkylether substituents and the C_{60}-imidazole adduct" (P).
19-23 September 2011	The VIth Ukrainian Congress on Electrochemistry, the Ukrainian State University of Chemical Technology (Dnepropetrovsk, Ukraine). Pieta, P., **Obraztsov, I.**, Das S. K., D'Souza, F. and Kutner, W., "A Composite of the Red-ox Conducting C_{60} Polymer and Single-Wall Carbon Nanotubes for a Symmetric Supercapacitor" (S).
1-7 February 2010	The 4th NASCENT International Meeting within the Marie Curie Action, Ben Gurion University of the Negev (Beersheba, Israel). Subbaiyan, N., **Obraztsov, I**., Kutner, W., Kim, T., D'Souza, F.,

"Structured composite films based upon electron donor-acceptor dyads for solar energy conversion" (S).

6-10 November 2009	The 4th International Workshop on Surface Modification for Chemical and Biochemical Sensing, SMCBS'09 (Przegorzaly near Cracow, Poland). **Obraztsov, I.**, Noworyta, K. R., Kutner, W., Wijesinghe, C. A., D'Souza, F., "Structure-reactivity effects in electrocatalytic dioxygen reduction in aqueous solutions at electrodes coated by electrochemically synthesized molecularly imprinted polymers of a cobalt porphyrin diphenylamine derivative" (P).
20-29 July 2009	The 3rd NASCENT International Meeting (Budapest, Hungary). **Obraztsov, I.**, Noworyta, K., Kutner, W., Wijesinghe, C. A., and D'Souza, F., "Quantum dots based structured composite films for solar energy conversion" (S).
22-25 March 2009	The 7th International Spring Meeting of the International Society of Electrochemistry (Szczyrk, Poland). **Obraztsov, I.**, Noworyta, K., Kutner, W., Wijesinghe, C. A., and D'Souza, F., "Structural effects in electrocatalytic dioxygen reduction by the electrochemically synthesized polymer of a cobalt porphyrin derivative" (S).
2-6 February 2009:	The 3rd NASCENT Winter School within the Marie Curie Action, Institute of Physical Chemistry PAS (Warsaw, Poland). „Structured polymer films" and "Characterization of molecularly imprinted polymer films with AFM" (L).
29-30 July 2008	The 2nd NASCENT International Meeting within the Marie Curie Action, Institute du Management de I'Information (Paris, France). **Obraztsov, I.**, Kutner, W., Wijesinghe, C. A., D'Souza, F., "Electrocatalytic dioxygen electroreduction and electron donor-acceptor dyad formation by polymers of diphenyl derivatives of some metalloporphyrins" (S).
18 May 2008	ChemSession'08, The Polish Chemical Society (Warsaw, Poland). **Obraztsov, I.**, Kutner, W., Wijesinghe, C. A., D'Souza, F., "Electrochemical preparation and electrocatalytic dioxygen

electroreduction by the structured polymer of an aminophenyl derivative of cobalt porphyrin" (P).

04-08.11.2007   The 3rd International Workshop on Surface Modification for Chemical and Biochemical Sensing, SMCBS'2007 (Włodowice, Poland). **Obraztsov, I.**, Kutner, W., Wijesinghe, C. A., D'Souza, F., "Electrochemical polymerization and electrocatalytic properties of structured selected aminophenyl derivatives of some metalloporphyrins" (P).

10-12 September 2007   The 1st NASCENT International Meeting within the Marie Curie Action, Queen Mary University of London (London, U.K.). **Obraztsov, I.**, Kutner, W., Wijesinghe, C. A., and D'Souza, F., "Mechanistic aspects of electrochemical polymerisation of selected amino derivatives of some metalloporphyrins" (S).

Contents

viii

ix

x

List of abbreviations

Abbreviation	Meaning
2-AP	2-aminopurine
3-BrPYR	3-bromopyridine
A	electron-acceptor molecule
a.u.	arbitrary unit
ACN	acetonitrile
AFM	atomic force microscopy
ATR-FTIR	attenuated total reflection Fourier-transform infrared (spectroscopy)
BAM	Brewster angle microscopy
BE	(electron) binding energy
BPY	4,4'-bipyridine
$C_{60}Fc$	2´-ferrocenylfulleropyrrolidine
$C_{60}im$	N-methyl-2-(4'-N-imidazolylphenyl)-3,4-fulleropyrrolidine
$C_{60}ur$	2(5′-uracil)fulleropyrrolidine
CE	counter electrode
CV	cyclic voltammetry
D	electron-donor molecule
D*	excited electron-donor molecule
DPV	differential pulse voltammetry
ECP	π-electron conducting polymers
EQCM	electrochemical quartz crystal microbalance
FC	fuel cell
FF	fill factor of a photovoltaic cell
FIA	flow-injection analysis
FTO	fluorine-doped tin oxide
GCE	glassy carbon electrode
HOMO	highest occupied molecular orbital
IPCE	incident-photon-to-current efficiency
ITO	tin-doped indium oxide
LB	Langmuir-Blodgett

LS	Langmuir-Schaefer
LSV	linear sweep voltammetry
LUMO	lowest unoccupied molecular orbital
MIP	molecularly-imprinted polymer
MIP	non-imprinted polymer
NHE	normal hydrogen electrode
NMP	1-methyl-2-pyrrolidinone
NPV	normal pulse voltammetry
ODCB	1,2-dichlorobenzene
OPV	organic photovoltaics
PCE	power conversion efficiency (of a photovoltaic cell)
$Pd(Ac)_2$	palladium(II) diacetate
PEM	proton-exchange membrane
PET	photoinduced electron transfer
$(Ph_3N)_4CoP$	*tetrakis*[4-(*N*,*N*-diphenylamino)phenyl]porphyrinatocobalt(II)
$(Ph_3N)_4ZnP$	*tetrakis*[4-(*N*,*N*-diphenylamino)phenyl]porphyrinatozinc(II)
PM	piezoelectric microgravimetry
PV	photovoltaics
PPZ	piperazine
PVC	photovoltaic cell
PY-TZ-PY	3,6-di-4-pyridyl-1,2,4,5-tetracene
QCM	quartz crystal microbalance
QCR	quartz crystal resonator
RDE	rotating disk electrode
RE	reference electrode
RCP	redox-conducting polymers
RRDE	rotating ring-disk electrode
SAM	self-assembled monolayer
SCE	saturated calomel electrode
SWCNT	single-wall carbon nanotube
TBA	tetrabutylammonium (cation)
TL	toluene

TPA	triphenyalamine
UV-vis	ultraviolet-visible (light)
WE	working electrode
XPS	X-ray photoelectron spectroscopy
Zn(TPPE)	tetrakis[(2,9,16,23-triethyleneglycolmonomethylether)phthalocyaninato]zinc(II)

List of symbols

Symbol	Meaning	Units
A	area	cm^2
A_{ac}	acoustically active area of a quartz crystal resonator	cm^2
A_0^L	absorbance	a.u.
A_m	area per molecule in a Langmuir film	nm^2
C	capacity	F
c	concentration in solution	M
c_A	analyte concentration	M
c^f	concentration in film	M
C_{dl}	capacity of an electrical double layer	F
c_{O_2}	dioxygen concentration in bulk solution	M
c_R^0	receptor concentration	M
C_s	specific capacitance	$F\ g^{-1}$
D	diffusion coefficient	$cm^2\ s^{-1}$
D_{O_2}	diffusion coefficient of dioxygen in solution	$cm^2\ s^{-1}$
d_p	depth of an IR light beam penetration	nm
d	distance between a capacitor conducting plates	m
E	potential	V
E_b	base potential	V
E_f	final potential	V
E_i	initial potential	V
E_k	electron kinetic energy	J
E_p	peak potential in CV, DPV, and LSV	V
E_{pa}	anodic peak potential in CV and LSV	V
E_{pc}	cathodic peak potential in CV and LSV	V
E^{SC}	energy of supercapacitor	J
F	Faraday constant	$C\ mol^{-1}$
f_0	fundamental frequency of a quartz crystal resonator	Hz
F_k	force of an AFM cantilever-sample interaction	N
f_r	disk electrode rotation frequency	rev.p.m.

xiv

G	Gibbs free energy	J
i	current	A
i_{lim}	limiting current	A
i_{mp}	photocurrent corresponding to maximum power photovoltaic cell	Aof a
I_p	intensity of p-polarized component of radiation	$W\ m^{-2}$
i_p	peak current in LSV, CV, and DPV	A
i_{pa}	anodic peak current in LSV, CV, and DPV	A
i_{pc}	cathodic peak current in LSV, CV, and DPV	A
I_s	intensity of s-polarized component of radiation	$W\ m^{-2}$
i_{sc}	short-circuit current	A
j	current density	$A\ cm^{-2}$
j_d	disk current density	$A\ cm^{-2}$
j_k	kinetic current density	$A\ cm^{-2}$
j_{lim}	diffusion-limited current density	$A\ cm^{-2}$
j_r	limiting ring current density	$A\ cm^{-2}$
k_c	QCR electromechanical coupling factor	$A^2\ s^2\ cm^{-2}$
k_e	heterogeneous electron transfer rate constant	$cm\ s^{-1}$
k_{scc}	spring constant of a cantilever	
K_s^s	stability constant of a complex in solution	
l	light pass distance of a cuvette	cm
N	collection coefficient of a rotating ting-disk electrode	
n	number of electrons	
n_i	number of moles of a substance	
n_{otn}	overtone number	
n^r	refractive index	
P	power	W
P_{in}	incident light power	$W\ m^{-2}$
P_{ir}	light irradiation power	W
$P_{max,ideal}^{PVC}$	maximum power of an ideal photovoltaic cell	W
P_{max}^{PVC}	maximum power of a photovoltaic cell	W
P^{SC}	power of a supercapacitor	W

P_{out}	output power of a photovoltaic cell	W
Q	charge	C
R	molar gas constant	$J\ K^{-1}\ mol^{-1}$
R_c	equivalent series resistance of a supercapacitor	Ω
R_d	dynamic resistance	Ω
R^L	light reflectance	%
R_{sa}	relative surface area	m^2
S	area of an interface	m^2
T	absolute temperature	K
t	time	s
v	potential sweep rate in LSV and CV	$V\ s^{-1}$
V	volume	dm^3
V_c	voltage	V
V_f	volume of a film	dm^3
V_{mp}	voltage corresponding to maximum power (of a photovoltaic cell)	V
V_{oc}	open circuit voltage	V
V_s	surface potential	V
z	tip-to-sample distance in AFM	nm

α	Brewster angle	degree
γ	surface tension of a subphase solution in a Langmuir trough with a Langmuir film spread	$J\ m^{-2}$
γ_0	surface tension of a subphase solution in a Langmuir trough without a Langmuir film	$J\ m^{-2}$
δ_{pulse}	diffusion layer thickness in potential pulse electrochemical methods	μm
δ_{sweep}	diffusion layer thickness in potential sweep electrochemical methods	μm
Δf	frequency change of a quartz crystal resonator	Hz
Δm	mass change of a quartz crystal resonator	g
ΔW	difference between the work function of the sample and the XPS detector material	eV
ε_0	electric permittivity of vacuum	$F\ m^{-1}$

ε_r	electric permittivity of a material	F m^{-1}
ε_A	molar absorptivity of a substrate	
ε_e	relative electric permittivity of a material	F m^{-1}
ε_p	incident electric vector of p-components of radiation	
ε'_p	reflected electric vector of p-components of radiation	
ε_s	incident electric vector of s-components of radiation	
ε'_s	reflected electric vector of s-components of radiation	
ε_R	molar absorptivity of an analyte	
ε_{RA}	molar absorptivity of a complex	
θ_c	angle of incidence of an IR light beam	degree
κ	compression coefficient of a Langmuir film	μN μ^{-1}
λ	wavelength	nm
μ	electric dipole moment	D
$\mu_\perp$	component of a dipole moment normal to the interface plane	D
μ_q	shear modulus of quartz	g cm^{-1} s^{-2}
π	surface pressure	mN m^{-1}
ρ_q	density of quartz	g cm^{-3}
ρ_L	density of a working solution	g cm^{-3}
σ_p	phase change in the p-component of radiation	degree
σ_s	phase change in the s-component of radiation	degree
η	overall power conversion efficiency of a photovoltaic cell	%
η_L	dynamic viscosity	g cm^{-1} s^{-1}
η_k	kinematic viscosity	kg s-1 m-1
ϕ	solar energy conversion efficiency, i.e., quantum yield	
ω	angular velocity of a rotating disk electrode	rad.p.s.
ω_t	AFM tip oscillation frequency	Hz
$\omega_{t,0}$	AFM tip resonance frequency	Hz

xvii

Streszczenie pracy doktorskiej

Tytuł: „Cienkie warstwy funkcjonalnych materiałów redox do przetwarzania energii słonecznej, elektrokatalizy i gromadzenia energii".

Autor: mgr inż. Ievgen Obraztsov

Promotor: Prof. dr hab. Włodzimierz Kutner

Niniejsza praca doktorska opisuje przygotowanie i właściwości cienkich warstw funkcjonalnych materiałów organicznych, zbudowanych z [C_{60}]fulerenu, pochodnych porfiryny kobaltu lub ftalocyjaniny cynku, jak również nanorurek węglowych, do przetwarzania energii słonecznej, elektrokatalitycznej redukcji tlenu i gromadzenia energii elektrycznej.

Najpierw przedstawiane są diady donorowo-akceptorowe. Pierwszy rozdział opisuje przygotowanie i właściwości diady donorowo-akceptorowej [C_{60}]fulerenu z dołączoną grupą uracylową oraz 2-aminopuryny, [C_{60}ur-(2-AP)]. Diada ta była przygotowana przez samoorganizację w warstwie Langmuira na granicy faz wody i powietrza za pomocą parowania zasad nukleinowych typu Watsona-Cricka. Drugi rozdział opisuje badania warstw Langmuira i Langmuira-Blodgett (LB) diady donorowo-akceptorowej zbudowanej z pochodnej ftalocyjaniny cynku, z peryferyjnymi podstawnikami eterowymi, i [C_{60}]fulerenu z dołączonym pierścieniem imidazolowym, Zn(TPPE)-C_{60}im. Trzeci rozdział przedstawia wyniki badań diady składającej się z polimeru porfiryny cynku z trifenyloaminowymi grupami peryferyjnymi jako donora i C_{60}im, jako akceptora, osiowo przykoordynowanego do centralnego atomu cynku, [(Ph_3N)$_4$ZnP polimer]-C_{60}im. Struktura tych diad została zoptymalizowana za pomocą obliczeń DFT. Powstawanie diad w warstwach Langmuira i ich morfologię uwidoczniono za pomocą mikroskopii kąta Brewstera. Wielowarstwy LB diady Zn(TPPE)-C_{60}im i [(Ph_3N)$_4$ZnP polimeru]-C_{60}im przeniesiono na różne podłoża stałe i ich właściwość zbadano za pomocą spektroskopii UV-vis, femtosekundowej przejściowej spektroskopii absorpcyjnej i PM-IRRAS oraz uwidoczniono za pomocą AFM jak i pomiarów elektrochemicznych. Zbadane zostały również właściwości fotoelektrochemiczne warstw LB diady Zn(TPPE)-C_{60}im i [(Ph_3N)$_4$ZnP polimeru]-C_{60}im.

Druga część pracy przedstawia badania materiału do elektrokatalitycznej redukcji tlenu, zbudowanego z polimeru porfiryny kobaltu z dołączonymi peryferyjnymi podstawnikami trifenyloaminowymi. Za pomocą dwukleszczowego ligandu organicznego, przed elektropolimeryzacją przygotowywano dimer zbudowany z dwóch cząsteczek monomeru. Aktywność elektrokatalityczna tego polimeru względem redukcji tlenu uległa znacznemu podwyższeniu dzięki zastosowaniu tego ligandu. Warstwę polimeru scharakteryzowano za pomocą różnych technik elektrochemicznych i spektroskopowych oraz za pomocą AFM.

Trzecia część pracy jest poświęcona badaniom sprawności elektrochemicznej nowego kompozytu do odwracalnego gromadzenia ładunku elektrycznego. Kompozyt ten składał się z elektrochemicznie spolimeryzowanego [C_{60}]fulerenu, z dołączonym podstawnikiem ferrocenowym, na powierzchni elektroforetycznie osadzonej na elektrodzie warstwy niekowalencyjnie zmodyfikowanych jednościennych nanorurek węglowych. Zmontowano kondensator electrochemiczny do gromadzenia ładunku, składający się z dwóch jednakowych elektrod złotych pokrytych warstwą kompozytu. Następnie zbadano elektrochemiczną trwałość tych warstw w trakcie galwanostatycznego wielocyklicznego ładowania i rozładowania. Wyznaczono również moc całkowicie lub tylko częściowo naładowanego kondensatora.

Summary of the Ph.D. thesis

Title: "Thin films of functional redox materials for solar energy conversion, electrocatalysis, and energy storage".

Author: Ievgen Obraztsov, M.Sc.

Supervisor: Prof. Włodzimierz Kutner, Ph.D., D.Sc.

The present Ph.D. thesis describes research on preparation and characterization of thin films of organic functional materials based on the $[C_{60}]$fullerene, Co porphyrin, and Zn phthalocyanine derivatives as well as on carbon nanotubes, for solar energy harvesting, dioxygen electrocatalytic reduction, and electric energy storage.

The first part of the thesis is composed of three chapters devoted to electron donor-acceptor dyads. The first chapter describes preparation and characterization of the electron donor-acceptor dyad of uracil-appended $[C_{60}]$fullerene and 2-aminopurine, C_{60}ur-(2-AP). The dyad was self-assembled in a Langmuir film on the water-air interface by the Watson-Crick nucleobase paring. The second chapter describes investigations of the Langmuir and Langmuir-Blodgett (LB) films of the electron donor-acceptor dyad of (alkylether-appended Zn phthalocyanine)-(imidazole-derivatized $[C_{60}]$fullerene), $Zn(TPPE)$-C_{60}im. The third chapter presents results of the research of an electron donor-acceptor dyad composed of a polymer of triphenylamine-appended Zn porphyrin as the donor moiety and C_{60}im axially self-assembled to the Zn central atom, $[(Ph_3N)_4ZnP$ polymer]-C_{60}im. Structure of the dyads was optimized with the DFT computing. Formation of dyads in Langmuir films and the film morphology were unraveled by Brewster angle microscopy imaging. Multilayer LB films of dyads and the $[(Ph_3N)_4ZnP$ polymer]-C_{60}im construct were prepared on different solid substrates and characterized with the UV-vis, PM-IRRAS, and femtosecond transient absorption spectroscopic as well as electrochemical measurements, and AFM imaging. Finally, photoelectrochemical behavior of the multilayer LB film of the $Zn(TPPE)$-C_{60}im dyad and the $[(Ph_3N)_4ZnP$ polymer]-C_{60}im construct was examined.

The second part of the thesis presents investigations of an electrocatalytic material for dioxygen reduction based on a polymer of Co porphyrin appended with triphenylamine peripheral substituents. A bidentate templating organic ligand was used to form a face-to-face dimer of two monomer molecules prior to electropolymerization. This templating enhanced electrocatalytic activity towards dioxygen reduction of the resulting polymer film. The film was characterized with different electrochemical and spectroscopic techniques as well as by AFM imaging.

The third part of the thesis describes electrochemical performance of an electric charge storage material composed of the electropolymerized ferrocene adduct of $[C_{60}]$fullerene immobilized over an electrophoretically deposited film of non-covalently modified single-wall carbon nanotubes. The electrophoretic deposition procedure was optimized and a charge storage device, composed of two identical Au disk electrodes coated with the composite films, was assembled. Then, electrochemical stability of the films in galvanostatic multi-cycle charging and discharging was evaluated. Finally, power of the fully or partially charged device was determined.

1. Motivation and research goals

Energy becomes one of the most important resources in the world of 21st century and its importance is expected to increase even more in the nearest future.[1] Current access to energy sources and its perspectives become an issue of economic security.[2] Globally, ~15 trillion watts (15 TW) of power is consumed annually and this value is expected to grow by 50% till 2035.[3,4] Despite decreasing reserves of fossil fuels, they are intensively being used providing nearly 86% of total energy consumed in 2011.[5] Moreover, the use of fossil fuels produces harmful side effects, such as environmental pollution that threatens human health.[6] One of the prospective ways to address the energy issue is to devise new materials and to develop new technologies, which will make energy generation and storage cleaner, safer, and cheaper.

The present research is focused on fabrication and characterization of new organic molecular constructs for use as electrode materials for solar energy conversion, electrocatalysis, and energy storage. Until recent years, conventional photovoltaic cells, fuel cells, or supercapacitors were primarily used in the space and military applications. The main reason limiting their widespread personal use was a high cost. Now, billions of energy demanding mobile devices along with a global energy shortage problem require alternate solutions to the fossil fuel energy and "an electric socket in the wall". One of the ways to address the energy issue is to devise functional materials for solar energy conversion, oxygen reduction catalysis, and energy storage devises. This field of materials science has intensively been explored for the last decades.

Photovoltaics is an efficient way of conversion of solar energy into electric energy. Traditional photovoltaics is based on silicon. It is relatively efficient and modestly durable. However, a high purity silicon required and limited production capacity make the large-scale application of silicon-based photovoltaics costly.[7,8] A viable alternative to silicon semiconductors are organic semiconducting materials.[9]

Energy storage is complementary to energy generation, particularly by the photovoltaic and fuel cells. Here, one of the main goals in devising electrode materials is to combine such properties as high energy density, high capacity, and fast charge-discharge ability in one electroactive material. Successful combination of these functional characteristics of faradaic capacitors and rechargeable batteries in novel active materials for energy storage devices may result in another energy revolution. A promising candidate for

1

that is a mixed-type energy storage material, revealing both the double-layer capacity and faradaic, i.e., redox pseudocapacity properties.

Despite a huge effort and massive investment made, devices such as photovoltaic cells and supercapacitors based on organic functional materials were commercialized only recently still leaving much room for improvement, which is addressed in the present thesis.[10]

2. Critical literature survey

The present chapter describes both fundamentals and critical review of selected recent research on organic photovoltaics, dioxygen electrocatalytic reduction, carbon nanomaterial composites in application to energy storage devices, and mechanisms of electropolymerization of monomers used in the present research. Moreover, it briefly depicts all techniques used.

2.1 Organic photovoltaics

Sun is a powerful and inexhaustible source of energy. It delivers to Earth more energy than the mankind consumes now and will need in far perspective. That is, only one hour of sunshine illumination (3.8×10^{23} kW) is more than enough to satisfy human energy demand for the entire year (1.6×10^{10} kW in 2005)[11] (Fig. 2.1-1).
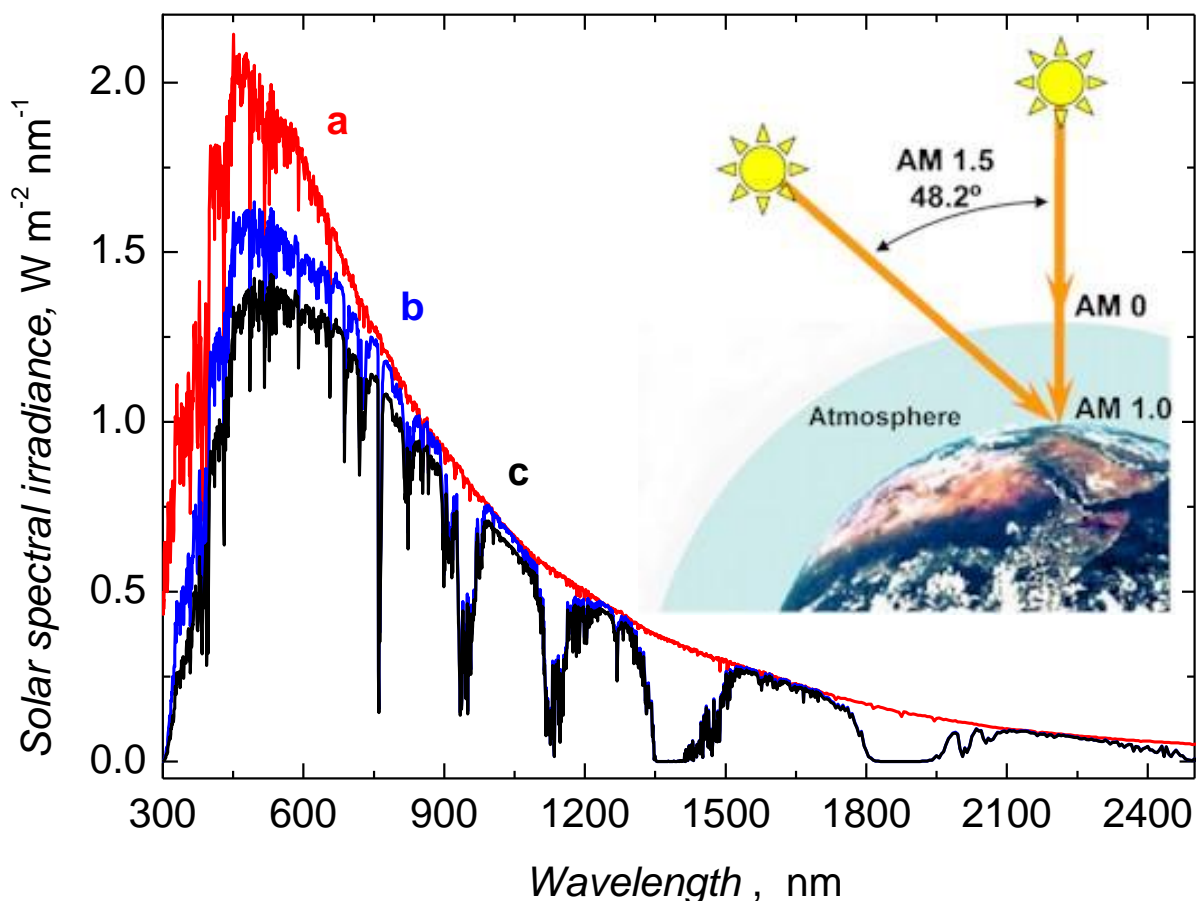
Figure 2.1-1. Reference solar spectral irradiance, (a) AM 0 standard, (b) direct normal spectral irradiance, (c) AM 1.5 standard. (Adapted from www.rredc.nrel.gov/solar/spectra/am1.5).

3

Although the photovoltaic effect was discovered by Alexandre-Edmond Becquerel as early as in 1839, first commercial solar cells were manufactured, for the space program, over a century afterwards, and, their use had been very limited for a long time.

Organic photovoltaic (OPV) materials are single molecules, complexes, oligomers, or conjugated semiconducting polymers capable of charge separation upon photoexcitation. Their advantages over the crystalline silicon photovoltaic materials consist in (1) low-to-negligible cost of an active photovoltaic material,[12] (2) easy to up-scale production, (3) variety of sources of materials, i.e., different systems can be used as active photovoltaic materials, (4) exceptional processability as they can be transferred onto a solid substrate from solution with a range of low-cost techniques including drop-casting, spray-coating, ink-jet printing, offset printing, gravure technique, Langmuir-Blodgett technique, etc., (5) high light absorbance in a wide range of wavelengths, (6) exceptional mechanical flexibility,[13] which allows for broad application. However, they reveal also drawbacks with respect to inorganic semiconductors, which include (i) lower long-term photochemical stability,[14] (ii) relatively lower efficiency, (iii) challenging solvent- and electrolyte-free cell construction for some types of OPV, as the solvent presence in an OPV cell introduces a range of problems including solvent evaporation and solvent toxicity. Intensive research on the OPV materials aims at eliminating these deficiencies.
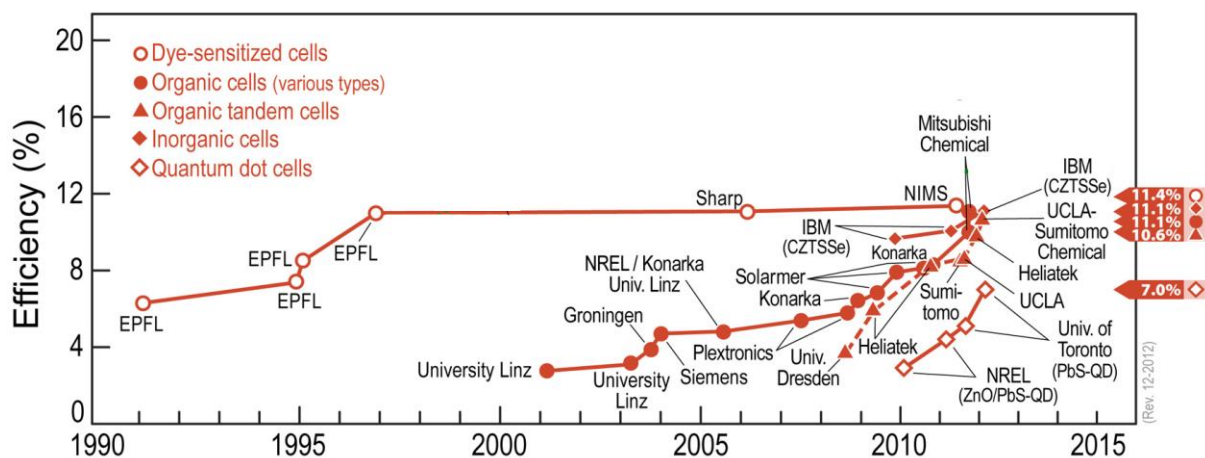
Figure 2.1-2. Research on photovoltaic cells made of emerging photovoltaic materials, efficiency records. (Adapted from www.nrel.gov/ncpv).

4

An active material must be in an electric contact with two electrodes in a PV cell. At least one of them must be transparent. A tin-doped indium oxide (ITO) or fluorine-doped tin oxide (FTO) film modified glass is commonly used as a photoelectrode due to high light transparency and electric conductivity. Indium is very expensive. Therefore, devising and fabricating a cheap electrode material, as efficient and durable as the best quality ITO or FTO transparent electrode, for commercial solar cells is another task. It is attractive and challenging both scientifically and technologically.[15-17]

Despite of a relative immaturity of the OPV compared to the silicon photovoltaics, research on the OPV cell efficiency has rapidly been growing for the last five years. The actual world record of the OPV cell efficiency exceeds 11% (Fig. 2.1-2), which is still much lower than that of a record silicon solar cell exceeding 40%.[18] However, it is already approaching efficiency of commercial silicon solar cells.

2.1.1 Types of organic photovoltaics

With respect to the photoactive material used, photovoltaics can be divided into three large groups, i.e., to that using the inorganic, organic, and hybrid materials. The last two groups appeared in 1986 and 1991, respectively.[19,20]
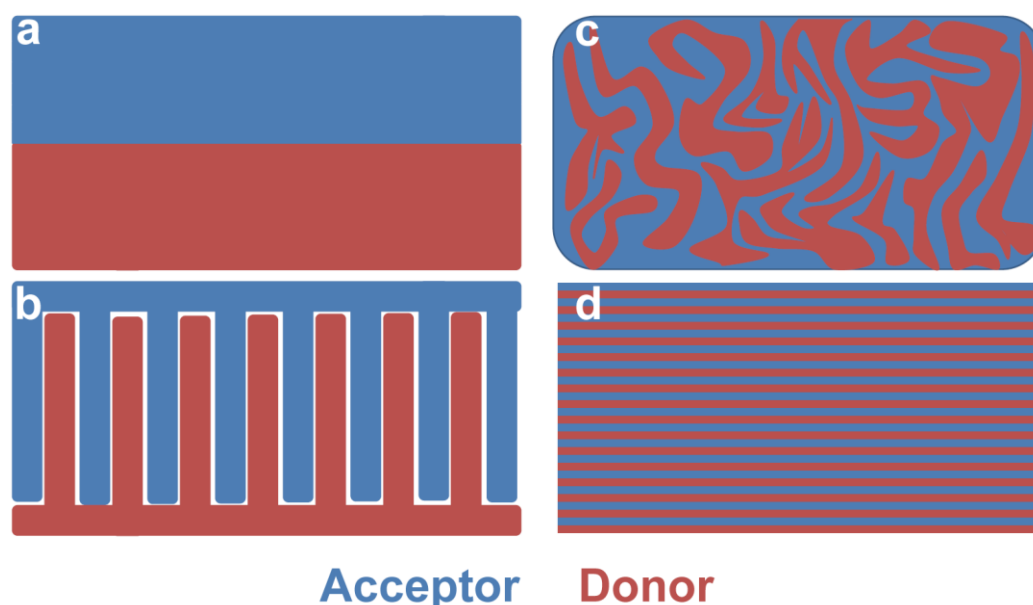
Figure 2.1-3. A simplified cross-sectional view of relative orientation of the donor and acceptor molecular layers in an OPV cell with respect to each other in a (a) flat heterojunction, (b) ideal bulk heterojunction, (c) typical bulk heterojunction, and (d) molecular multilayer. (Adapted from Ref.[21])

5

With respect to molecularity of the donor and acceptor moieties, pristine OPV cells can be classified as either the small-molecule,[22] polymer, and/or block-copolymer OPVs.[23] Other classification defines the OPV cells by mechanical organization of the donor and acceptor moieties into a single layer, flat heterojunction (Fig. 2.1-3a), bulk heterojunction (Fig. 2.1-3c), multilayer molecular (Fig. 2.1-3d), tandem OPVs, etc.

The hybrid photovoltaics usually uses an organic donor and inorganic acceptor moiety. A classic example is the dye-sensitized or Grätzel cell (Scheme 2.1-1) where TiO_2 is used as the electron acceptor and some efficient dye, such as a ruthenium complex, metalloporphyrin, or metallophthalocyanine, as the electron donor.
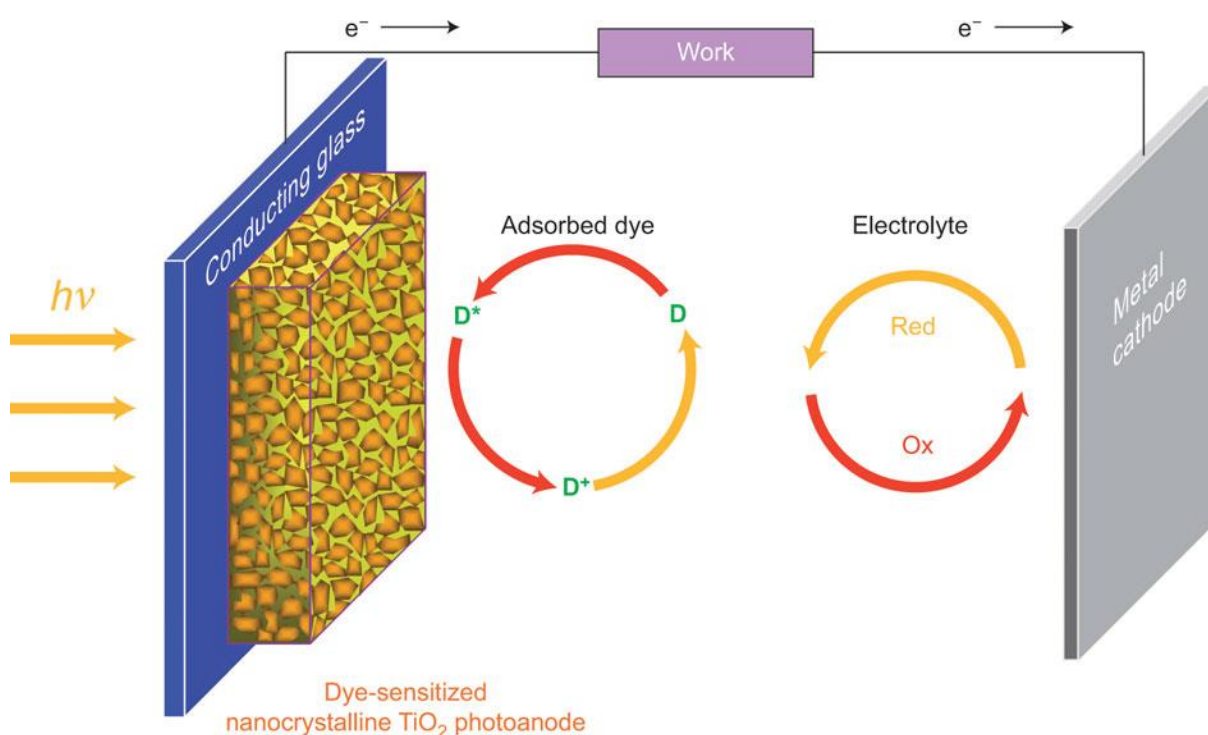
Scheme 2.1-1. A simplified diagram of a TiO_2 dye-sensitized solar cell operation. (Adapted from Ref.[24])

2.1.2 Mechanisms of solar energy conversion by organic photovoltaic cells

Different nature of active materials applied in the OPV and silicon photovoltaic cells is the cause of a fundamental difference in their operation principles. That is, light absorption by the OPV material results in formation of excitons in organic molecular materials rather than free electrons and holes,[25] as is the case for inorganic semiconductors. An exciton is

6

considered as a tightly electrostatically bound electron-hole (e^- - h^+) pair. Due to its electrical neutrality and strong electron-hole binding, the exciton can be regarded as a mobile excited state. In other words, after photon absorption by a donor moiety of an organic electron donor-acceptor dyad, an electron is promoted from the donor highest occupied molecular orbital $(HOMO)_D$ to its lowest unoccupied molecular orbital $(LUMO)_D$ energy level (Fig. 2.1-5). Then, the electron migrates to the $(LUMO)_A$ energy level of the acceptor because this level is lower. The energy diagram for a photovoltaic cell under two limiting conditions, i.e., showing maximum open circuit voltage, V_{oc}, and maximum short-circuit current, I_{sc}, (defined in Fig. 2.1-6) is shown in Fig. 2.1-5a and 2.1-5b, respectively.
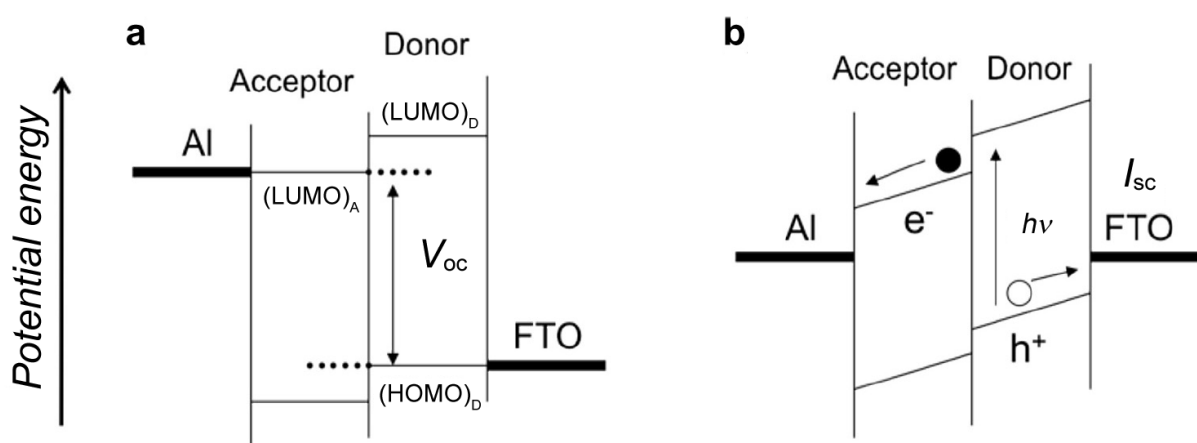
Figure 2.1-5. Potential energy diagram for a molecular solar cell under (a) the open-circuit conditions and (b) the short-circuit conditions where an exciton dissociates at the donor-acceptor interface. (Adapted from Ref.[26])

For a flat-heterojunction OPV with the one donor and one acceptor layer, five stages in the mechanism of energy conversion can be distinguished (Scheme 2.1-2). (1) First, light is absorbed by an electron donor (D), which results in generation of an exciton. (2) Next, the exciton, during its short lifetime, appears at or migrates to the donor-acceptor interface. (3) Subsequently, at the interface, electron is transferred from the excited donor (D*) to acceptor (A) molecule; a physical requirement for that is a small distance between D and A, so that this electron transfer is fast. (4) The charges in the acceptor and donor diffuse by hopping to neighboring molecules. (5) The charge is abstracted from the cathode and injected via an external electric current to the donor at the anode.[21]

In the most simple case, when there is only one molecular layer of a donor and one of an acceptor at the anode and cathode, respectively, there is no need for charge transport to the D-A interface. However, if the donor and acceptor moieties are bound within one dyad, then the order of stages in the mechanism of the photovoltaic energy generation is different. That is, the charge is separated between the donor and the acceptor moieties immediately after light absorption by the donor molecule and its transition to an excited state. Then, the charge separated state rather than an exciton migrates towards the electrode.
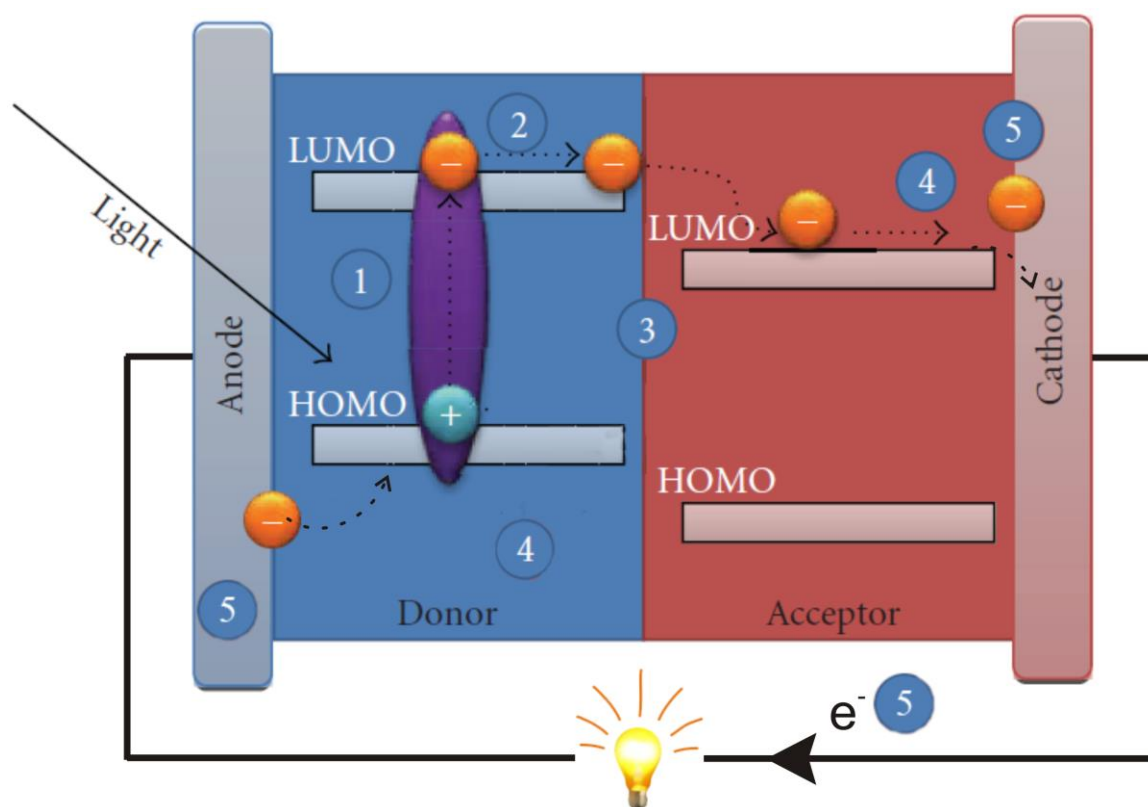
Scheme 2.1-2. A simplified energy diagram and operation scheme of an organic photovoltaic cell. The processes numbered are explained in text. (Adapted from Ref.[21])

2.1.3 Performance of a photovoltaic cell

In order to experimentally determine operational parameters of a PV cell, the current-voltage (*I-V*) curves for the cell in the dark and under light illumination are recorded (Fig. 2.1-7). The light used in our experiment is the AM 1.5 standard light.[27] It corresponds to the solar light passed through the 1.5 Earth atmosphere thicknesses (Fig. 2.1-1). Solar energy conversion efficiency, ϕ, may be expressed as the number of electron/hole pairs generated per *absorbed*

8

photon called quantum yield or internal quantum efficiency. Another parameter is the number of electron/hole pairs generated per *incident* photon, IPCE (incident-photon-to-current efficiency) or external quantum efficiency (Eqn. 2.1-1).

$$\text{IPCE}\ (\lambda) = \frac{n_{\text{electrons}}}{n_{\text{photons}}} = \frac{j/e}{P_{in}/h\nu} = \frac{j}{P_{in}} \times \frac{h\nu}{e\lambda} = \frac{j}{P_{in}} \times \frac{1240}{\lambda\ (\text{nm})} \qquad (2.1\text{-}1)$$

Here, j is the photocurrent density (A m^{-2}), and P_{in} is the incident light power (W m^{-2}). Other symbols have their usual meanings. The IPCE parameter provides a deep insight into the performance of a photovoltaic cell. It characterizes its three parameters, i.e., efficiency of light absorption by an active material, efficiency of charge separation between the donor and the acceptor, and efficiency of collection of electrons on external electrodes.
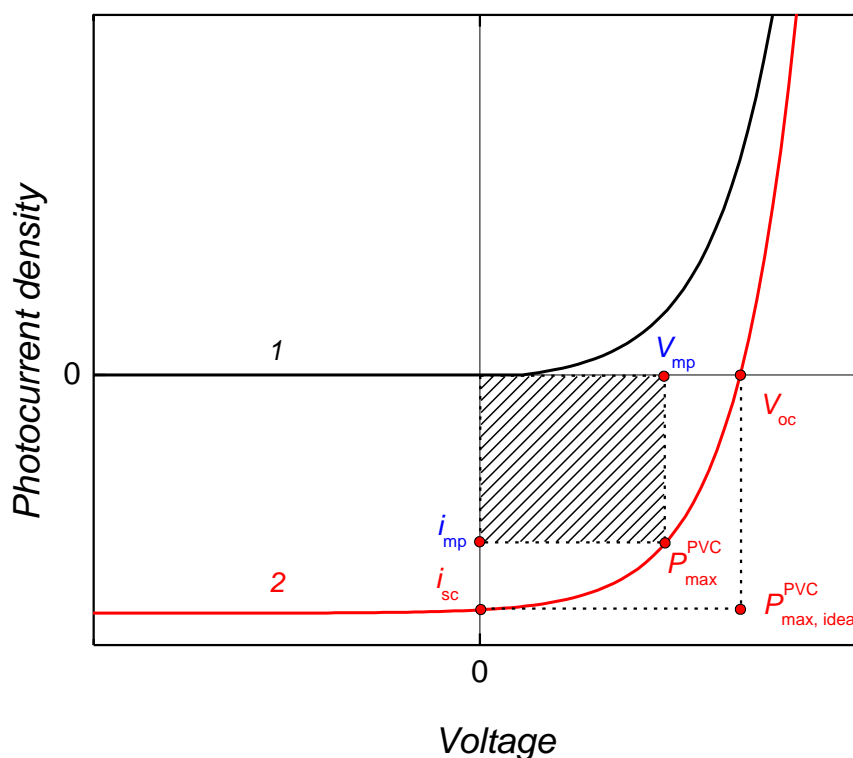
Figure 2.1-7. Schematic photocurrent-voltage curves for a PV cell (*1*) in the dark and (*2*) under light illumination; V_{oc} – open circuit voltage; V_{mp} and I_{mp} – voltage and photocurrent corresponding to maximum power of the photovoltaic cell, respectively; I_{sc} – short-circuit current; $P_{\text{max}}^{\text{PVC}}$ – maximum power of the PV cell; $P_{\text{max,ideal}}^{\text{PVC}}$ – maximum power of an ideal PV cell.

9

The most complex parameter describing the solar cell efficiency is the ratio of the output power of a photovoltaic cell, P_{out}, to the irradiation power, P_{in}, i.e., the overall power conversion efficiency (PCE), η, (Eqn. 2.1-2).[26]

$$\eta \ = \ \frac{P_{out}}{P_{in}} = FF \times \frac{V_{oc}\, I_{sc}}{P_{in}} \tag{2.1-2}$$

Here, FF is the so called fill factor, reflecting "ideality" of the cell, determined as a fraction of the maximum power divided by the ideal power (Eqn. 2.1-3).

$$FF \ = \ \frac{i_{mp}\, V_{mp}}{i_{sc}\, V_{oc}} \tag{2.1-3}$$

2.1.4 (Metallo-porphyrin or -phthalocyanine donor)-(C_{60} acceptor) OPV materials

Promising examples of solar light converting systems, which include photoelectroactive molecules as well as efficient mechanisms of charge separation upon photoexcitation and transfer, are provided by nature.[9,22,28-31] To mimic nature, electron donor-acceptor dyads of the metallophthalocyanine or metalloporphyrin and C_{60} adducts have, among other systems, been studied intensively (Fig. 2-8).[26,32,33]
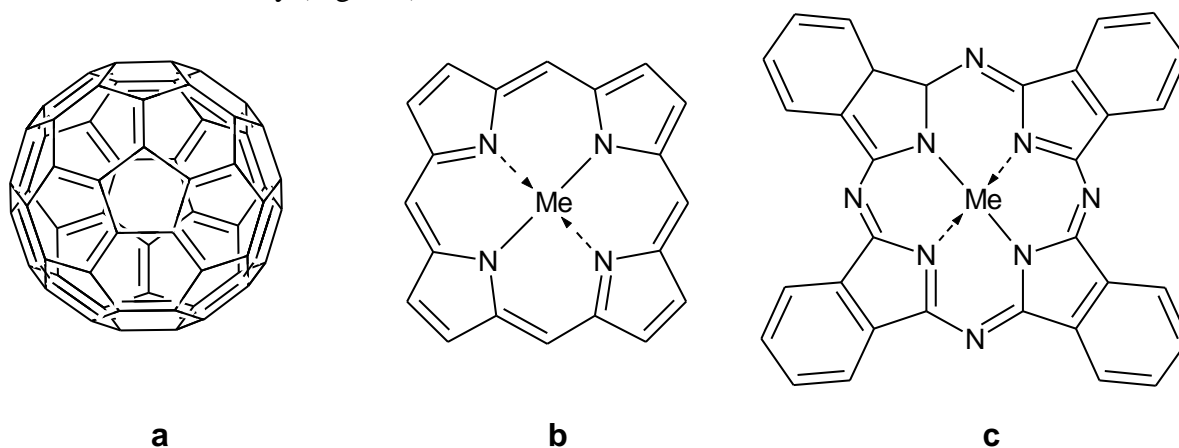
Figure 2.1-8. Commonly used compounds as building blocks of the photoactive, electrocatalytic, and energy storage materials. Structural formulas of (a) C_{60}, (b) metalloporphyrin, and (c) metallophthalocyanine.

Nature uses various derivatives of metalloporphyrins as photoexcitable electron donors for photosynthesis.[34] Properties of metallophthalocyanines are similar to those of

10

metalloporphyrins [35] while C_{60} is an efficient electron acceptor. Electronic properties of both electron donor and acceptor are relatively easily tuned for achieving desirable mechanical and electronic properties of the resulting donor-acceptor dyads. [36-38]

The simplest OPV cell material is just a mixture of the mentioned above donor and acceptor compounds. [39] This material can be prepared by vapor deposition, spray-coating, or Langmuir-Blodgett (LB) transfer onto a conducting transparent support, such as ITO or FTO, resulting in a film of organized D and A layers, as shown in Fig. 2.1-4.

More sophisticated strategy of the donor and acceptor organization for improved photovoltaic performance involves a tailor-synthesized donor-acceptor dyad. For instance, a donor-acceptor dyad of (metallophthalocyanine or metalloporphyrin)-C_{60} can be constructed according to at least two routes. [40,41] One uses covalent linking of D and A (Fig. 2.1-9).

a   b
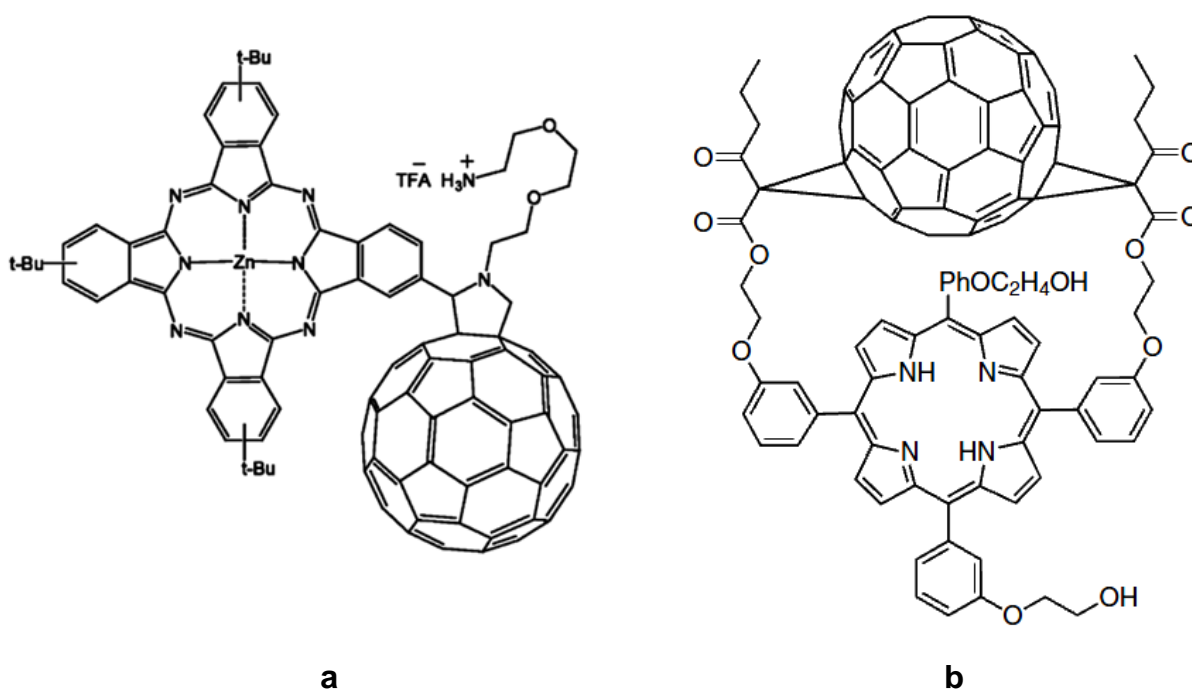
Figure 2.1-9. Structural formulas of examples of the covalently linked (a) (zinc phthalocyanine)-C_{60} and (b) (free-base porphyrin)-C_{60} D-A synthetic dyads. (Adapted from Refs. [42,43])

The other approach involves supramolecular arranging [44] of the donor and acceptor molecules by labile metal-ligand coordination (Fig. 2.1-10a), metal-ligand coordination and electrostatic interaction (Fig. 2.1-10b), and hydrogen bonds (Fig. 2.1-10c). Moreover, $\pi-\pi$

11

plane-to-plane stacking of the aromatic rings can be used.[11,45,46]   Advantages and disadvantages of all these approaches are different.
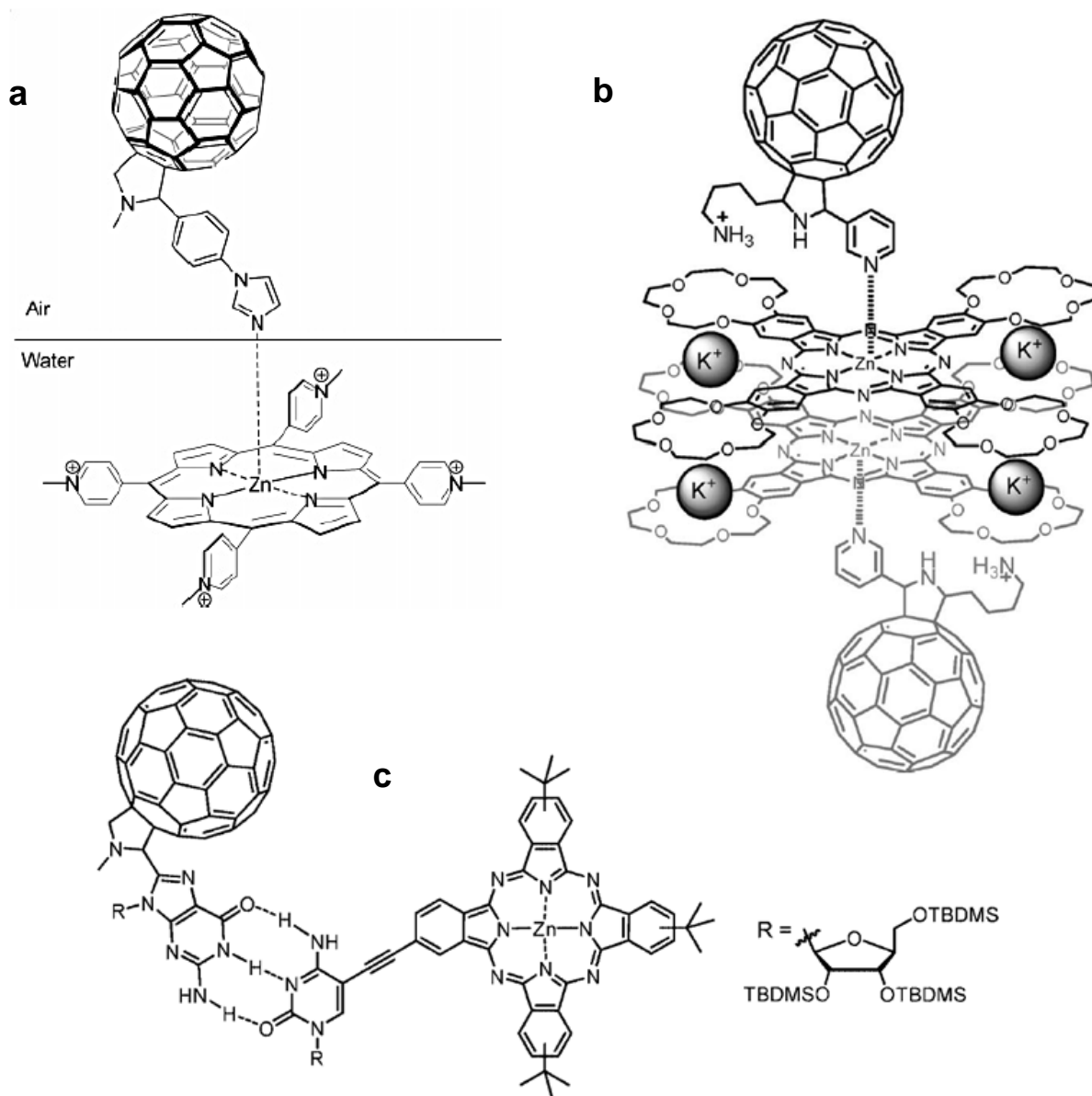
Figure 2.1-10. Structural formulas of examples of a supramolecularly assembled D-A dyads by (a) coordination,[47] (b) ion-dipole interaction and coordination,[48] and (c) hydrogen bonds (Watson-Crick nucleobase pairing).[49]

Covalent linking of the donor and acceptor moieties requires adoption of the time- and resource-consuming synthetic procedures. Photovoltaic efficiency of majority of the resulting dyads is moderate. This architecture prevailingly reveals a short lifetime of the charge separated state upon photoexcitation. This deficiency is due to close proximity of the D and

A moieties and low energy barrier for electron transfer back to HOMO level of the D molecule. However, the resulting dyad molecule is easily processable and stable.

Supramolecular approaches allow easier tuning of the distance between the D and A moieties, and, as a result, charge separation lifetimes of these systems are usually longer. Additionally, synthesis of smaller molecules requires less synthetic work and resources.

Variety of approaches to self-assembling of D and A allows for easy and precise tuning of electronic properties of the resulted dyads.

2.2 Oxygen electrocatalytic reduction

2.2.1 Pathways and mechanisms of oxygen electroreduction

Mechanism of oxygen electroreduction is one of the most experimentally and theoretically studied electrochemical processes over the history of electrochemistry. Nevertheless, it is still in focus of the scientific interest due to its widespread occurrence in nature and high practical importance.[50] On the one hand, products of the reaction are obvious; on the other, however, the mechanism of generation of products is rather complicated. It proceeds through several intermediates primarily depending on the nature of the electrode material, catalyst, and electrolyte.[51,52] In aqueous solutions, two paths of this reaction dominate. In acidic aqueous solutions, either direct one-step four-electron reduction of O_2 to water (Reaction 1 in Table 2.2-1) or two-electron reduction of O_2 to hydrogen peroxide (Reaction 2 in Table 2.2-1) followed by two-electron reduction of the latter (Reaction 3 in Table 2.2-1) may occur. In non-aqueous aprotic solvent solutions, one-electron reduction of oxygen to superoxide radical ($O_2^{\bullet-}$) proceeds (Reaction 7 in Table 2.2-1). In basic aqueous solutions, however, either one-step four-electron reduction of O_2 to hydroxide (Reaction 4 in Table 2.2-1) or two-step two-electron O_2 reduction to the hydrogen peroxide anion (Reaction 5 in Table 2.2-1) followed by this anion two-step two-electron reduction to hydroxyl (Reaction 6 in Table 2.2-1) is encountered.

Table 2.2-1. Standard redox potentials of different paths of electrochemical oxygen reduction.[53,54]

Electrolyte	Oxygen reduction reaction	Standard thermodynamic redox potentials, V vs. NHE at 25 °C
Acidic aqueous solution	(1) $O_2 + 4H^+ + 4e^- \rightarrow 2H_2O$	1.229
	(2) $O_2 + 2H^+ + 2e^- \rightleftarrows H_2O_2$	0.695
	(3) $H_2O_2 + 2H^+ + 2e^- \rightarrow 2H_2O$	1.763
Alkaline aqueous solution	(4) $O_2 + 2H_2O + 4e^- \rightarrow 4OH^-$	0.401
	(5) $O_2 + H_2O + 2e^- \rightleftarrows HO_2^- + OH^-$	-0.065
	(6) $HO_2^- + H_2O + 2e^- \rightarrow 3OH^-$	0.867
Non-aqueous aprotic solvents	(7) $O_2 + e^- \rightleftarrows O_2^{\bullet-}$	The potential is strongly solvent dependent

14

The rate-limiting step of the oxygen electroreduction in both acidic and basic aqueous solutions involves oxygen in a molecular form, i.e., the high energy double bond between oxygen atoms in a dioxygen molecule (498 kJ/mol) must be either fully or partially cleaved as the first step of the reaction. This initial step establishes an energetic barrier for the reaction, which must be overcome to end up with the final product. A rapid one-step four-electron oxygen electroreduction with a low overpotential is highly desired for efficient fuel cell operation and other applications. In order to decrease the activation energy, a catalyst is applied. The presence of a catalyst allows decreasing overpotential of the reaction.

According to the Butler-Volmer electrode kinetics, the current-overpotential dependence is given by Eqn. (2.2-1)

$$j_c = j^0_{O_2}(e^{\frac{\alpha n_\alpha F \eta_c}{RT}} - e^{\frac{(1-\alpha) n_\alpha F \eta_c}{RT}}) \tag{2.2-1}$$

where j_{O_2} – the oxygen reduction current density, $j^0_{O_2}$ – the exchange current density of the oxygen electrode reaction, n_α – the number of electrons transferred in the rate determining step, α – the charge transfer coefficient, η_c – the cathodic overpotential (E-E_{eq}) for oxygen electroreduction, F – the Faraday constant, R – the gas constant, T – the temperature in kelvins.

If the cathodic overpotential is higher than 25 mV, then the rate of the anodic reaction is negligibly slow and Eqn. (2.2-1) can be simplified to

$$j_{O_2} = j^0_{O_2}\, e^{\frac{\alpha n_\alpha F \eta_c}{RT}} \tag{2.2-2}$$

or

$$\eta = -\frac{RT}{\alpha n F}\ln j^0_{O_2} + \frac{RT}{\alpha n F}\ln j_{O_2} \tag{2.2-3}$$

By substituting $a = -\frac{RT}{\alpha n F}\ln j^0_{O_2}$ and $b = \frac{2.3\,RT}{\alpha n F}$, one arrives to the Tafel equation.

$$\eta = a + b\lg j_{O_2} \tag{2.2-4}$$

15

The Tafel plot of η_c vs. $\lg j_{O_2}$ is linear and its slope is $b = \frac{2.3\,RT}{\alpha\,n_\alpha\,F}$ at room temperature. As R, T, and F are constant, the only parameters determining this slope are α and n_α. The higher the Tafel slope, the more the current density increases with the overpotential. Thus, the reaction should exhibit a high Tafel slope, i.e., high α and n_α for high current at a low overpotential. The charge transfer coefficient for this reaction is a key factor determining the Tafel slope. For oxygen reduction, this coefficient is temperature dependent.

For oxygen electroreduction on carbon electrodes, usually two Tafel slopes are obtained, i.e., ~60 mV/dec and ~120 mV/dec. For noble metal electrodes, usually the ~60 and ~120 mV/dec slope is observed for a low and high overpotential, respectively. For electrodes coated with complexes of macrocycles with transition metals, different slopes are obtained including those, higher than that for the platinum electrode.

Fundamentals of cyclic voltammetry (CV) and linear sweep voltammetry (LCV) on a rotating ring electrode (RRE) and a rotating ring-disk electrode (RRDE), the most commonly used electroanalytical techniques for studies of oxygen electroreduction, are described in Section 2.5.5 below.

2.2.2 Organic electrode materials for oxygen electrocatalytic reduction

For decades, platinum has been used as the electrocatalytic electrode material for FCs. Platinum catalyzes both oxygen reduction and hydrogen oxidation at the cathode and anode, respectively, exhibiting unparalleled efficiency and stability.[55-57] Usually, it is used in a form of small particles deposited on a conducting support. So far, no cheap, comparably stable, and efficient catalyst for commercial applications is available. The cost of platinum embedded in a modern catalytic material is nearly $10 for a 1 kW PEM FC.[58,59] Noble-metal-free catalysts for fuel oxidation at an FC anode is another broad topic, which is out of scope of the present research.[60]

In recent years, organic electrocatalytic electrode materials for FC application attract much attention.[61-63] Among organic electrocatalytic materials, the biomaterials, such as certain enzymes, reveal high performance. However, their instability at high temperatures, at high and low solution pH values, and in the presence of certain ions limits the FC application of enzyme catalysts. In attempt to overcome these limitations, several different free-of-noble-metal cathode materials were devised for fabrication of an inexpensive, efficient, and technologically viable FC.[64-67] Among them, different metalloporphyrins and

16

metallophthalocyanines, viz. those of Co, Fe, Ir, Ru, etc., were promising catalysts for the oxygen electroreduction.[54,68]

Single-macrocycle metalloporphyrins or metallophthalocyanines catalyze oxygen reduction to hydrogen peroxide. However, the catalytic cathode efficiency toward O_2 electroreduction dramatically increases for the co-facially stacked Co or Fe porphyrin dimers (Scheme 2.2-1).[69-71] If the plane-to-plane distance of the stacked metalloporphyrin rings is fixed at ~0.35 nm, to accommodate the dioxygen molecule in a way that both oxygen atoms interact with the metal atoms, then the resulting dimer catalyzes oxygen electroreduction in aqueous solutions of low pH directly to water via the one-step four-electron transfer.[72] If this mechanism holds, then no hydrogen peroxide is produced. The presence of hydrogen peroxide as a product of oxygen reduction causes fast degradation of the catalyst thus precluding application of this catalyst to FCs.
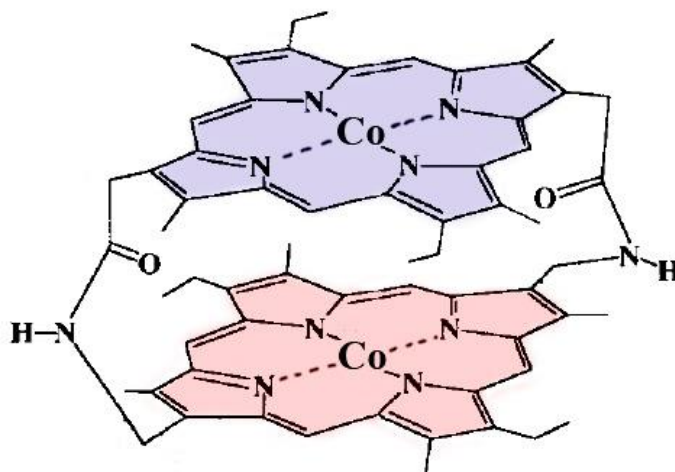
Scheme 2.2-1. Simplified structural formula of the dicobalt diporphyrin. (Adapted from Ref.[54])

The following mechanism of the oxygen electrocatalytic reduction to water by co-facial dicobalt diporphyrins was proposed (Fig. 2-12).[54]

Procedures of syntheses of co-facial porphyrin dimers are not trivial. It took over a decade to reproduce this synthetic procedure. Therefore, other ways, which allowed to avoid a complicated and tedious synthesis of a stacked Co porphyrin dimer were developed. A simple and elegant way in that direction was to arrange co-facially ion-pairs of commercially available Co porphyrin derivatives of opposite charges located on their four peripheral substituents (Fig. 2-13).[73]

17
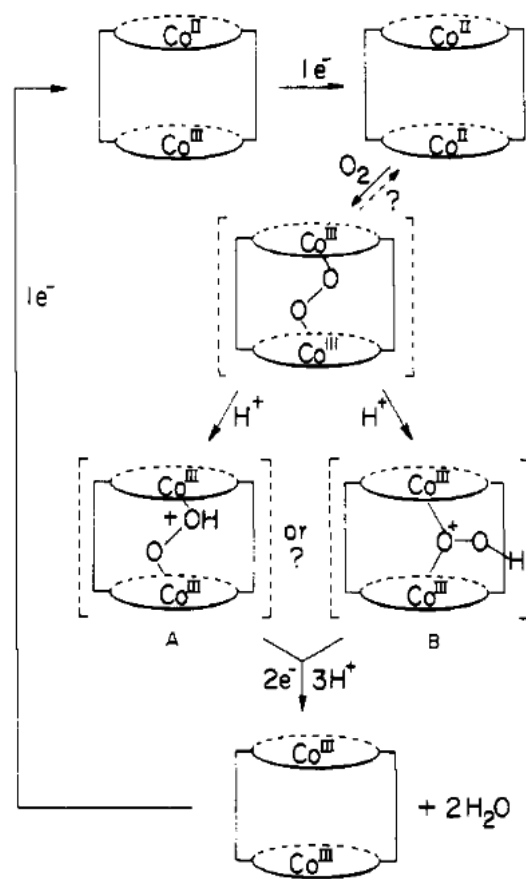
Figure 2.2-2 The proposed mechanism of the oxygen dicobalt-diporphyrin catalyzed electroreduction. (Adapted from Ref.[69])
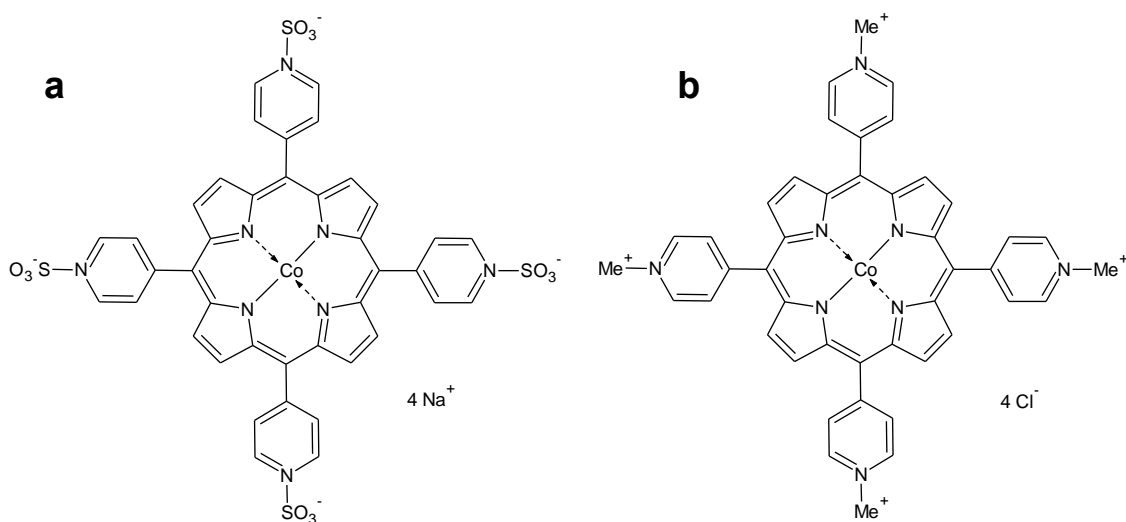
Figure 2.2-3 Structural formulas of cobalt porphyrins (a) tetrasodium salt of [tetrakis(4-sulfonatophenyl)porphyrinato]cobalt and (b) [tetrakis(*N*-ethylpyridyl)porphyrinato]cobalt tetrachloride used to form an ion-pair dimer adsorbed on GCE used for dioxygen electrocatalytic reduction.[73]

18

Similar to the initial Co porphyrin dimer approach was explored using so-called "Pacman" metalloporphyrin dimers (Fig. 2-14).[74] In these dimers, two metalloporphyrin moieties were linked together at only one side of the macrocycle. These dimers electrocatalyzed dioxygen reduction, partially, via one-step four-electron mechanism.
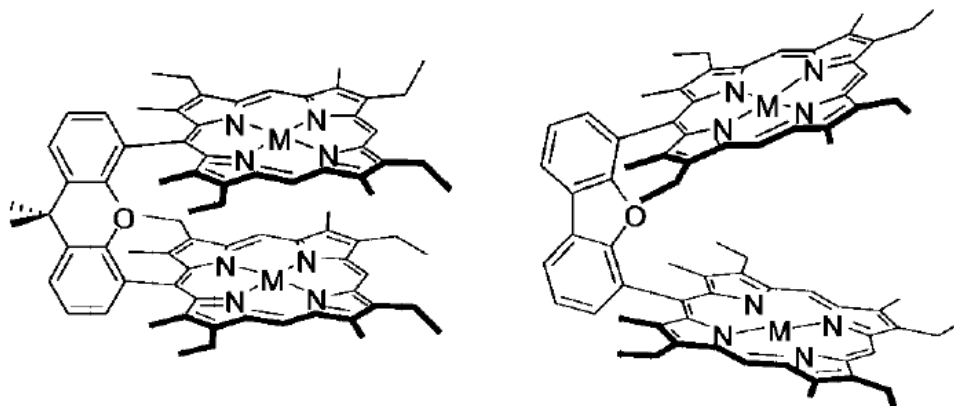
Figure 2.2-4. Structural formula of the "Pacman" dimer metalloporphyrins. (Adapted from Ref.[74])

However, flexibility of the metalloporphyrins bound only at one point resulted in lower efficiency towards direct dioxygen electroreduction to water and in the presence of hydrogen peroxide as the oxygen electroreduction product. The mechanism proposed for oxygen electroreduction by the "Pacman" Co porphyrin dimers is shown in Fig. 2.2-2. The small and large cycles correspond to the two-electron oxygen electroreduction to hydrogen peroxide and to the four-electron electroreduction to water, respectively. In most of the reported works, monomers of Co porphyrins were adsorbed on an electrode surface. Beside the demand of high efficiency, processability, low cost of the precursors, and ecological compatibility, the application of an electrocatalytic material in a commercial fuel cell needs meeting several extreme requirements with respect to its performance. These include operation in a wide pH range as well as high durability, and reproducibility of electrocatalytic activity. Unfortunately, the adsorbed metalloporphyrin films can relatively easy be peeled off the electrode surface. Therefore, they cannot be considered as optimized materials for application in commercial FCs.

Because the one-step four-electron reduction was reported for successful electrocatalytic oxygen reduction involving co-facially stacked Co porphyrins, this

19

mechanism seems to be very appealing for development of an electrocatalytic cathode material. One of the routes of preparation of an efficient and feasible material of that kind may, therefore, involve synthesis of a polymer film using prearranged axially stacked template Co porphyrin monomer molecules.[75] Therefore, this approach has been explored in the present research. Moreover, catalytic efficiency of a metalloporphyrin polymer may be enhanced by attaching certain substituents to the porphyrin macrocycle.
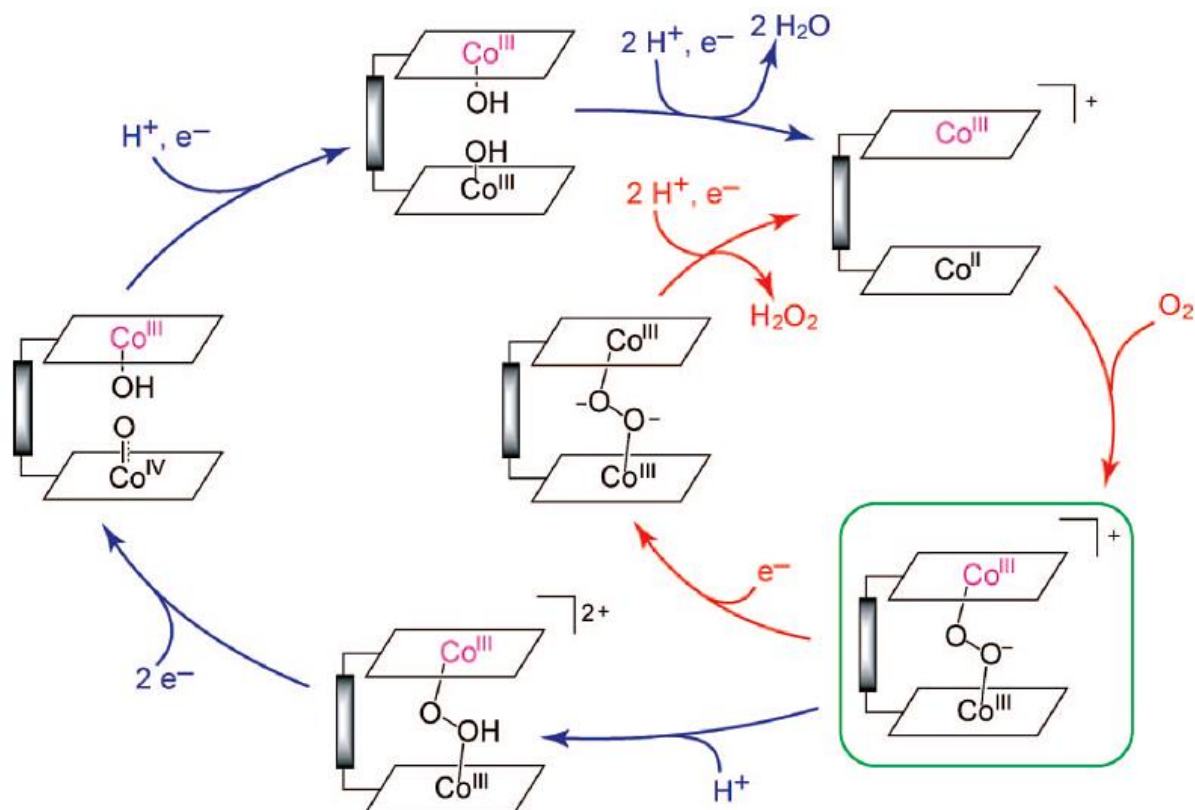
Scheme 2.2-2. The proposed pathways of dioxygen electrocatalized reduction by the "Pacman" cobalt porphyrin dimer.[74]

2.2.3 Applications of oxygen electrocatalytic reduction

Application of the dioxygen reduction catalysts is most attractive in the fuel cell (FC) cathodes. FCs are devices for electrical energy generation through electrochemical redox reactions rather than combustion. FCs are in the focus of attention because of prominent fuel conversion efficiency, easy scalability, low to zero harmful emission, simple construction, ability to use various types of fuel, and bringing energy to remote locations with no infrastructure, and as an energy source for electric vehicles.

20

The simplest fuel cell contains three basic components, such as electrically connected platinum anode and platinum cathode, and an electrolyte. A fuel is delivered to the platinum anode and oxygen to the platinum cathode.[59]

There are many types of FCs. They can be split into two subsets, i.e., proton exchange membrane (PEM) FCs and high temperature FCs.[58] Each FC type uses different fuel and is characterized by different electrochemical reactions, operating temperatures, electrolytes, etc. However, overwhelming majority of them uses oxygen as an oxidant on the cathode. The reaction kinetics is slow at moderate temperatures and a catalyst is needed to reach useful reaction rate for FC practical operation.
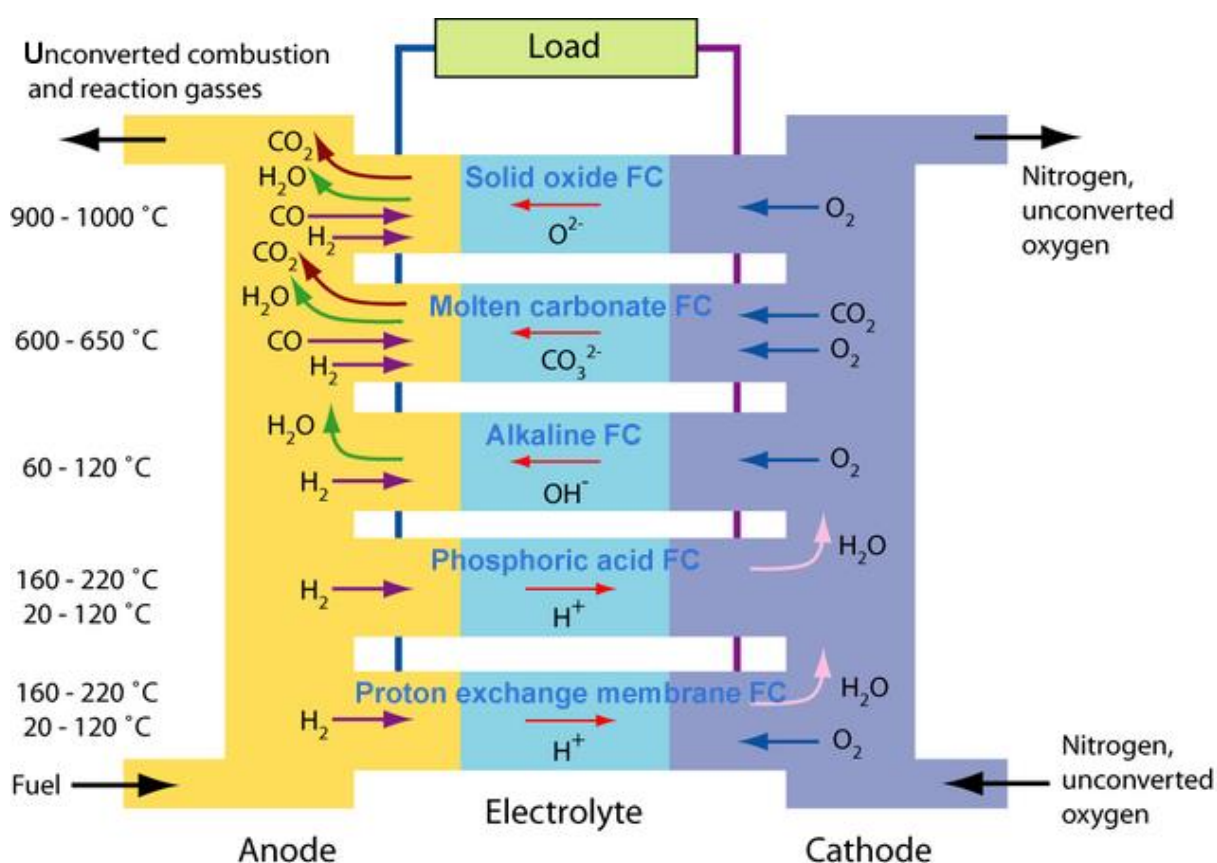
Figure 2.2-6. Principle of operation of a fuel cell. (Adapted from www.doitpoms.ac.uk)

Particularly promising for powering portable electronic devices and mechanical vehicles is the PEM FC with a subset of FCs utilizing different fuels. The key component of a PEM FC is the membrane electrode assembly.[59] It is composed of two main parts, namely, the catalyst (or catalysts) and the membrane. Electrochemical reactions inside the FC proceed

21

on electrodes coated with catalysts and the membrane serves for transporting protons from the anode, where they are generated, to the cathode, where the redox reaction product and heat are generated. While the membrane is proton conductive, it must be impermeable to the fuel and the oxidant.

As long as a fuel and an oxidant are supplied to the FC from an external source, the device works continuously (Fig. 2.2-6). If the fuel is hydrogen and the oxidant is oxygen, the reactions on the electrodes are as follows (Eqns. 2.2-5 and 2.2-6).

$$\text{Anode: } H_2 \rightarrow 2H^+ + 2e^- \qquad\qquad (2.2\text{-}5)$$

$$\text{Cathode: } O_2 + 4H^+ + 4e^- \rightarrow 2H_2O \qquad\qquad (2.2\text{-}6)$$
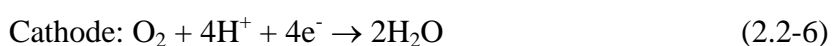
The only product of the FC operating on the hydrogen fuel is water. Due to high power density and environmental neutrality, the hydrogen-fuelled PEM FC is attractive on the one hand, however, it raises important issues of hydrogen production and/or storage on the other.[76]

Beside fuel cells, there are many other important fields of application of oxygen electrocatalytic reduction, such as metal-air batteries,[77] wastewater purification,[78,79] determination of oxygen in a gas or liquid medium,[80] etc.

22

2.3 Carbon nanomaterial composites for energy storage devices

A rapid growth of portable electronics and interest in energy sources for electric vehicles of recent decades generate demand of the electric energy storage devices and compact power sources. One of such sources is an electrochemical capacitor, also known as a supercapacitor or ultracapacitor.[81] With respect to their power density and energy density, supercapacitors provide a bridge between double-layer capacitors and batteries (Fig. 2.3-1).[82] Thus, they are devised not to substitute batteries or fuel cells but to be used where their advantages allow overcoming deficiencies of other energy storage devices. These include viability during fast charging and discharging, energy density higher than that of electrostatic capacitors, and high durability with respect to the number of charging-discharging cycles.
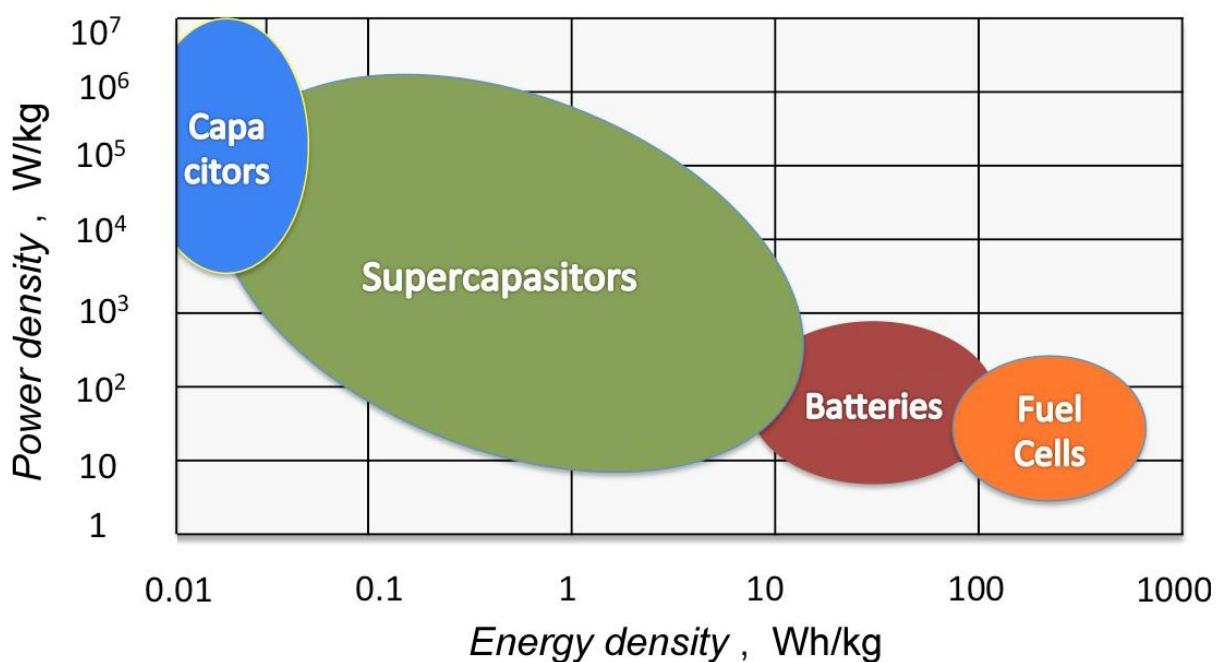
Figure 2.3-1. The Ragone plot of power density vs. energy density for various energy-storing electrochemical devices. (Adapted from www.large.stanford.edu)

The drawback of supercapacitors consist in a relatively low energy density compared to that of batteries. In practice, it results in a need to build these electric energy storage devices of a large size and, thus, limits their applications. To solve this issue, carbon nanomaterials with highly developed surface, such as carbon nanotubes, graphene, and activated carbon, are widely used for fabrication of functional materials for

23

supercapacitors.[83,84] Furthermore, carbon functional materials are commonly modified with redox films resulting in composites with a high energy density.

2.3.1 Important parameters of supercapacitors

Capacitance of an electrostatic capacitor (Scheme. 2.3-1) is descried by Eqn. 2.3-1.

$$C = \frac{\varepsilon_0 \varepsilon_r A}{d} \tag{2.3-1}$$

Here C is the capacitance of the capacitor while ε_0 and ε_r are the electric permittivity of a dielectric material and free space, respectively, d is the distance between the capacitor conducting plates, and A is the plate surface area.
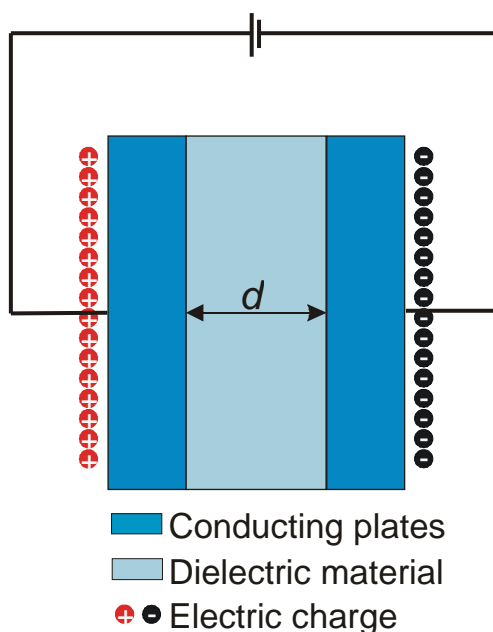
Scheme 2.3-1. A sketch of an electrostatic capacitor. (Adapted from Ref.[85])

Thus, the lager the A and the smaller the d the higher is the capacitance. A simple way to increase area of plates is to use carbon nanomaterials, like single-wall carbon nanotubes or graphene, because their surface area is the highest with respect to mass of the material. Besides, these carbon materials feature high conductivity as well as high chemical and electrochemical stability.[86] Electroactive surface area of these materials reaches thousands $m^2\ g^{-1}$ (Fig. 2.3-2a).

24

Further increase of energy density of a supercapacitor is achieved by engaging pseudocapacitance, which is due to faradaic processes occurring on the electrodes. Towards that, nanostructured carbon materials modified with redox species, such as conducting polymers or inorganic oxides, are used (Fig. 2.3-2b).[87]

Carbon-like nanostructured material
Conducting polymer
Electrolyte solution
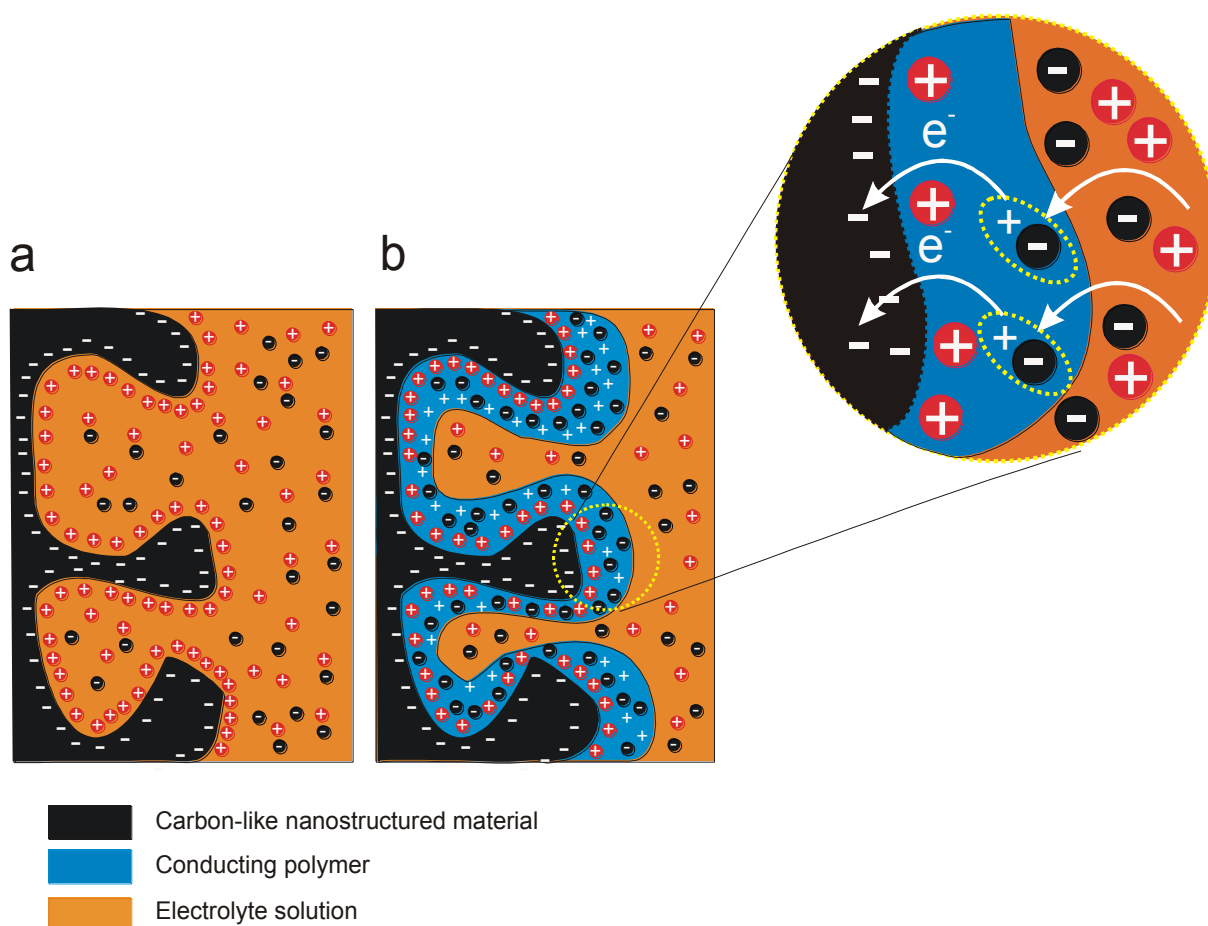
Scheme 2.3-2. The charge stored (a) in a double-layer capacitor using, e.g., carbon, and (b) in a pseudo-capacitor using, e.g., a conducting polymer modified carbon. (Adapted from Ref.[85])

The latter capacitors are called "pseudocapacitors". The redox species applicable for that purpose should be electrochemically stable, reversibly electro-oxidizable or -reducible and, moreover, this redox process should be fast. The charge stored in these devices highly depends upon the polarizing voltage according to Eqn. 2.3-2.

$$C = \frac{\mathrm{d}Q}{\mathrm{d}V_c} \qquad (2.3\text{-}2)$$

25

Here, Q is the charge accumulated and V_c is the voltage applied. The addition of a redox material solves the issue of a low energy density. However, it decreases power density and stability of the resulting pseudocapacitor.

Other important supercapacitor parameters involve its energy, E^{sc}, maximum power density, P^{sc}, determined according to Eqns. 2.3-3 and 2.3-4, respectively.

$$E^{SC} = \frac{1}{2} C_s \, U^2 \tag{2.3-3}$$

$$P^{SC} = \frac{U^2}{4R_c} \tag{2.3-4}$$

Here, C_s (F g^{-1}) is the total specific capacitance of the capacitor, U (V) is the capacitor operating voltage, and R_c (Ω) is the equivalent series resistance.

The capacity of a supercapacitor is more precisely determined in a galvanostatic charge-discharge experiment using a two identical electrode system (Scheme 3.2-2).
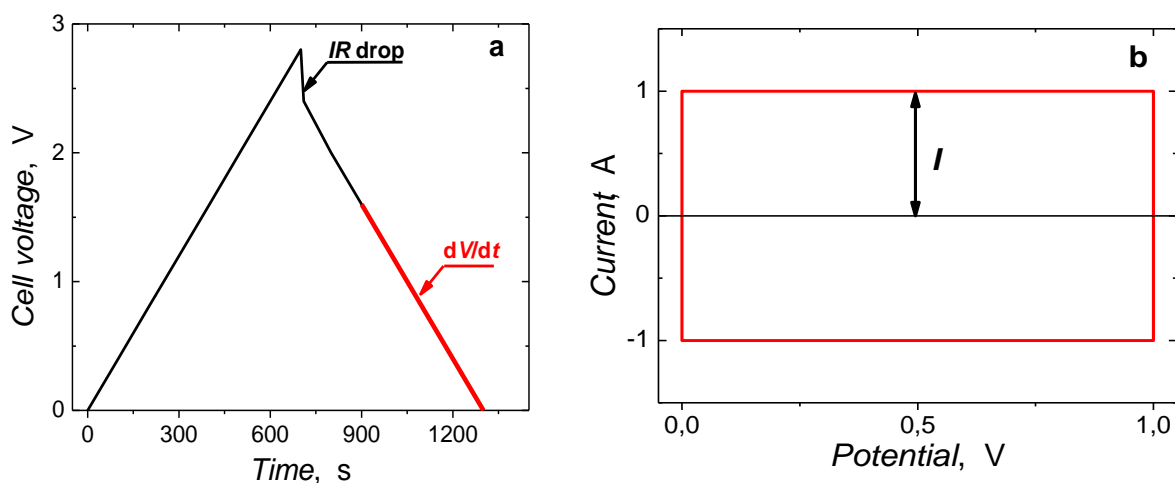
Figure 2.3-4. Idealized (a) a charge-discharge galvanostatic curve and (b) a CV curve for an electrochemical double-layer capacitor used for determination of specific capacitance. (Adapted from Ref.[85])

26

This system simulates electrochemical behavior of a supercapacitor better than a three-electrode system with only one WE, which is coated with an electroactive material film. In the two-electrode system, C_s of the supercapacitor is determined using Eqn. 2.3-5.

$$C_s = \frac{i}{m\left(\frac{dV}{dt}\right)}$$ (2.3-5)

Here, i is the constant discharge current, dV/dt is the slope of the charge-discharge curve (Fig. 2.3-4a), and m is the mass of the electroactive material film of the WE.

The power of a supercapacitor is more precisely determined in a real-life system by discharging the supercapacitor through a resistor. In this discharging, the power, P^{sc}, is described by Eqn. 2.3-6.

$$P^{SC} = \frac{1}{R}\int_{t_1}^{t_2} U^2(t)\, dt$$ (2.3-6)

Here, U is the voltage decaying from time t_1 to t_2 due to discharging of the device through the resistor of the resistance R.

A relative capacity measurement is commonly performed for determination of stability of an active material of a supercapacitor. For that purpose, the ratio of time, required to discharge a capacitor in a first charge-discharge cycle, to that, subsequent in a multiple galvanostatic charge-discharge cycling, is used.

Initially, supercapacitors were categorized into three types. Supercapacitors of type I use the same p-doping polymer for both electrodes. Those of type II use different p-doping polymers; they can be either symmetric or asymmetric. Type III supercapacitors are symmetric, advantageously utilizing the same p-doping and n-doping material. Then, type IV of supercapacitors was introduced.[88] This type involves supercapacitors utilizing different p- and n-doping polymers. In general, supercapacitors of type I and III have no inherent polarity, but the others are polar and require proper connection, like batteries.

An ideal supercapacitor should feature high C_s, U, and P, long life in charge-discharge cycling, and low R.[89]

2.3.2 Polymers for energy storage materials

Two types of polymers are used for supercapacitors, i.e., π-electron conducting polymers (ECPs) and redox-conducting polymers (RCPs). The most commonly used ECPs include polypyrrole, polyaniline, and polythiophene as well as their derivatives.[85] These polymers can easily be synthesized chemically or electrochemically. They feature high C_s values and high conductivity.[90] The ECPs developed so far are electroactive mostly in the positive potential range and, therefore, their maximum operating voltage is quite limited. The C_s of the composites of these polymers with carbon nanomaterials is in the range of 120 to 900 F g^{-1}.[85] However, it is difficult to compare mutually these values, because they are determined under different conditions and by using different methods. Both ECPs and RCPs are prepared and tested mainly with respect to their potential application for energy storage as composites with carbon nanomaterials. Commonly, a two-step procedure is applied, where the first step consists in deposition of a carbon nanomaterial on an electrode and the second involves deposition of a polymer film onto the deposited carbon nanomaterial.
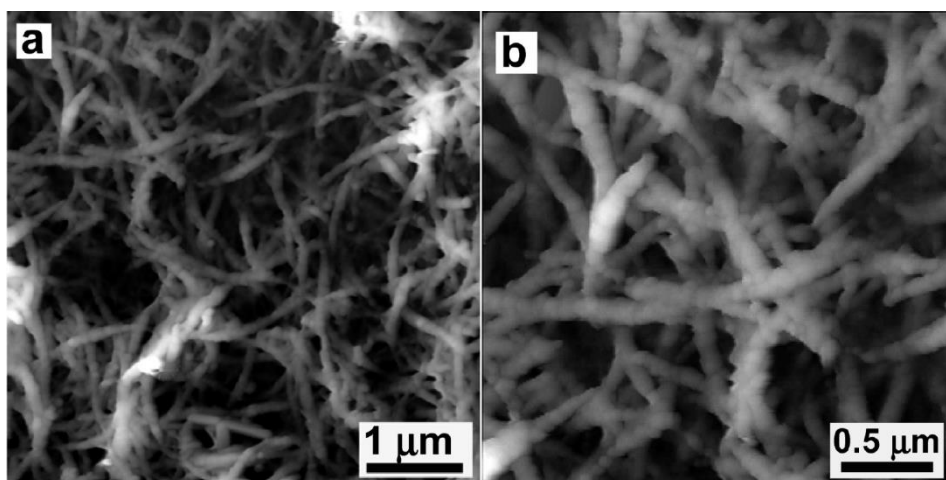
Figure 2.3-5 The AFM images of the C_{60}-O polymer film deposited by potentiodynamic electropolymerization over the electrophoretically deposited pyr-SWCNTs. (Adapted from Ref.[91])

Among RCPs, C_{60}-based polymers are those most extensively studied. Importantly, those polymers are electroactive in the negative potential range. For instance, a C_{60}-O polymer film was deposited onto a pyr-SWCNTs film, resulting in the pyr-SWCNTs/C_{60}-O composite (Fig. 2.3-5).[91] For that, first, pyr-SWCNTs were electrophoretically deposited onto

an ITO electrode. Then, a C_{60}-O polymer film was deposited onto pyr-SWCNTs by the (superoxide anion radical)-induced electropolymerization. Importantly, the C_{60}-O polymer was formed around the pyr-SWCNTs. Specific capacity of this composite was, $C_s = 184$ F g^{-1}. It was determined using a three-electrode system by CV at the potential scan rate of 100 mV s^{-1}.

The Pd-assisted electropolymerization of C_{60} is another way to obtain a fullerene polymer film. Such a polymer was deposited by electropolymerization onto MWCNTs, SWCNTs, and oxidized carbon nano-onions (ox-CNOs).[92] The C_s value of the resulting composite was dependent on the (carbon nanomaterial)-to-(C_{60}-Pd) ratio. The highest C_s value was rather low equaling 65, 60, and 20 F g^{-1} for the SWCNTs-to-C_{60}-Pd ratio of 2 : 1, MWCNTs-to-C_{60}-Pd ratio of 15 : 1, and ox-CNOs-to-C_{60}-Pd ratio of 2 : 1, respectively. These C_s values were determined from the CV measurements in a three-electrode cell at the potential scan rate of 10 mV s^{-1}. These low C_s values may be due to the deposition procedure used, i.e., to drop-casting deposition of the CNTs film on the electrode. In this procedure, CNTs tend to aggregate and, therefore, the specific surface area is low.

Electrochemical properties of redox conducting in the negative potential range Pd-bridged C_{60} polymers, synthesized by electropolymerization and by chemical polymerization, were compared.[93] Generally, the chemically synthesized C_{60}-Pd polymer film was composed of bigger aggregates (~150 nm in diameter) than that prepared by electropolymerization. The electrochemical stability of the chemically synthesized C_{60}-Pd polymer was low because of a limited electric contact between huge polymer aggregates. The C_s value of this polymer was 35 F g^{-1}, determined by CV, in the range of the potential scan rate of 20 to 300 mV s^{-1} with 1.5 μg of the composite deposited on the 1.5-mm diameter Au disk WE. However, the C_s was lower the higher was the potential scan rate for the composite mass exceeding 18.5 mg. The C_s value of the electropolymerized C_{60}-Pd was ~300 F g^{-1} at the same potential scan rate.[94]

Combination of polymers with electrochemical activity in different potential ranges results in a material with the highly desirable extended potential range. The combination of ECP and RCP is very promising for that purpose. One of the elegant ways to combine ECP and RCP in a polymer composite is to synthesize monomers that polymerize resulting in polymers conducting both in the positive and negative potential range.

Polymers of C_{60}, electroactive in both the positive and negative potential range, were synthesized by electropolymerization.[95] The piperazine (PPZ-C_{60}), pyrrolidine [CH$_3$-(pyr-

29

C_{60})], and pyrrolidine salt [(CH_3)$_2$-(pyr-C_{60})]$^+$ fullerene adduct monomers were reductively electropolymerized in the presence of Pd(ac)$_2$ to form the 3-D Pd-bridged polymers of C_{60}. The polymer of the piperazine adduct of C_{60} revealed redox activity both in the negative and positive potential range. However, the authors did not provide details on its C_s.

A C_{60}-polyaniline emeraldine based hybrid was fabricated by chemical polymerization. In this hybrid, polyaniline nanowires and aggregates were interconnected with the C_{60} cores (Scheme 2.3-5) resulting in a string-of-beads-like film morphology.[96,97] The C_s value of the resulting polymer material was evaluated by galvanostatic charging and discharging in a three-electrode system in the potential range of -0.1 to 0.7 V vs. Ag pseudo-reference electrode. The maximum C_s value of 776 and 492 F g^{-1} was determined for the C_{60}-palyaninline emeraldine based hybrid and the polyaniline-emeraldine based hybrid, respectively, at the 1 mA cm^{-2} current density. The specific energy of the C_{60}-polyaniline emeraldine based hybrid was 64 and 43 W h kg^{-1} at the current density of 1 and 100 mA cm^{-2}, respectively.
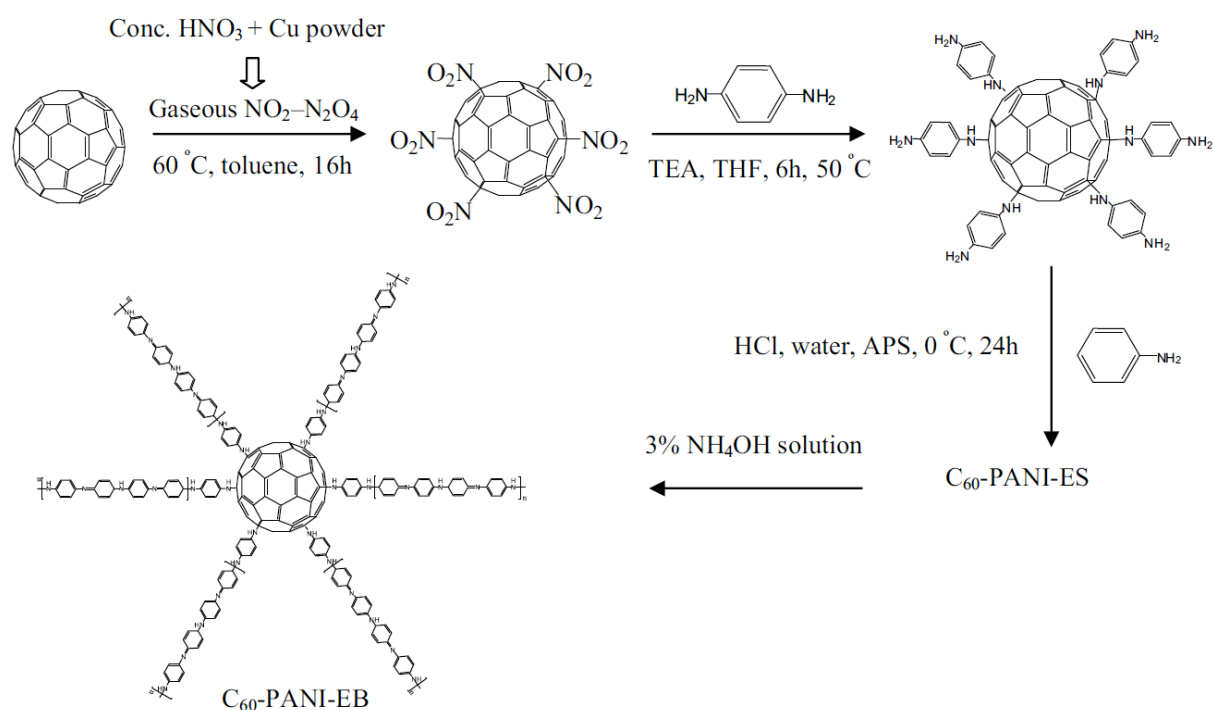
Scheme. 2.3-5 The synthesis of a hybrid fullerene-aniline polymer material conducting in both the positive and negative potential range. (Adapted from Ref.[96])

The main drawback of conducting polymers is their low stability with respect to repeated electrooxidation and electroreduction. This is mainly because of the accompanying transfer of ions with their solvation shells across the polymer-solution interface for charge compensation. Because of that, the polymers repeatedly swell and shrink during oxidation and reduction. This "breathing" breaks the polymer 3-D structure. This undesired effect may largely be decreased by using conducting polymers in a form of thin films in composites with conducting carbon nanomaterials. Particularly, a conductive carbon nanomaterial with high surface area increases mechanical stability of a composite, decreases ion diffusion depth by developing area coated by the polymer and enhances electrical contact between polymer aggregates.

2.4 Selected mechanisms of electrochemical polymerization

2.4.1 Electropolymerization of porphyrin derivatives

An active polymer film material for photovoltaics, electrocatalysis, or energy storage is more versatile than that, adsorbed on a solid substrate. Electrochemical polymerization is advantageous with respect to chemical polymerization enabling a precise control over the process. Towards that, a range of electropolymerizable porphyrin monomers was synthesized and several procedures of porphyrin electropolymerization were developed.
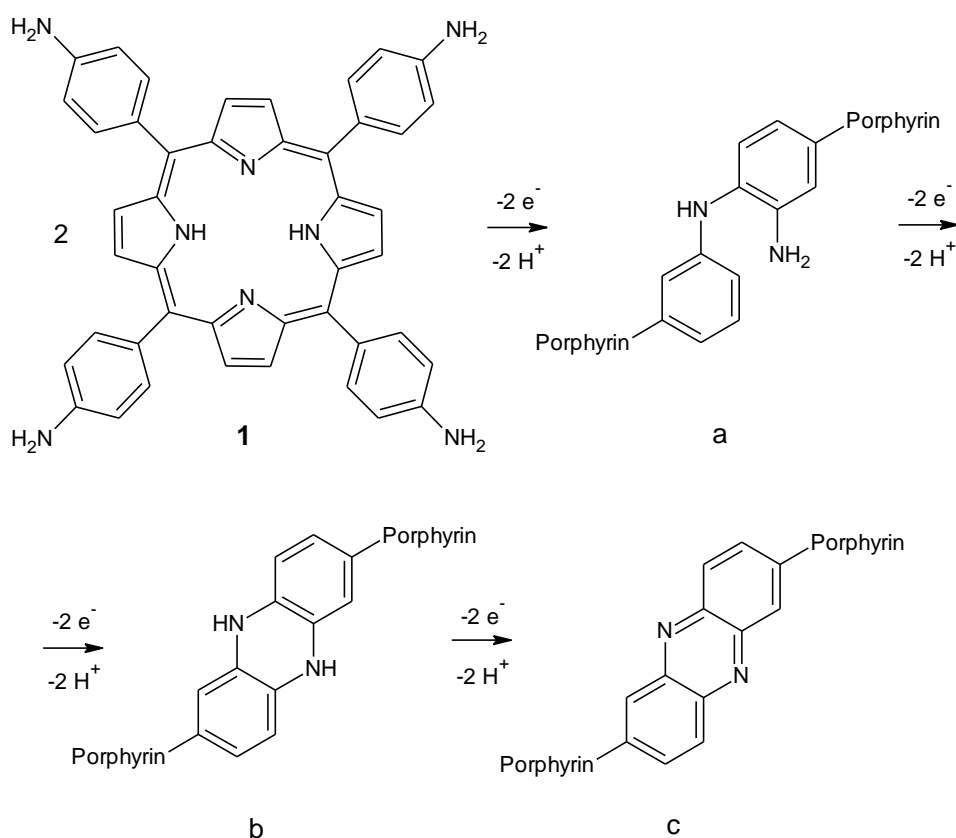
Scheme 2.4-1. Oxidative possibilities of (1) *tetrakis*-5,10,15,20-(4-aminophenyl) porphyrin coupling, which leads to formation of linking units of (a) 1,2-aminodiphenylamine, (b) dihydrophenazine, and (c) phenazine.[98]

There are two main approaches to electropolymerization of porphyrins. One, the most commonly used, involves organic synthesis of a porphyrin bearing electropolymerizable peripheral substituents capable of oxidative radical coupling. For instance, porphyrins with

aminophenyl substituents at *meso*-positions are electropolymerized in a polyaniline fashion that way (Scheme 2.4-1).[98,99]

Alternately, other peripheral substituents, including pyrrole, hydroxyphenyl, thiophene, vinyl-terminated, etc., may be used. Then, the reaction mechanisms follow the fashion of those of polymerization of the substituents.

The other approach requires the presence of a bidentate nucleophilic ligand, such as 4,4'-bipyridine (BPY) or 3,6-di-4-pyridyl-1,2,4,5-tetrazine (PY-TZ-PY) in the solution for electropolymerization.[100] First, this ligand is coordinated by the central metal atom of the macrocycle, and then in excess of the ligand it may be incorporated into the macrocycle by consecutive potential cycling.[101]
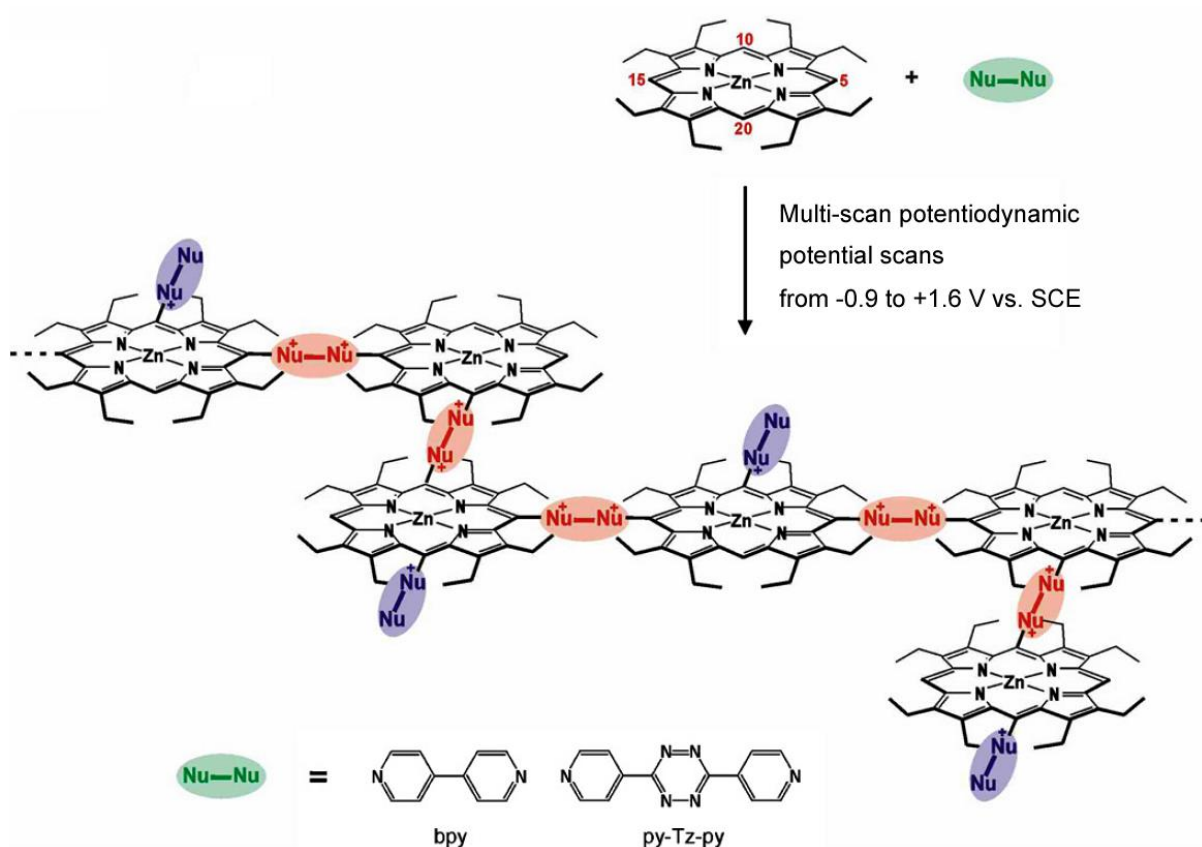
Scheme 2.4-2. Electrochemical polymerization of a zinc porphyrin in the presence of a nucleophilic ligand, such as BPY or PY-TZ-PY. (Adapted from Ref. [100])

That way, a 3-D polymer structure is formed. Linear potential cycling in a relatively narrow potential range, e.g., between 0 and 1.30 V, does not result in formation of a polymer film.
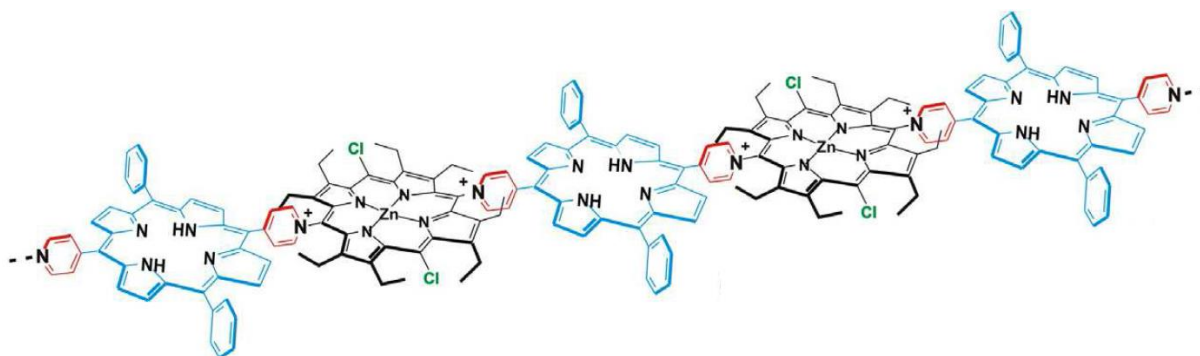
Figure 2.4-3. One-dimensional porphyrin copolymer prepared by electropolymerization. (Adapted from Ref.[102])

However, a one-dimensional polymer is formed if two *meso*-positions of the macrocycle are blocked, e.g., with the phenyl substituent (Fig. 2.4-3).[102]

2.4.2 Electropolymerization of [C$_{60}$]fullerene

There are many ways of fullerene polymer assembling. By type, they can be divided into chemical or electrochemical polymerization, and supramolecular assembling. That way, different structures of a fullerene polymer can be obtained (Scheme 2.4-2).
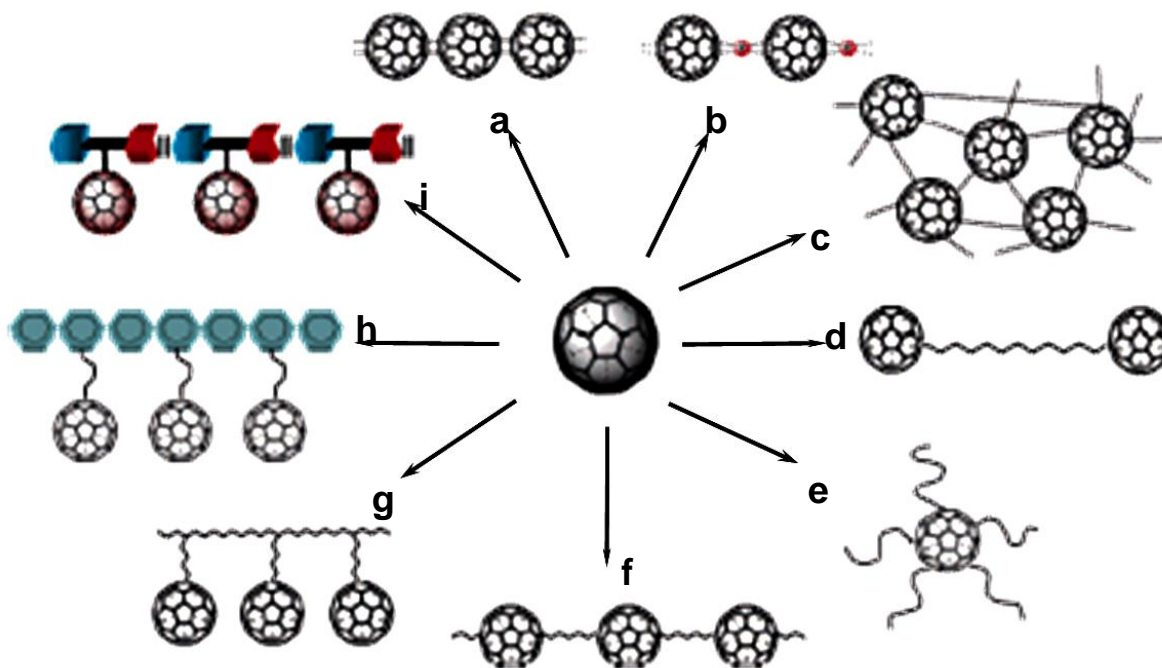
Scheme 2.4-2. [C$_{60}$]Fullerene polymers: (a) all carbon, (b) sandwiched, (c) cross-linked, (d) end-capped, (e) star-capped, (f) main-chained, (g) side-chained, (h) double-cabled, and (i) a supramolecular assembly. (Adapted from Ref.[103])

34

In our research, a fullerene polymer was prepared by (transition metal complex)-assisted electropolymerization (Scheme 2.4-3).[104,105]
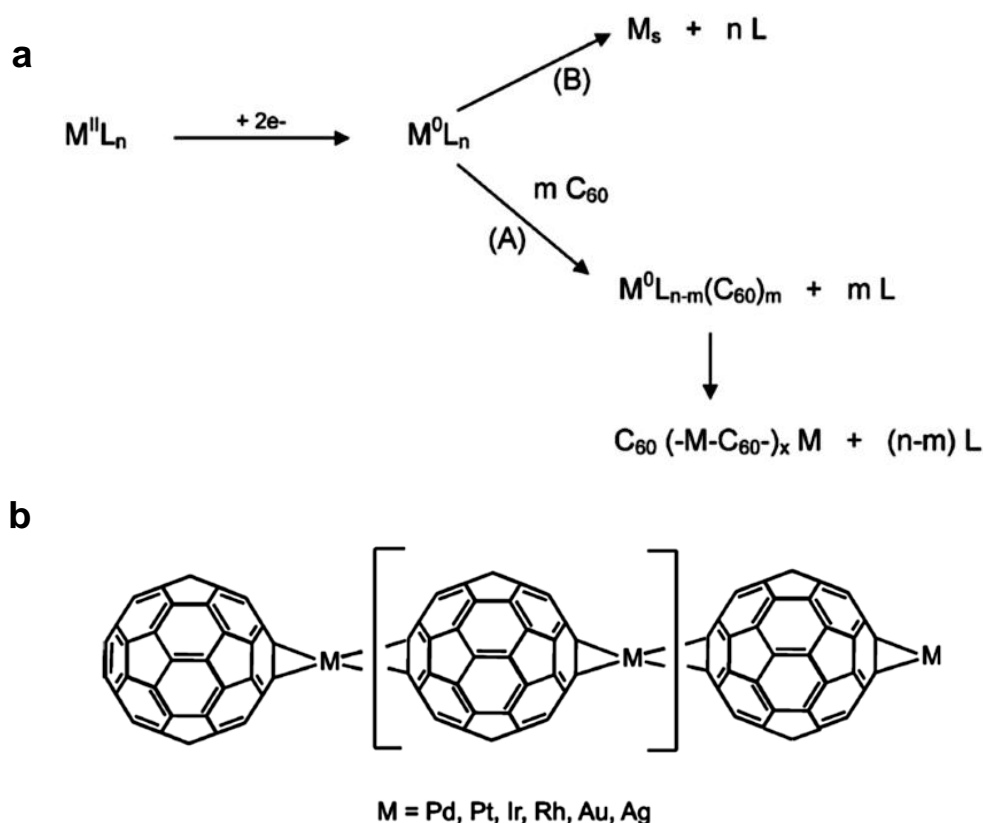
Scheme 2.4-3 (Metal complex)-assisted electropolymerization of C_{60}. (a) The polymer formation mechanism and (b) the resulted polymer backbone simplified structural formula. (Adapted from Refs.[104,105])

In this electropolymerization, negative polarization of a WE results in reduction of the metal complex to the zero-valent metal complex. This complex initiates growth of a C_{60}-M (M = Pd or Pt) polymer. Simultaneously, metal nanoparticles can be deposited if the (metal complex)-to-fullerene ratio is too high. This ratio can be varied by changing concentration of both the fullerene and the metal complex.

2.5 Techniques used

2.5.1 Computational modeling

Quantum chemistry computing using the density functional theory (DFT) method is a convenient tool for theoretical optimization of molecular structures, Gibbs free energy gains due to complex formation, determination of the HOMO and LUMO levels, and other electronic parameters. At the time, it is the most commonly used method for computation of electronic structure of matter. The DFT method is very popular because of its precision higher than that of the Hartree-Fock theory method, and relatively moderate computing resources required.

2.5.2 Langmuir film studies

A molecular layer of amphiphile molecules at a water-air interface is named the Langmuir film.[106] This monolayer is formed by self-ordering of these molecules spread onto a water subphase from a solution of a volatile and immiscible with water solvent, like chloroform.
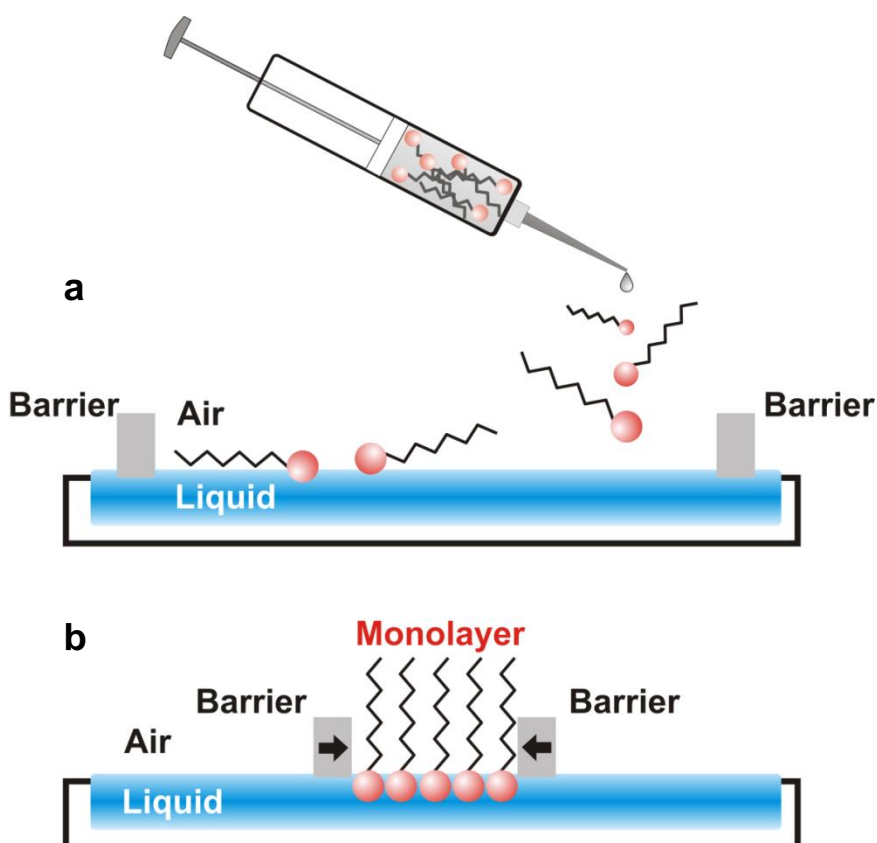
Figure 2.5-1 A monolayer of molecules arranged in a (a) two-dimensional gas and (b) compressed film.

After evaporation of the solvent, the Langmuir film is formed as the nature of the spread molecule dictates, i.e., with the hydrophilic moieties oriented towards the water subphase (Fig. 2.5-1). If the distance between the spread molecules is large (Fig. 2.5-1a), their interactions are negligibly small and they behave like a two-dimensional gas.[107] If the water-air interface surface area is decreased, the molecules begin to repulse each other (Fig. 2.5-1b). This 2-D analogue of pressure is called surface pressure, π, described by Eqn. 2.5-1

$$\pi = \gamma - \gamma_0 \qquad (2.5\text{-}1)$$

where γ_0 is the surface tension in the film absence and γ is this tension in the film presence. The surface tension is given by Eqn. 2.5-2

$$\gamma = \left(\frac{\partial G}{\partial S}\right)_{T,p,n_i} \qquad (2.5\text{-}2)$$

where G is the Gibbs free energy of the system, S is the surface area of the interface, at constant kelvin temperature, T, pressure, p, and the number of moles of the substance spread, n_i.

Table 2.5-1 Phases of Langmuir films and the corresponding ranges of compression coefficients.[108]

Monolayer	κ, mN m^{-1}
Clean surface	0
Protein ($A \approx 1$ m^2 mg^{-1})	1 to 20
Liquid expanded	12.5 to 50
Liquid condensed	100 to 250
Solid condensed	1000 to 2000

Thus, a plot of the dependence of surface pressure on area of water surface available for each molecule provides important information on properties of the film. This plot, recorded at constant temperature, is the pressure-area isotherm or compression isotherm (Fig. 2.5-2).
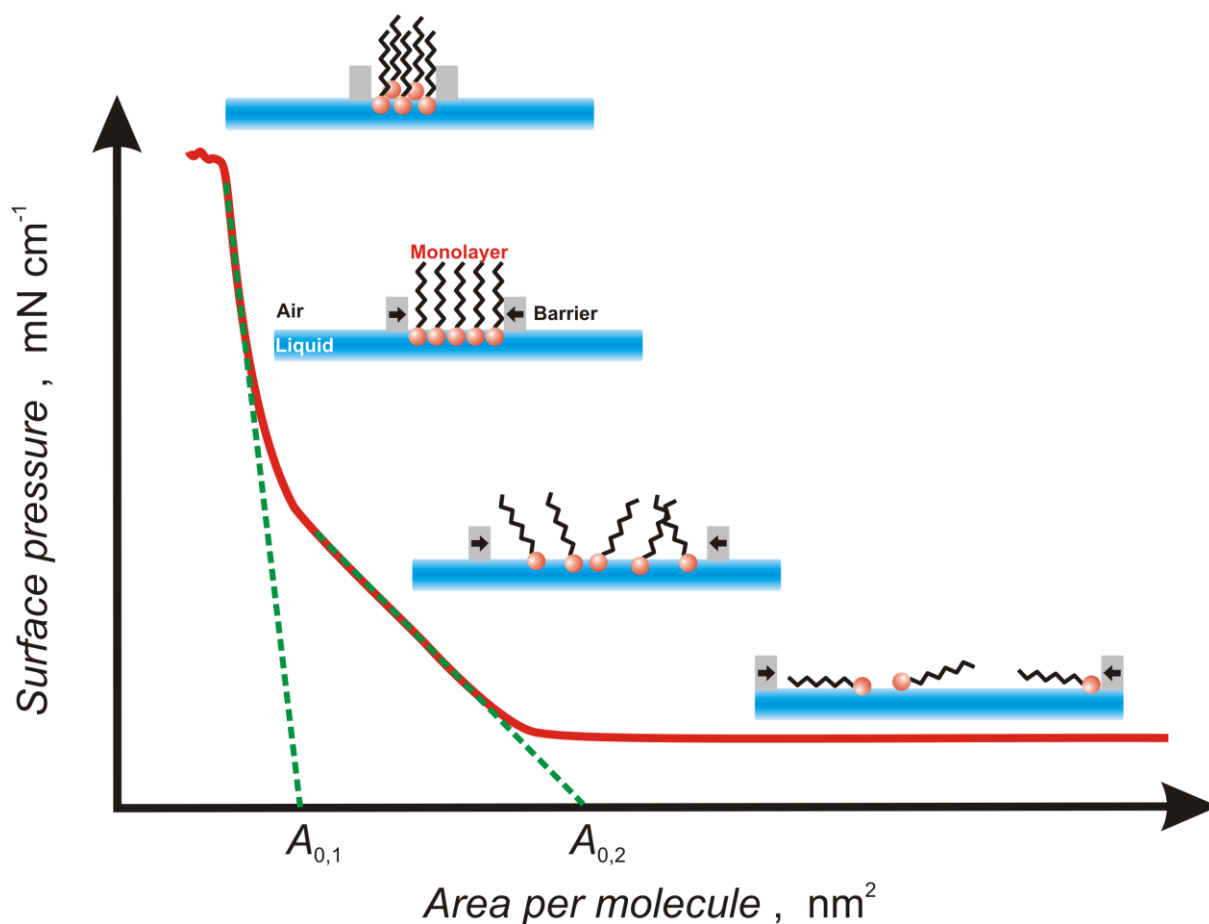
Figure 2.5-2 A typical compression isotherm for a fatty acid and corresponding phases of a Langmuir film spread on an aqueous subphase.

Several regions can be distinguished in this isotherm. First, a horizontal linear part at the high A values represents a 2-D gas behavior of the molecules at the water-air interface. Then, the molecules begin to repulse each other and the surface pressure increases with the A decrease. Changes of the isotherm slope correspond to phase transitions of the film. Finally, film collapses at the lowest A_m values and surface pressure stops to increase. At the steep part of the compression isotherm, molecules are densely packed and the compressibility coefficient (κ) of a Langmuir film is determined from the π-A compression isotherm according to Eqn. 2.5-3

$$\kappa = -\frac{1}{A_0}\left(\frac{\partial A_m}{\partial \pi}\right)_T \tag{3.2-3}$$

38

where A is the area per molecule at a given surface pressure π, $\partial A/\partial \pi$ is the inverse of the slope of the compression isotherm for a given phase. The κ value characterizes the nature of a phase of the Langmuir film (Table 2.5-1).

The surface pressure is measured by the method using the Wilhelmy plate.[109] In this method, a hanging probe of a quartz slide or a rectangular (~2 × ~3 cm^2) piece of a small pore size filter paper, connected to a balance, is immersed in the liquid subphase. Surface tension acting on the probe pulls it down. This force is measured by the balance.

2.5.3 Measurements of surface potential of Langmuir films

Surface pressure changes are measured when molecules have already rearranged and mutually interact. However, the measurement of surface potential, V_s, allows for detection of reorganization of the film before, i.e., at lower surface pressures than those at which these changes are observed in the compression isotherm.

Surface potential is measured simultaneously with surface pressure (Fig. 2.5-3). It is measured by a non-contact vibrating Kelvin probe producing a varying capacity.
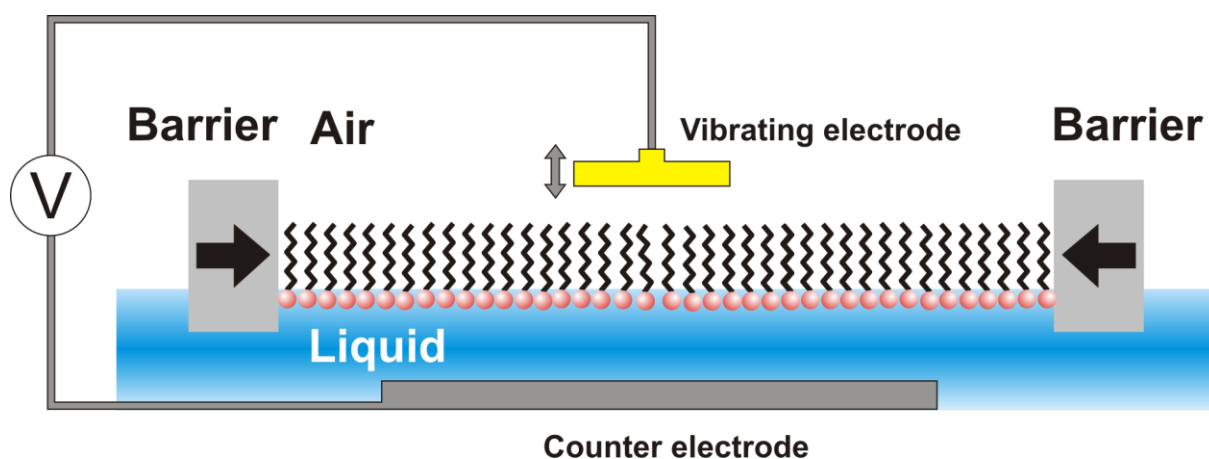
Figure 2.5-3 A Langmuir film surface potential measurement.

The dipole moment component normal to the interfase plane, $\mu_\perp$, of the molecules in a Langmuir film is determined from the V-A isotherm using the Helmholtz equation (Eqn. 2.5-4)

$$\mu_\perp = \varepsilon_0 \varepsilon_e A_m \Delta V_s \qquad (2.5\text{-}4)$$

39

where ε_0 and ε_e is electric permittivity of free space and the film (assumed to be 5 for C_{60}im and 10 for the Zn(TPPE)-C_{60}im film, respectively).[110]

2.5.4 Langmuir-Blodgett and Langmuir-Schaefer film transfer

There are several different ways to transfer a Langmuir film floating on a liquid subphase onto a solid substrate including the LB and Langmuir-Schaefer (LS) transfer.
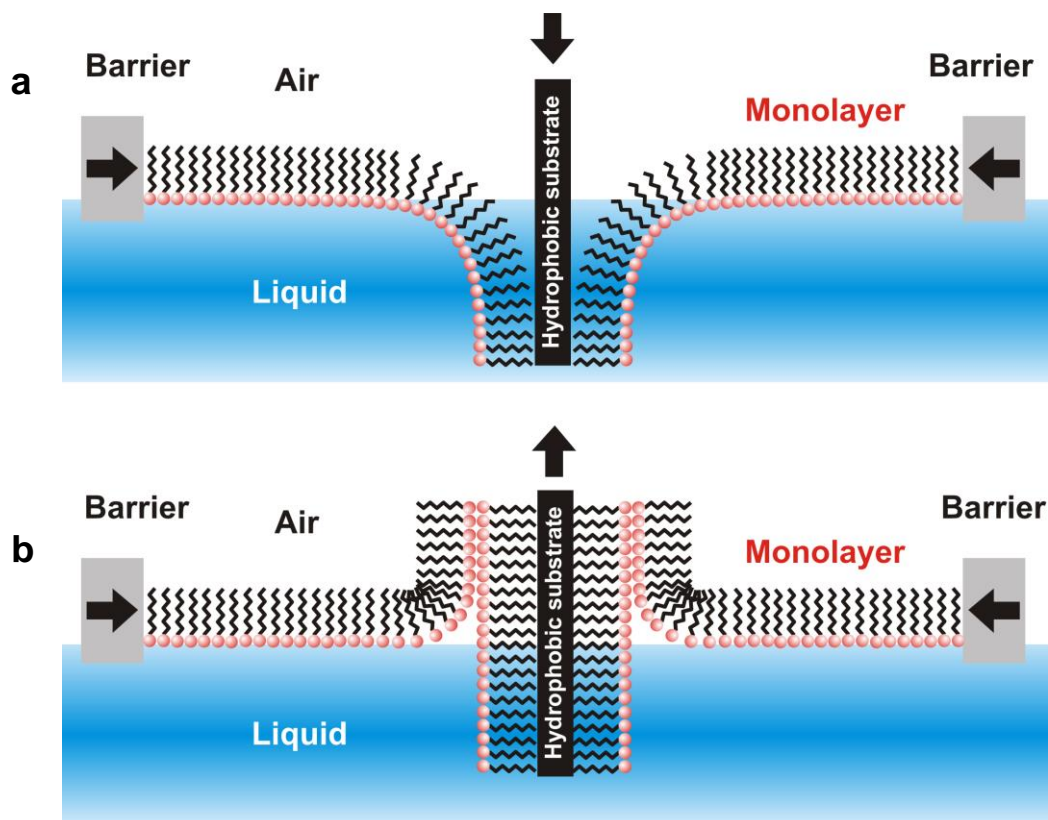
Figure 2.5-4 The Langmuir-Blodgett transfer of a Langmuir film onto a hydrophobic substrate: (a) the first layer, (b) the second layer (a Y-type LB film is formed on a hydrophobic substrate, cf. Fig. 2.5-5).

The LB technique was the first to construct ordered multilayer molecular films on solid substrates. This technique consists in consecutive immersing and withdrawing a solid substrate in and out of a subphase solution with a Langmuir film spread.[106] If monolayers of amphiphilic molecules are transferred, then the first monolayer transferred changes the hydrophobic nature of the substrate being coated to hydrophilic and vice versa. If the first monolayer is transferred by immersing a hydrophobic substrate in a subphase through the

40

Langmuir film, then the transferred film is oriented with its hydrophobic moieties of the molecules toward the substrate and hydrophilic moieties sticking out (Fig. 2.5-4a). The second layer is transferred during substrate withdrawal. Thus, the film is transferred with its hydrophilic moieties oriented toward those present on the substrate already (Fig. 2.5-4b).

Moreover, the first monolayer can be deposited by immersing a solid substrate in a subphase solution through the Langmuir film or by withdrawing that initially immersed. In dependence of the hydrophobic/hydrophilic nature of the substrate, this transfer results in films of differently oriented molecules. Preferably, the first monolayer of amphiphilic molecules is transferred on a hydrophobic substrate by immersion and on a hydrophilic substrate by withdrawal. Another transfer may result in reorientation of molecules during the transfer.[111]

An LB film may differently be organized during the transfer. Consecutive immersions and withdrawals of a substrate results in the most common so-called Y-type of the LB film (Fig. 2.5-5a). If the film is transferred only by immersion or withdrawal, then the X-type (Fig. 2.5-5b) or Z-type (Fig. 2.5-5c) LB film is obtained, respectively. A quantitative measure of the film transfer is the transfer ratio, i.e., the ratio of the area of the monolayer removed from the subphase surface to the area of the substrate used for the transfer.
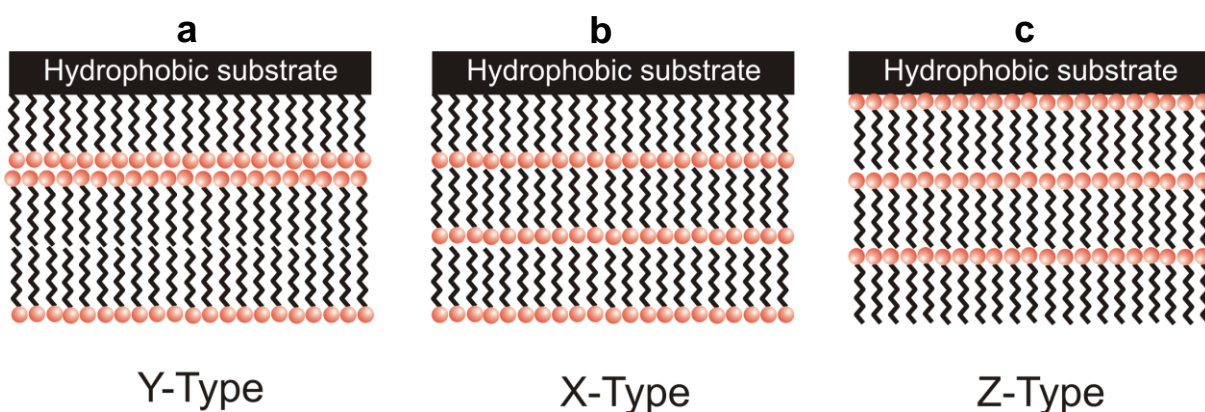
Figure 2.5-5 Organization of the LB multilayer films on a hydrophobic substrate, the first layer is deposited by immersion (Y- and Z-type).

The LS method is another way of transfer of an ordered multilayer molecular film spread on a liquid subphase. It consists in horizontal lifting of the film.[106] Mostly, it is useful for transfer of very rigid films being nearly two-dimensional solids. In this method, first, a compressed Langmuir film is formed on a water-air interface. Then, a solid substrate is

horizontally contacted with the film, and then lifted up. That way, the first layer is deposited. The subsequent layers are transferred in the same manner (Fig. 2.5-6), expectedly resulting in the X-type film (Fig. 2.5-5b). Obviously, the LS transfer onto hydrophilic substrates is expected not to be successful.
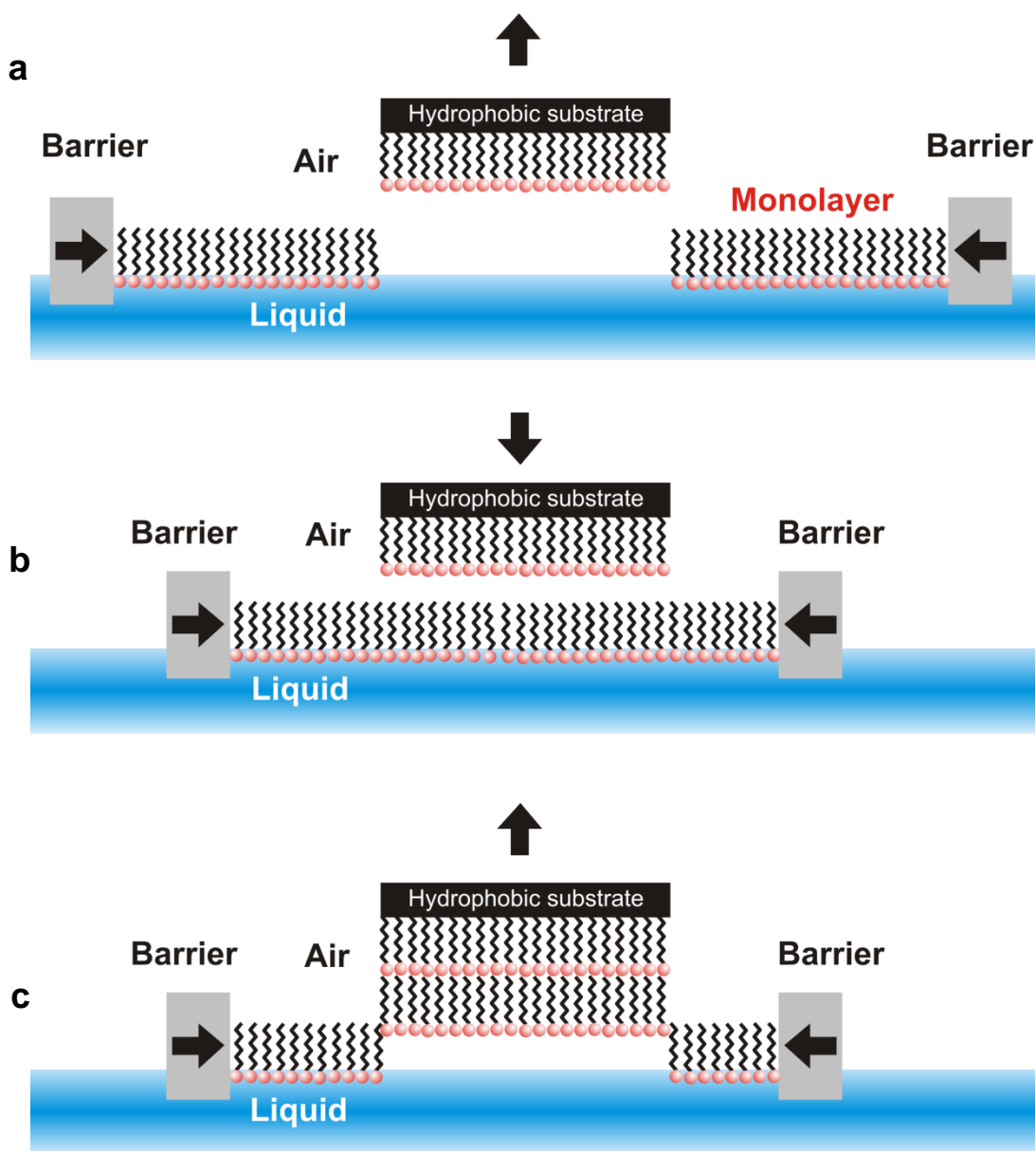
Figure 2.5-6 The Langmuir-Schaefer transfer of a Langmuir film onto a hydrophobic substrate.

Beside the LB and LS techniques, there are other techniques of the Langmuir film transfer, including continuous transfer after Barraud and Vandevyver and alternate-layer transfer in troughs with more than one working surface (double-Langmuir trough, etc.).[112]

42

2.5.5 Voltammetry

In voltammetry, the effects of the linearly changed with time potential applied to the working electrode (WE) on the redox current are well described. Cyclic voltammetry (CV) and linear sweep voltammetry (LSV) are, probably, the most often used electroanalytical techniques for studying redox processes and understanding electrochemical reaction mechanisms in particular. LSV consists in sweeping the WE potential, measured versus a reference electrode (RE), from an initial, E_i, to a final, E_f, potential with the constant sweep rate and recording the current vs. potential curves using a three-electrode cell.[113] In CV, the potential is swept with the same rate in the forward, and then backward direction (Fig. 2.5-7).

The anodic, E_{pa}, and cathodic, E_{pc}, peak potentials and corresponding peak currents (i_{pa} and i_{pc}) are important CV parameters. If an electrode reaction, i.e., the heterogeneous electron transfer, is faster than other processes occurring, e.g., diffusion, the reaction is said to be electrochemically reversible. Then, concentration of a redox species under the diffusion rate control is related to the peak current, i_p (A), by the Randles-Ševčík equation

$$i_p = 2.69 \times 10^5 \, n^{3/2} \, A \, c \, D^{1/2} \, v^{1/2} \qquad (2.5\text{-}5)$$

where n is the number of electrons transferred, A (cm^2) is the electrode area, c (M) is the concentration of the redox substance in solution, D (cm^2 s^{-1}) is the diffusion coefficient, and v (V s^{-1}) is the potential sweep rate.

For reversible electrochemical reactions, the anodic-to-cathodic peak potential separation is

$$\Delta E_p = E_{pa} - E_{pc} = 2.303 \, \frac{RT}{nF} \qquad (2.5\text{-}6)$$

Thus, the ΔE_p should be 0.0592/n V for a reversible redox reaction at 25 °C with n electrons transferred or ~60 mV for one electron transferred.

If the redox substance is deposited in the form of a thin film on the electrode surface, then the peak current is described by the Eqn. 2.5-7.

$$i_p = 9.39 \times 10^5 \, n^2 \, V_f \, c_f \, v \qquad (2.5\text{-}7)$$

43

In this equation, V_f is the volume of the film of the redox substance on the electrode and c_f is the concentration of the redox active sites in the film.
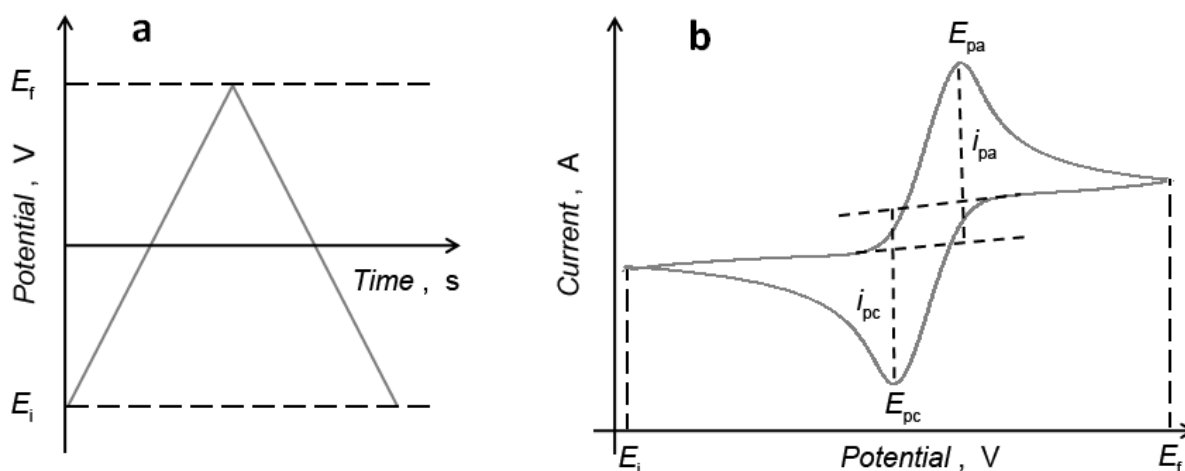
Figure 2.5-7. (a) A potential-time program for cyclic voltammetry and (b) a typical cyclic voltammogram for a reversible redox couple. Symbols E_i and E_f stand for the initial and final potential, respectively. (Adapted from www.intechopen.com)
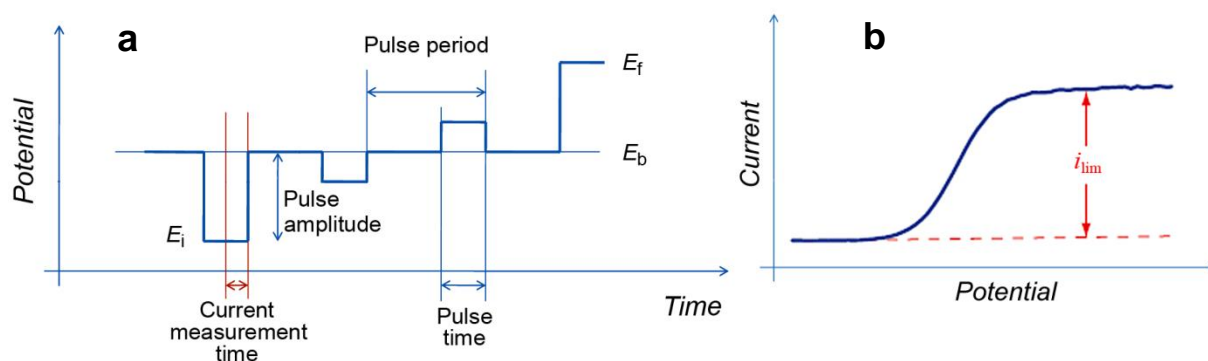
Figure 2.5-8. (a) A potential-time program for normal pulse voltammetry, NPV. The E_b symbol stands for the base potential, while E_i and E_f stand for the initial and final potential, respectively and (b) a typical current-potential curve for NPV. (Adapted from www.ecochemie.nl)

In normal pulse voltammetry, the electrode is kept at a base potential, E_b, i.e., that where no faradaic process occurs, for most of the pulse period. Short pulses of linearly increasing amplitude applied to the electrode generate high currents with substantial contribution from the capacity charging current (Fig. 2.5-8). Therefore, the current is

44

measured just before the end of the pulse at which time the capacity current is negligible. NPV allows decreasing the influence of products of the electrochemical reaction on the electrode reaction.
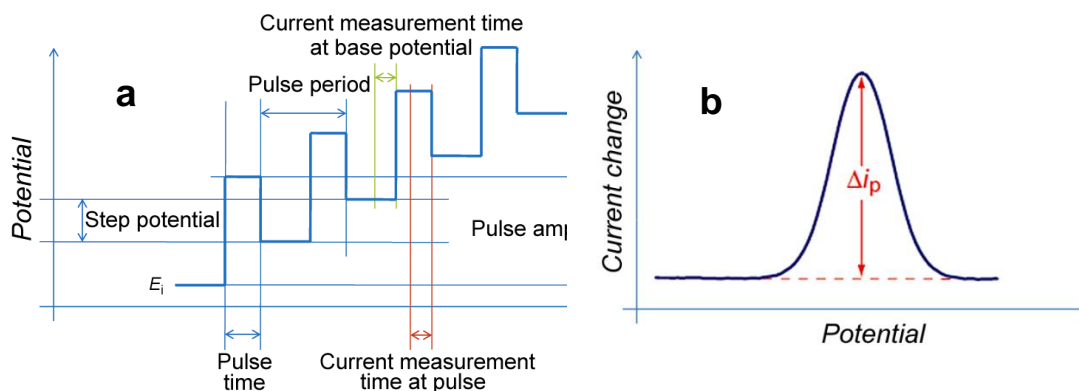
Figure 2.5-9. (a) A potential-time program for DPV with both positive the potential step and potential amplitude and (b) a typical current-potential curve for DPV. (Adapted from www.ecochemie.nl)

An important parameter of the potential sweep and pulse electrochemical techniques is the diffusion layer thickness. Particularly, morphology of electrodeposited films depends on thickness of this layer. Thickness of this layer depends on time and potential. For the potential sweep and pulse methods, it can be written as Eqn. 2.5-6a and Eqn. 2.5-6b, respectively.[114]

$$\delta_{\text{sweep}} = 0.355 n^{-1/2} D^{1/2} v^{-1/2} \qquad (2.5\text{-}7a)$$

$$\delta_{\text{pulse}} = \sqrt{2D t_{\text{pulse}}} \qquad (2.5\text{-}7b)$$

Where, n is a number of electrons transferred, D is the diffusion coefficient, v is the potential sweep rate, t_{pulse} is the potential pulse time.

Differential pulse voltammetry (DPV) uses potential pulses of constant amplitude and stepped base potential of a constant step.[115] During the pulse period the current is measured first, just before, and then near the end of the pulse (Fig. 2.5-9a). These points of current sampling are selected to allow for the extensive exponential decay of the capacity current. Then, the measured faradaic current, decaying proportionally to $t^{-1/2}$ (Cottrell decay), can be more efficiently discriminated from the background capacity current than in NPV. The adopted current sampling procedure allows recording the current difference. Therefore, the current peaks are obtained (Fig. 2.5-9b).

LSV at an RDE and RRDE involves diffusion-convection mass transport of redox reactants and products allowing for measurement of limiting currents in the resulting voltammograms.[116] The advantage of the hydrodynamic transport is that a steady state is attained relatively quickly. Therefore, measurements can be performed with high precision and, moreover, double-layer charging does not affect the measurement at steady state.

The RDE and RRDE voltammetry techniques are convenient tools for study electrochemical reaction mechanisms and dioxygen electroreduction in particular. The Koutecky-Levich relation (Eqns. 2.5-8, 2.5-9, and 2.5-10) allows determining the number of electrons involved in the dioxygen reduction, thus providing information about the reaction mechanism.

$$\frac{1}{j} = \frac{1}{j_{lim}} + \frac{1}{j_k} = \frac{1}{(B\omega^{1/2})} + \frac{1}{j_k} \qquad (2.5\text{-}8)$$

$$B = 0.62\, n\, F\, c_{O_2}(D_{O_2})^{3/2}\, \eta_k^{-1/6} \qquad (2.5\text{-}9)$$

$$j_k = n\, F\, k_e\, c_{O_2} \qquad (2.5\text{-}10)$$

Symbol j (A cm^{-2}) is the measured total current density, j_k and j_{lim} (A cm^{-2}) is the kinetic and diffusion limited current density, respectively, ω is the angular velocity of the rotating disk electrode ($\omega = 2\pi f$, f is the rotation frequency in r.p.m.), n is the overall number of electrons transferred in dioxygen reduction reaction, F is the Faraday constant, c_{O_2} is the bulk concentration of dioxygen, D_{O_2} is the diffusion coefficient of dioxygen, η_k is the kinematic viscosity of the electrolyte, and k_e is the heterogeneous electron transfer rate constant.

46
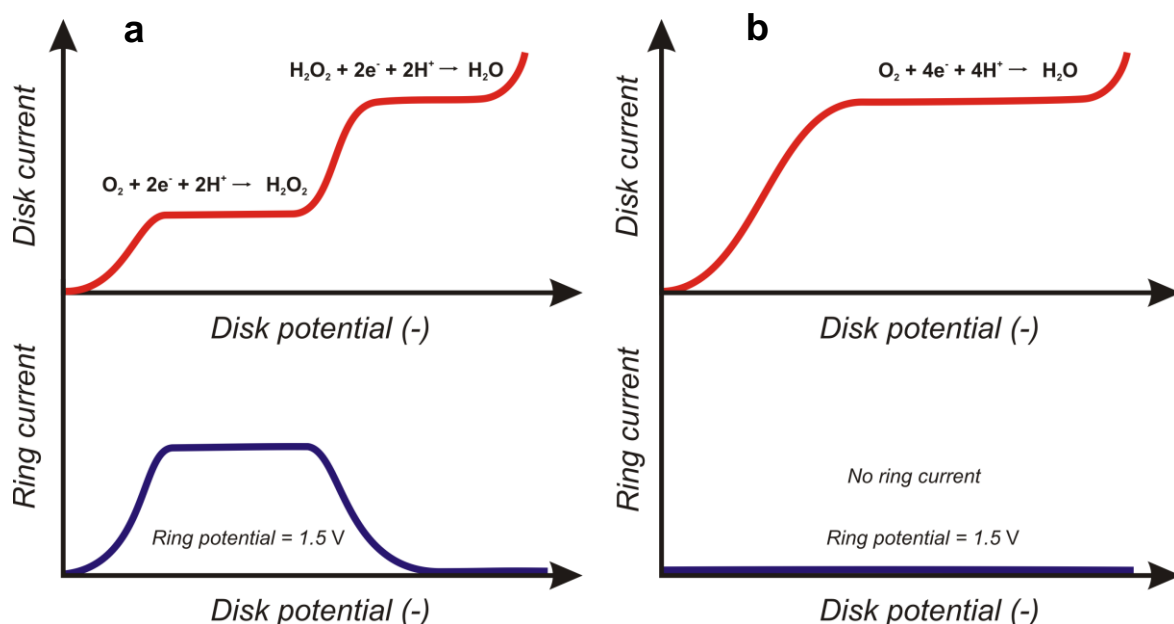
Figure 2.5-10. The LSV voltammograms for (a) two-step two-electron and (b) one-step four-electron dioxygen electroreduction at the RRDE.

The number of electrons and kinetically limited current can be obtained from the slope and intercept of the Koutecky-Levich plot, i.e., the dependence of reciprocal current on the inverse square root of the rotation rate of the RRDE.

The RRDE voltammetry allows taking closer insight into mechanisms of electrochemical reactions by detecting its intermediate products at the independently potential-controlled ring electrode placed around the working disk electrode (Fig. 2.5-10). The amount of H_2O_2 generated on the disk electrode of the RRDE can be determined using Eqn. 2.5-11

$$\% H_2O_2 = \frac{i_r}{i_d N}100 \qquad (2.5\text{-}11)$$

where i_r and i_d is the limiting ring and disk current, respectively, and N is the collection coefficient of the RRDE, which was 0.47 for the used system (Eqn. 2.5-12).

$$N = \frac{-i_r}{i_d} \qquad (2.5\text{-}12)$$

47

2.5.6 Piezoelectric microgravimetry (PM)

Piezoelectric microgravimetry (PM) uses a quartz crystal microbalance (QCM) to determine tiny mass changes with a nanogram resolution via measuring the change in the resonance frequency, Δf_0, of a quartz crystal resonator (QCR) during deposition or dissolution of a film from the QCR surface. The measured Δf_{total} consists of two components.

One component, Δf_{mass}, corresponds to the mass change, Δm, QCR during film deposition or dissolution. It is described by the Sauerbrey relation[117] (Eqn. 2.5-13).

$$\Delta f_{\text{mass}} = -\frac{2\,f_0^2\,\Delta m}{A_{\text{ac}}(\mu_q\,\rho_q)^{1/2}} \tag{2.5-13}$$

Here, f_0 (10 MHz for the EQCM used herein) is the fundamental frequency of the QCR, A_{ac} (cm^2) is the acoustically active area of the QCR, $\mu_q = 2.947 \times 10^{11}$ g cm^{-1} s^{-2} is the shear modulus of quartz, $\rho_q = 2.648$ g cm^{-3} is the quartz density.

The other component, Δf_{vis}, describes the change of mechanical properties (viscosity and density) of the contacting liquid, applicable to those of the growing film as well (Eqn. 2.5-14).

$$\Delta f_{\text{vis}} = -\frac{k_c^2\,R_d\,f_0}{\pi\,A_{\text{ac}}\,(2\,\mu_q\,\rho_q)^{1/2}} \tag{2.5-14}$$

Here, $k_c^2 = 7.74 \times 10^{-3}$ (A^2 s^2 cm^{-2}) is the QCR electromechanical coupling factor, and R_d (Ω) is the dynamic resistance (Eqn. 2.5-15).

$$R_d = \frac{A_{\text{ac}}}{k_c^2}\left(2\pi\,f_0\,\eta_L\,\rho_L\right)^{1/2} \tag{2.5-15}$$

Symbol η_L (g cm^{-1} s^{-1}) and ρ_L (g cm^{-3}) is the dynamic viscosity and density of the working solution, respectively.

Thus, the total resonanc frequency change of QCR, Δf_{total}, is described by Eqn. 2.5-16.

$$\Delta f_{total} = \Delta f_{mass} + \Delta f_{vis} = -\frac{2\, f_0^2\, \Delta m}{A_{ac}\, (\mu_q\, \rho_q)^{1/2}} + (-f_0^{3/2})\left(\frac{\eta_L\, \rho_L}{\pi\, \mu_q\, \rho_q}\right)^{1/2} \qquad (2.5\text{-}16)$$

2.5.7 Absorbance and reflectance ultraviolet-visible (UV-vis) spectroscopy

Ultraviolet-visible (UV-vis) spectroscopy is an analytical technique visualizing transitions of electrons from their ground to excited state in a molecule. As a rule, energetically favored electron promotion will be from the HOMO to the LUMO, and the resulting species is called an excited state. An optical spectrophotometer records the wavelengths at which absorption occurs together with the extension of absorption at each wavelength. The resulting spectrum is presented as a graph of absorbance, A^L, versus wavelength. The UV-vis spectroscopy is a convenient and widely used technique for studying complex formation in solution. Quantitatively, the amount of an analyte present in the examined solution can be determined from the absorbance spectra using the Lambert-Beer law (Eqn. 2.5-17).

$$A_0^L = \varepsilon_R\, l\, c_R^0 \qquad (2.5\text{-}17)$$

Here, A_0^L is the solution absorbance, ε_R is the molar absorptivity of the receptor in solution, l is the light-pass distance of the cuvette, and c_R^0 is the total molar concentration of the receptor.

If a receptor and an analyte absorb light at different wavelengths in a free and complexed state, it is possible to estimate concentrations of both states. Then, isosbestic point(s) occur(s).

For determination of the stability constant of the complex formation (Eqn. 2.5-18)

$$A + R \;\rightleftharpoons\; AR \qquad (2.5\text{-}18)$$

the Benesi-Hildebrand relation (Eqn. 2.5-19) is widely used.[118]

$$\frac{l}{\Delta A^L} = \frac{1}{c_R^0\, K_s^s\, \Delta\varepsilon_{RA}\, [A^0]} + \frac{1}{c_R^0\, \Delta\varepsilon_{RA}} \qquad (2.5\text{-}19)$$

49

Here, K_s^s is the stability constant of the complex in solution

$$\Delta A^L = A^L - A_0^L \qquad (2.5\text{-}20)$$

and

$$\Delta \varepsilon_{RA} = \varepsilon_{RA} - \varepsilon_R - \varepsilon_A \qquad (2.5\text{-}21)$$

where ε_{RA} and ε_A is the molar absorptivity of the complex and the analyte, respectively. The K_s^s and $\Delta \varepsilon_{RA}$ values can be determined from the Benesi-Hildebrand plot of $1/(A_0^L - A^L)$ vs. $1/c_A$, where c_A is the analyte concentration, for the 1-cm light pass cuvette, as (*y*-intercept) / (slope) and $1 / [c_R^0](y\text{-intercept})$, respectively.

2.5.8 X-ray photoelectron spectroscopy (XPS)

The X-ray photoelectron spectroscopy (XPS) is one of the most commonly used spectroscopic techniques applied for both quantitative and qualitative surface analysis of various solid materials ranging from rigid metals or ceramics to soft polymers and gels. In this technique, the incident X-ray beam strikes the surface of a sample under ultrahigh vacuum conditions promoting the core electrons of atoms of the sample from their ground state to an excited state well above the Fermi level and to escape to vacuum.[119] The kinetic energy of the escaped electron is measured and the electron binding energy, *BE*, is calculated using Eqn. 2.5-22

$$BE = h\upsilon - E_k + \Delta W \qquad (2.5\text{-}22)$$

where $h\upsilon$ is the energy of the incident photon, E_k is the electron kinetic energy, and ΔW is the difference in the work function of the sample and that of the detector material assuming that there is no charge accumulated at the sample surface.

The recorded spectrum contains peaks corresponding to the electron *BE* characteristic of a given element in a given atom environment (Eqn. 2.5-22). The *BE* of the emitted electron provides information not only on the elemental composition of the sample but also on the chemical state of the elements examined and its neighboring atoms or molecules as

50

well. Typically, the depth of analysis is ~1.1 nm for organic compounds, like polymers, i.e., ~5-8 atomic layers for most materials. This depth is limited by the inelastic mean free path of the emitted electron inside the sample towards its surface.

2.5.9 Attenuated total reflectance Fourier-transform infrared (ATR-FTIR) spectroscopy and polarization-modulation infrared reflection-absorption spectroscopy (PM-IRRAS)

Attenuated total reflectance Fourier-transform infrared (ATR-FTIR) spectroscopy is one of the most commonly exploited IR analytical techniques using light reflectance principle and providing information mostly on vibrational modes in molecules. It allows for both qualitative and quantitative analysis of samples with relatively easy sample preparation. The main advantage of the ATR-FTIR spectroscopy measurement over classical IR spectroscopy measurements with samples, diluted in IR-transparent salts and pressed into pellets or thin films, is a very thin sampling pathlength and depth of penetration of the IR beam in the sample. This sample arrangement prevents full absorption of bands in the infrared spectrum.

In ATR-FTIR spectroscopy, the IR beam is directed into a crystal of a refractive index relatively higher than that of the sample. The IR beam is reflected from the internal surface of the crystal with generation of an evanescent wave. This wave propagates orthogonally into the sample remaining in an intimate contact with the ATR crystal. Partially, the energy of the evanescent wave is absorbed by the sample and the rest of reflected radiation is returned to the detector (Fig. 2.5-11). In ATR-FTIR spectroscopy, the angle of incidence of the IR beam relative to a perpendicular to the crystal surface, θ, is measured.

Two important parameters in ATR-FTIR spectroscopy include (i) critical angle of incidence of the IR light beam, θ_c, and (ii) the depth of IR light beam penetration, d_p.

$$\theta_c = \sin^{-1}\left(\frac{n_2^r}{n_1^r}\right) \tag{2.5-23}$$

Here, n_2^r is the refractive index of the sample and n_1^r is the refractive index of the crystal. An ATR-FTIR spectrum is observed for θ values exceeding that of θ_c. If the n_1^r-to-n_2^r ratio is too high and θ is too low, then the measurement results in combination of ATR and external reflectance.

51

$$d_{\mathrm{p}} = \frac{\lambda}{2\pi \sqrt{(n_1^{\mathrm{r}})^2 \sin^2 \theta - (n_2^{\mathrm{r}})^2}} \qquad (2.5\text{-}24)$$

Here, λ is the wavelength of light. Typically, the depth of penetration in ATR-FTIR spectroscopy measurements is in the range of $0.5 \leq d_{\mathrm{p}} \leq 5$ mm.
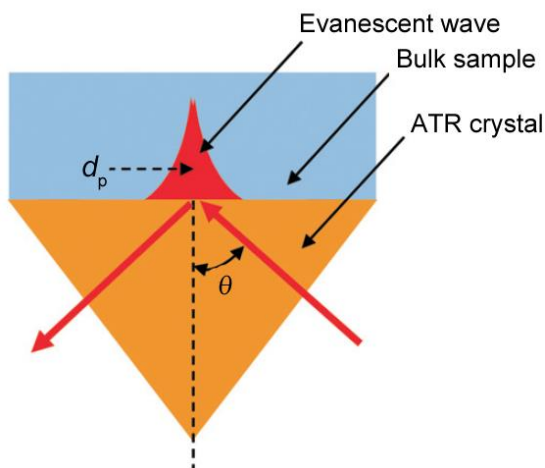
Figure 2.5-11. Principle of single-reflection ATR-FTIR spectroscopy operation. (Adapted from www.piketech.com)
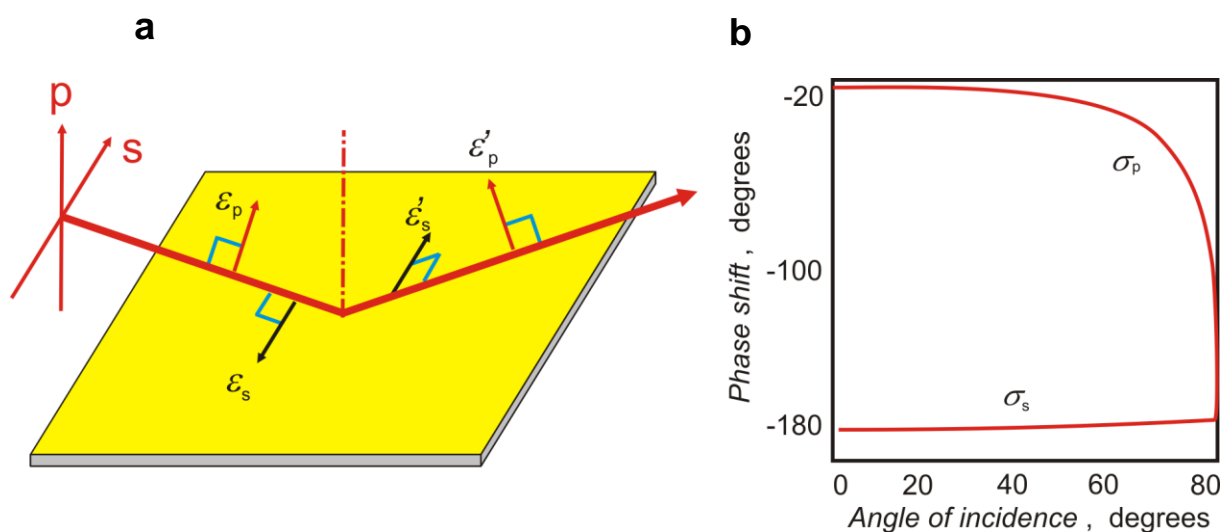
Figure 2.5-12 (a) Schematic illustration of reflectance of the s- and p-polarized radiation and (b) variation of the phase change in the p- (σ_{p}) and s-component (σ_{s}) of radiation as a function of the incidence angle of the light beam. (Adapted from www.epic.ms.northwestern.edu)

52

Polarization-modulation infrared reflection-absorption spectroscopy (PM-IRRAS) combines the polarization-modulation and reflection-absorption measurements of infrared light resulting in a sensitive FTIR spectroscopy and surface-selective technique. It is primarily used for characterization of thin films, including monolayers, deposited on metal (usually gold) substrates.[120]

Reflection of the non-absorbed IR light from the sample is dependent on the optical constants of the thin film and the substrate, the angle of the light beam incidence as well as the polarization of the incident IR radiation. A photomodulator generates alternating s- and p-polarized light pulses (Fig. 2.5-12a). The phase shift of the perpendicular component, s-, exhibits no significant dependence upon the variation of the angle of incidence (Fig. 2.5-12b).

The incident and reflected electric vectors of so-called p- and s-components of radiation, ε_p, ε_p', ε_s and ε_s', respectively, are shown in Fig. 2.5-12a. Here, p refers to parallelly polarized radiation and s to perpendicularly polarized radiation with respect to the plane of incidence. Because the phase shift of the s component, σ_s, is nearly -180° for all angles of incidence, the net amplitude of the IR radiation parallel to the substrate surface is zero. In contrast, the phase shift of the parallel component, σ_p, strongly depends upon the angle of incidence. The p-polarized component goes through a maximum at 88°. At this grazing incidence, the p-polarized radiation sums up of ε_p and ε_p' leading to a net combined amplitude that is almost twice that of the incident radiation. This feature is utilized to obtain the differential reflectance spectrum of the adsorbed surface species, $\Delta R^L / R^L$, which is expressed, as follows.

$$\frac{\Delta R^L}{R^L} = \frac{(I_p - I_s)}{(I_p + I_s)} \qquad (2.5\text{-}25)$$

Here, I_p and I_s is the intensity of the p- and s-polarized component of radiation, respectively.

Only the p-polarized radiation component interacts with the sample surface. Consequently, the active vibrations that can be detected in IRRAS must have a component of the dynamic dipole polarized in the direction normal to the surface of the sample. From this behavior, the so-called "surface selection rule" for PM-IRRAS follows. The "surface selection rule" is used to study orientation of molecules in thin films, and monolayers in particular, deposited on the metal or dielectric substrates. That is, PM-IRRAS is sensitive to molecule orientation with respect to the substrate surface.

53

2.5.10 Raman spectroscopy

Raman spectroscopy is an analytical technique detecting scattered UV and visible light that provides information on vibrational, rotational, and other low-frequency modes in molecules. This is a technique commonly used for analysis of carbon materials as it allows for detection of changes in their structure or chemical environment.

In a typical Raman spectroscopy measurement, a sample is irradiated with a laser beam. The light reflected from the sample is collected in the UV-vis region close to that of the laser wavelength with the Rayleigh scattering being filtered out. The difference between the fluorescence and Raman spectroscopy is that in the latter the electrons in a molecule are promoted not to a discrete, but to a virtual energy level.

2.5.11 Time-of-flight mass spectrometry (TOF MS)

Time-of-flight mass spectrometry (TOF MS) is an analytical technique measuring the mass-to-charge ratio (m/z) and abundance of ions moving at high speed in vacuum (Fig. 2.5-13).[121]
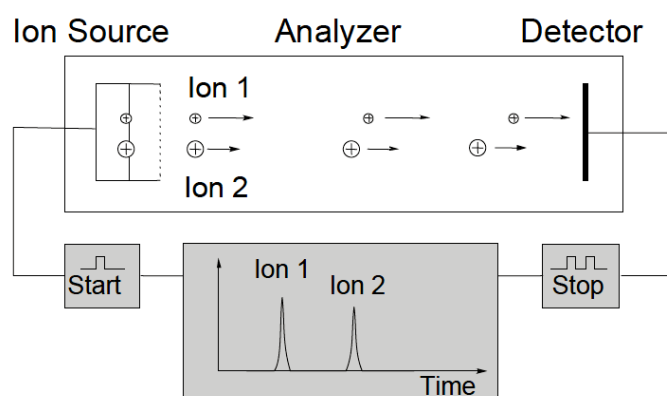
Figure 2.5-13 A block diagram and a flow chart of the time-of-flight mass spectrometry (TOF MS) operation.

It is widely used for determination of molecular mass of compounds upon their ionization using one of the available ionization techniques. In order to determine the m/z ratio, the measured sample is ionized and the ions produced are accelerated in an electric field applied. The velocity of the ions in the electric field depends upon their mass-to-charge ratio. That is, heavier ions move slower than those with the same charge but lighter. The time

54

required for ions to reach a detector is measured and the distance is known. This time and the known experimental parameters allow determining the mass-to-charge ratio of the ion. In our research, electrospray ionization was used.

2.5.12 Atomic force microscopy (AFM)

Atomic force microscopy (AFM) is an imaging technique, which allows visualizing surface of either conducting or non-conducting materials with up to atomic resolution.[122]

Basically, this imaging is afforded with a sharp microtip mounted on the edge of a cantilever. This cantilever is connected to a piezoelement-driven spatial positioning mechanism. The moving microtip interacts with an imaged surface and generates a raster 3-D pattern of the scanned surface. A laser beam, reflected from the cantilever to the photodetector, provides information on the cantilever deflection, thus changing height of the sample under the tip (Fig. 2.5-14a).

There are three main modes of AFM operation depending on the type of interaction between the tip and the sample. These include the non-contact, tapping, and contact mode. In most cases, they serve better for imaging very soft, soft, and rigid samples, respectively (Fig. 2.5-14b).
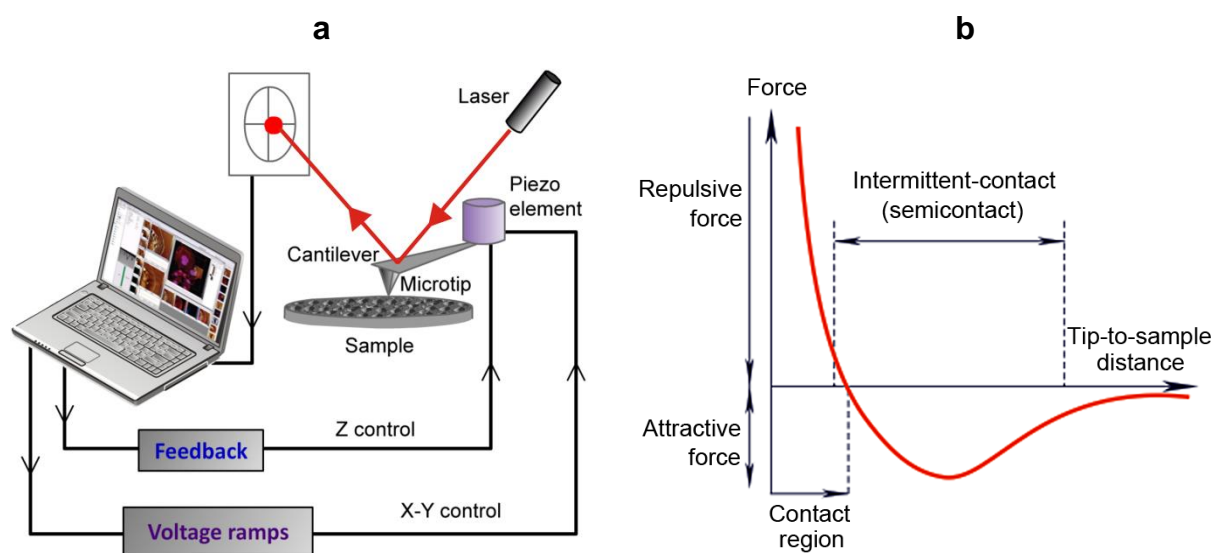
Figure 2.5-14. (a) A block diagram of an AFM instrument and (b) the summarized forces acting on an AFM tip vs. distance to the measured surface, respectively. (Adapted from www.doitpoms.ac.uk and www.ntmdt.com)

55

In our research, the tapping AFM mode was used. This mode is most suitable for imaging the LB, polymer, and CNT-polymer composite films. In the tapping mode, the cantilever oscillates vertically at or slightly below its resonance frequency. The amplitude of oscillation typically ranges from 20 nm to 100 nm. The microtip lightly "taps" on the sample surface during scanning, contacting the surface at the bottom of its swing. Because the forces on the microtip change as the microtip-surface distance changes, the resonance frequency of the cantilever is dependent on this distance according to Eqn. 2.5-26.

$$\omega_t \;=\; \omega_{t0}\sqrt{1 - \frac{1}{k_{scc}}\frac{dF_k}{dz}} \qquad\qquad (2.5\text{-}26)$$

Here, ω_t is the microtip oscillation frequency, $\omega_{t,0}$ is the microtip resonance frequency, F_k is the force of the cantilever-sample interaction, k_{scc} is the spring constant of the cantilever and z is the microtip-to-sample distance. Moreover, the oscillation is damped when the microtip is closer to the surface. Hence, changes in the oscillation amplitude can be used to measure the distance between the microtip and the surface. The feedback circuit adjusts the microtip (or the sample table) height to maintain constant amplitude of oscillation, i.e., the amplitude setpoint.

2.5.13 Brewster angle microscopy (BAM)

Brewster angle microscopy (BAM) is a technique for imaging thin films floating on a liquid surface.[123,124] In this technique, a sample is irradiated with a p- polarized monochromatic light under the Brewster angle, α. The Brewster angle (Eqn. 2.5-25) is a particular angle of light incidence where p-polarized light cannot be reflected from an interface (Figure. 2.5-15). Therefore, the incident at 53° p-polarized monochromatic light is not reflected from the water-air interface if there is no film on the air-water interface. Then, the detector does record anything and the picture recorded is black. If, however, a film is floating on the water subphase, the refractive index is then changed and the light is reflected to the detector. The BAM technique allows visualizing long-range orientation of molecules in the air-liquid interface, domains in a film, changes of orientation of molecules in film domains during film compression or expansion, and thickness of the film.

56
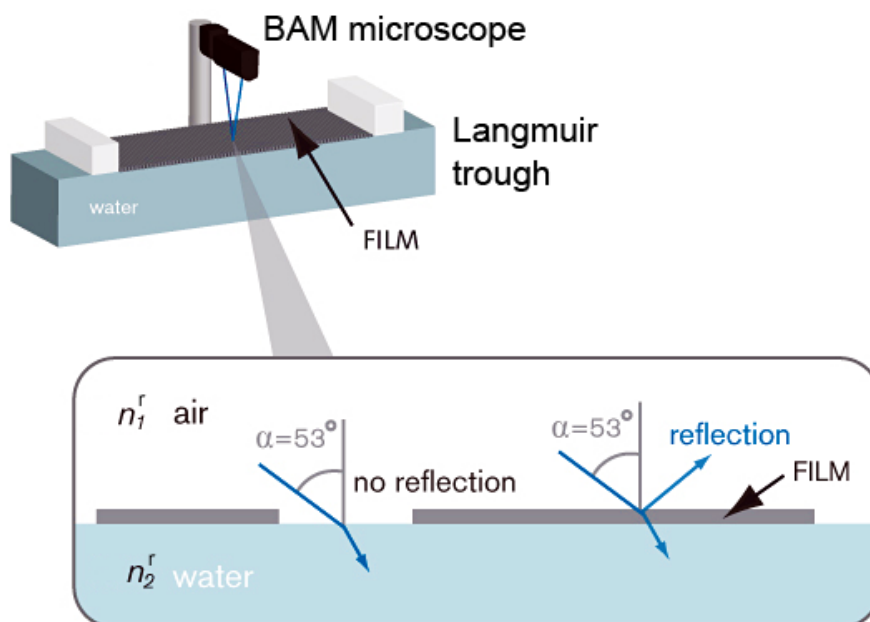
Figure 2.5-15. The operating principle of a BAM microscope. (Adapted from www.ksvnima.com)

$$\tan \alpha = \frac{n_2^{\mathrm{r}}}{n_1^{\mathrm{r}}} \qquad (2.5\text{-}27)$$

Here, α is the Brewster angle in radians, n_1^{r} is the refractive index of air ($n_1^{\mathrm{r}} \approx 1$) and n_2^{r} is the refractive index of the liquid subphase ($n_2^{\mathrm{r}} \approx 1.33$ for water). Thus, the Brewster angle for the air-water interface is 53°.

3. Experimental

3.1 Chemicals

[C_{60}]Fullerene, 99.5%, for syntheses of C_{60} adducts was from SES Research, (Houston TX, USA), BuckyUSA (Bellaire TX, USA), or M.E.R. Corp. (Tucson AZ, USA).

The HiPCO metallic single-wall carbon nanotubes (SWCNTs), 6,5-SWCNTs and 7,6-SWCNTs were from Carbon Nanotechnology, Inc. (Houston TX, USA).

2-(5′-Uracil)fulleropyrrolidine (C_{60}ur) was synthesized and purified according to the literature procedure.[125,126]

N-Methyl-2-(4'-*N*-imidazolylphenyl)-3,4-fulleropyrrolidine (C_{60}im) was synthesized according to the literature proceedure.[125,127]

2′-Ferrocenylfulleropyrrolidine (C_{60}Fc) was synthesized and purified according to the literature procedure.[125,128]

Tetrakis-4-(*N,N*-diphenylamino)-phenylporphyrinatocobalt(II), (Ph$_3$N)$_4$CoP, and *tetrakis*-4-(*N,N*-diphenylamino)phenylporphyrinatozinc(II), (Ph$_3$N)$_4$ZnP, were synthesized and purified according to the literature proceedures.[129]

Tetrakis[(2,9,16,23-triethyleneglycolmonomethylether)phthalocyaninato]zinc(II), Zn(TPPE), was synthesized according to the procedure described below in Section 4.1.2.1.

2-Aminopurine (2-AP), 99%, 1-pyrenebutyric acid, 97%, for non-covalent modification of SWCNTs, palladium(II) diacetate [Pd(Ac)$_2$], 98%, 3-bromopyridine, 99 %, piperazine, 99 %, analytical grade, anhydrous solvents for electrochemical measurements, i.e., 1,2-dichlorobenzene (ODCB), 99%, acetonitrile (ACN), 99.8%, and toluene (TL), 99.8 %, 1-methyl-2-pyrrolidinone (NMP), 99.6%, 1-cyclohexyl-2-pyrrolidone (CHP), 99%, all from Sigma-Aldrich (St. Louis MO, USA), were used without further purification.

Supporting electrolytes, namely, tetrabutylammonium (TBA) salts, such as (TBA)CH$_3$SO$_3$, (TBA)ClO$_4$, (TBA)BF$_4$, and (TBA)PF$_6$, all of electrochemical grade and (TBA)OH × 20 H$_2$O, from Sigma-Aldrich (St. Louis MO, USA), were stored in a dry box and used without further purification.

All other chemicals were of analytical grade from POCh (Gliwice, Poland) or Chempur (Piekary Slaskie, Poland).

Ethanol : (line ether), 96.3 : 3.7 (mass : mass) was from Linegal Chemicals Co. (Warsaw, Poland).

58

Dioxygen ("analyzed"), used for saturation of the working solutions of supporting electrolytes and argon for their deaeration, were from Multax, s.c. (Stare Babice, Poland).

Water for preparation of solutions for electrochemical experiments and subphase solutions for Langmuir film preparation was doubly distilled and further purified (18.2 MΩ cm) with a Mili-Q filtering system of Millipore Corp. (Bedford MA, USA).

3.2 Apparatus and procedures

The electrochemical experiments were performed using an AUTOLAB computerized electrochemistry system driven by the Nova or GPES software of Metrohm Autolab. Voltammetric measurements with the RDE or RRDE were performed on the RRDE-3A system of ALS Co., Ltd. (Tokyo, Japan).

The UV-vis spectroscopy measurements were carried out with a UV2501PC UV-vis recording spectrophotometer of Shimadzu (Kyoto, Japan).

Composition of the films was analyzed with the XPS by the Escalab-210 spectrometer of VG Scientific (East Grinstead, U.K.) using Al Kα ($h\nu$ = 1486.6 eV) X-ray radiation.

Orientation of molecules in the Langmuir-Blodgett and Langmuir-Schaefer films with respect to the substrate surface was estimated from polarization modulation-infrared reflection-adsorption spectroscopy (PM-IRRAS) spectra recorded with a Vertex 80v FT-IR spectrophotometer of Bruker (Ettlingen, Germany) equipped with a PMA50 accessory for the PM-IRRAS measurements.

The Raman spectroscopy measurements were performed using an Almega Raman spectroscope of Nicolet (Madison, WI, U.S.A.) equipped with a confocal Raman microscope and laser with λ = 780 nm.

Morphology and thickness of films deposited on solid substrates were characterized with the atomic force microscope at the tapping mode imaging with a MultiMode NS3D microscope of Veeco Instruments Inc. (Woodbury NY, USA) or MultiMode® 8 AFM/STM under control of a Nanoscope V controller of Bruker/Veeco.

3.2.1 Quantum chemistry calculations

In order to optimize structures and determine electronic properties of dyads, first, structures of their components, separately, were optimized to a stationary point on the Born-Oppenheimer potential energy surface with the DFT method at the B3LYP/3-21G* level. Then, the

optimized molecules were allowed to interact and form the H- or metal-ligand coordination bonds.

The DFT quantum-chemical calculations were performed on a workstation with four quad-core Xeon processors using Gaussian 09 rev C software[130] of Gaussian, Inc. (USA). The B3LYP functional along with the 3-21G* basis set, implemented in the software, were used for all the calculations.

3.2.2 Modification of electrodes

All metal electrodes were consecutively ultrasonicated in water for 5 min, immersed for 3 min in a "piranha" solution (H_2O_2 : H_2SO_4; 1 : 3, v : v; *caution: the "piranha" solution is dangerous in contact with skin and eye because it vigorously reacts with most organic substances*), rinsed with purified water, followed by ethanol, and then dried in an argon stream before each experiment. A 160 W power IS-3R ultrasonic bath of InterSonic (Olsztyn, Poland) was used for ultrasonication of electrodes as well as preparation of solutions and fine suspensions.

Before surface modification, the FTO glass slides were consecutively rinsed with water and acetone, then dried, and then Ar plasma cleaned or O_2 plasma activated. A plasma cleaner model Zepto of Denier Electronic GmbH (Ebhausen, Germany) was used for cleaning the electrodes and activating their surfaces before chemical modification with silanes. Electrochemical experiments with oxygen- and moisture-sensitive substances were performed in an anaerobic and moisture-free environment with a LabStar glove box of MBraun (Garching, Germany).

3.2.3 Preparation of subphase solutions for the Langmuir trough

The Langmuir films of individual compounds and their complexes in films spread on aqueous subphases were prepared by using a computerized system of 601BAM trough (total area of 490 cm^2) of Nima Technology, Ltd. (Coventry, UK). Surface pressure was measured with accuracy of ~0.1 mN m^{-1} by using a PS4 sensor (Nima) of a Wilhelmy plate type. The surface of the subphase solution was cleaned by repeated compressing, aspirating of traces of surface active impurities, and then expanding prior to spreading a sample solution. Changes of surface pressure of blank subphase solutions did not exceed 0.2 mN m^{-1} in the cleaning compression-aspiration-expansion cycles. Surface potential was measured with accuracy of

~10 mV by using a Model 320C-H-CE electrostatic voltmeter with a Model 3250 Probe by TREK, Inc. (Medina NY, USA) or with the KP-2 sensor (Nima) of a Kelvin probe type.

3.2.4 Preparation of Langmuir films of C_{60}ur and the C_{60}ur-(2-AP) conjugate

A sample of 0.2 to 1.5 ml of 0.05 to 0.112 mM C_{60}ur in chloroform was evenly drop-wise spread over the subphase solution surface. Then, the sample solvent was allowed to evaporate for 15 min. Isotherms of surface pressure (π) and surface potential (ΔV) vs. area per molecule (A) were then recorded simultaneously, under a compression-expansion regime, at the rate of 25 cm^2 min^{-1}. Morphology of the Langmuir films floating on aqueous subphases was characterized by a Brewster angle microscope type EP3-BAM or MiniBAM of NFT-Nanofilm Technologie, GmbH (Göttingen, Germany).

3.2.5 Langmuir-Blodgett transfer of Langmuir films of C_{60}ur and the C_{60}ur-(2-AP) conjugate

A Langmuir film of C_{60}ur was spread on (i) water (pH $\approx$ 5.6), (ii) 0.05 mM phosphate buffer (pH = 7.1), (iii) Britton-Robinson buffer (pH = 11.7) or (iv) KCl and HCl (pH = 1.65) subphase. The C_{60}ur-(2-AP) conjugate was formed by spreading C_{60}ur on (i) 0.1 mM 2-AP in the 0.05 M phosphate buffer (pH = 7.1), (ii) 0.1 mM 2-AP in the Britton-Robinson buffer (pH = 11.8), (iii) 0.1 mM 2-AP in 4 M CaCl$_2$ or glycerol as the subphase. Then, this film was allowed to stabilize for 5 min at surface pressure of 15 mN m^{-1}, i.e., that selected for the subsequent LB transfer. Next, the LB transfer was initiated with the immersion and withdrawal speed of 5 mm min^{-1}. A 10 $\times$ 15 mm^2 quartz slide served as the substrate. The Langmuir-Blodgett and Langmuir-Schaefer films were prepared with a D1L linear dipper of Nima.

3.2.6 Preparation of Langmuir films of the Zn(TPPE)-C_{60}im dyad

A sample of 150 to 300 μl of the 0.1 mM Zn(TPPE)-C_{60}im chloroform solution was evenly drop-wise spread onto the water subphase surface. Then, the sample solvent was allowed to evaporate for 15 min from the subphase surface, followed by simultaneous recording of the π-A and π-ΔV isotherms under a compression-expansion regime at the rate of 25 cm^2 min^{-1}.

3.2.7 Langmuir-Blodgett and Langmuir-Schaefer transfer of the Langmuir films of the Zn(TPPE)-C$_{60}$im dyad

First, the Langmuir film of the Zn(TPPE)-C$_{60}$im donor-acceptor dyad was spread on a water subphase. Then, this film was allowed to stabilize for 15 min at surface pressure of 10 mN m^{-1}, i.e., that selected for the subsequent LB transfer. The Langmuir films were then transferred using the LB technique at the immersion and withdrawal speed of 3, 5, 10, 15, or 30 mm min^{-1}. The LS transfer was accomplished at the speed of 1 mm min^{-1}. An FTO or Au-over-Cr coated glass slide, or an HOPG specimen served as the substrate.

3.2.8 Spectroelectrochemical measurements on LB films of the Zn(TPPE)-C$_{60}$im dyad

Spectroelectrochemical parameters of the multilayer LB film of the Zn(TPPE)-C$_{60}$im complex, transferred onto the FTO substrate and immersed in a solution, which was 5 mM in methyl viologen and 0.1 M in Na$_2$SO$_4$ or a solution, which was 1 mM in ascorbic acid and 0.1 in M NaH$_2$PO$_4$, were determined using a homemade PTFE cell featuring a quartz window. An FTO/[C$_{60}$im-Zn(TPPE) LB film], a platinum plate, and an Ag/AgCl electrode served as the photoelectrode, counter electrode, and reference electrode, respectively. A 5-mm diameter area of the photoelectrode was exposed to light. The electrode was illuminated from the electrolyte/electrode interface side with light of 100 mW cm^{-2} intensity. The measurements of IPCE of conversion were performed using a Cornerstone 260 monochromator of Newport Corp. (Irvine CA, USA).

3.2.9 Electropolymerization of (Ph$_3$N)$_4$ZnP

Electropolymerization was performed using a three-electrode one-compartment V-shaped glass cell with an ITO glass slide, a Pt disk, or an Au/quartz resonator serving as the working electrode, a Pt foil or a Pt wire as the counter electrode, and an Ag/AgCl electrode as the reference electrode in an ODCB solution, which was 0.1 mM in (Ph$_3$N)$_4$ZnP and 0.1 M in the (TBA)ClO$_4$ supporting electrolyte. Thickness of the film was controlled by the number of potential cycles completed or the potential scan rate. An ITO glass slide of ~0.8 cm^2 area was used for the film deposition.

The C$_{60}$im-(Ph$_3$N)$_4$ZnP polymer film for photoelectrochemical studies was deposited by soaking the ITO-[(Ph$_3$N)$_4$ZnP polymer film] electrode in an ODCB solution of 0.1 mM

C_{60}im for ~1 h. The electrode was then rinsed with the ODCB solvent to remove excess of uncoordinated C_{60}im, and then immediately used for photoelectrochemical measurements.

Electrochemical measurements on the $(Ph_3N)_4ZnP$ film with the electrochemical quartz crystal microbalance (EQCM) were performed by using an EP-21 potentiostat of Elpan (Lubawa, Poland) connected to an EQCM 5710 electrochemical quartz crystal microbalance of the Institute of Physical Chemistry (Warsaw, Poland) under control of an EQCM 5710-S2 software of the same manufacturer.

3.2.10 Flow-injection analysis (FIA) of C_{60}im complexation by the $(Ph_3N)_4ZnP$ polymer

The setup for FIA of the C_{60}im complexation by the $(Ph_3N)_4ZnP$ polymer was assembled according to Scheme 3.2-1. The $(Ph_3N)_4ZnP$ polymer film was prepared using an ODCB solution of 0.1 mM $(Ph_3N)_4ZnP$ in 0.1 (TBA)ClO_4 during 10 CV cycles between 0 and 1.3 V at the potential sweep rate of 0.1 V s^{-1}. Then, the film was rinsed with the blank ODCB solvent.
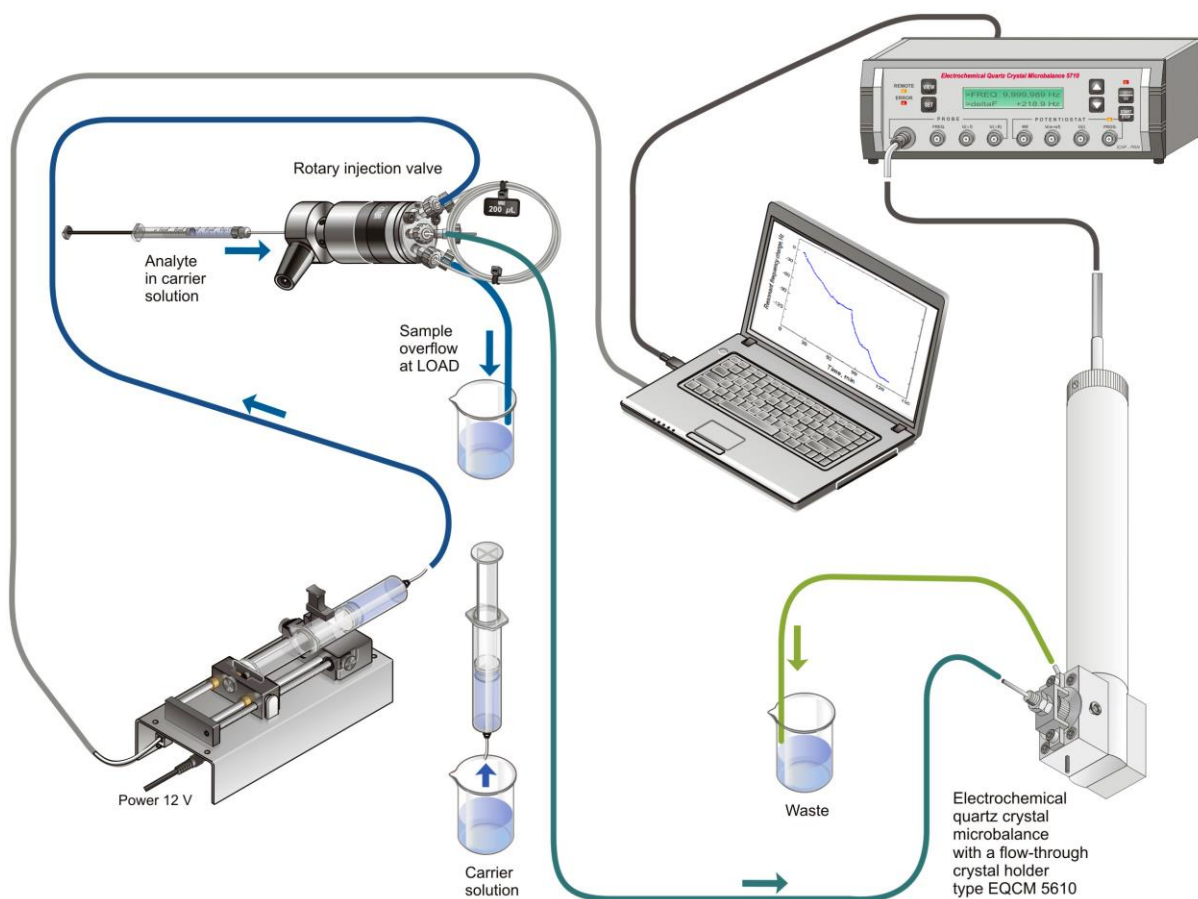
Scheme 3.2-1. The setup used for the flow-injection analysis measurement using the electrochemical quartz crystal microbalance.

The flow rate of the ODCB carrier solvent was 50 μL/min. The blank solvent was allowed to flow until frequency of the QCR stabilized. Then, 200-μL samples of C_{60}im in the same solvent were injected through the rotary injection valve. The QCR resonance frequency change was recorded.

The piezoelectric microgravimetry experiments under FIA conditions were performed with an EQCM 5610 flow-through QCR holder connected to an EQCM 5710 controller. The holder was connected with a stainless-steel capillary tubing to a NE-500 syringe pump of New Era Pump Systems, Inc. (Wantagh NY, USA), under a WinPump Term software control via a Model 7725i six-port rotary injection valve of Rheodyne (Cotati CA, USA).

3.2.11 Spectroelectrochemical measurements on LB films of the [(Ph$_3$N)$_4$ZnP polymer]-C_{60}im dyad

Spectroelectrochemical parameters of the pristine $(Ph_3N)_4ZnP$ polymer and the $[(Ph_3N)_4ZnP$ polymer]-C_{60}im dyad, deposited on the ITO electrode, in the acetonitrile solution containing (TBA)I and I_2 to generate the 0.1 M I_3^- mediating redox couple were determined. The ITO samples were placed in an open-top 1-cm light path UV cuvette, with the Pt-grid counter electrode. The film was illuminated from the ITO side. The photovoltage-photocurrent curves were recorded both in darkness and under illumination with a Newport 150 W Xe arc lamp under the AM 1.5 light filter using a Model 2400 Current/Voltage Source Meter of Keithley Instruments, Inc. (Cleveland OH, USA). The IPCE measurements were performed under the ~4 mW cm^{-2} monochromatic light illumination conditions using a setup composed of a 150 W Xe lamp with a Cornerstone 260 monochromator of Newport Corp. (Irvine CA, USA).

3.2.12 Electropolymerization of (Ph$_3$N)$_4$CoP and imprinting of the nitrogen-containing templating ligands in the (Ph$_3$N)$_4$CoP polymer

Electropolymerization of $(Ph_3N)_4CoP$ was performed using a three-electrode one-compartment cell with a GCE working electrode mounted upside down, a Pt wire and an Ag/AgCl electrode serving as the counter and reference electrode, respectively. An ODCB solution of 0.1 mM $(Ph_3N)_4CoP$ in the 0.1 M (TBA)ClO$_4$ supporting electrolyte was used. NPV with two potential steps at 0 and 1.3 V was used with the step time of 1 ms of each potential steps. The number of repetition of this potential program was adjusted to be equivalent of formation of ~20 monolayers of the $(Ph_3N)_4CoP$ polymer on the electrode

64

surface. The electrochemical equivalent of $(Ph_3N)_4CoP$ was determined using CV. Next, the electrode was rinsed with the ODCB solvent, and then immersed for 15 min in a $CHCl_3$ solution, which was 10 mM in a nitrogen-containing ligand. Finally, the electrode was gently rinsed with $CHCl_3$ to remove excess of the ligand, and then the electropolymerization was repeated.

Electrochemical measurements on the $(Ph_3N)_4CoP$ polymer film with the EQCM were performed similarly as those described in Section 3.2.9.

3.2.13 Electrophoretic deposition of the pyr-SWCNTs film

Two instrumental setups for electrophoretic deposition of pyr-SWCNTs were used. Both were composed of the horizontally mounted and facing up Au disk or Au-over-Ti/QCR electrode, with the spiraled Pt wire auxiliary electrode in parallel, positioned 6 mm above the working electrode. The working electrode was positively polarized with the 24 V dc in the 0.4 mg ml^{-1} pyr-SWCNTs fine dispersion in NMP or CHP. After ~6 min of electrophoresis, a black deposit of pyr-SWCNTs uniformly coated the surface of the electrode leaving the solvent colorless and transparent to signal completion of the deposition. Therefore, this time interval was used in all subsequent electrophoretic depositions of the pyr-SWCNTs films. Following the deposition, the electrode was rinsed with ACN, and then dried in an Ar stream. Addition of excess of (TBA)OH × 20 H_2O to the dispersion before electrophoretic deposition drastically increased the deposition rate.

Electrophoretic deposition of pyr-SWCNTs was performed using one of the following two setups. In one,[131] a 10 MHz AT-cut plano-plano QCR featuring an Au-over-Ti or Pt film circular electrodes was mounted in the holder of the EQCM 5710 electrochemical quartz crystal microbalance. The changes of the resonance frequency and dynamic resistance of the QCR were simultaneously recorded during deposition of the pyr-SWCNT film.

In the other setup, the flow-through quartz crystal holder Model EQCM 5610 of the Institute of Physical Chemistry (Warsaw, Poland) without the frequency generator board in it and assembled for batch measurements was used. Thus, this holder served as an electrochemical cell only.

3.2.14 Galvanostatic charging and discharging, and measurements of power of the fabricated energy storage device

In order to evaluate electrochemical stability of the pyr-SWCNTs/(C_{60}Fc-Pd) composite films, a simple laboratory model of a symmetrical charge storage device was assembled (Fig. 2.3-16).
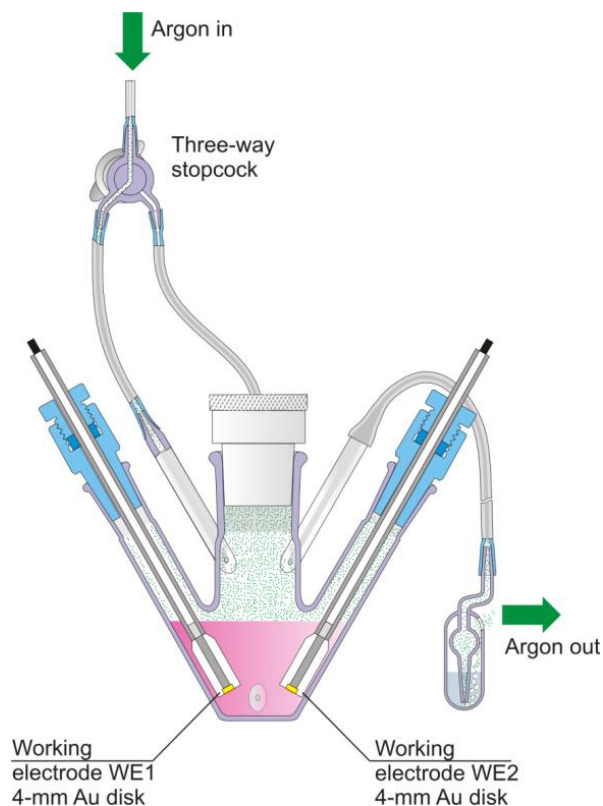
Scheme 3.2-2. Illustration of the cell assembled with two identical 4-mm diameter Au disk/pyr-SWCNTs/C_{60}Fc-Pd working electrodes, WE1 and WE2, for galvanostatic experiments.

It contained two identical Au disk electrodes, each coated with the composite film, immersed in a blank deaerated supporting electrolyte solution.

3.2.15 Preparation of the pyr-SWCNTs/(C_{60}Fc-Pd) film

The C_{60}Fc adduct was electropolymerized in the presence of Pd(Ac)$_2$ with the resulting polymer film deposition on a 3-mm diameter Au disk electrode either pre-coated or not with a film of electrophoretically deposited pyr-SWCNTs. The 0.30 mM C_{60}Fc, 4.56 mM Pd(Ac)$_2$, and the 0.1 M (TBA)ClO$_4$ solution of the toluene : acetonitrile (4 : 1, $v : v$) mixed solvents

66

was used for this electropolymerization. Initially, a sample of the $C_{60}Fc$ adduct and $Pd(Ac)_2$ was dissolved in TL and ACN, respectively. Then, a sample of $(TBA)ClO_4$ was dissolved in the ACN solution of $Pd(Ac)_2$, and, finally, the ACN solution of $Pd(Ac)_2$ and $(TBA)ClO_4$ was mixed with the TL solution of the $C_{60}Fc$ adduct. The electropolymerization was performed under conditions of potentiodynamic multi-cycling with the the potential ranging between 0 and -0.90 V at the potential sweep rate of $100\ mV\ s^{-1}$ under argon atmosphere. Electroanalytical measurements on films and on solutions were carried out with an Autolab electrochemical systems of Eco Chemie/Metrohm Autolab (Utrecht, The Netherlands), equipped with cards of either the PGSTAT 20, PGSTAT 30, or PGSTAT 301N potentiostat, or BIPOT bipotentiostat operated under control of a dedicated GPES 4.9 software or Nova 1.8 software or potentiostat PGSTAT 101 operated under control of a dedicated Nova 1.8 software, all of Eco Chemie/Metrohm Autolab. The polymer film was rinsed with ACN before further use.

4. Results and discussion

4.1 Organic electron donor-acceptor systems for photovoltaic solar energy conversion

4.1.1 Watson-Crick type nucleobase-paired C_{60}ur-(2-AP) conjugates in Langmuir films

Uracil forms hydrogen-bond complexes with complimentary nucleobases via the Watson-Crick nucleobase paring. This supramolecular molecule assembling can be applied to form functional constructs for various applications. Particularly interesting for us is the base pair of the conjugate of the uracil-derivatized C_{60}, 2-(5'-uracil)fulleropyrrolidine, (C_{60}ur), and the analogue of adenine, 2-aminopurine, (2-AP), C_{60}ur-(2-AP). This conjugate is promising for application as an active photovoltaic material.[132] Moreover, hydrogen bonding of these molecules may be used for preparation of selectively recognizing films for chemical sensors based on molecularly imprinted polymers (MIPs).[133]

The focus of the present research was to study self-assembling of C_{60}ur with 2-AP through Watson-Crick nucleobase paring in Langmuir films and possible LB transfer of the films of the resulting conjugate onto solid substrates.
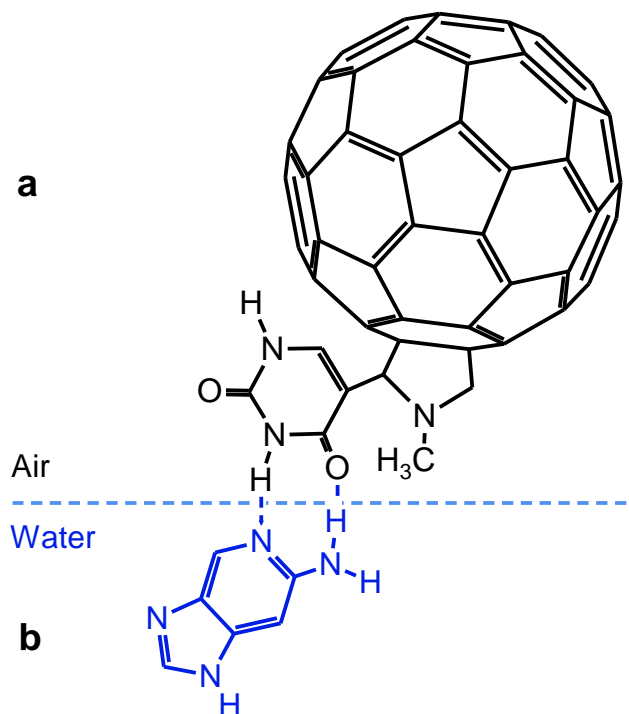

Figure 4.1.1-1. The proposed structural formula of the Watson-Crick nucleobase paired C_{60}ur-(2-AP) conjugate in the air-water interface. (a) 2-(5'-uracil)fulleropyrrolidine (C_{60}ur) and (b) 2-aminopurine (2-AP).

68

First, the π-A and V-A compression isotherms for C_{60}ur spread on the water subphase and on the 2-AP solution subphase of different pH and ionic strength values were simultaneously recorded, and then analyzed. Next, surface morphology of the Langmuir films was characterized by BAM. Then, C_{60}ur and also in situ formed C_{60}ur-(2-AP) Langmuir films spread on different subphases were transferred using the LB technique onto quartz slides. Finally, composition and morphology of the transferred films was examined with UV-vis spectroscopy and characterized by AFM, respectively.

4.1.1.1 Characterization of Langmuir films of C_{60}ur and the C_{60}ur-(2-AP) conjugate spread on different subphases

A series of Langmuir films of C_{60}ur (Fig. 4.1.1-1a) spread on different aqueous subphases or 2-AP solutions (Fig. 4.1.1-1b) were prepared. That way, the resulting Langmuir films were composed of pristine C_{60}ur or in situ formed C_{60}ur-(2-AP) conjugate, respectively. The π-A and π-V compression isotherms for these films were simultaneously recorded (Fig. 4.1.1-2).

The A_0 values for the C_{60}ur were determined from the intercept of the slope tangents of the π-A compression isotherms with abscissa at zero surface pressure. The A_0 value for the C_{60}ur film on a genuine water subphase was independent of the initial C_{60}ur concentration (curve 1 in Fig. 4.1.1-3). However, A_0 linearly depended on the initial C_{60}ur surface concentration for the 0.05 M phosphate buffer (pH = 7.5) and 2-AP subphase solutions (curves 2 and 3, respectively, in Fig. 4.1.1-3). The A_0 value was higher the lower was the initial surface concentration of C_{60}ur.

The A_0 value for C_{60}ur spread on either highly acidic (pH = 1.65) or highly basic (pH = 11.8) subphase solution was higher than that spread on water (pH $\approx$ 5.6) (Table 4.1-1). These higher former values might arise from charging the film by protonation (low pH) or deprotonation (high pH) of the uracil moiety of C_{60}ur. This inference well corresponds with the pK_a values for uracil being pK_{a1} = 0.5, pK_{a2} = 9.5, and pK_{a3} > 13.[134]
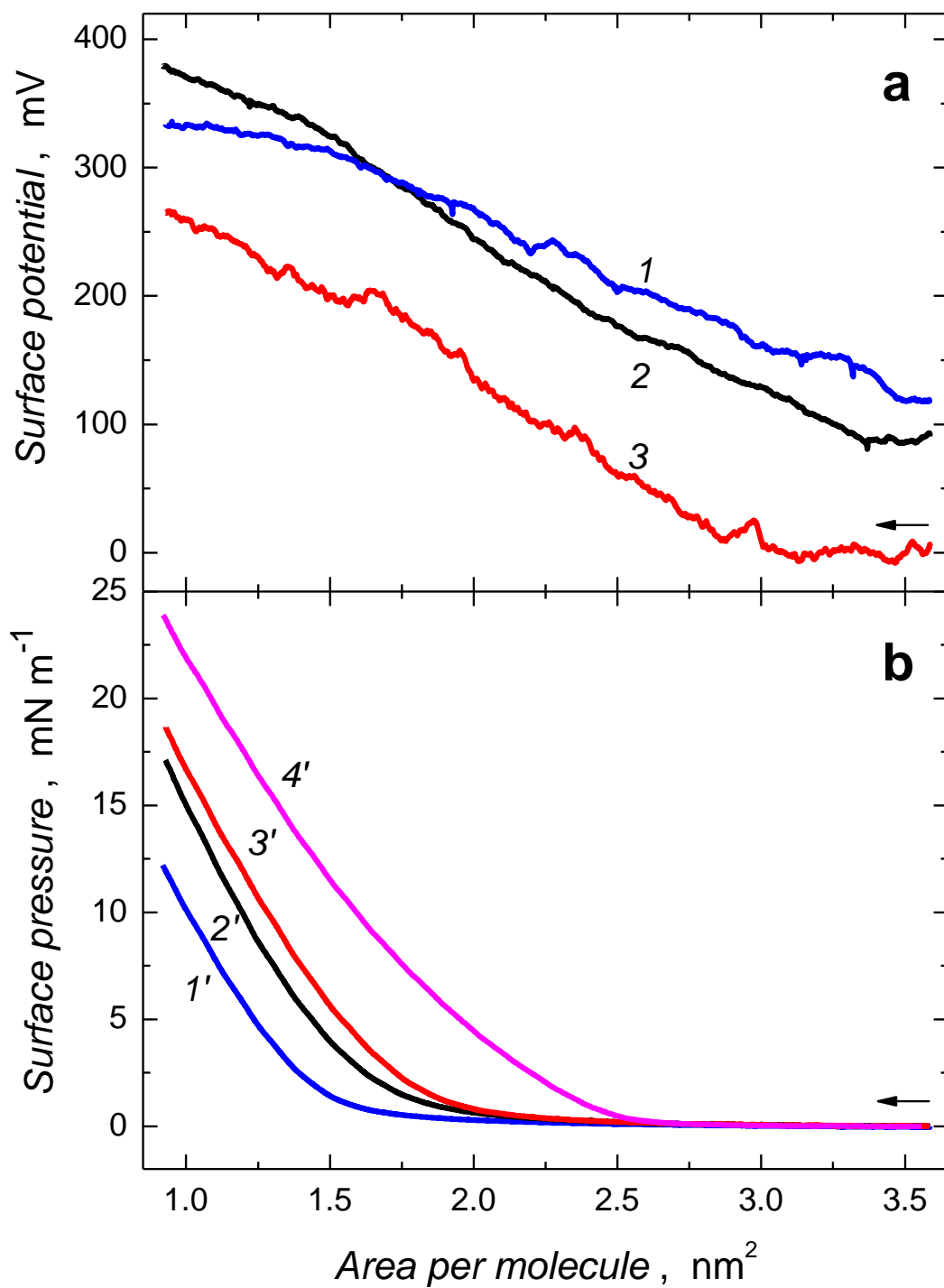
Figure 4.1.1-2. Compression isotherms of (a) surface potential and (b) surface pressure vs. area per molecule for a sample of 22.4 nanomoles of C_{60}ur spread from a chloroform solution onto (*1, 1'*) water (pH ≈ 5.6), (*2, 2'*) 0.05 M phosphate buffer (pH = 7.5), (*3, 3'*) 0.17 mM 2-aminopurine in 0.05 M phosphate buffer (pH = 7.1), and (*4'*) 0.1 mM 2-aminopurine in the Britton-Robinson buffer (pH = 11.8).
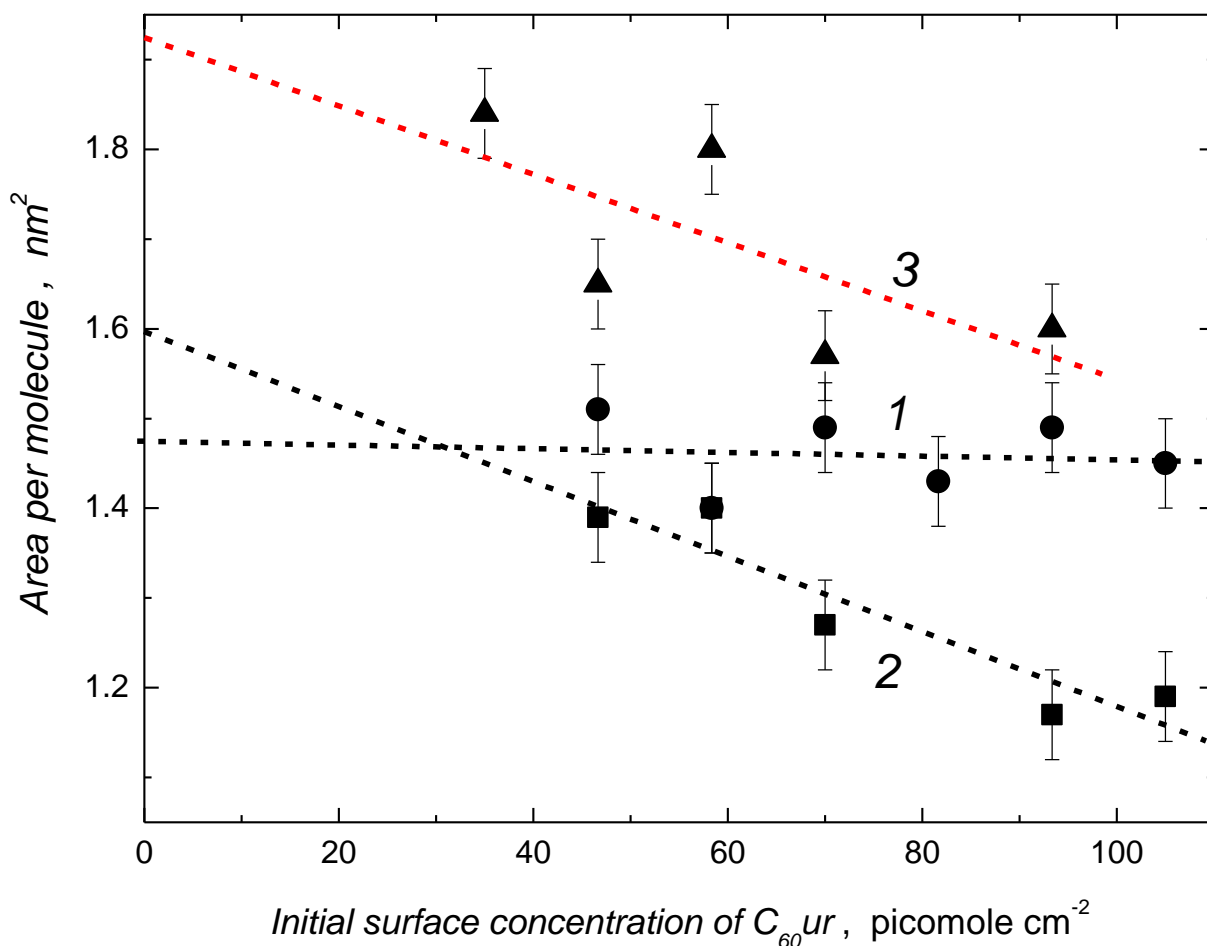
Figure 4.1.1-3. Dependence of the area per molecule on the initial surface concentration of C_{60}ur for the Langmuir films spread from chloroform solutions onto (*1*) water (pH $\approx$ 5.6), (*2*) 0.05 M phosphate buffer (pH = 7.5), and (*3*) 0.17 mM 2-aminopurine in 0.05 M phosphate buffer (pH = 7.1).

The values of A_0 for the acidic, nearly neutral, and basic subphases were compared with those theoretical estimated for two possible extreme orientations of molecules of pristine C_{60}ur and the C_{60}ur-(2-AP) conjugate in the interface. These orientations correspond to perpendicular (vertical) and parallel (horizontal) orientation of the plane of hydrogen bonds between the C_{60}ur and the 2-AP with respect to the interface plane (Fig. 4.1.1-4).

71
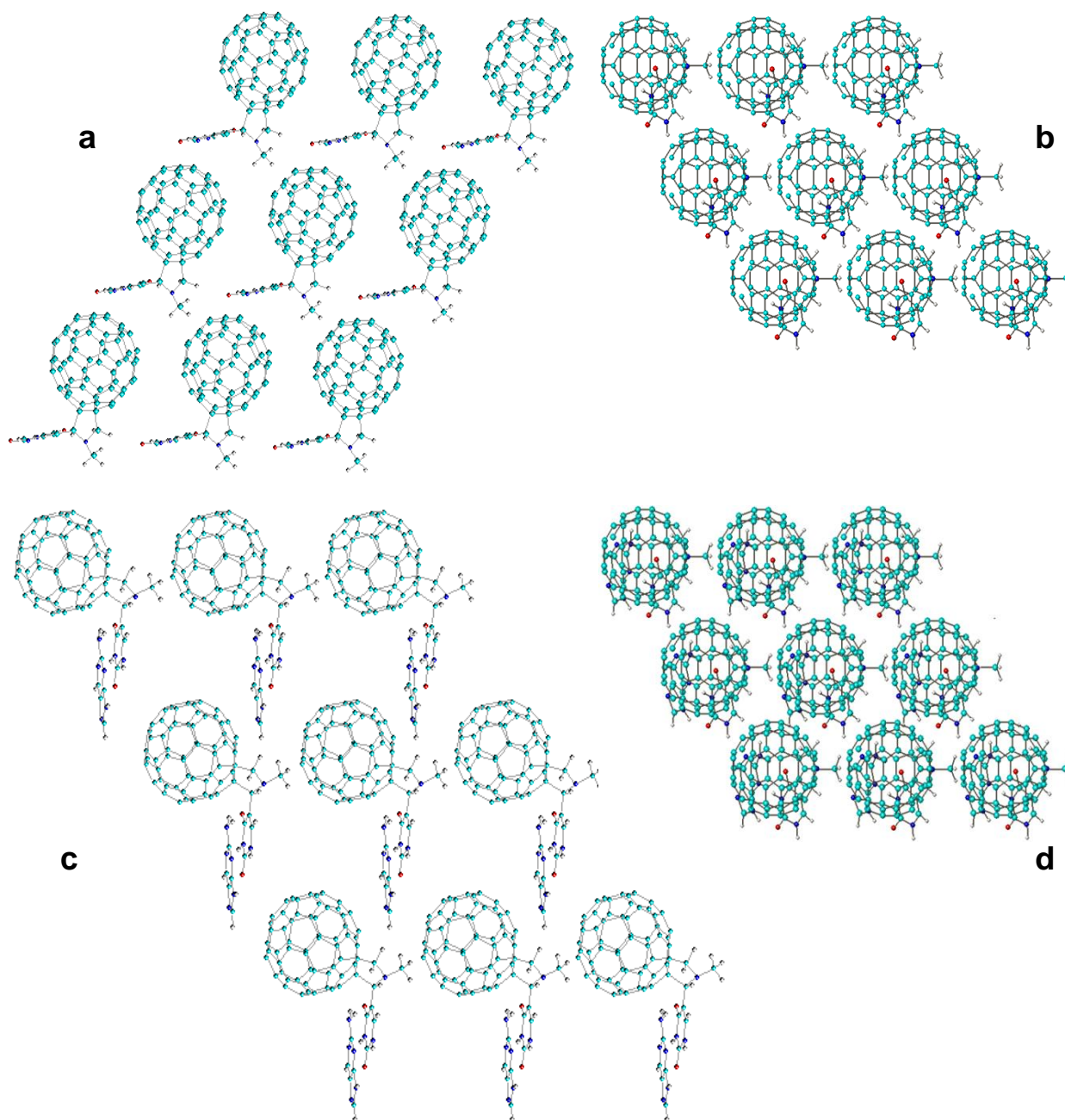
Figure 4.1.1-4. Proposed horizontal orientation of molecules of (a) C_{60}ur and (c) the C_{60}ur-(2-AP) conjugate, and vertical orientation of (b) C_{60}ur and (d) C_{60}ur-(2-AP) conjugate with respect to the air-subphase interface plane (in plane with the page plane).

The experimentally determined A_0 values suggested horizontal orientation of both the C_{60}ur and C_{60}ur-(2-AP) conjugate molecules in their Langmuir films. Moreover, the calculated value of the compressibility coefficient, κ, (Eqn. 4.1.1-1) for both Langmuir films corresponded to so-called "liquid-expanded" phase,[108] i.e., relatively loosely packed molecules (Table 4.1.1-1).

72

Table 4.1.1-1. The determined and calculated values of area per molecule (A_0), compressibility (κ), and the dipole moment component normal to the interface plane ($\mu_\perp$) for the C_{60}ur Langmuir films spread on different subphase solutions.

	Experimental data				Specie in the film	Calculated data			
						Molecule orientation			
						Horizontal		Vertical	
Subphase	A_0 (nm^2)	A_0^∞ (nm^2)	$\kappa \times 10^{-2}$ (m mN^{-1})	$\mu_\perp$ (D)		A_0 (nm^2)	$\mu_\perp$ (D)	A_0 (nm^2)	$\mu_\perp$ (D)
Water (pH $\approx$ 5.6)	1.39	1.60	2.77	5.2	C_{60}ur	1.21	3.43	0.90	0.99
0.05 M Phosphate buffer (pH = 7.5)	1.51	1.48	2.26	3.6	C_{60}ur				
0.17 mM 2-AP in 0.05 M phosphate buffer (pH = 7.1)	1.65	1.92	2.37	5.6	C_{60}ur-(2-AP)	1.51	5.20	0.90	2.10
Britton-Robinson buffer (pH = 11.7)	1.68	-	2.36	-	C_{60}ur				
0.1 mM 2-AP in Britton-Robinson buffer (pH = 11.8)	1.97	-	2.25	-	C_{60}ur-(2-AP)				
KCl and HCl (pH = 1.65)	1.74	-	2.45	-	C_{60}ur				

The determined from the *V-A* isotherms values of $\mu_\perp$ for the C_{60}ur films were highly dependent on the subphase nature. That is, the $\mu_\perp$ value determined for the water subphase substantially differed from that calculated using semi-empirical method (Table 4.1.1-1), and was higher than that for the C_{60}ur film spread on the phosphate buffer (pH = 7.5) subphase. In the presence of 2-AP in this subphase, the determined $\mu_\perp$ value was increased even more. This increase might be caused by organization of water molecules in a close vicinity of the interface. The calculated theoretical value of $\mu_\perp$ for horizontal orientation of the C_{60}ur-(2-AP) conjugate molecules on the phosphate buffer subphase was very close to that experimentally determined and, predictably, nearly twice that for C_{60}ur. This difference may suggest a lower order of water molecules around the 2-AP molecules due to high ionic strength of the subphase solution.
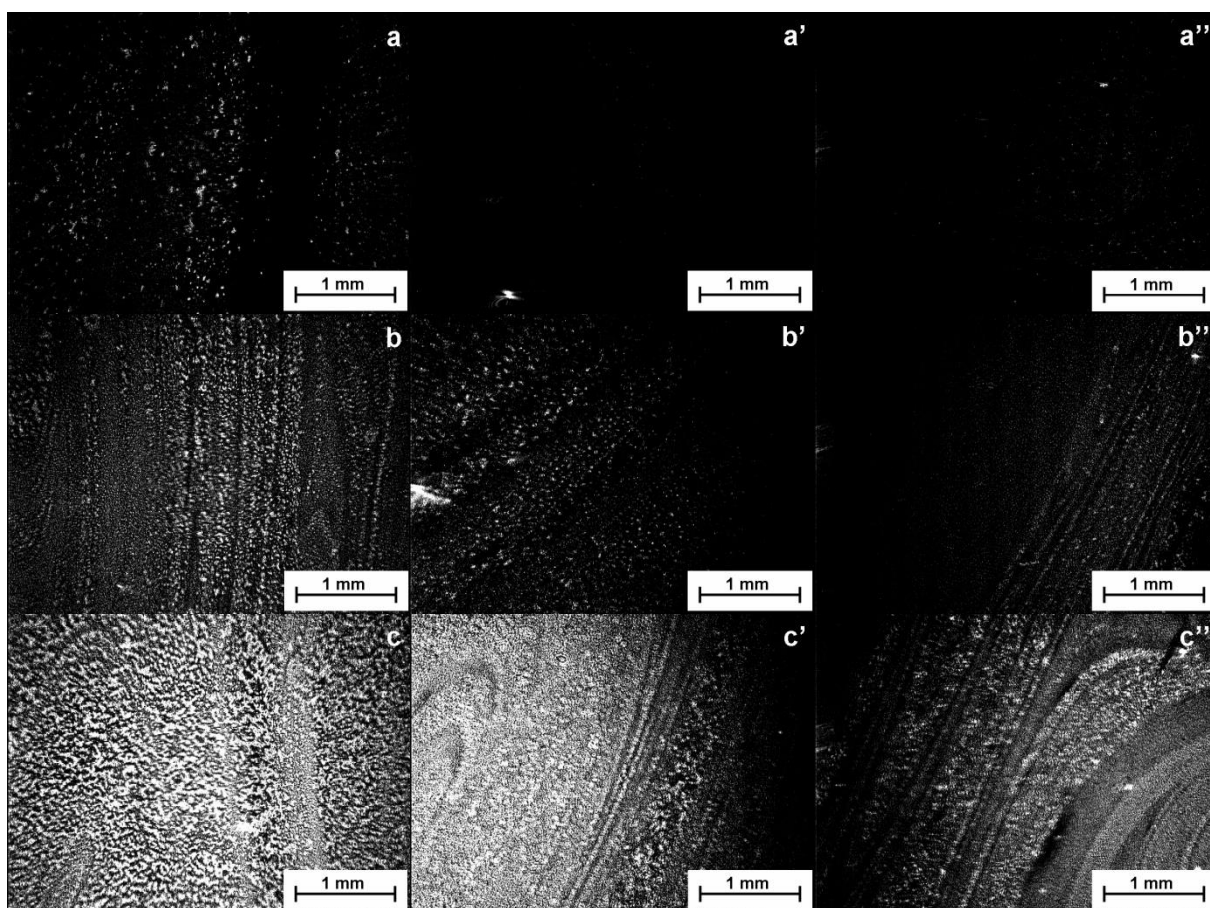

Figure 4.1.1-5. The Brewster angle microscopy images of the C_{60}ur Langmuir films spread on (*a-c*) water (pH ≈ 5.6), (*a'-c'*) 0.05 M phosphate buffer (pH = 7.5), and (*a''-c''*) 0.17 mM 2-aminopurine in 0.05 M phosphate buffer (pH = 7.1) recorded at surface pressure of (*a, a', a''*) 0, (*b, b', b''*) 1, and (*c, c', c''*) 10 mN m^{-1}.

74

The Langmuir films of C_{60}ur and those of the in situ formed C_{60}ur-(2-AP) conjugate, spread on different subphases, were characterized by BAM imaging during compression. Apparently, the C_{60}ur Langmuir film formed on the water substrate (pictures *a-c* in Fig. 4.1.1-5) was more aggregated than that on the 0.05 M phosphate buffer (pH = 7.5) subphase (pictures *a'-c'* in Fig. 4.1.1-5). Moreover, the C_{60}ur film was less aggregated and the Langmuir film was smoother in the presence of 2-AP in the phosphate buffer (pH = 7.1) subphase solution (pictures *a"-c"* in Fig. 4.1.1-5). Deaggregation of the C_{60}ur molecules in the Langmuir film in the presence of 2-AP in the subphase might indicate that the uracil adduct formed a complex with 2-AP in the interface.

4.1.1.2 Langmuir-Blodgett transfer and characterization of films of C_{60}ur and the C_{60}ur-(2-AP) conjugate

Langmuir films of the in situ formed C_{60}ur-(2-AP) conjugate, spread on different subphases, were transferred onto quartz slides using the LB technique. The transfer ratio of the films substantially decreased with the number of transfers (Fig. 4.1.1-6), being higher during withdrawal than immersion of the quartz slide.
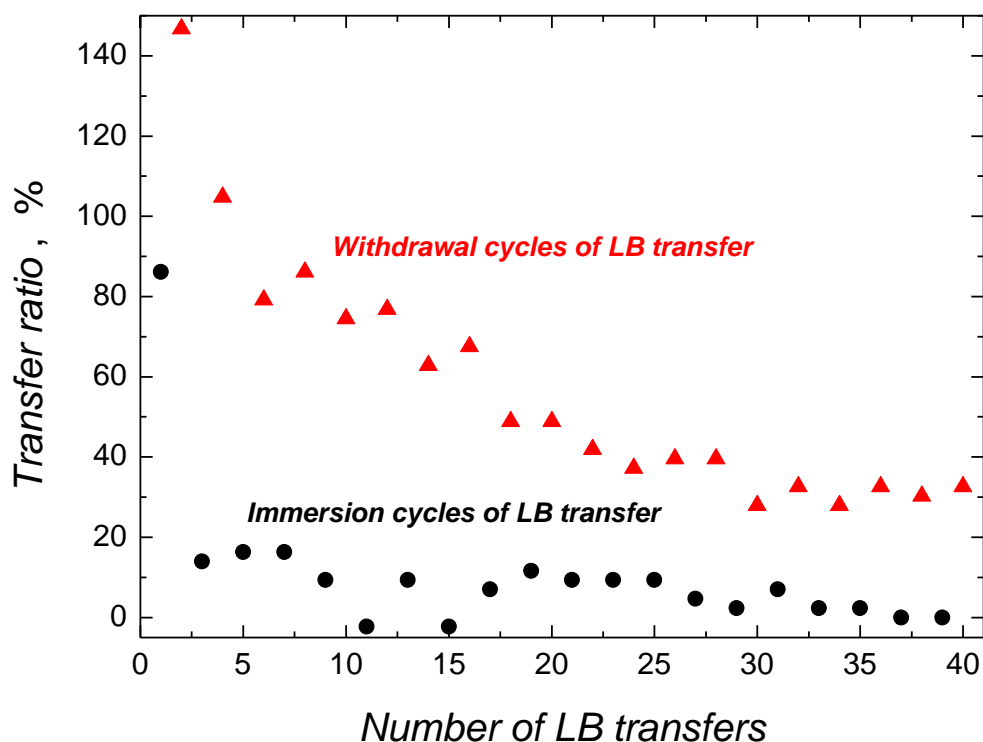
Figure 4.1.1-6. The ratio of the LB transfer of the C_{60}ur Langmuir film, spread on the 0.1 mM 2-AP in 0.05 M phosphate buffer (pH = 7.1) subphase, onto a quartz slide. The dipper speed was 5 mm min^{-1} and the surface pressure was 15 mN m^{-1}.

75

This difference might arise from hydrophilicity of the quartz slide. That is, hydrophilic uracil moieties of C_{60}ur in the Langmuir film were preferentially oriented towards aqueous subphase. Thus, immersion of a hydrophilic slide initially resulted in quartz contacting the hydrophobic C_{60} moiety and, hence, weaker adherence of the Langmuir film. During withdrawal, however, the quartz slide was in contact with the hydrophilic sites of the C_{60}ur or C_{60}ur-(2-AP) conjugate molecules, and, therefore, the transfer was more efficient.

For the first immersion and withdrawal of the quartz slide, the transfer ratio was ~100% (Fig. 4.1.1-6). However, this ratio dropped to merely ~20%, and then to zero during subsequent immersion cycles. The transfer ratio for the withdrawal cycles decreased as well but not as dramatically. That is, it decreased from 100% to ~40% after the initial 20 transfers, and then remained constant at ~30%.

The AFM imaging of the LB films of C_{60}ur transferred onto quartz slides from the water subphase resulted in rough and non-uniform films (Fig. 4.1.1-7a) while transfer of those films from the subphase solution containing 2-AP led to formation of nearly spheroidal islands of 5 to 10 μm in mean diameter (Fig. 4.1.1-7b).
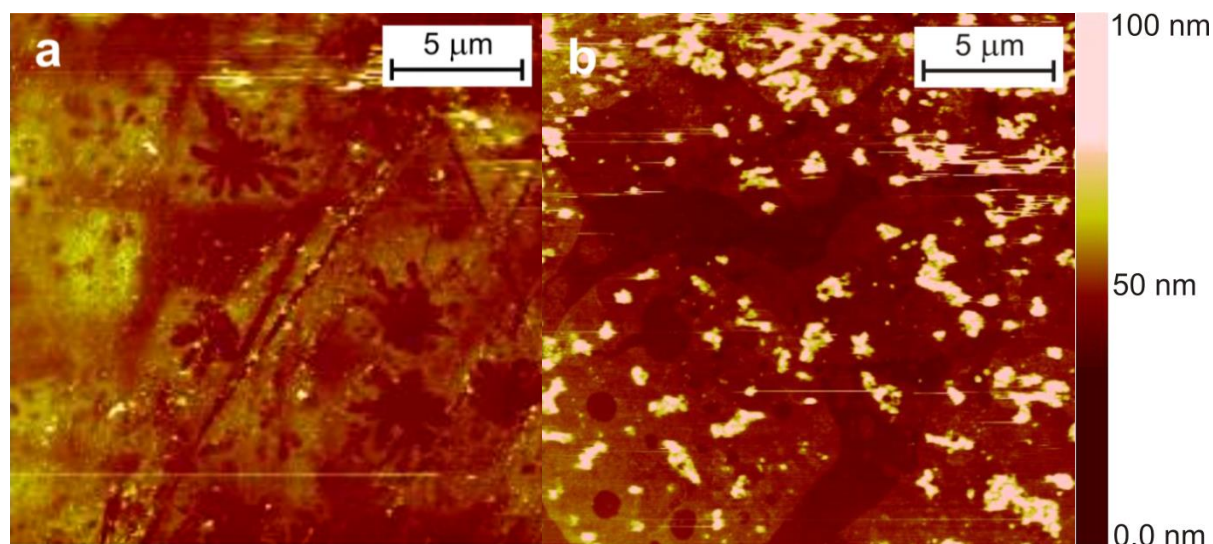
Figure 4.1.1-7. The AFM images of the C_{60}ur LB film deposited on a quartz slide during 40 transfers, at the dipper speed of 5 mm min^{-1} and surface pressure of 15 mN m^{-1}, from the surface of the subphase of (a) water and (b) 0.11 mM 2-AP in 0.05 M phosphate buffer (pH = 7.1).

The resulting LB films were thin because of low transfer ratio (Fig. 4.1.1-6). Nevertheless, the peaks at ~343 nm corresponding to absorbance of C_{60}ur were distinguishable in the UV-vis spectra recorded for the films transferred from both the water and 2-AP in phosphate buffer (pH = 7.1) subphase (Fig. 4.1.1-8).
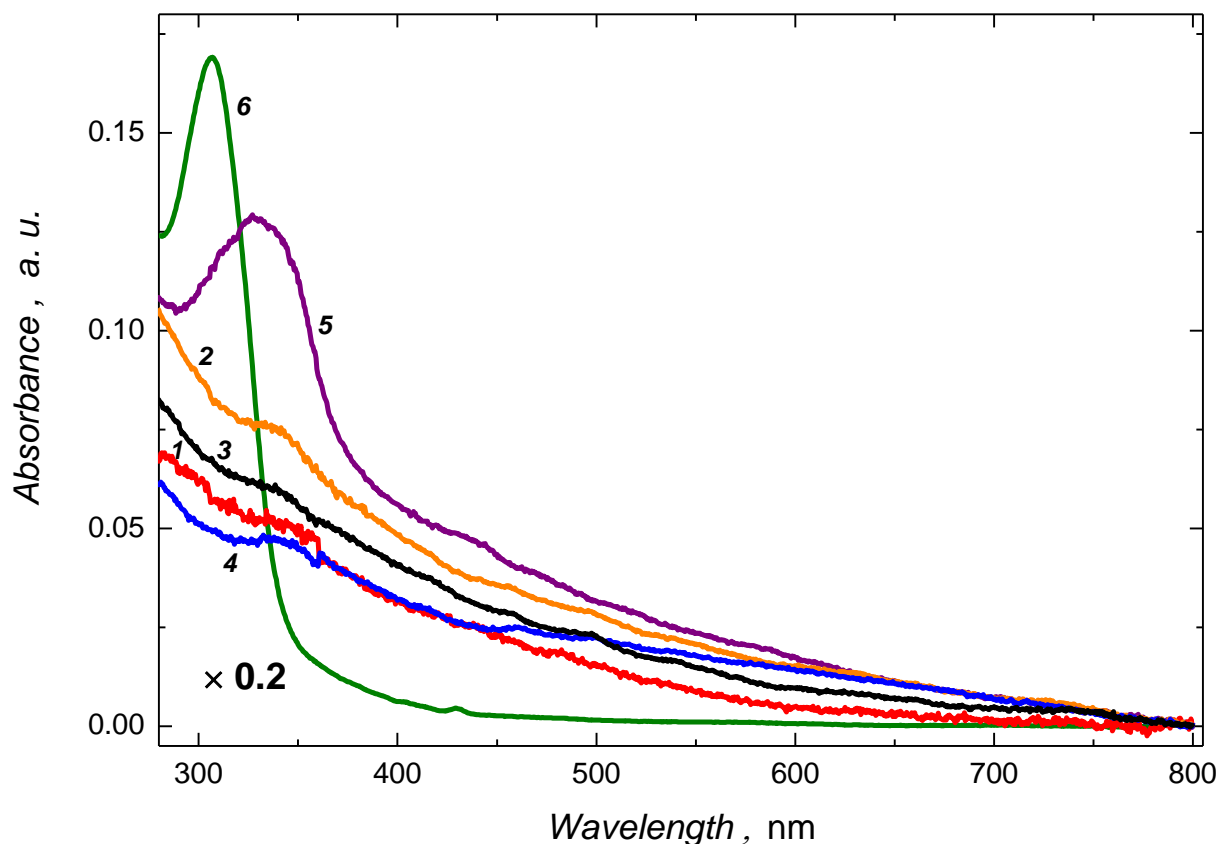
Figure 4.1.1-8. The UV-vis absorbance spectra of the C_{60}ur LB films transferred onto quartz slides at $\pi = 15$ mN m^{-1} from (*1*) 0.17 mM 2-aminopurine in 0.05 M phosphate buffer (pH = 7.5), (*2*) 0.1 mM 2-aminopurine in 4.0 M CaCl$_2$, (*3*) 0.1 mM 2-aminopurine in glycerol and (*4*) water. The spectra of the C_{60}ur-(2-AP), (1 : 1, mole : mole) complex (*5*) in solution and (*6*) in the film drop-coated onto a glass slide are given for comparison.

Unfortunately, there was no UV-vis spectral evidence of the 2-AP presence in the LB film. The 2-AP absorbance band was expected to appear in the 307-to-331 nm range, partially overlapping with that of C_{60}ur. The LB films transferred from neither the 0.1 mM nor 1 mM 2-AP subphase solution showed the 2-AP presence. A possible reason for that might be water competition in hydrogen bonding of the conjugate. As long as the water concentration was ~555 thousand times higher than that of the 2-AP in 0.1 mM 2-AP in

0.05 M phosphate buffer (pH = 7.1), the C_{60}ur-(2-AP) complex was formed under the conditions of strong interference of hydrogen bonding with water molecules. In order to decrease water activity and that way to decrease competition of hydrogen bonding of water to 2-AP, the 0.1 mM 2-AP in 4 M $CaCl_2$ or glycerol subphase solution were prepared. Water activity, a_w, in aqueous solutions of high ionic strength is much decreased (a_w is ~0.5 for 4 M $CaCl_2$) and water is absent in glycerol. However, the UV-vis spectra of the LB films transferred from these subphases did not show any 2-AP presence. One of the possible reasons for that might be breaking of the conjugate during the LB transfer of the film.

4.1.2 Intermolecular distance controlled Langmuir-Blodgett films of self-assembled (Zn phthalocyanine)-C_{60}im electron donor-acceptor dyad

Nature provides numerous examples of solar energy conversion using dedicated photoelectroactive substances and efficient mechanisms of this process.[28,29,135] A lot of effort has been paid to transfer these principles of solar energy harvesting to photovoltaics[136,137] and, recently, to organic photovoltaics.[9,22] For that, metallophthalocyanine-fullerene electron donor-acceptor dyads have, among others, been studied intensively.[26,32,33] That way, Nature is mimicked with metallophthalocyanines, used as photoexitable electron donors, while C_{60} derivatives - as efficient electron acceptors. Chemical modification of both allowed for tuning mechanical and electronic properties of the dyads.[36-38]
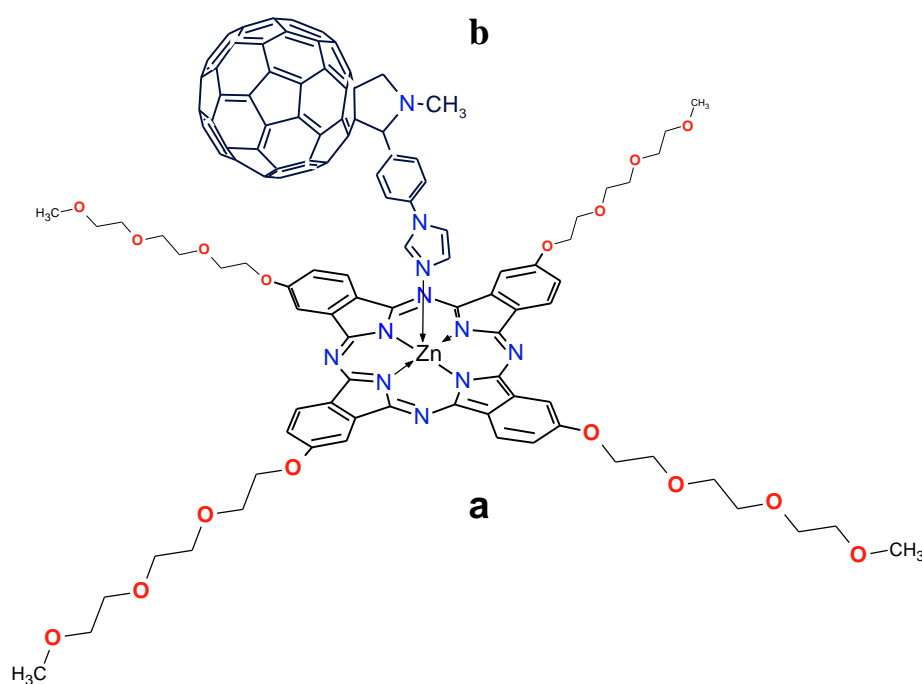
Scheme 4.1.2-1. The proposed structural formula of the Zn(TPEE)-C_{60}im electron donor-acceptor dyad used for preparation of the Langmuir and Langmuir-Blodgett films. (a) The tetrakis(2,9,16,23-[triethyleneglycolmonomethylether]phthalocyaninato)Zn(II), Zn(TPPE), donor and (b) the 2-(phenylimidazolyl)fullerenopyrrolidine, C_{60}im, acceptor.

Accordingly, we focused on formation, characterization and photoelectrochemical properties of a supramolecularly assembled donor-acceptor dyad composed of the Zn(phthalocyanine) donor bearing peripheral alkylether substituents (vis., tetrakis[(2,9,16,23-

79

triethyleneglycolmonomethylether)phthalocyaninato]Zn(II), Zn(TPPE), and the imidazole adduct of [C_{60}]fullerene (viz., 2-(phenylimidazolyl)fullerenopyrrolidine), C_{60}im, acceptor (Scheme 4.1.2-1).

First, Zn(TPPE) was synthesized according to the procedure developed herein. Then, the Zn(TPPE)-C_{60}im dyad was prepared and its optical and electrochemical properties in solution were determined. Next, Langmuir films of the dyad and its components, separately, were prepared at the air-water interface. The Langmuir films were characterized by simultaneous recording the π-A and V-A compression isotherms, and BAM imaging. Then, the Langmuir films of the dyad were transferred onto the fluorine-doped tin oxide (FTO) coated glass slides or the Au-over-Ti coated glass slides by the LB technique. Orientation of the molecules in the film transferred at different surface pressures was revealed with the PM-IRRAS measurements. Moreover, photoelectrochemical properties of the resulted films were unraveled. The procedure resulting in the LB film samples with the best photovoltaic performance was selected for transfer of the films onto different solid substrates. Finally, these LB films were characterized using several physicochemical techniques.

4.1.2.1 Synthesis of the Zn(TPPE)

The Zn(TPPE) donor was synthesized and purified according to Scheme 4.1.2-2. The synthesis involved the following two steps.

4-*Triethyleneglycolmonomethyletherphthalonitrile*. This ether was synthesized by mixing 4-hydroxyphthalonitrile, triethyleneglycol monomethylether tosylate, and K_2CO_3 in DMF (1 : 1 : 4, mole : mole : mole; 2.08 mmole, and 8.32 mmole, respectively). Then, the mixture was stirred for 15 h at 80 °C under nitrogen. After cooling, the mixture was filtered. The solvent of the filtrate was evaporated and the crude product residue purified by LC on a silica gel column. The pure compound was eluted with CH_2Cl_2. The yield was 1.4 mmole (67%).

Tetrakis(*2,9,16,23*-[*triethyleneglycolmonomethylether*]*phthalocyaninato*)*Zn*(II), Zn(TPPE). A mixture of 4-triethyleneglycolmonomethyletherphthalonitrile and $ZnCl_2$ (1 : 2, mole : mole; 0.72 mmole and 1.44 mmole, respectively) was kept in a 100-ml round-bottom flask for 20 min under nitrogen. Next, 4 ml of dimethylaminoethanol (DMAE) was added, and then the mixture refluxed for 16 h. After cooling this mixture to room temperature, the solvent was evaporated and the residue purified by LC using a silica gel column. Pure

80

Zn(TPPE) was eluted with the solution of the CH_2Cl_2-to-CH_3OH volume ratio of 9 : 1. The yield was 0.32 mmole (45%). TOF MS ES+: calcd. 1226.44, found 1226.44 (Fig. 4.1.2-1).

$$(1)$$

$$(2)$$
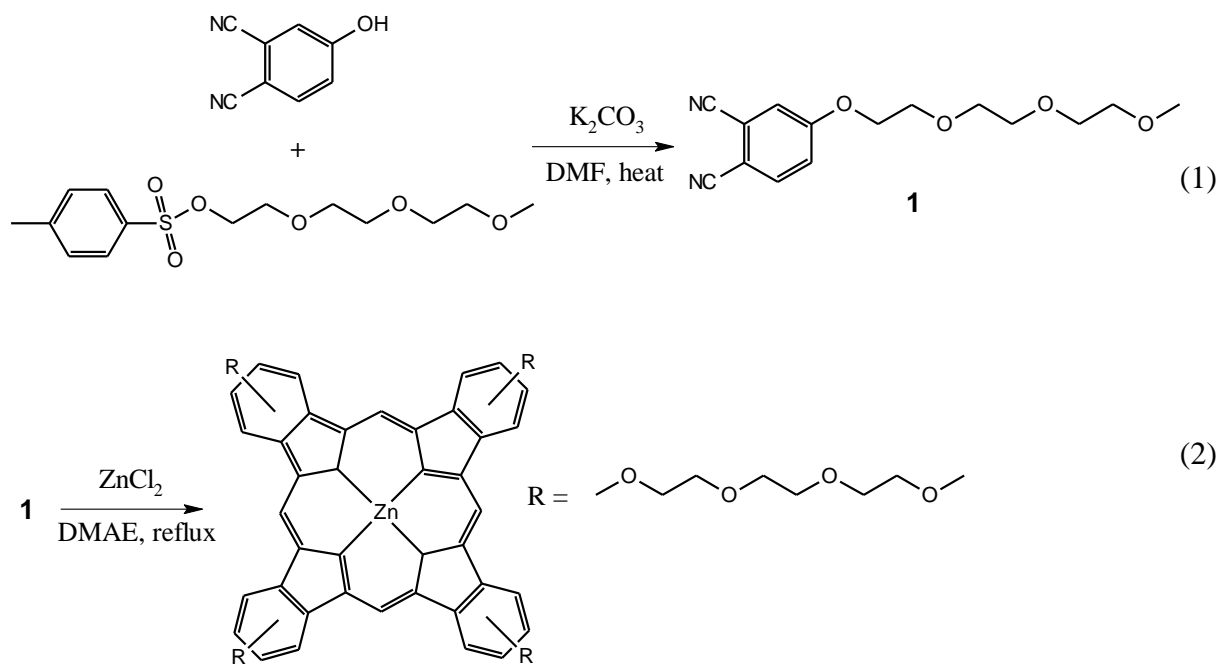
Scheme 4.1.2-2. Reaction equations of the Zn(TPPE) synthesis.
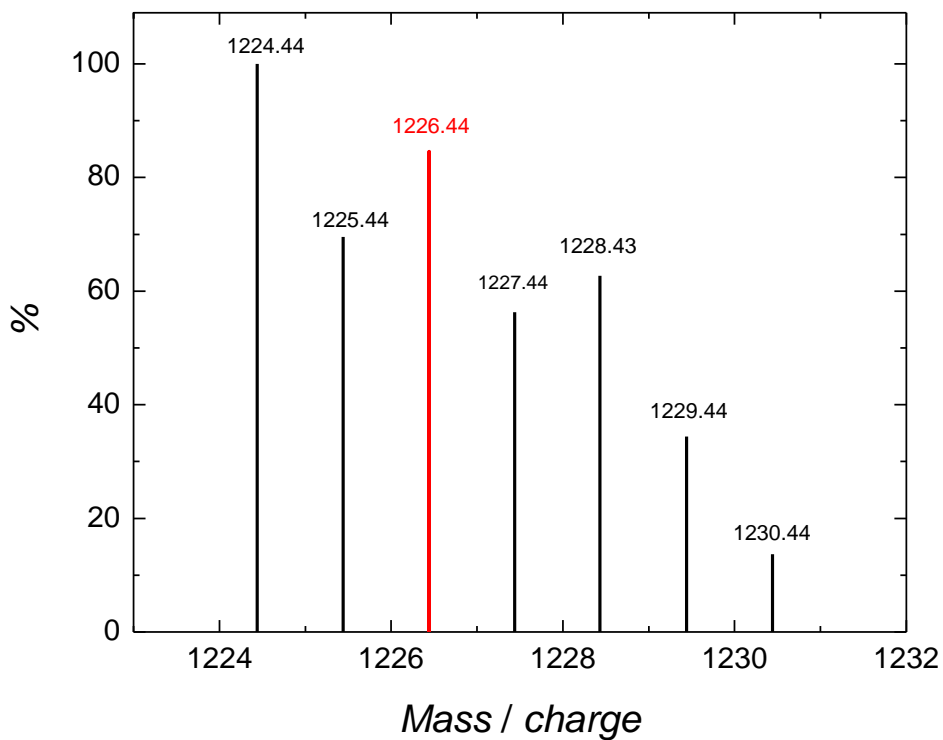
Figure 4.1.2-1. The time-of-flight mass spectrometry electrospray+ (TOF MS ES+) spectra for Zn(TPPE). The determined molar mass of the Zn(TPPE) was 1226.44 g mol^{-1}.

81

4.1.2.2 Computational modeling and experimental determination of properties of the Zn(TPPE)-C$_{60}$im dyad in solution

In order to determine geometry and electronic structure of the dyad, structures of Zn(TPPE), C$_{60}$im, and Zn(TPPE)-C$_{60}$im were optimized with the DFT method at the B3LYP/3-21G* level (Gaussian 09 software).[130]

Table 4.1.2-1. The DFT estimated dipole moments and dipole moment components normal to the subphase plane ($\mu_\perp$) for the molecules of Zn(TPPE) and C$_{60}$im as well as that of the Zn(TPPE)-C$_{60}$im dyad.

Molecule orientation	Dipole moment component normal to the subphase ($\mu_\perp$), D
C$_{60}$im	
Long axis of the imidazole-benzene moiety perpendicular to the surface	1.7
Long axis of imidazole-benzene moiety parallel to the surface	3.8
Molecule "laying on the back"	0.9
Total dipole moment	4.5
Zn(TPPE)	
Macrocycle parallel to the surface*	0.0
Macrocycle perpendicular to the surface*	0.6
Total dipole moment. If the ether substituents are perpendicular to the macrocycle plane, then the dipole moment is much higher and oriented in the direction of the substituents	0.6
Zn(TPPE)-C$_{60}$im	
Macrocycle parallel to the surface	1.8
Macrocycle perpendicular to the surface	8.5
Total dipole moment	8.7

* Peripheral ether substituents are in plane of the Zn(TPPE) macrocycle.
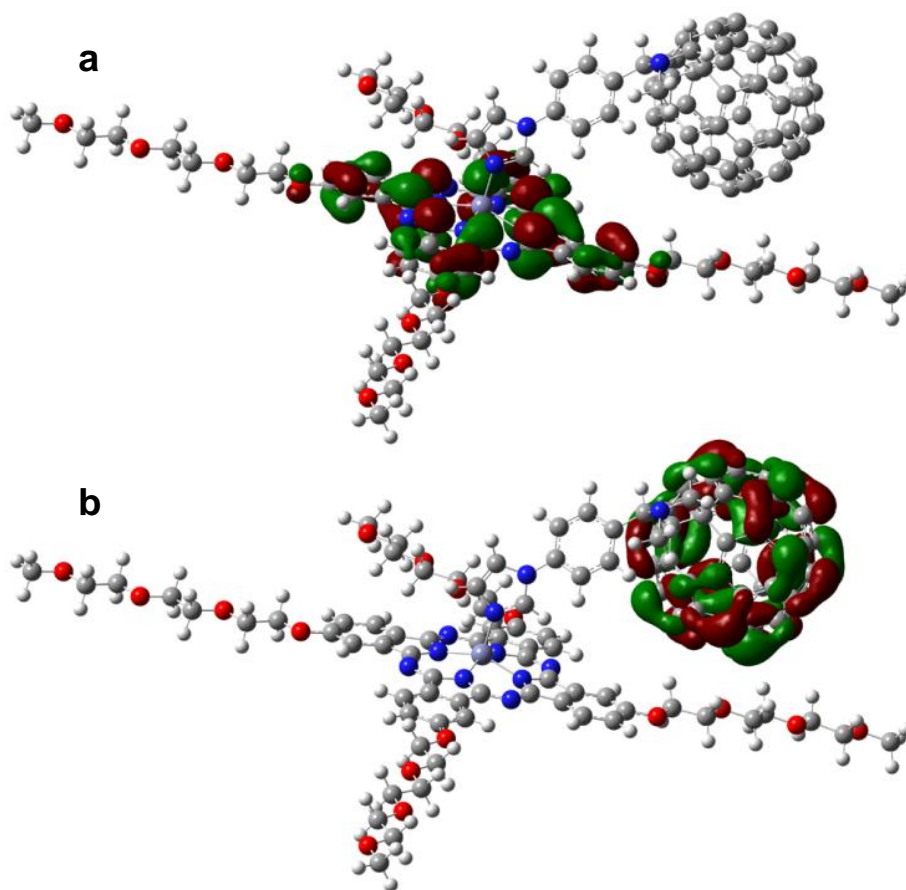
Scheme 4.1.2-3 The DFT/(B3LYP/3-21G*) optimized structure of (a) HOMO and (b) LUMO of the Zn(TPPE)-C_{60}im complex at $t = 298.16$ °C in vacuum.

The HOMO was delocalized over the Zn(TPPE) macrocycle with no electron density on the ether peripheral substituents (Scheme 4.1.2-3a) while the LUMO was localized on the fullerene cage of the C_{60}im moiety (Scheme 4.1.2-3b). Furthermore, these calculations resulted in values and orientation of dipole moments of the dyad and the dyad moieties separately (Table 4.1.2-1). Predictably, the dipole moment of the Zn(TPPE) molecule was located within the macrocycle plane, as expected for highly symmetric molecule. Apparently, elasticity of peripheral groups resulted in the change of the Zn(TPPE) dipole moment upon compression of the Langmuir film. The C_{60}im dipole moment was nearly perpendicular against the imidazole-benzene axis. Formation of the Zn(TPPE)-C_{60}im dyad resulted in the increase of the dipole moment value. Its direction was perpendicular to the macrocycle plane.

83
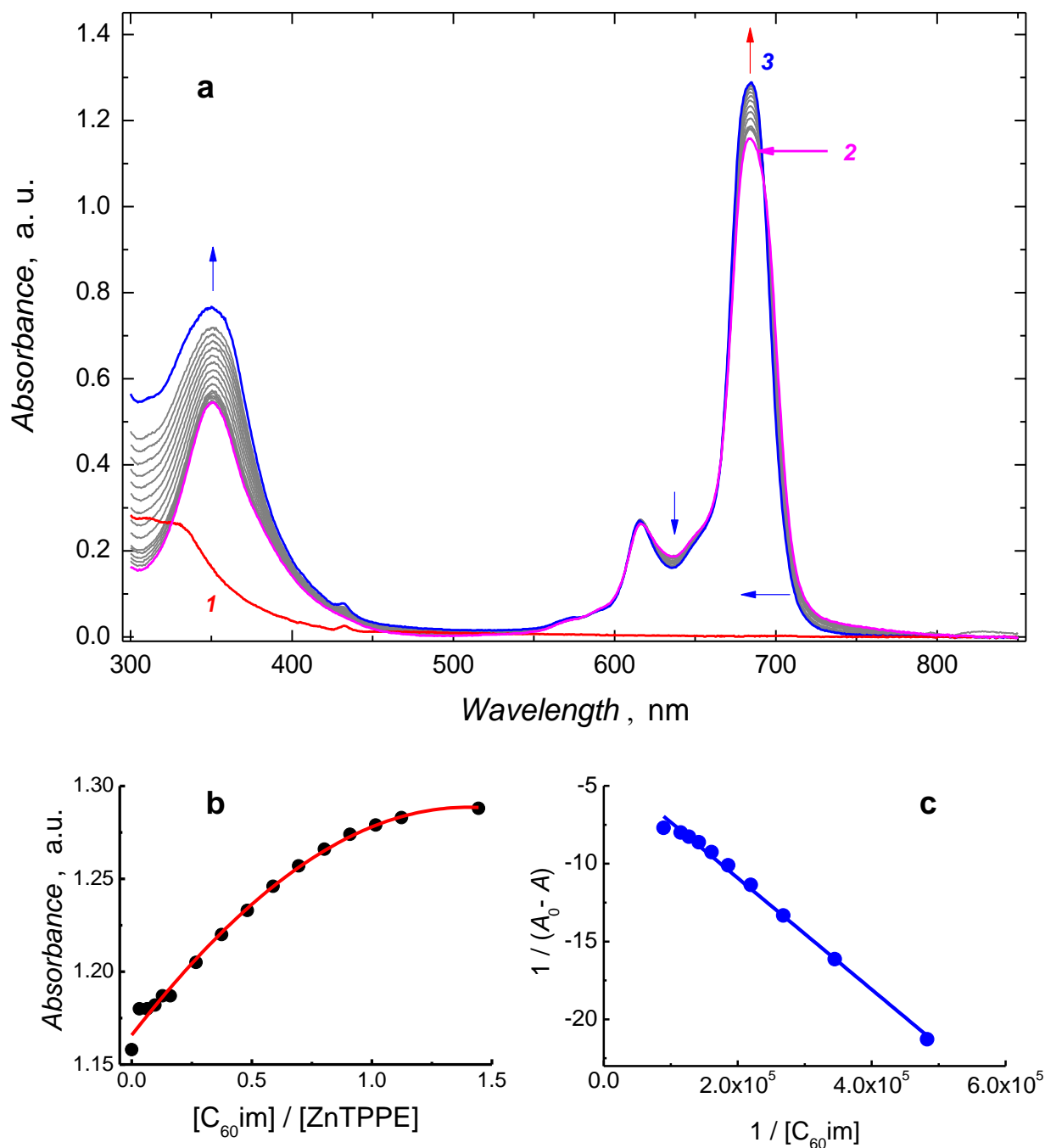
Figure 4.1.2-2. (a) The UV-vis spectra for titration of Zn(TPPE) with 0.207 mM C_{60}im in ODCB (3-μL and 5-μL injections) as well as (*1*) 6.905 μM C_{60}im, (*2*) 7.74 μM Zn(TPPE) and (*3*) the Zn(TPPE)-C_{60}im dyad. (b) Absorbance at the Soret band vs. [C_{60}im]/[Zn(TPPE)], (c) the Benesi-Hildebrand plot constructed for determination of the complex stability constant. A_0 stands for absorbance of the Zn(TPPE) Soret band, *A* stands for absorbance of the Zn(TPPE) Soret band upon addition of the C_{60}im titrating ligand.

84

The Zn(TPPE) donor was titrated with the C_{60}im acceptor using UV-vis spectroscopy in order to determine the stability constant of the Zn(TPPE)-C_{60}im dyad (Eqn. 3.2-18) and to confirm its 1 : 1 stoichiometry (Fig. 4.1.2-2a).

The consecutive addition of 3-μL and 5-μL solution samples of the C_{60}im ligand to the Zn(TPPE) solution caused the increase of absorbance of the Soret band of Zn(TPPE) at $\lambda = 685$ nm. The Zn(TPPE)-to-C_{60}im mole ratio was determined as 1 : 1 from the absorbance at the Soret band vs. [C_{60}im]/[Zn(TPPE)] (Fig 4.1.2-2b). The determined from the Benesi-Hildebrand plot (Fig. 4.1.2-2c) stability constant of the Zn(TPPE)-C_{60}im (1 : 1, mole : mole) complex in solution was, $K_s^s = 1.05 \times 10^5$ M^{-1}.

4.1.2.3 Preparation and properties of Langmuir films of the Zn(TPPE)-C_{60}im dyad and, separately, its components

The Langmuir films of the Zn(TPPE)-C_{60}im dyad and its components, separately, were characterized by simultaneous recording of the compression isotherms of π–A (Fig. 4.1.2-3b) and V-A (Fig. 4.1.2-3a) as well as by BAM imaging (Fig. 4.1.2-4).

For Zn(TPPE), C_{60}im, and the Zn(TPPE)-C_{60}im dyad, two phases were consecutively formed during compression. The determined from the slope of the π–A isotherms dynamic compressibility values (Table 4.1.2-1) suggested that all these phases were of a liquid-expanded type. The measurement of the surface potential as a function of area per molecule was more sensitive to orientation changes of molecules in the films than that of the surface pressure. That is, the orientation changes of the C_{60}im molecules accompanying surface potential changes were nearly completed when surface pressure just started to grow. The proposed interpretation of these changes is, as follow. At zero pressure and the barriers of the Langmuir trough open, the C_{60}im molecules were preferentially oriented horizontally in the Langmuir film (Scheme 4.1.2-4a). With the decrease of the area per molecule available in the Langmuir trough, C_{60}im molecules started to repel each other, and then rearranged to assume vertical orientation with the hydrophilic imidazole moiety oriented toward water (Scheme 4.1.2-4b). This transition was accompanied by a linear increase of V (curve *2* in Fig. 4.1.2-3a). When V reached plateau, a new phase was formed while π just started to grow (curve *2'* in Fig. 4.1.2-3b). Further increase of π resulted in pushing the C_{60}im molecules out of the monolayer and formation of a multilayer.

85
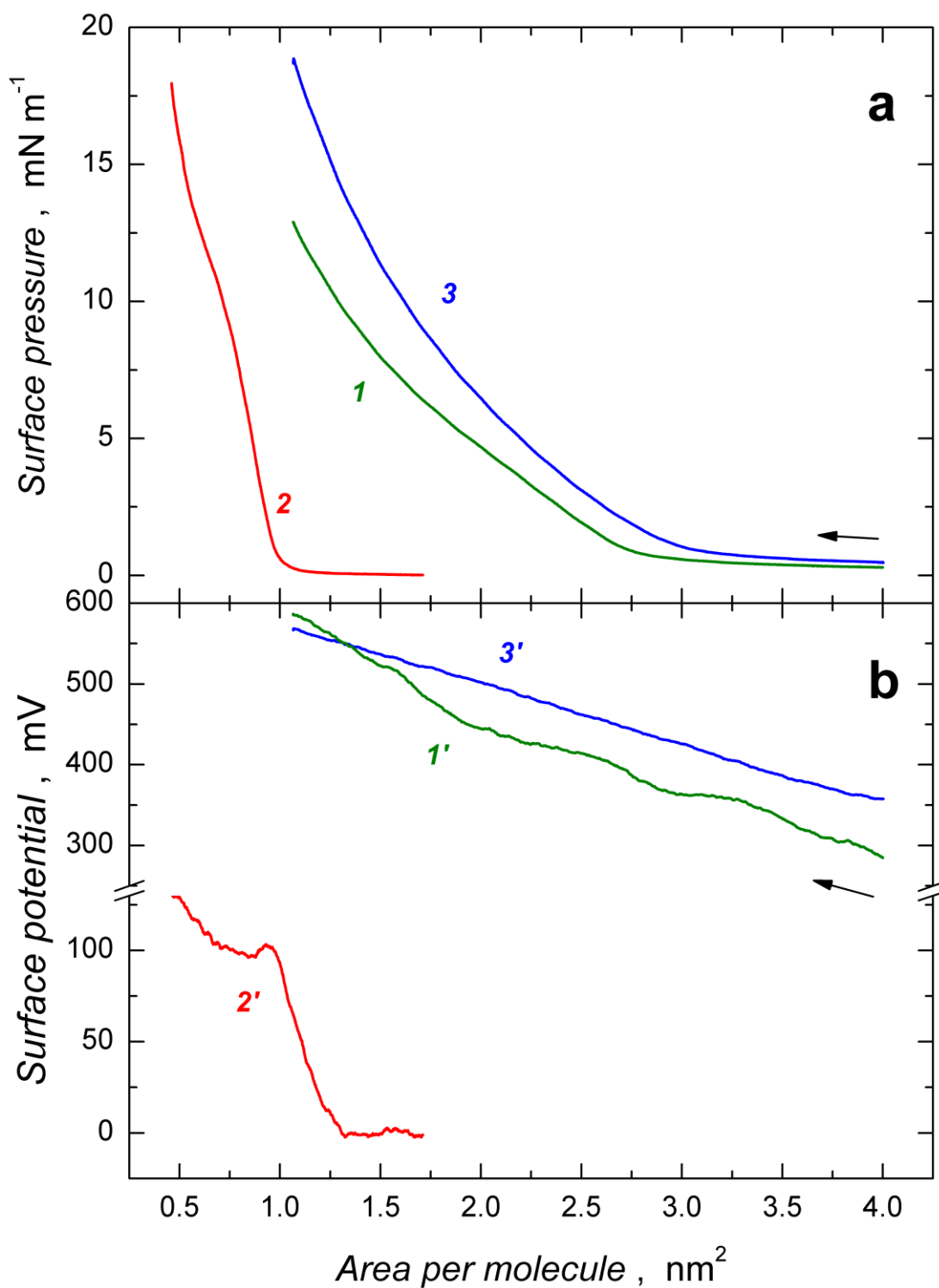
Figure 4.1.2-3. The compression isotherms of (a) surface potential and (b) surface pressure vs. area per molecule for a Langmuir film of (*1, 1'*) 35 nanomoles of $C_{60}im$, (*2, 2'*) 15 nanomoles of Zn(TPPE), and (*3, 3'*) 15 nanomoles of the Zn(TPPE):$C_{60}im$ (1 : 1, mole : mole) complex.
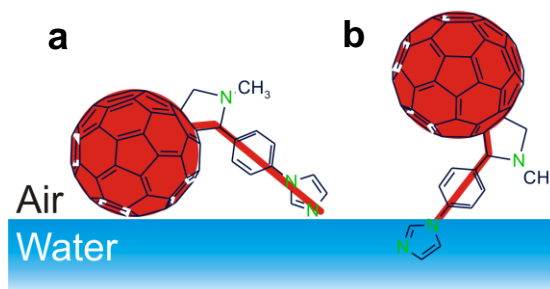
Scheme 4.1.2-4. (a) Horizontal and (b) vertical orientation of the C_{60}im molecule in the air-water interface.
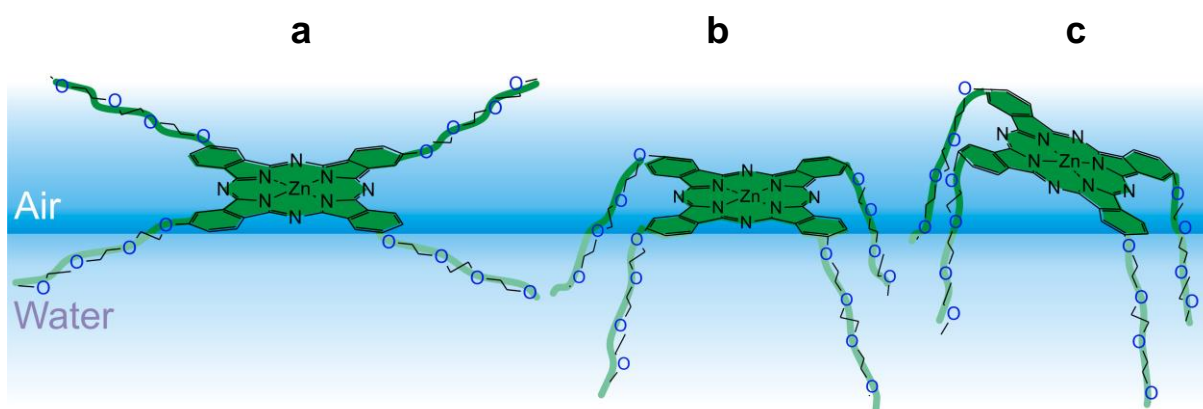
Scheme 4.1.2-5. The Zn(TPPE) molecule orientation in the air-water interface at (a) $\pi = 0$, (b) $0 < \pi < 10$, and (c) $\pi > 10$ mN m^{-1}.

Interfacial behavior of Zn(TPPE) in its Langmuir film can be interpreted, as follows. The presence of four hydrophilic alkylether peripheral groups in the Zn(TPPE) molecule suggested flat orientation of the phthalocyanine macrocycle at the air-water interface at zero surface pressure (Scheme 4.1.2-5a). The *V-A* isotherm for the Zn(TPPE) Langmuir film, however, was linear and increased with the compression increase of the film. This behavior might be caused by "sinking" of flexible peripheral groups and the increase of the dipole moment of the molecule (Scheme 4.1.2-5b). Finally, at $\pi \approx 10$ mN m^{-1} the macrocycles, most likely, were pushed away from the film and started tilting (Scheme 4.1.2-5c). The same behavior for the film of the Zn(TPPE)-C_{60}im dyad was observed at slightly lower pressure (curves *3* and *3'* in Fig. 4.1.2-3a and 3b and Scheme 4.1.2-6).

The simultaneously recorded BAM image of the Zn(TPPE) Langmuir film at this pressure revealed that the film collapsed (Fig. 4.1.2-4c). However, there was no evidence for

it either on the *V-A* or *π-A* isotherm (curves *1* and *1'* in Fig. 4.1.2-3a and 3b, respectively). At $\pi > 20$ mN m^{-1}, the *V-A* isotherm reached maximum and started to decrease (not shown).
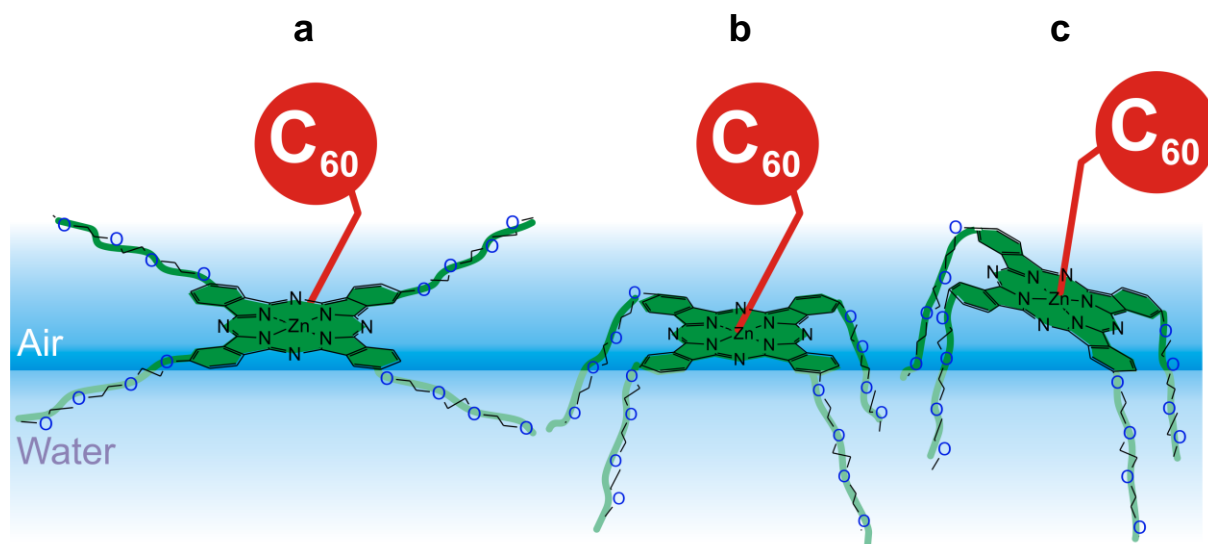
Scheme 4.1.2-6. The Zn(TPPE)-C$_{60}$im dyad orientation in the air-water interface at (a) $\pi = 0$, (b) $0 < \pi < 10$, and (c) $\pi > 10$ mN m^{-1}.

Table 4.1.2-2. Values of area per molecule, determined from the *π-A* compression isotherms, for the Langmuir films of Zn(TPPE), C$_{60}$im, and the Zn(TPPE)-C$_{60}$im (1 : 1, mole : mole) dyad spread on the water subphase.

Langmuir film	Parameters of the *π-A* compression isotherms			
	Determined			Estimated
	$A_{0,1}$; $A_{0,2}$ (nm^2)	$(\kappa_1; \kappa_2) \times 10^{-2}$ (m mN^{-1})	$\mu_\perp$ (D)	$A_{0,1}$; $A_{0,2}$ (nm^2)
C$_{60}$im	0.99; 0.87	2.61; 2.83	0.50; 0.56	1.38; 1.17
Zn(TPPE)	2.84; 2.09	6.38; 3.82	6.86; 9.25	~8.53; 1.85
Zn(TPPE)-C$_{60}$im	2.03; -	2.59; -	4.26; -	~8.53; 1.85

The films were prepared by dispensing 150-μL samples of 0.1 mM Zn(TPPE) or Zn(TPPE)-C$_{60}$im in CHCl$_3$ or a 350-μL sample of 0.1 mM C$_{60}$im in CHCl$_3$.
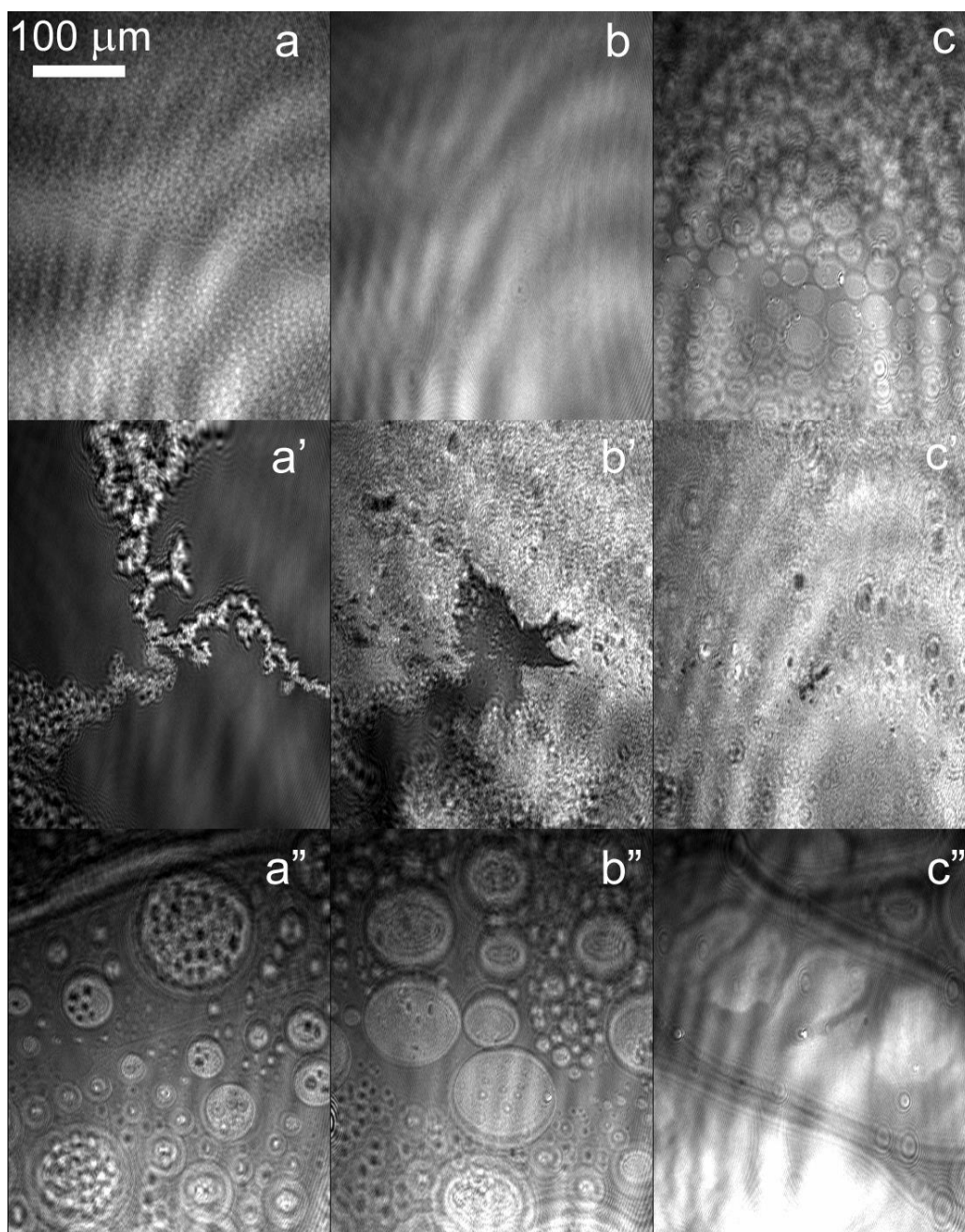
Figure 4.1.2-4. Brewster angle microscopy images of the Langmuir films of (a, b, c) Zn(TPPE) as well as (a', b', c'), and (a", b", c") the Zn(TPPE)-C_{60}im (1 : 1, mole : mole) dyad spread on the water subphase, recorded at the surface pressure of 0, 1, and 10 mN m^{-1}, respectively.

Addition of C_{60}im to the Zn(TPPE) chloroform solution to form a 1 : 1 (mole : mole) complex made the Langmuir film of the resulting dyad more rigid (the dynamic compressibility values are compiled in Table 4.1.2-2). The determined and estimated values

of the area per molecule, dynamic compressibility, and dipole moment are compiled in Table 4.1.2-2.

BAM imaging of the Langmuir films in the course of compression (Fig. 4.1.2-4) allowed observing phase transitions. Moreover, formation of domains of differently organized molecules was observed in the BAM images during compression of the film of the Zn(TPPE)-C_{60}im dyad (images a", b", and c" in Fig. 4.1.2-4). The changes in images of the Langmuir films were consistent with the surface potential changes (curves *1*, *2*, and *3* in Fig. 4.1.2-3a).
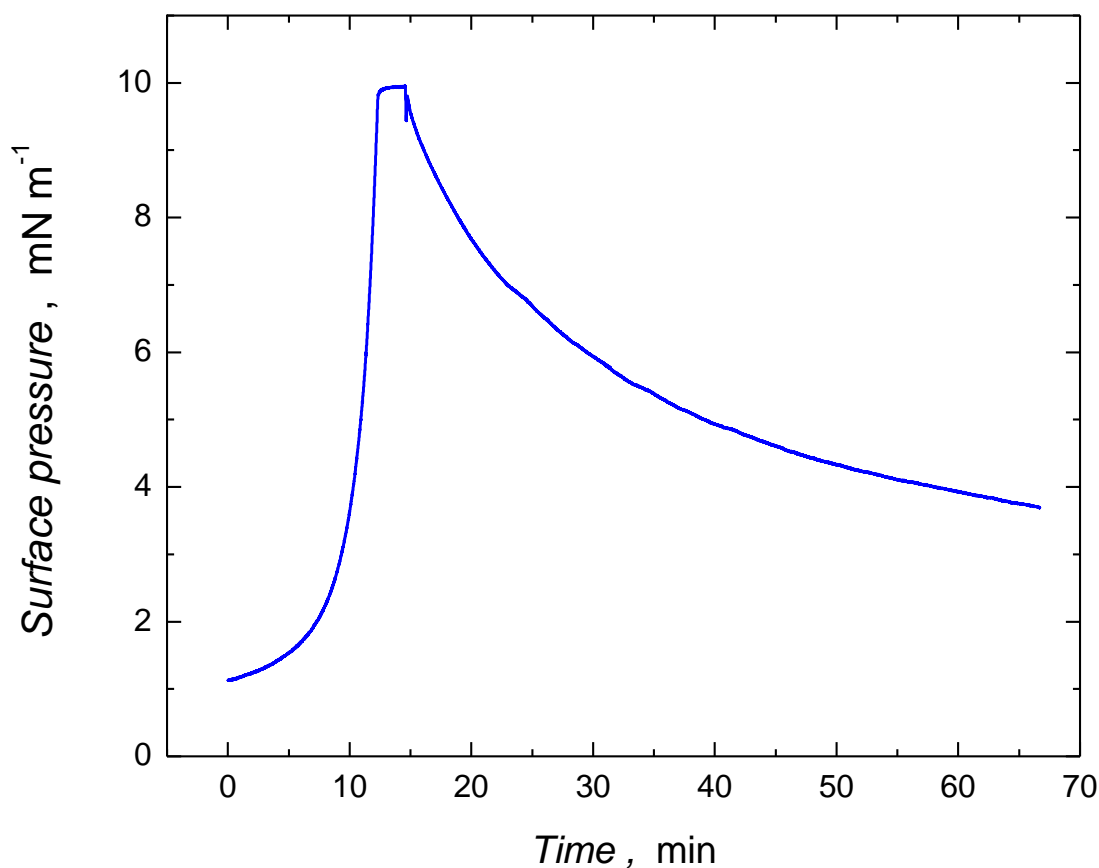
Figure 4.1.2-5. The surface pressure vs. time dependence for a 150-μL sample of 0.1 mM Zn(TPPE)-C_{60}im dyad spread on the water subphase to form a Langmuir film.

Stability of the Langmuir film of the dyad was evaluated by compressing the film to surface pressure of 10 mN m^{-1} and recording the surface pressure vs. time transient at constant barrier separation (Fig. 4.1.2-5). Apparently, surface pressure at the constant barrier separation decreases because of presumable reorganization of the Zn(TPPE) peripheral substituents in the dyad Langmuir film.

90

4.1.2.4 Properties of the Langmuir-Blodgett films of the Zn(TPPE)-C$_{60}$im dyad

Langmuir films were transferred onto either pristine FTO-glass slides or those hydrophobized with methoxytrimethylsilane or trimethoxyphenylsilane, at different surface pressure and/or transfer speed, the number of transfers, and/or transfer technique.
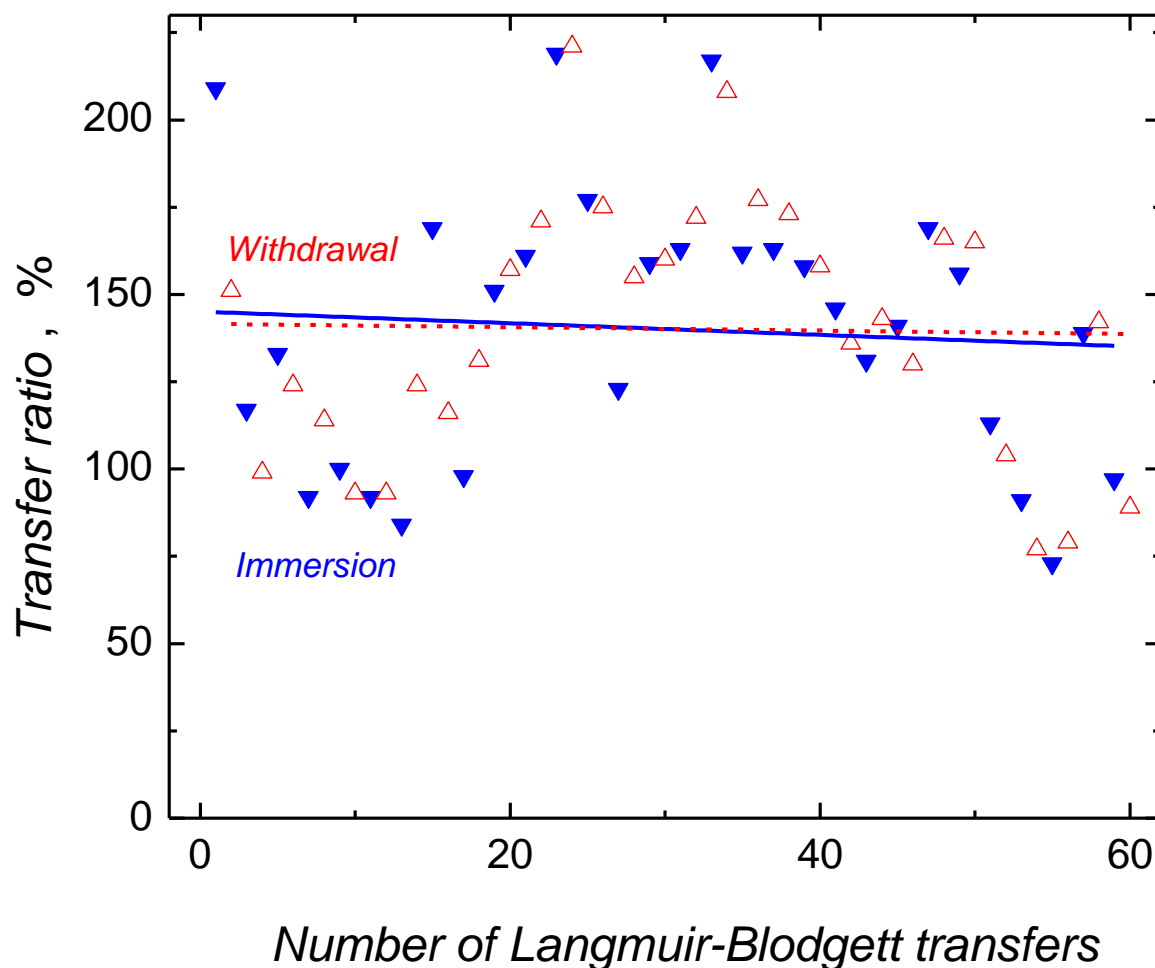
Figure 4.1.2-6. The transfer ratio for the Zn(TPPE)-C$_{60}$im dyad Langmuir film, spread on a water subphase, during the Langmuir-Blodgett transfer, transferred onto the trimethoxyphenylsilane hydrophobized FTO slide at the rate of 5 mm min^{-1} and the surface pressure of 10 mN m^{-1}.

The LB transfer of the Zn(TPPE) Langmuir film was successful only in the presence of the C$_{60}$im ligand. The factors determining the efficient transfer of the dyad Langmuir film involved the decrease of both the transfer ratio and the organization of the dyad molecules in the LB film with the number of transfers. For the trimethoxyphenylsilane hydrophobized FTO slide, the average transfer ratio exceeded 100% for the first 60 transfer cycles

91

(Fig. 4.1.2-6). This effect might be caused by rearranging the peripheral ether substituents of the Zn(TPPE) molecules with time. That is, the film might become more compact and the surface pressure decreased at the constant distance between the trough barriers (Fig. 4.1.2-5). This behavior resulted in the decrease of area of the Langmuir film at constant surface pressure, additional to that characteristic of the LB transfer, thus artificially inflating the transfer ratio. Generally, the higher number of transfers the higher was the light absorption of the LB films and the higher the photoelectrochemical performance was.

The LB transfer ratio of the Zn(TPPE)-C_{60}im dyad was, advantageously, higher for hydrophobic substrates. However, the FTO surface chemical hydrophobization with methoxytrimethylsilane resulted in a poor photovoltaic performance. A different ratio of absorbance of the Soret band to absorbance at 345 nm for the Zn(TPPE)-C_{60}im (1 : 1, mole : mole) dyad film, drop coated onto an FTO glass slide, (curve *3'* in Fig. 4.1.2-7b) and that LB transferred (curve *3'* in Fig. 4.1.2-7c) suggested partial dissociation of the dyad in the course of transferring. That is, absorbance of the Soret band for the drop-coated dyad film was higher than that at 435 nm. However, this ratio was opposite for the LB film of the dyad. Thus, the Zn(TPPE)-to-C_{60}im mole ratio in the LB film was not 1 : 1 but the amount of Zn(TPPE) transferred was lower. The LB transfer of the pristine Zn(TPPE) was successful for neither the hydrophilic nor hydrophobic substrate (curve *1"* in Fig. 4.1.2-7c).

The procedure resulting in the LB film samples with the best photovoltaic performance was selected for transferring Langmuir films onto different solid substrates, including the FTO and Au-over-Ti coated glass slides, HOPG, and other atomically flat substrates for the spectroscopic, microscopic, and electrochemical characterization, respectively.

The DPV curves for the dyad and, separately, for its components in solution were recorded in order to determine precisely the formal redox potentials (Fig. 4.1.2-8). The Zn(TPPE)-C_{60}im dyad showed reversible peaks *1'* through *5'* (curve c in Fig. 4.1.2-8) corresponding to those recorded both for the Zn(TPPE) (peaks *1* and *2* in curve a, in Fig. 4.1.2-8) at the formal potential of $E^{0'}$ = +0.33 and -1.29 V, respectively. Moreover, there were peaks *3*, *4*, and *5* (curve b, in Fig. 4.1.2-8) at $E^{0'}$ = -0.77, -1.15, and -1.68 V, respectively, corresponding to electroreduction of the C_{60}im moiety. The Zn(TPPE) donor showed one irreversible broad peak at -1.09 V (curve a in Fig. 4.1.2-8). Formal potentials of the C_{60}im redox processes were not shifted after formation of the dyad (cf. peaks *3*, *4*, *5* and *3'*, *4'*, *5'* in curves b and c, in Fig. 4.1.2-8, respectively). However, the formal potential of

92

the Zn(TPPE) redox process was then shifted by ~10 mV (peaks *1* and *1'* in curves a and c, in Fig. 4.1.2-8, respectively). Peaks at -1.09 and -1.29 V for the Zn(TPPE) overlapped the second cathodic peak of C_{60}im electroreduction (peaks *2'* and *4'* in curve c, in Fig. 4.1.2-8).
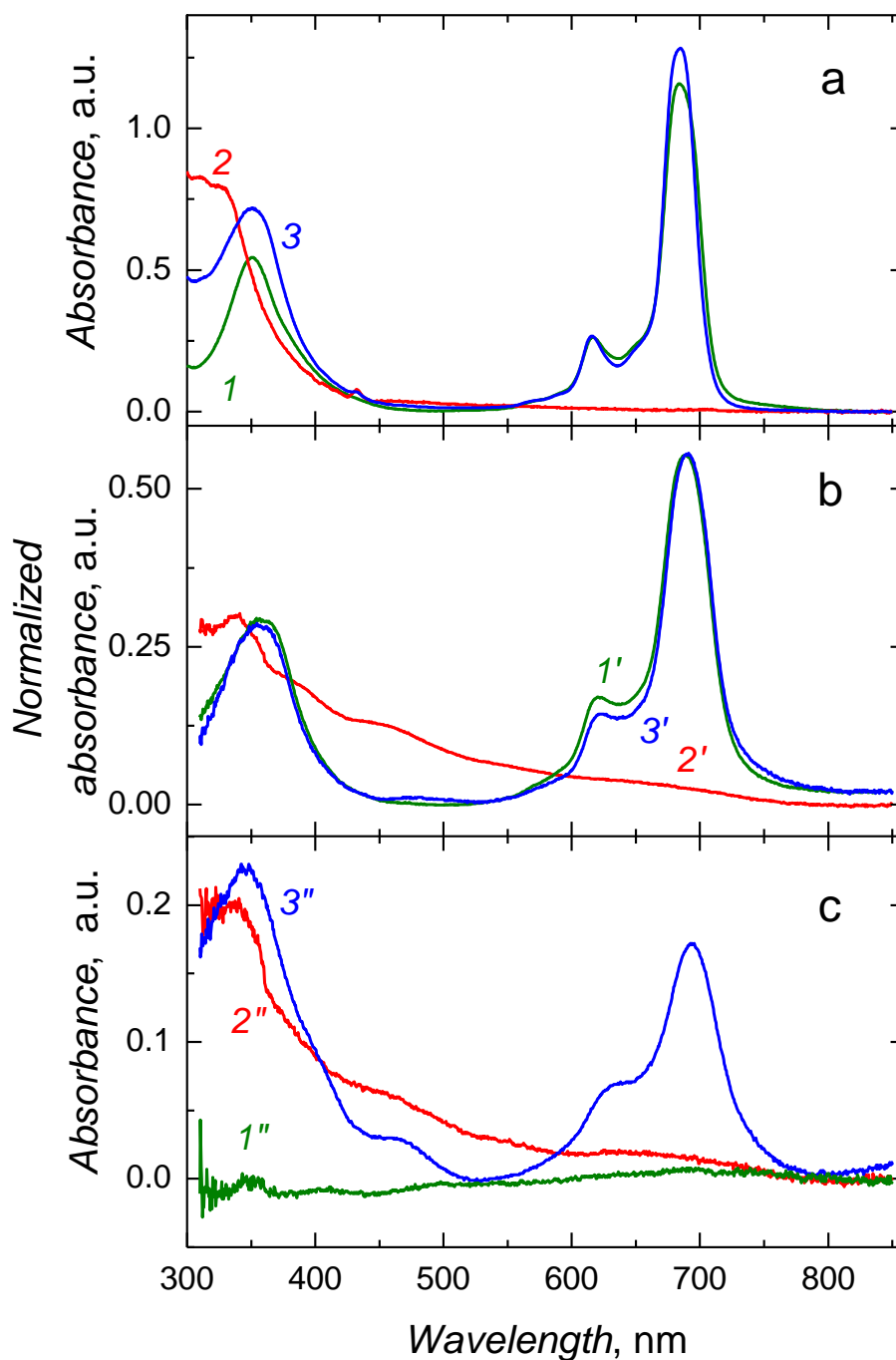
Figure 4.1.2-7. The UV-vis absorbance spectra for (*1*, *1'*, *1''*) Zn(TPPE), (*2*, *2'*, *2''*) C_{60}im, and (*3*, *3'*, *3''*) the Zn(TPPE)-C_{60}im (1 : 1, mole : mole) dyad (a) in ODCB, (b) in the film drop coated onto the FTO glass slide, and (c) in the LB film transferred onto the FTO glass slide by 40 immersions at the immersion speed of 5 mm min^{-1} and 10 mN m^{-1} surface pressure.

93
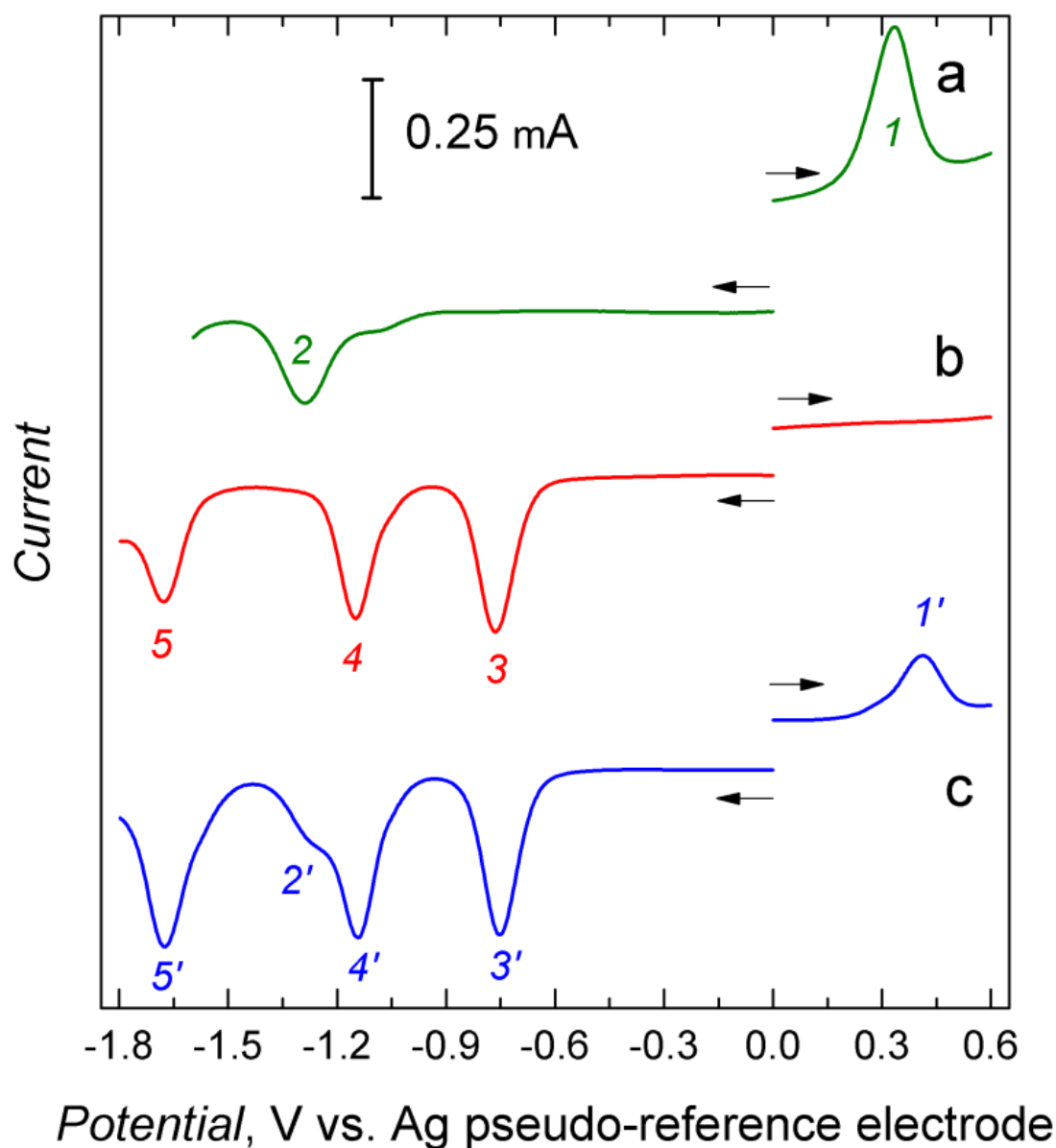
Figure 4.1.2-8. The DPV curves for 0.1 mM (a) $C_{60}im$, (b) Zn(TPPE), and (c) the ZnTPPE-$C_{60}im$ complex in 0.1 M (TBA)ClO$_4$, in ODCB. The 0.02-cm^2 Pt disk, Pt wire, and Ag wire served as the working, counter, and pseudo-reference electrode, respectively. Solutions were deaerated with Ar prior to the measurements.

The resulting LB films of the Zn(TPPE)-$C_{60}im$ dyad were smooth and uniform compared to the bare Au-over-Ti coated glass slides (Fig. 4.1.2-9). The relative surface area of the film transferred onto a hydrophobic Au-over-Ti glass slide by 50 immersions was 1.010 while that for the bare substrate was 1.029. Artifacts on the image (Fig. 4.1.2-9b), i.e., linear traces made by the AFM tip, suggested that the film was soft.

94
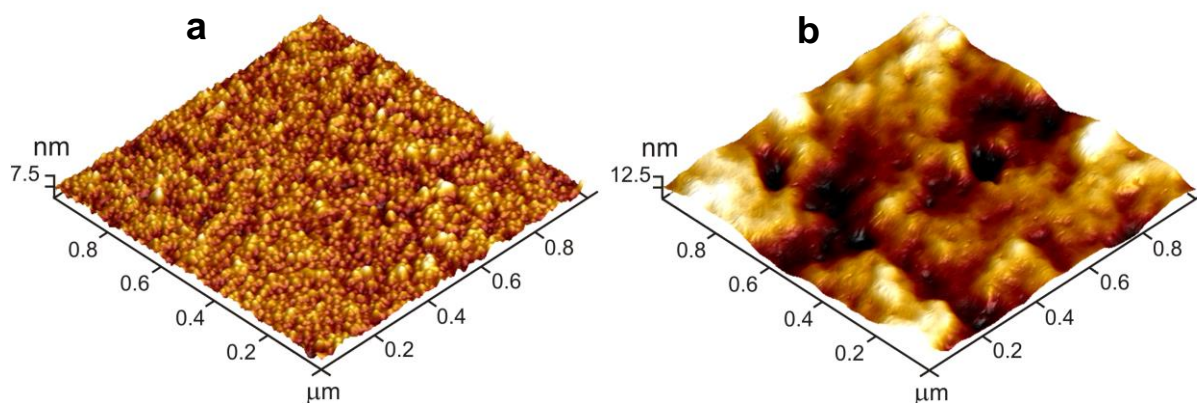
Figure 4.1.2-9. The $1 \times 1 \ \mu m^2$ AFM image of (a) the bare Au-over-Ti glass slide and (b) the Zn(TPPE)-C_{60}im dyad transferred onto a hydrophobized Au-over-Ti glass slide by 50 LB immersions. The relative surface area, R_{sa}, was 1.029 and 1.010 for the bare substrate and the LB film coated substrate, respectively.

Orientation of the dyad molecules in the LB films, transferred at different surface pressures, with respect to the substrate surface plane was evaluated with the polarization modulation-infrared reflection-adsorption spectroscopy (PM-IRRAS) measurements. However, first, the attenuated total reflectance ATR-FTIR spectra for the dyad components were recorded separately (curves *1* and *2* in Fig. 4.1.2-10b) in order to localize vibrations of bonds in non-ordered films. Then, the PM-IRRAS spectra for the dyad LB films transferred at 10 (Fig. 4.1.2-10a) and 24 mN m^{-1} (not shown) were recorded.

The Zn(TTPE) bands dominated both in the ART-FTIR and the PM-IRRAS spectrum. Nevertheless, the presence of the C_{60}im moiety in the dyad LB film was confirmed by the peaks at 1526 and 1180 cm^{-1} in the PM-IRRAS spectrum. The band at 1526 cm^{-1} corresponded to the imidazole ring antisymmetric vibration[138] while that at 1180 cm^{-1} was assigned to the C_{60} cage vibration.[138] Apparently, the C_{60}im molecule was perpendicular to the substrate surface plane with its imidazole-benzene axis oriented as shown in Scheme 4.1.2-1b.

Two groups of bands, one containing vibrations at 2963, 2924, 2852, and 1092 cm^{-1}, and the other at 1607, 1486, 1465, 1241, and 1122 cm^{-1} in the PM-IRRAS spectrum (Fig. 4.1.2-10a), allowed the conclusion on orientation of the Zn(TPPE) peripheral substituents and that of the macrocycle. That is, the peripheral ether chains were not parallel

95

to the substrate surface plane; they were substantially tilted against the perpendicular to this plane. The conclusion drawn on the second group of vibrations was that the macrocycle was nearly flat oriented on the substrate plane. The films of the dyad transferred at 24 mN m^{-1} did not generate photocurrents at all upon light irradiation. However, the PM-IRRAS spectrum for this film (not shown) was not much different from that for the film transferred at 10 mN m^{-1} indicating that the molecules in this film were not dramatically rearranged. The change consisted in the higher tilt of both the Zn(TPPE) peripheral alkylether substituents and the macrocycle plane with respect to the substrate plane.
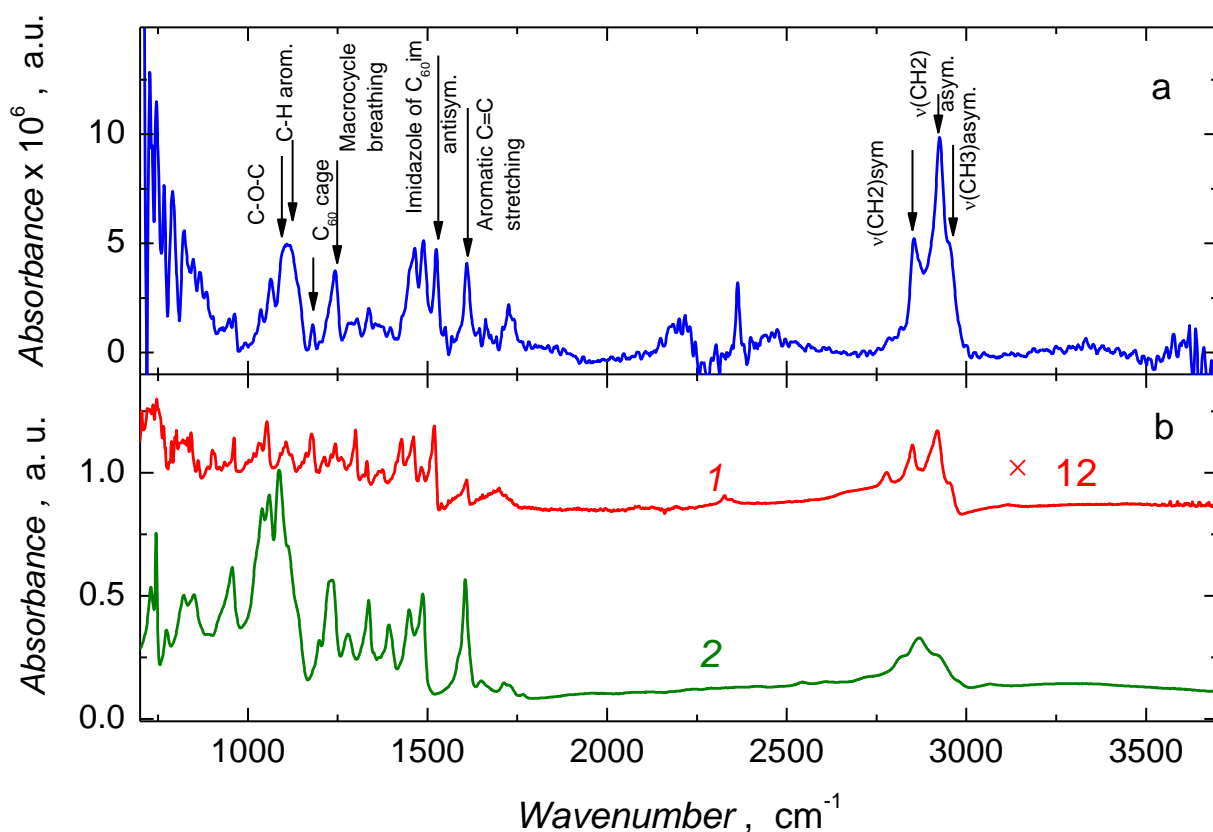
Figure 4.1.2-10. (a) The PM-IRRAS spectrum for the LB film of the Zn(TPPE)-C$_{60}$im dyad transferred by 100 immersions at 10 mN m^{-1} onto the Au-over-Ti coated glass slide with the transfer rate of 5 mm min^{-1}, recorded at the incidence angle of 83°, (b) the ATR IR spectra for powders of (*1*) C$_{60}$im and (*2*) Zn(TPPE).

4.1.2.5 Photoinduced electron transfer in the Zn(TPPE)-C_{60}im LB film

To evidence formation of the charge separated state in the Zn(TPPE)-C_{60}im LB film and to study kinetics of charge separation and recombination, the femtosecond transient absorption spectroscopic measurements were performed.
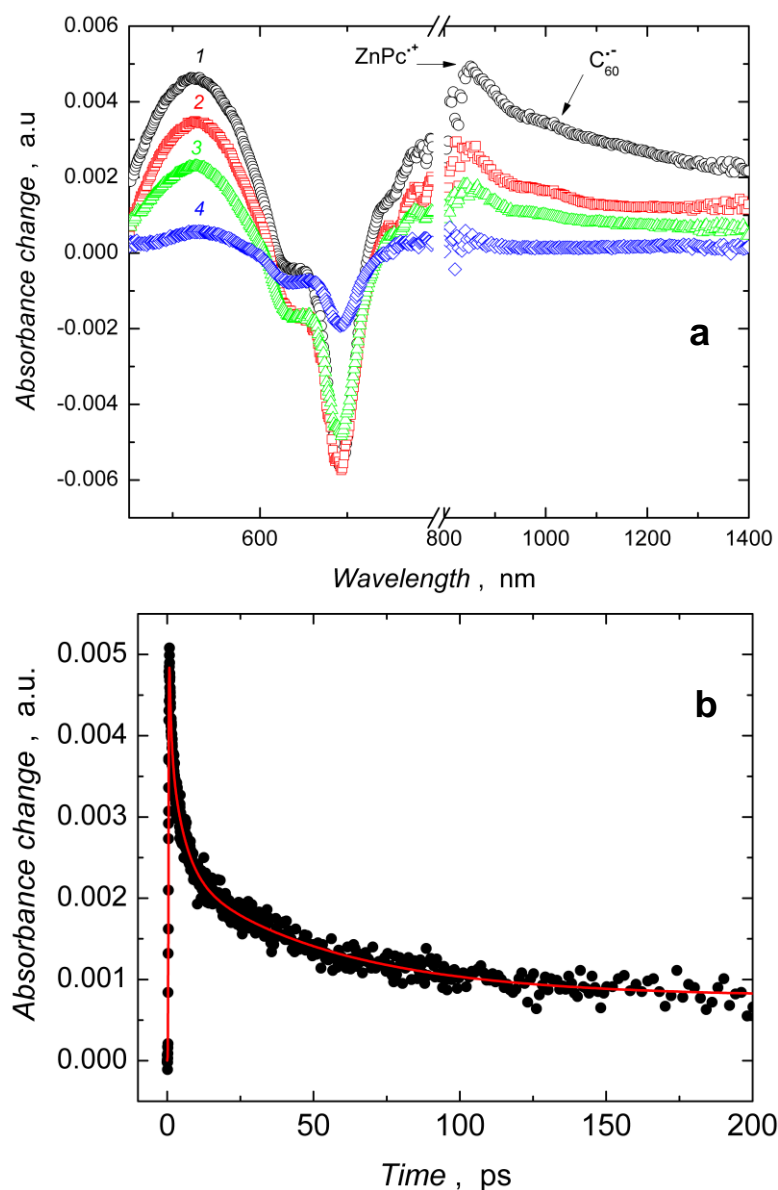
Figure 4.1.2-11. (a) The transient absorbance spectra of the Zn(TPPE)-C_{60}im LB film, transferred onto the trimethoxyphenylsilane hydrophobized FTO electrode by 100 immersions at 5 mm min-1, after excitation at 400 nm with 100 fs pulses, recorded for (1) 0.830, (2) 7.66, (3) 33.8 and (4) 2298 ps. (b) The time profile of the transient absorbance band at 856 nm.

The 100-fs pulses of a 400-nm laser light were used to excite the dyad LB films, transferred onto the trimethoxyphenylsilane hydrophobized FTO electrode. Figure 4.1.2-11a shows transient spectra recorded at different delay times. Immediately after excitation, a positive peak at 525 nm characteristic of the S_0-to-S_1 transition and a negative peak at 694 nm corresponding to the fluorescence emission of the Zn(TPPE) moiety were observed. These peaks were accompanied by two peaks at 856 nm and 1020 nm corresponding to the formation of the Zn(TPPE)$^{•+}$ and C_{60}im$^{•-}$ species, respectively, thus confirming formation of an ion-pair radical within the Zn(TPPE)-C_{60}im LB film.[139,140] The time profile of the 856 nm band was analyzed to evaluate the kinetics of charge separation and recombination (Figure 4.1.2-11b). The determined rate constants of charge separation, k_{cs}, and charge recombination, k_{cr}, were $2.6 \times 10^{11}$ s^{-1} and 9.7×10^9 s^{-1}, respectively. The magnitude of k_{cs} indicates the occurrence of efficient vectorial electron transfer whose time constant is close to that of the laser pulse. The magnitude of k_{cr} was by an order magnitude lower, a general trend expected for tetrapyrrole-fullerene type dyads.[141]

4.1.2.6 Spectroelectrochemical studies of the Langmuir-Blodgett films of the Zn(TPPE)-C_{60}im dyad

Photovoltaic cells with multilayer LB films of the Zn(TPPE)-C_{60}im dyad transferred onto the hydrophobized FTO slides were constructed for evaluation of the photoelectrochemical performance of the dyad (Scheme 4.1.2-7). An aqueous electrolyte was used because of high solubility of Zn(TPPE) in organic solvent solutions and, practically, insolubility in aqueous solutions.

First, the current-potential (*I-E*) curves for the photocells in the dark and when exposed to the AM1.5 light illumination were recorded (Fig. 4.1.2-12). In the dark, the dyad film revealed electrochemical behavior typical for semiconductors (curves *1* and *2* in Fig. 4.1.2-12).

The presence of a positively or negatively charged electron-mediating species in solution was preferred for the working electrode to operate as a photocathode or photoanode, respectively. Toward that, monoascorbate (AscH$^-$)[142] and methylviologen (MV^{2+})[143] was used to make the photoelectrode operating as the photoanode and photocathode, respectively (Scheme 4.1.2-7a and 7b, respectively).

98
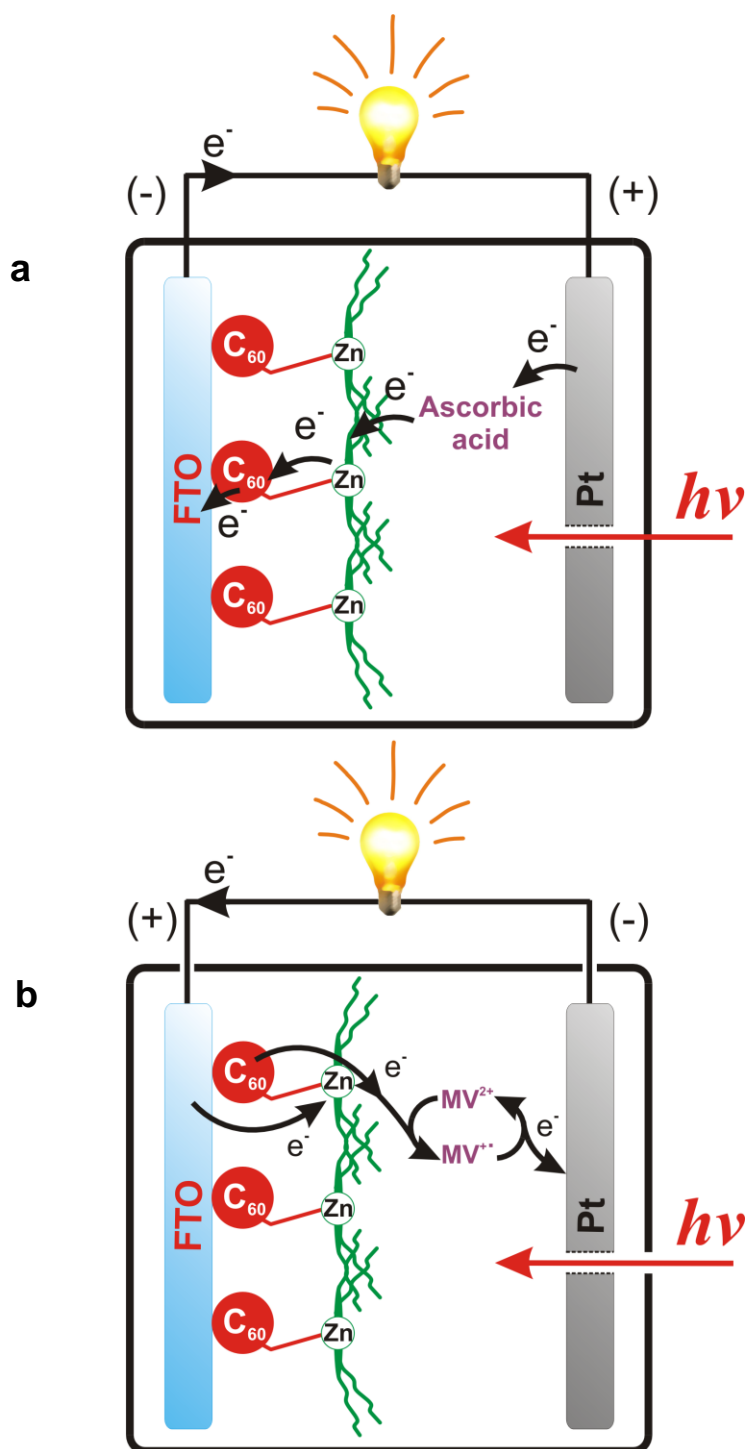
Scheme 4.1.2-7. A sketch of the photovoltaic cell illustrating generation of (a) anodic photocurrent in 1 mM ascorbic acid and 0.1 M NaH$_2$PO$_4$ (pH ≈ 4.1) and (b) cathodic photocurrent in 5 mM methylviologen in 0.1 M Na$_2$SO$_4$ (pH ≈ 5.8) by the Zn(TPPE)-C$_{60}$im multilayer LB film transferred onto the hydrophobized FTO electrode. A Pt plate with an opening for the light beam served as the (a) cathode and (b) anode.
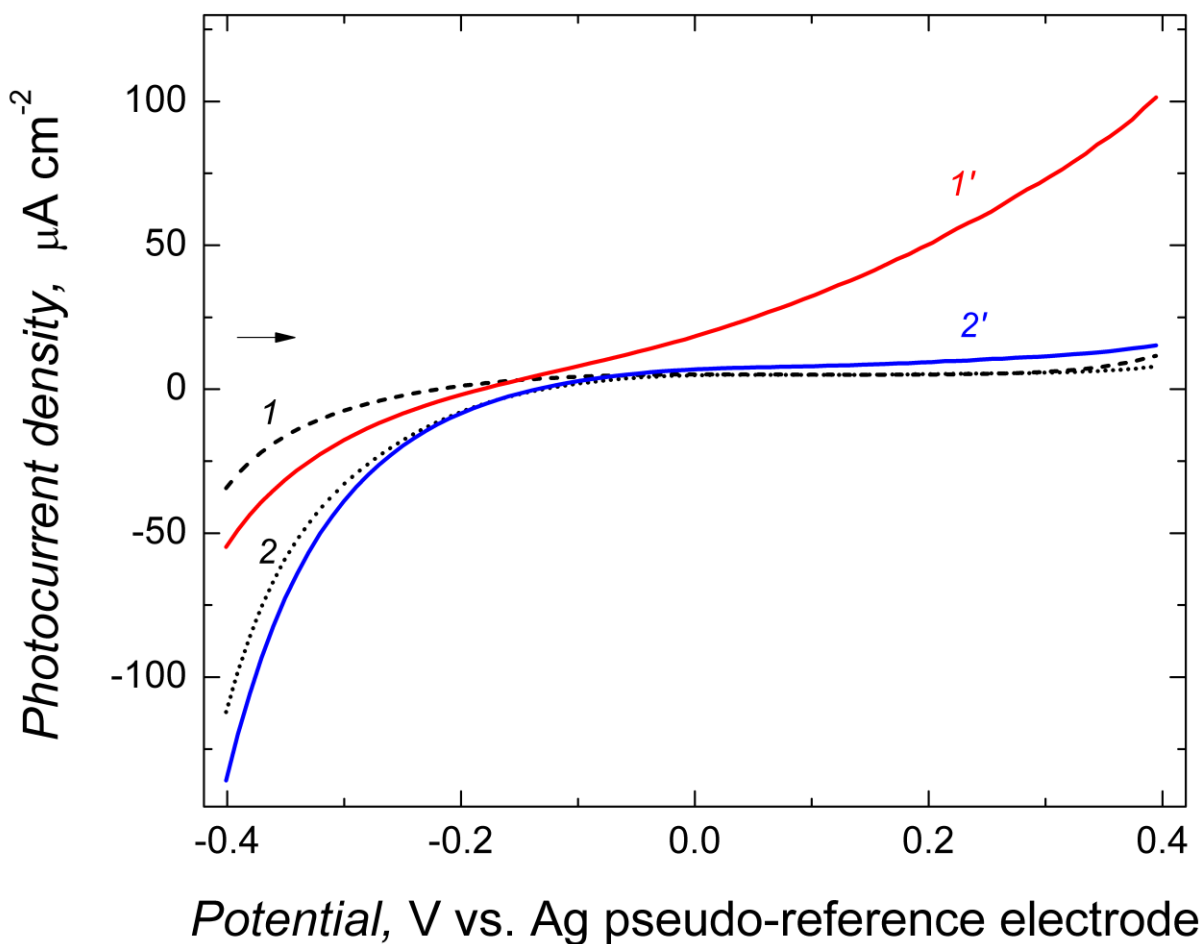
Figure 4.1.2-12. The photocurrent-potential characteristics of the trimethoxyphenylsilane hydrophobized FTO electrode, operating as the (*1*, *1'*) photoanode and (*2*, *2'*) photocathode, coated with the Zn(TPPE)-C$_{60}$im dyad LB film, transferred by 200 LB immersions, at the 5 mm min^{-1} transfer rate (*1* and *2*) in the dark and (*1'* and *2'*) under the AM1.5 light irradiation conditions in (*1* and *1'*) 1 mM ascorbic acid, in 0.1 M NaH$_2$PO$_4$ (pH $\approx$ 4.1) and in (*2* and *2'*) 5 mM methylviologen, in 0.1 M Na$_2$SO$_4$ (pH $\approx$ 5.8), respectively.

Photocurrents were considerably high for the dyad LB film transferred at the 5 mm min^{-1} transfer rate and the 10 mN m^{-1} surface pressure. The photocurrent density was proportional to the number of LB transfers (not shown). In consecutive *I-E* curves for the LB film of the dyad in the ascorbic acid solution, the photocurrent density increased (curves *2* through *6* in Fig. 4.1.2-13). Apparently, this increase was due to reorganization of the film.

The photoanodic and photocathodic current density was dependent on the potential applied and it was 61.6 μA cm^{-2} at +0.30 V in the solution of ascorbic acid and 5.7 μA cm^{-2} at -0.20 V in the solution of methylviologen (Fig. 4.1.2-14).

100
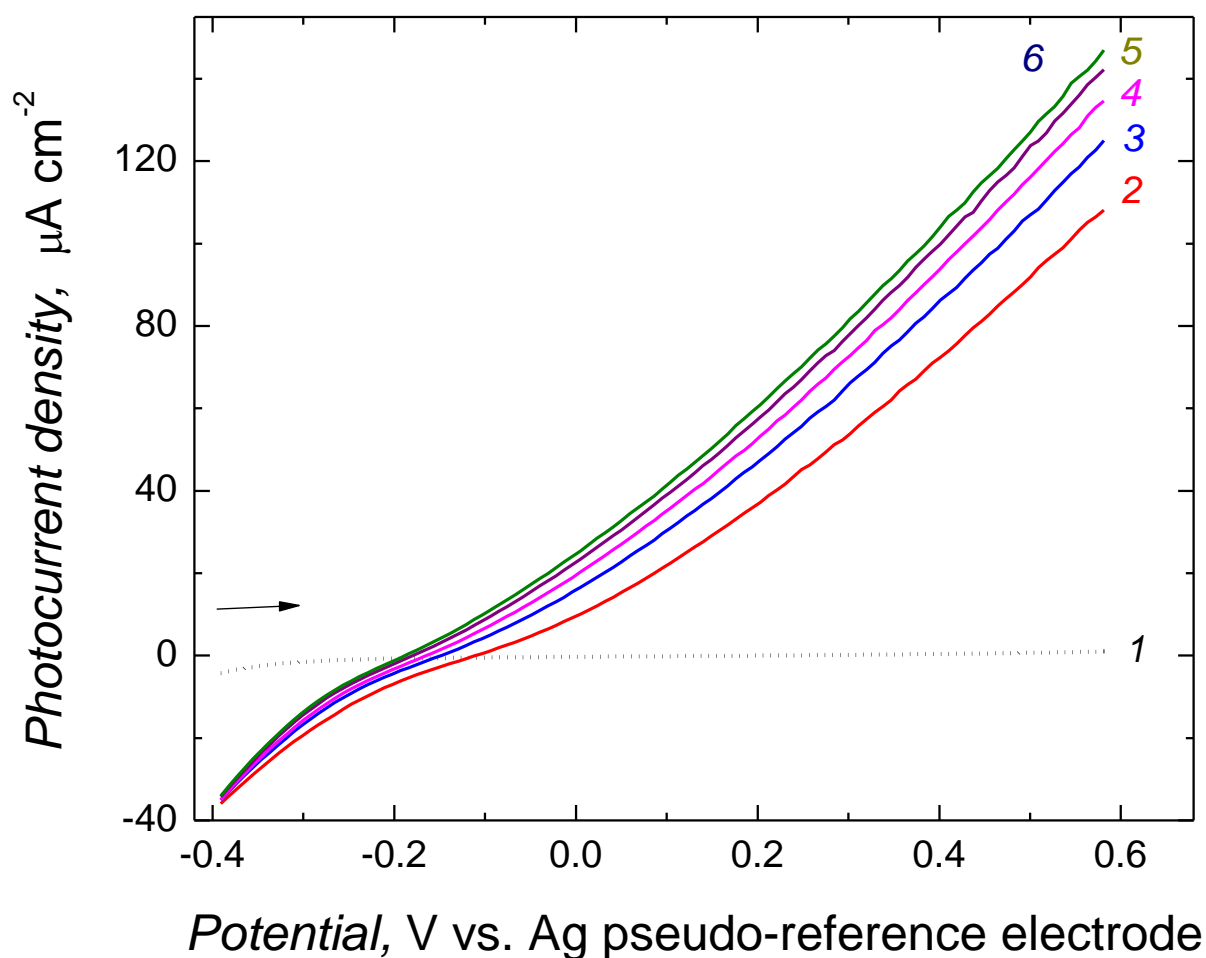
Figure 4.1.2-13. Consecutive linear sweep voltammograms for the hydrophobized FTO electrode coated with the Zn(TPPE)-C$_{60}$im dyad multilayer LB film, transferred by 125 immersions, at the transfer rate of 5 mm min^{-1} and surface pressure of 10 mN m^{-1}, in 1 mM ascorbic acid and 0.1 M NaH$_2$PO$_4$ (pH ≈ 4.1) (*1*) in the dark and (*2-6*) under AM1.5 light illumination.

At pH = 4.1, i.e., that of pK_{a1} of ascorbic acid, half of the acid is dissociated forming a monoanion (Eqn. 4.1.2-1), which then undergoes one-electron electroreduction on a Pt cathode to form a stable anion radical (Eqn. 4.1.2-2). Next, the electron is delivered to the LB film, where the photo-oxidized Zn(TPPE)-C$_{60}$im dyad accepts the electron.

$$\text{AscH}_2 \underset{+\text{H}^+}{\overset{\text{p}K_{a1} \\ -\text{H}^+}{\rightleftharpoons}} \text{AscH}^- \underset{+\text{H}^+}{\overset{\text{p}K_{a2} \\ -\text{H}^+}{\rightleftharpoons}} \text{Asc}^{2-} \qquad (4.1.2\text{-}1)$$

101
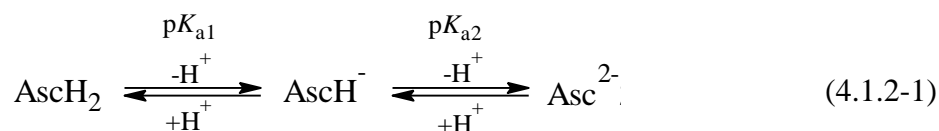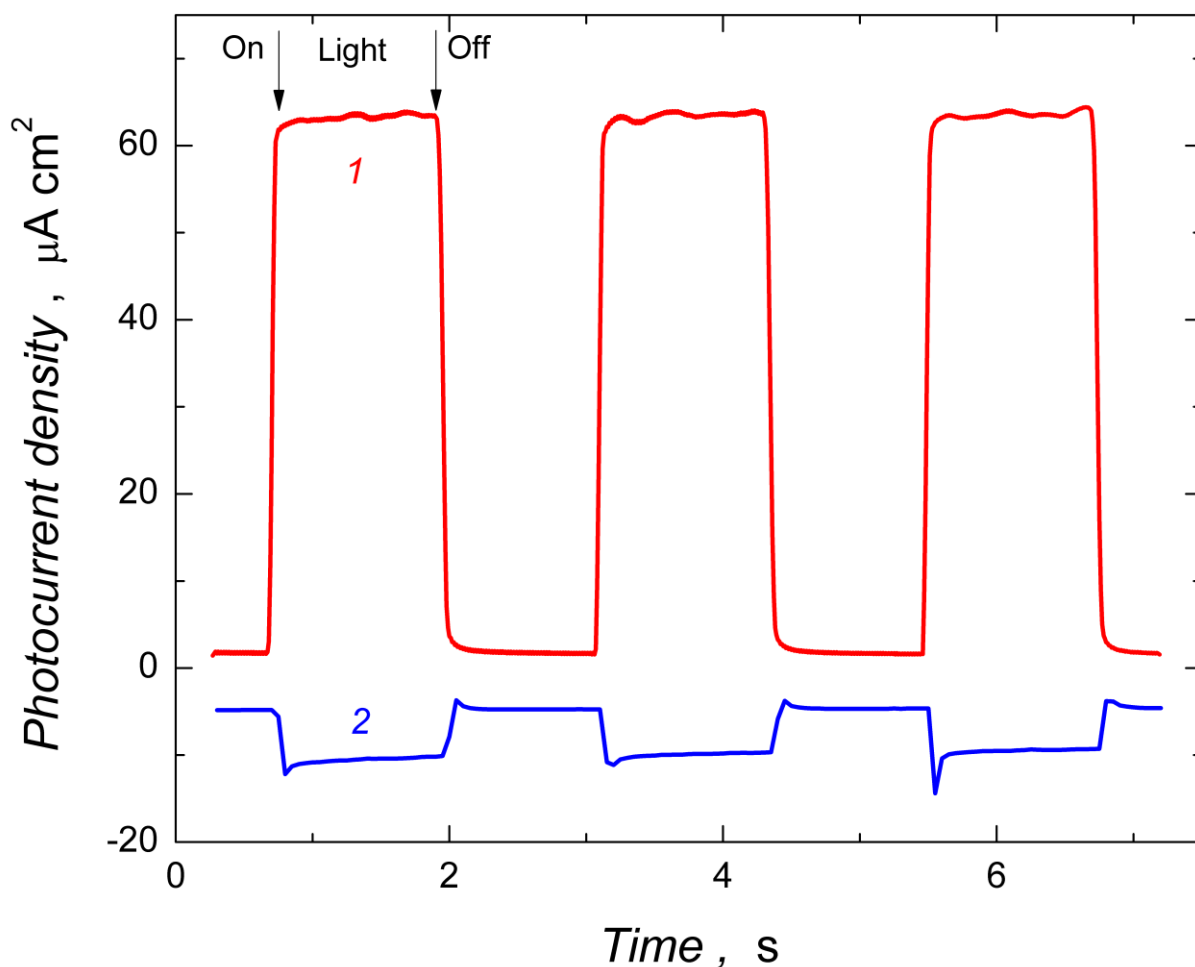
Figure 4.1.2-14. The (*1*) photoanodic and (*2*) photocathodic current density changes with time due to alternate light switching "on" and "off" for the Zn(TPPE)-C_{60}im LB film transferred by 200 immersions onto the trimethoxyphenylsilane hydrophobized FTO electrode at the 5 mm min^{-1} transfer rate for (*1*) 1 mM ascorbic acid, in 0.1 M NaH$_2$PO$_4$ (pH $\approx$ 4.1), and (*2*) 5 mM methylviologen in 0.1 M Na$_2$SO$_4$ (pH $\approx$ 5.8), recorded at +0.3 and -0.20 V vs. the Ag pseudo-reference electrode, respectively.

In the presence of the AscH$^-$ mediator, the proposed mechanism of the photoanodic activity of the FTO/[C_{60}im-Zn(TPPE) LB multilayer film] working electrode is, as follows (Scheme 4.1.2-7a).

The first step of this mechanism involves intramolecular charge transfer from the photoexcited Zn(TPPE) donor to the C_{60}im acceptor resulting in formation of the Zn(TPPE) cation radical and the C_{60}im anion radical, respectively, within the dyad (Eqn. 4.1.2-2).

$$\text{Zn(TPPE)-C}_{60}\text{im} \underset{}{\overset{h\nu}{\rightleftarrows}} \text{Zn(TPPE)}^{\bullet +}\text{-}\overset{\bullet -}{\text{C}}_{60}\text{im} \qquad (4.1.2\text{-}2)$$

102

Then, the extra electron on the $C_{60}im$ anion radical facing the hydrophobized surface travels through the FTO anode (Eqn. 4.1.2-3) to the Pt cathode via an external circuit.

$$\text{Photoanode, FTO(-): } Zn(TPPE)^{\bullet+}\text{-}C^{\bullet-}_{60}im \underset{+e^-}{\overset{-e^-}{\rightleftharpoons}} [Zn(TPPE)^{\bullet+}\text{-}C^{\bullet-}_{60}im]^+ \qquad (4.1.2\text{-}3)$$
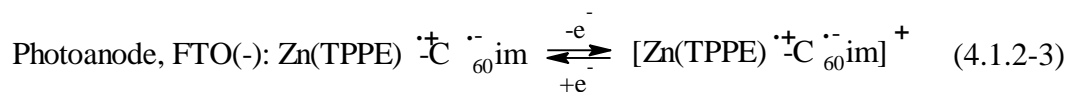
Simultaneously, the monoascorbate donates the electron to the $Zn(TPPE)^{\bullet}$ moiety of the dyad, thus oxidizing it to the $AscH^{\bullet}$ neutral radical (Eqn. 4.1.2-4).

$$[Zn(TPPE)^{\bullet+}\text{-}C^{\bullet-}_{60}im]^+ + AscH^- \rightleftharpoons Zn(TPPE)\text{-}C_{60}im + AscH^{\bullet} \qquad (4.1.2\text{-}4)$$
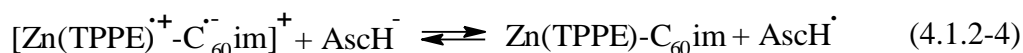
The $AscH^{\bullet}$ radical produced is then electroreduced to the anion radical on the Pt cathode according to Eqn. 4.1.2-5.

$$\text{Cathode, Pt(+): } AscH^{\bullet} + e^- \rightleftharpoons AscH^{\bullet-} \qquad (4.1.2\text{-}5)$$
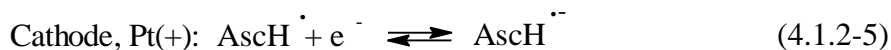
The proposed mechanism of the photocathodic operation of the photoelectrode requires the MV^{2+} presence and an opposite electron transfer through the cell. The first step, which is photo-oxidation of Zn(TPPE), is the same as that above (Eqn. 4.1.2-2). However, next, the electron is donated by the $C^{\bullet-}_{60}im$ moiety of the dyad to the cation, MV^{2+} (Eqn. 4.1.2-6).

$$Zn(TPPE)^{\bullet+}\text{-}C^{\bullet-}_{60}im + MV^{2+} \rightleftharpoons [Zn(TPPE)\text{-}C_{60}im]^+ + MV^{\bullet+} \qquad (4.1.2\text{-}6)$$
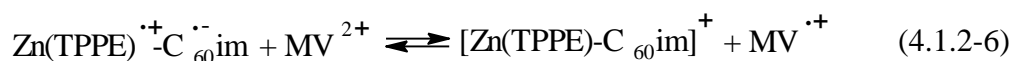
Then, the electron from the monocation radical, $MV^{\bullet+}$, is delivered to the Pt electrode, serving now as the anode, and $MV^{\bullet+}$ is electrooxidized to MV^{2+} (Eqn. 4.1.2-7).

$$\text{Anode, Pt (-): } MV^{\bullet+} \underset{+e^-}{\overset{-e^-}{\rightleftharpoons}} MV^{2+} \qquad (4.1.2\text{-}6)$$
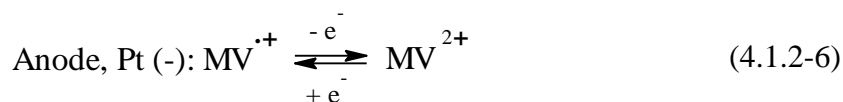
Simultaneously, the $[Zn(TPPE)\text{-}C_{60}im]^+$ cation is electroreduced at the FTO photocathode (Eqn. 4.1.2-7).

$$\text{Photocathode, FTO (+): } [Zn(TPPE)\text{-}C_{60}im]^+ \underset{-e^-}{\overset{+e^-}{\rightleftharpoons}} C_{60}im\text{-}Zn(TPPE) \qquad (4.1.2\text{-}7)$$

103
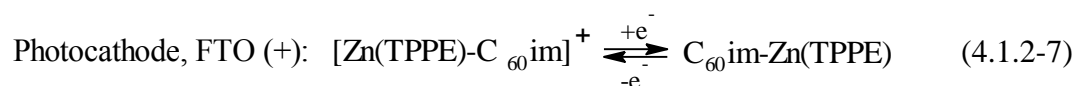
The photocurrent generation in the solution of AscH$^-$ or MV^{2+} was evaluated in the light switching on and off experiment. For the same film, the absolute value of photocurrent for the AscH$^-$ solution was over an order of magnitude higher than that for the MV^{2+} solution (curves *1* and *2* in Fig. 4.1.2-14). The open circuit potential, V_{oc}, for the light-irradiated cell was -0.207 V vs. V_{oc} of the same cell in the dark for the LB film transferred by 200 immersions, at the 10 mN m^{-1} surface pressure and the 5 mm min^{-1} transfer rate, in the AscH$^-$ solution.
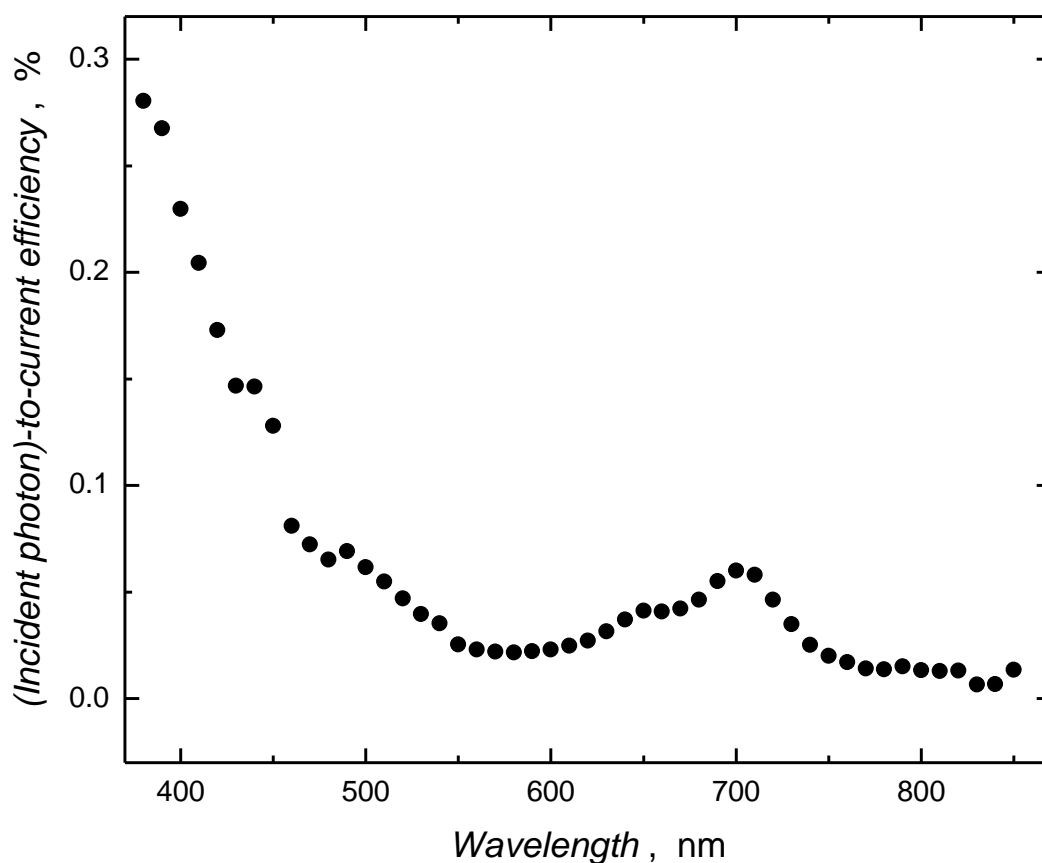
Figure 4.1.2-15. The dependence of the (incident photon)-to-current conversion efficiency (IPCE) on wavelength for the multilayer LB film of the Zn(TPPE)-C$_{60}$im dyad transferred onto the optically transparent FTO electrode, hydrophobized with trimethoxyphenylsilane, in 1 mM ascorbic acid and 0.1 M NaH$_2$PO$_4$ (pH $\approx$ 5.8). The LB film was transferred by 100 immersions of the FTO substrate.

The IPCE of the multilayer LB film of the $Zn(TPPE)$-C_{60}im dyad, transferred by 100 immersions at the applied potential of 0.0 V vs. Ag pseudo-reference electrode, revealed maximum of nearly 0.3% at ~400 nm (Fig. 4.1.2-15). An elevated IPCE was observed at ~690 nm corresponding to the Soret band wavelength for the $Zn(TPPE)$. However, the photovoltaic performance of this system was dependent upon the film thickness and the saturation was not reached. That was because the photocurrent density was proportional to the number of LB transfers.

4.1.3 Supramolecularly assembled [(Ph$_3$N)$_4$ZnP polymer]-(C$_{60}$im) donor-acceptor dyad films

Porphyrins are attractive for potential applications in photovoltaics. Their advantages in that respect include easily adjustable electronic properties tuned by derivatizing their macrocycles with electron accepting or donating substituents. Triphenylamine, TPA, is a well-known and widely used chromophore. Being attached to the porphyrin macrocycle, it may enhance efficiency of charge separation in the photoexcited (porphyrin electron donor)-(C$_{60}$ fullerene) dyads. Moreover, porphyrin derivatizing with the triphenylamine peripheral substituents allows for electropolymerization the resulting monomer molecule.
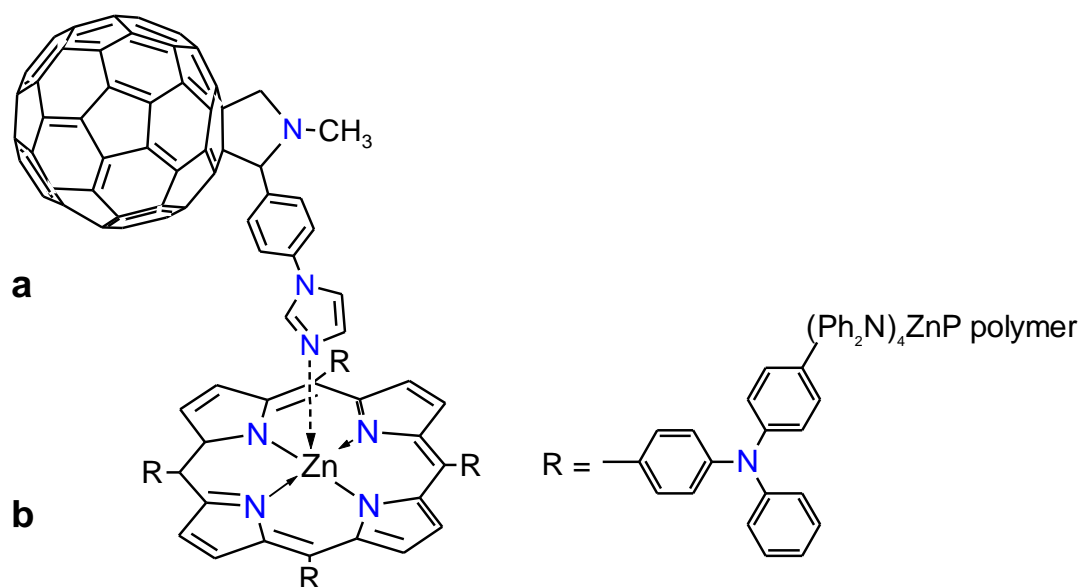
Scheme 4.1.3-1. Simplified structural formula of (a) the dyad of the *tetrakis*(4-(*N,N*-diphenylamino)phenyl)porphyrinatozinc(II), (Ph$_3$N)$_4$ZnP, polymer electron donor and (b) the C$_{60}$im acceptor.

Our research was focused on formation, characterization, and studies of photoelectrochemical properties of the [(Ph$_3$N)$_4$ZnP polymer electron donor]-(C$_{60}$im acceptor) self-assembled dyad. First, electrochemical properties of the (Ph$_3$N)$_4$ZnP monomer were characterized. Then, the monomer was electropolymerized using EQCM and electrochemical properties of the resulting polymer were revealed. Next, a dyad of the (Ph$_3$N)$_4$ZnP polymer film with C$_{60}$im was formed and this formation was monitored using flow-injection analysis. Subsequently, electrochemical properties of the [(Ph$_3$N)$_4$ZnP polymer]-C$_{60}$im dyad were investigated. Afterwards, the (Ph$_3$N)$_4$ZnP polymer and the

106

[(Ph$_3$N)$_4$ZnP polymer]-C$_{60}$im dyad were imaged with AFM and, finally, their photoelectrochemical properties were examined.

4.1.3.1 Electropolymerization and selected electrochemical properties of (Ph$_3$N)$_4$ZnP

The (Ph$_3$N)$_4$ZnP donor was electropolymerized under potentiodynamic conditions using EQCM.

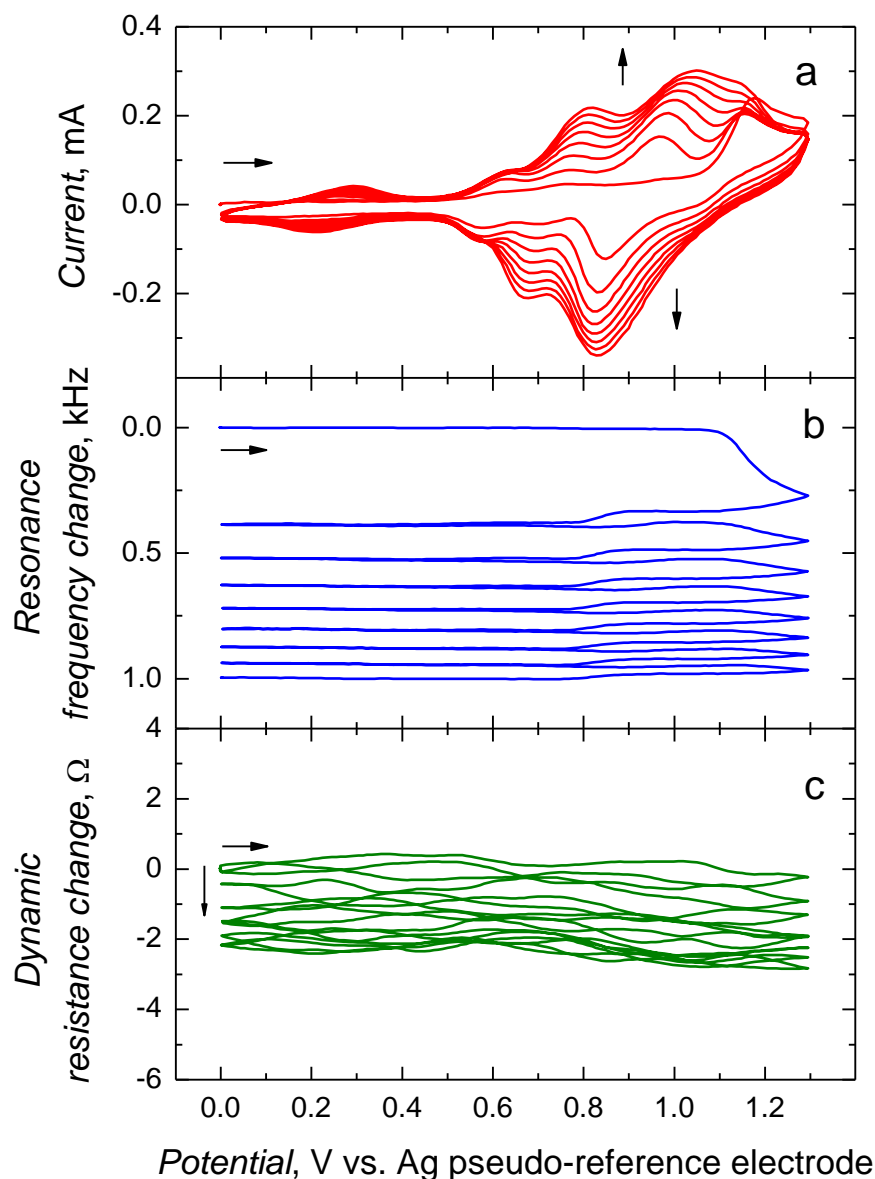**Figure 4.1.3-1**. Curves of (a) multi-cyclic potentiodynamic deposition as well as the potential dependence of (b) resonance frequency change, and (c) dynamic resistance changes for 0.124 mM (Ph$_3$N)$_4$ZnP in 0.1 M (TBA)ClO$_4$, in ODCB. The potential sweep rate was 100 mV/s. A 5-mm diameter gold-film electrode of the 10-mHz Au/Ti quartz crystal resonator served as the working electrode.

107

The current vs. potential curves were recorded at the Au-over-Ti electrode of QCR simultaneously with the change of the resonance frequency, Δf, and dynamic resistance, R. The film deposition on the electrode was manifested by the Δf decrease (Fig. 4.1.3-1b). The redox current increase in consecutive potential cycles suggested formation of a conducting polymer (Fig. 4.1.3-1a). The measured total resonance frequency change (Δf_{total}) after 8 potential cycles was 996 Hz while the dynamic resistance change was merely 2.2 Ω. The Δf_{vis} value, calculated using the measured dynamic resistance (Fig. 4.1.3-1c) and Eqn. 4.1.3-2, was 0.22 Hz being negligibly small with respect to that of Δf_{total}. The total mass change of the QCR due to the $(Ph_3N)_4ZnP$ polymer film deposition was (863 ± 1) ng, as calculated using the Sauerbrey equation (Eqn. 3.2-13).

The plot of the deposited polymer mass vs. charge transferred, determined from the first potential cycle and the Δf vs. E curves in Fig 4.1.3-1a and Fig 4.1.3-1b, respectively, resulted in determination of the electrochemical equivalent of (42.8 ± 4.9) g F^{-1} for the $(Ph_3N)_4ZnP$ monomer (Fig. 4.1.3-2). This value is half that of ~84 g F^{-1} expected assuming that all four TPA peripheral substituents of the macrocycle participate in the electropolymerization.
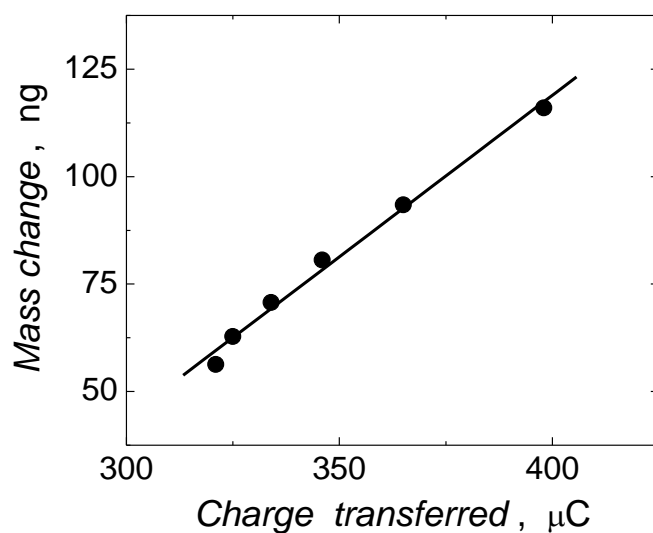
Figure 4.1.3-2. The deposited $(Ph_3N)_4ZnP$ polymer mass vs. charge transferred in the first potential cycle shown in Fig. 4.1.3-1.

The TPA electropolymerization mechanism has already been studied in details.[99,144] Herein, we adopted this mechanism to account for the electropolymerization of $(Ph_3N)_4ZnP$

108

(Scheme 4.1.3-2). Initially, the TPA peripheral substituents of the porphyrin are electro-oxidatively being linked to form the benzidine-type structures.

The determined electrochemical equivalent value, being half that expected, suggests that, on average, each monomer molecule is bound to two other monomer molecules. However, a linear polymer is not formed (see AFM images, below). A perpendicular orientation of the phenyl group with respect to the porphyrin macrocycle plane may be responsible for that. Hence, a simplified structural formula of the polymer can be proposed (Scheme 4.1.3-4).
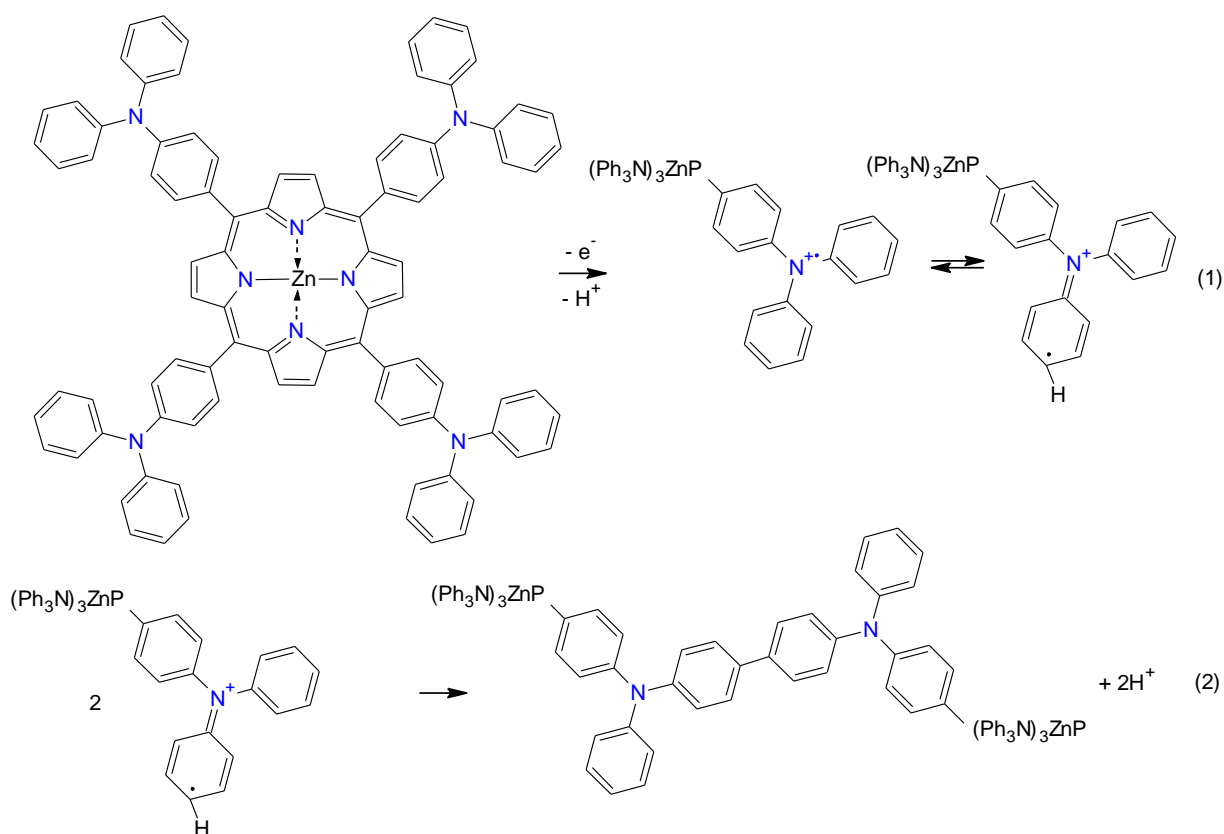
Scheme 4.1.3-2. The proposed mechanism of electrochemical polymerization of $(Ph_3N)_4ZnP$. (1) Electrooxydation of the $(Ph_3N)_4ZnP$ and (2) recombination of the resulting cation radicals.

Then, further potential increase results in reversible oxidation of these substituents (Scheme 4.1.3-3).

A nanoscale porosity of the $(Ph_3N)_4ZnP$ polymer film, prepared using the $(TBA)ClO_4$ supporting electrolyte, was evaluated by cyclic voltammetry for a blank supporting electrolyte of 0.1 M tetrabutylammonium cation and different size anions, namely, BF_4^-, ClO_4^-, PF_6^-,

109

$CH_3SO_3^-$, and $C_6H_5SO_3^-$ (Fig. 4.1.3-3). Apparently, the anodic peak currents were inversely proportional to the anion radius (inset in Fig. 4.1.3-3).
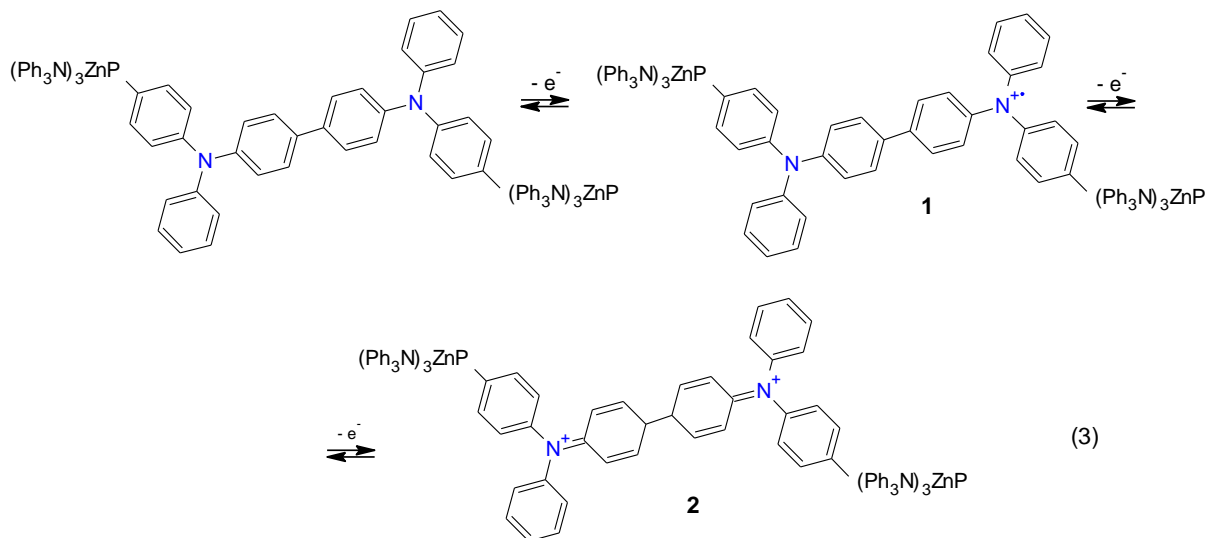
Scheme 4.1.3-3. The proposed mechanism of reversible electro-oxidation of the $(Ph_3N)_4ZnP$ polymer.
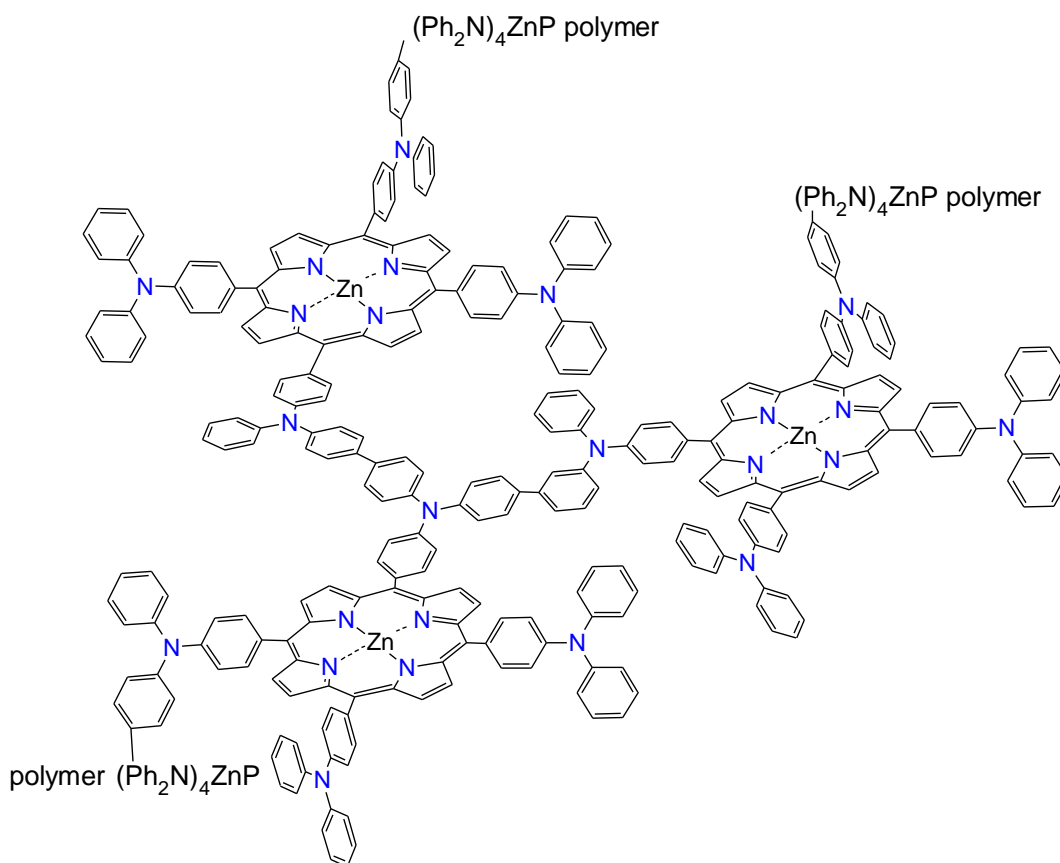
Scheme 4.1.3-4. The proposed simplified structural formula of the $(Ph_3N)_4ZnP$ polymer.

110
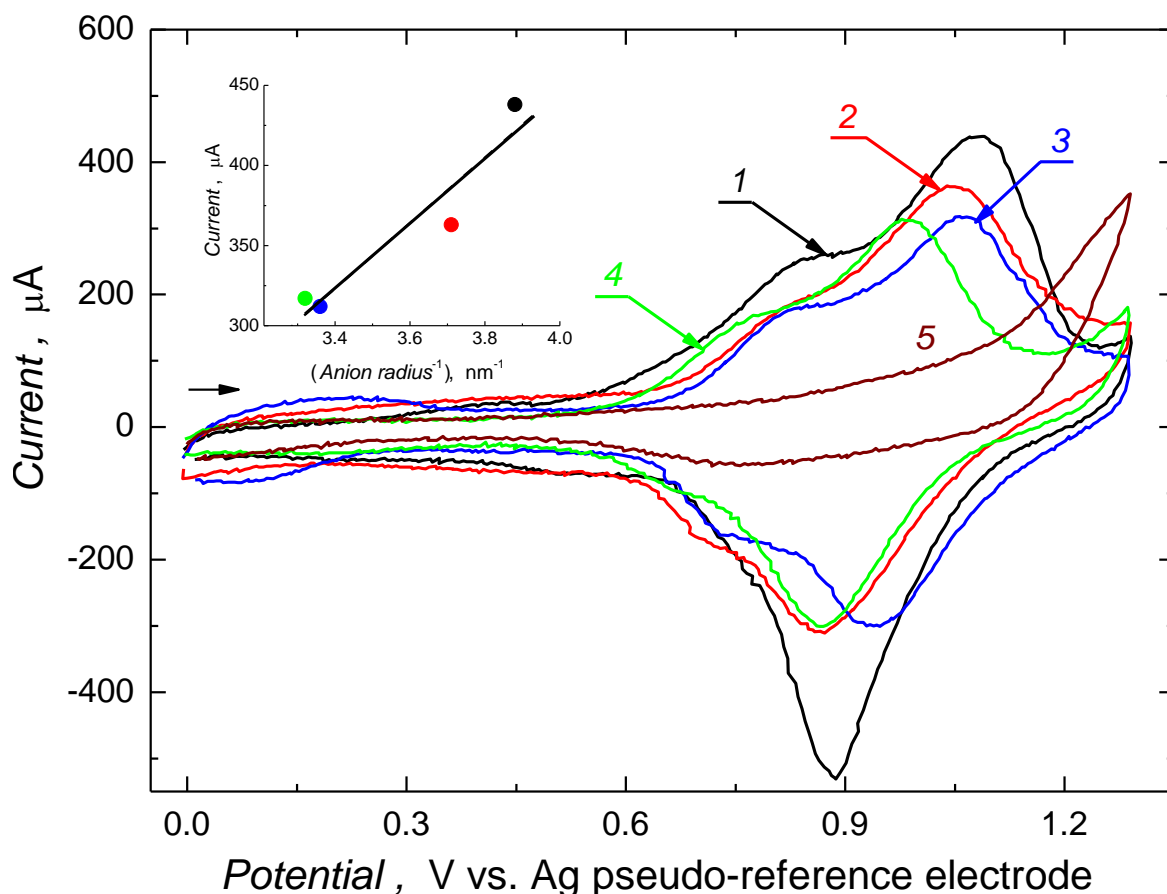
Figure 4.1.3-3. Cyclic voltammetry curves for the $(Ph_3N)_4ZnP$ polymer film in a blank supporting electrolyte of the 0.1 M tetrabutylammonium salt of (*1*) BF_4^-, (*2*) ClO_4^-, (*3*) PF_6^-, (*4*) $CH_3SO_3^-$, and (*5*) $C_6H_5SO_3^-$ in ODCB. A 5-mm diameter Au-over-Ti film of a 10-MHz QCR served as the working electrode, a Pt wire was used as the counter electrode. The potential scan rate was 100 mV/s.

Moreover, the CV peaks for the $(Ph_3N)_4ZnP$ polymer in the blank supporting electrolyte of the anion of the biggest diameter, $C_6H_5SO_3^-$, completely vanished (curve *5* in Fig. 4.1.3-3).

4.1.3.2 Evaluation of the [(Ph₃N)₄ZnP polymer film]-C₆₀im dyad formation

Formation of the $[(Ph_3N)_4ZnP$ polymer film]-$C_{60}im$ dyad was in situ monitored by piezoelectric microgravimetry at EQCM. For that, the QCR with the $(Ph_3N)_4ZnP$ polymer film coated electrode was mounted in the EQCM 5610 flow-through holder. Then, a blank ODCB carrier solution was passed through the holder. Next, ODCB solution samples of $C_{60}im$ were consecutively injected and the accompanying resonance frequency changes were

111

recorded. The resulting frequency change steps corresponding to three initial injections are shown in Fig. 4.1.3-4.
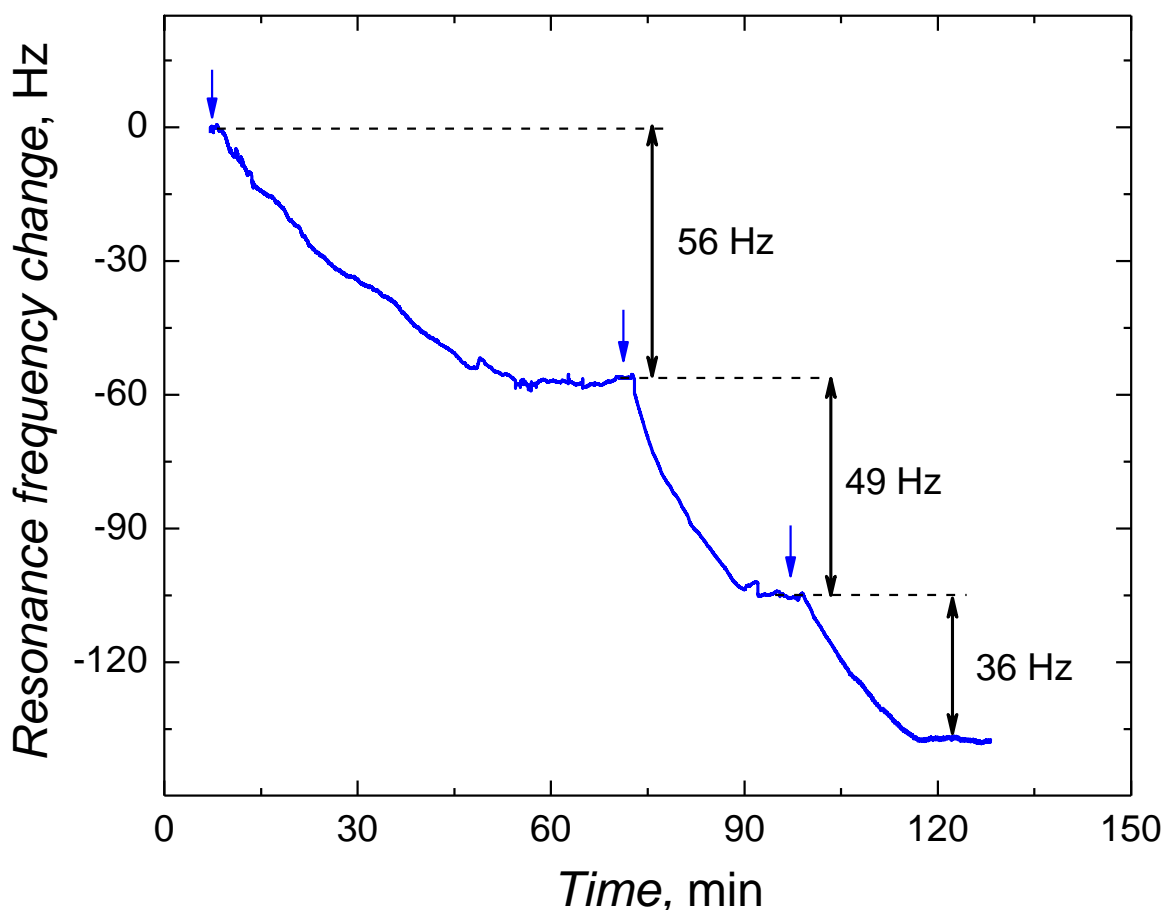
Figure 4.1.3-4. (a) Flow-injection analysis measurements with the EQCM detection of C_{60}im binding to the $(Ph_3N)_4ZnP$ polymer film to form a donor-acceptor dyad. The sample volume of each injection of 17.4 mM C_{60}im in ODCB was 1 mL. The flow rate of the ODCB carrier liquid was 50 μL/min. The frequency changes accompanying initial three consecutive injections are shown.

Resonance frequency irreversibly decreased after each injection. This means that the dyad formed did not dissociate after the injected C_{60}im sample had passed through the holder. Each consecutive injection caused smaller resonance frequency decrease due to gradual saturation of the Zn sites available for complexation in the $(Ph_3N)_4ZnP$ polymer. The total frequency change after three injections was 141 Hz. The mass change corresponding to this change determined, using the Sauerbrey equation, was 122 ng. This value corresponds to

112

~2.1 monolayers of C_{60}im of hexagonal packing on the polymer flat surface. As expected from Fig. 4.1.3-3, the C_{60}im ligand does not penetrate deeply into the film but rather stays on or near its surface.
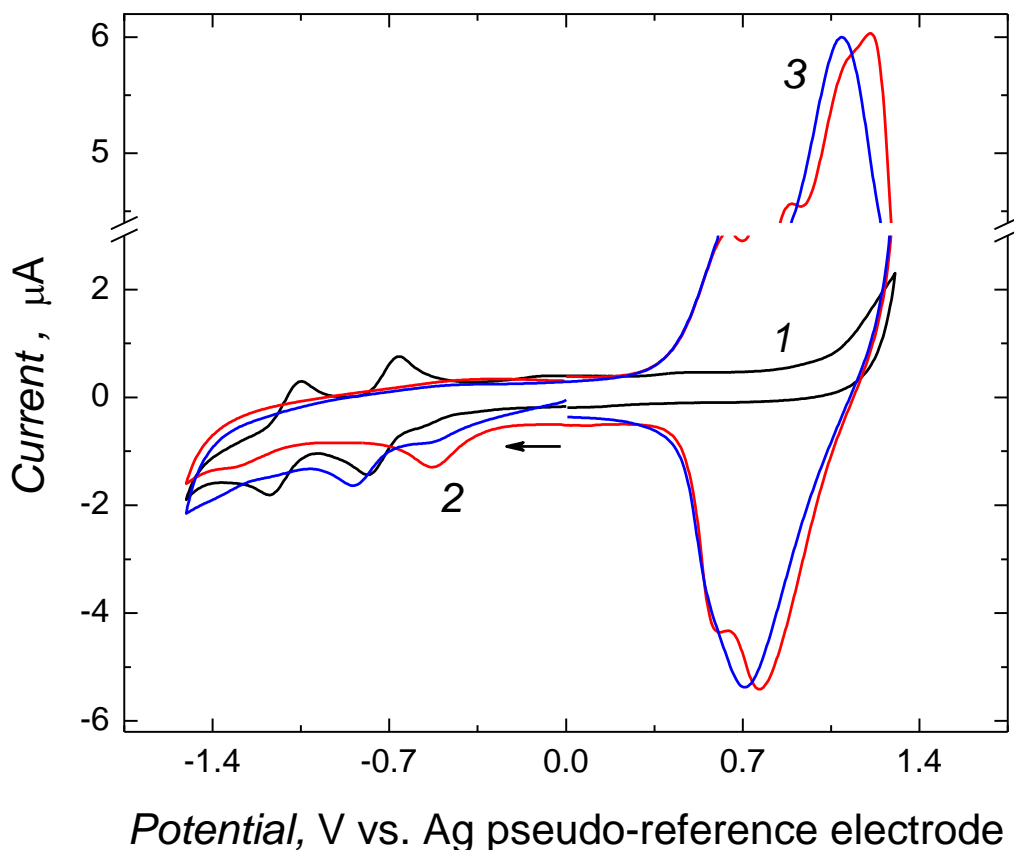
Figure 4.1.3-5. Cyclic voltammograms at the 1.6-mm diameter Au disk electrode for (*1*) 0.5 mM C_{60}im, (*2*) the $(Ph_3N)_4ZnP$ polymer film and (*3*) C_{60}im bound to the $(Ph_3N)_4ZnP$ polymer film demonstrating formation of an electro-active [$(Ph_3N)_4ZnP$ polymer film]-C_{60}im donor-acceptor dyad in the 0.1 M $(TBA)ClO_4$ solution of ODCB. The potential scan rate was 100 mV/s.

The presence of coordinated C_{60}im in the $(Ph_3N)_4ZnP$ polymer film was confirmed by the CV measurements (Fig. 4.1.3-5). For that, an Au disk electrode coated with the $(Ph_3N)_4ZnP$ polymer was soaked in the 0.1 mM C_{60}im solution of ODCB for 15 min. Then, the electrode was carefully rinsed with blank ODCB. Next, the CV curves for the pristine $(Ph_3N)_4ZnP$ polymer film, the film with the coordinated C_{60}im and, separately, C_{60}im in solution were recorded. The presence of the coordinated C_{60}im in the $(Ph_3N)_4ZnP$ polymer film was manifested by the cathodic peak at ~ -0.85 V being close to that of C_{60}im in solution.

113

Neither the second cathodic nor the anodic peak was observed for C_{60}im. Presumably, this was caused by dissociation of the dyad and dissolution of the resulting C_{60}im anion radical in the solvent because of its higher solubility.

4.1.3.3 Surface morphology of the [(Ph$_3$N)$_4$ZnP polymer]-C$_{60}$im dyad films

The AFM images of the (Ph$_3$N)$_4$ZnP film in the absence and presence of the coordinated C_{60}im ligand were recorded (Fig. 4.1.3-6a and b, respectively).
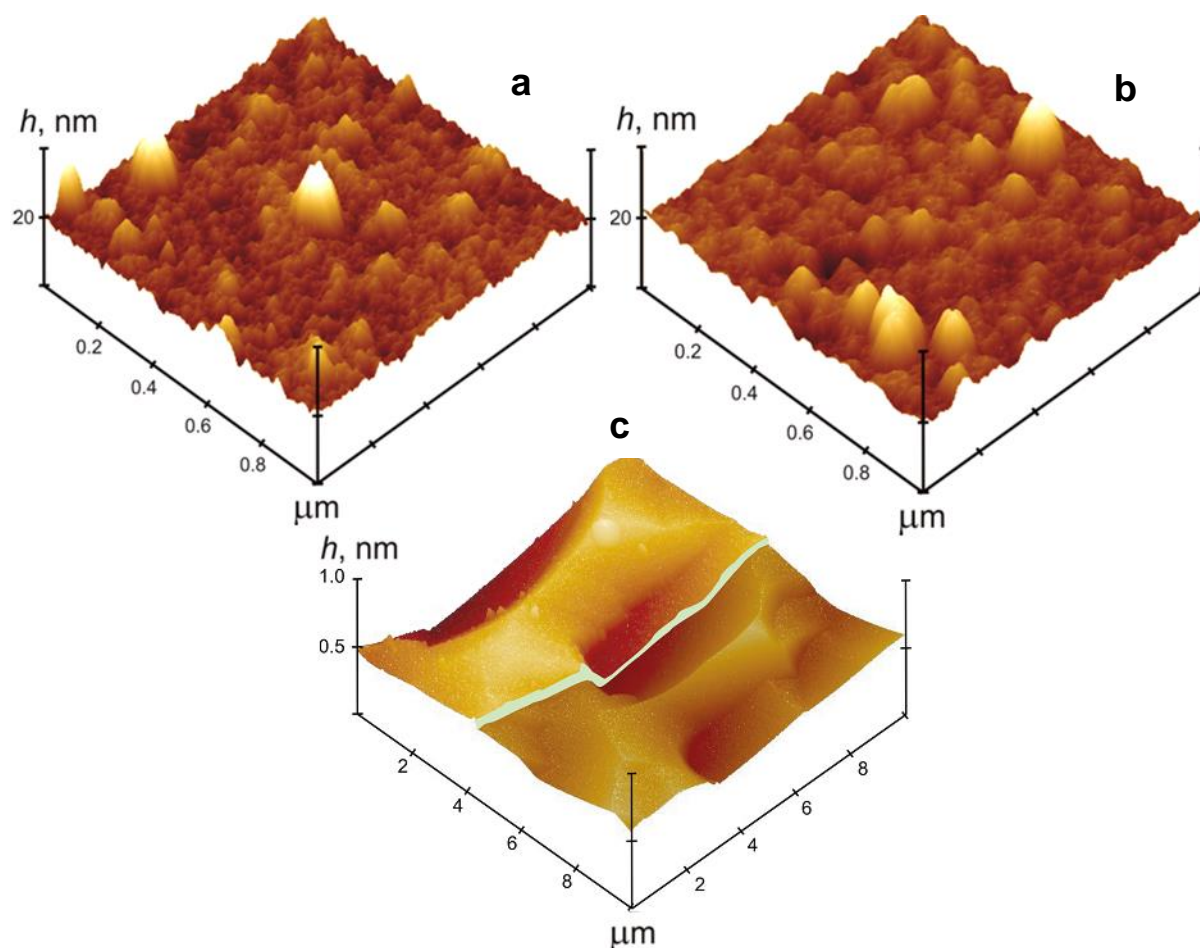
Figure 4.1.3-6. The atomic force microscopy tapping mode 1×1 μm^2 image of (a) the (Ph$_3$N)$_4$ZnP polymer film and (b) the (Ph$_3$N)$_4$ZnP polymer film with the bound C_{60}im ligand, deposited by potentiodynamic electropolymerization on an Au-over-Ti coated glass slide as well as (c) the 10×10 μm^2 image of the edge of the (Ph$_3$N)$_4$ZnP polymer film deposited on the polished Au-over-Ti electrode of QCR, using EQCM under potentiodynamic conditions during 33 potential cycles at the scan rate of 100 mV/s from 0.12 mM (Ph$_3$N)$_4$ZnP in the 0.1 M (TBA)ClO$_4$ solution of ODCB.

114

Both films were uniform and composed of 150-200 nm aggregates. Morphology of the polymer changed upon binding the ligand. That is, the film became more diffuse as compared to that of the pristine $(Ph_3N)_4ZnP$ polymer. The relative surface area, R_{sa}, of the pristine polymer film and that with the ligand bound was 1.010 and 1.022, respectively. The average film thickness, deposited on the Au-over-Ti electrode of QCR by potentiodynamic electropolymerization during 33 potential cycles from 0.12 mM $(Ph_3N)_4ZnP$ was 107.4 nm (Fig. 4.1.3-6c). This deposition resulted in the 3.4 kHz resonance frequency decrease. Hence, density of the resulted film was 0.51 g/cm^3 and concentration of the Zn porphyrin sites was 0.38 M.

4.1.3.4 Spectroscopic characterization of the [(Ph₃N)₄ZnP polymer]-C₆₀im dyad film

The UV-vis absorbance in solution (Fig. 4.1.3-7) and reflectance of the film on the Au-over-Ti electrode of QCR spectra (Fig.4.1.3-8) of the $[(Ph_3N)_4ZnP$ polymer]-C_{60}im dyad and its moieties, separately, were recorded.
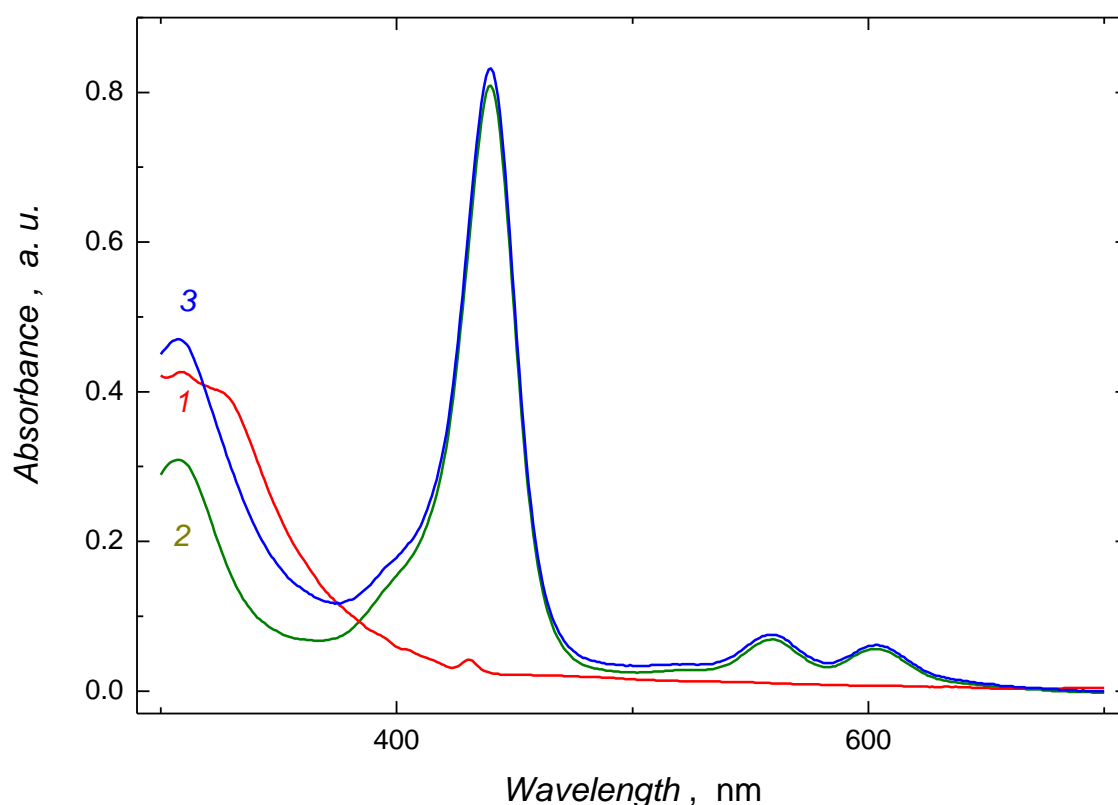
Figure 4.1.3-7. The UV-vis absorbance spectra of (*1*) 20.5 μM C_{60}im, (*2*) 7 μM the $(Ph_3N)_4ZnP$ monomer, and (*3*) 7 μM the $[(Ph_3N)_4ZnP$ monomer]-C_{60}im dyad $CHCl_3$ solutions.

115
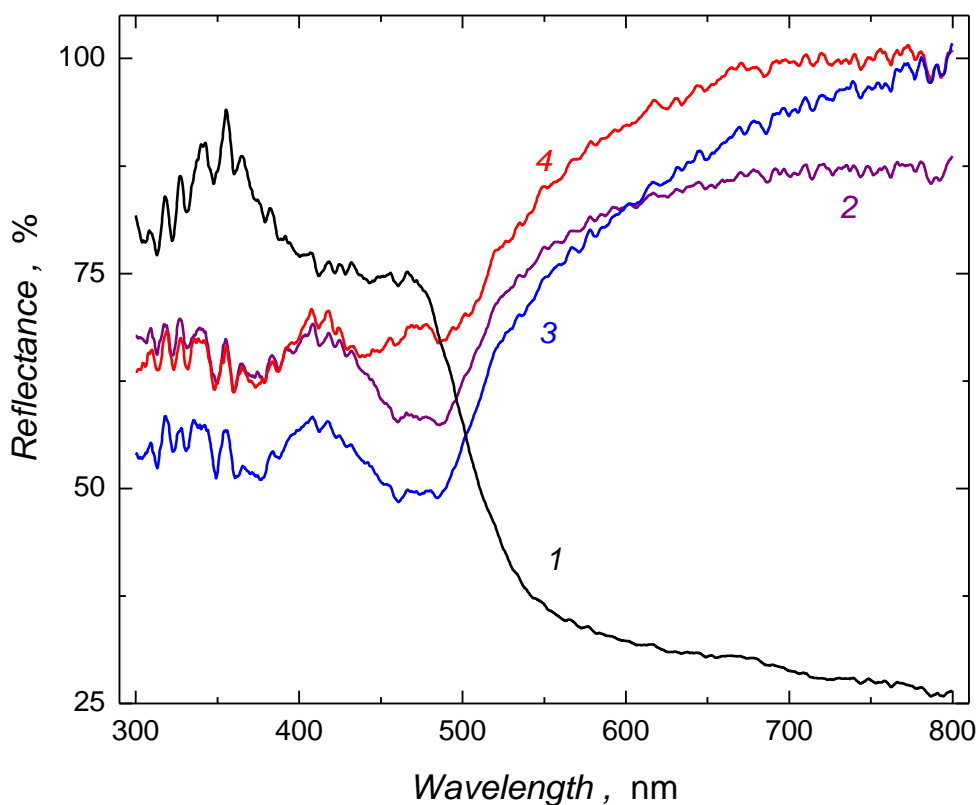
Figure 4.1.3-8. The UV-vis reflectance spectra of (*1*) the drop-coated C_{60}im film, (*2*) the $(Ph_3N)_4ZnP$ polymer film, (*3*) the $[(Ph_3N)_4ZnP$ polymer]-C_{60}im film after binding by the $(Ph_3N)_4ZnP$ polymer film of the C_{60}im ligand under FIA conditions, and (*4*) the electropolymerized $[(Ph_3N)_4ZnP$ polymer]-C_{60}im, 1 : 1 (mole : mole), dyad on the 5-mm diameter Au-over-Ti electrode of 10-MHz QCR using the EQCM, under potentiodynamic conditions.

The spectra for both the electropolymerized dyad (curve *4* in Fig. 4.1.3-8) and that deposited by electropolymerization of the $(Ph_3N)_4ZnP$ monomer and then dip-soaking of the $(Ph_3N)_4ZnP$ polymer in the C_{60}im ligand solution (curve *3* Fig. 4.1.3-8) were recorded separately. The changes in reflectivity of the films suggest that the porphyrin macrocycle remained intact after the electropolymerization.

The Raman microscopy spectra for these films as well as for the drop-coated film of C_{60}im were recorded to confirm the presence of the C_{60}im in the film (Fig. 4.1.3-9). There were no any remarkable changes in the spectra of the $(Ph_3N)_4ZnP$ polymer after its ligation with C_{60}im to produce the $[(Ph_3N)_4ZnP$ polymer]-C_{60}im dyad.

116
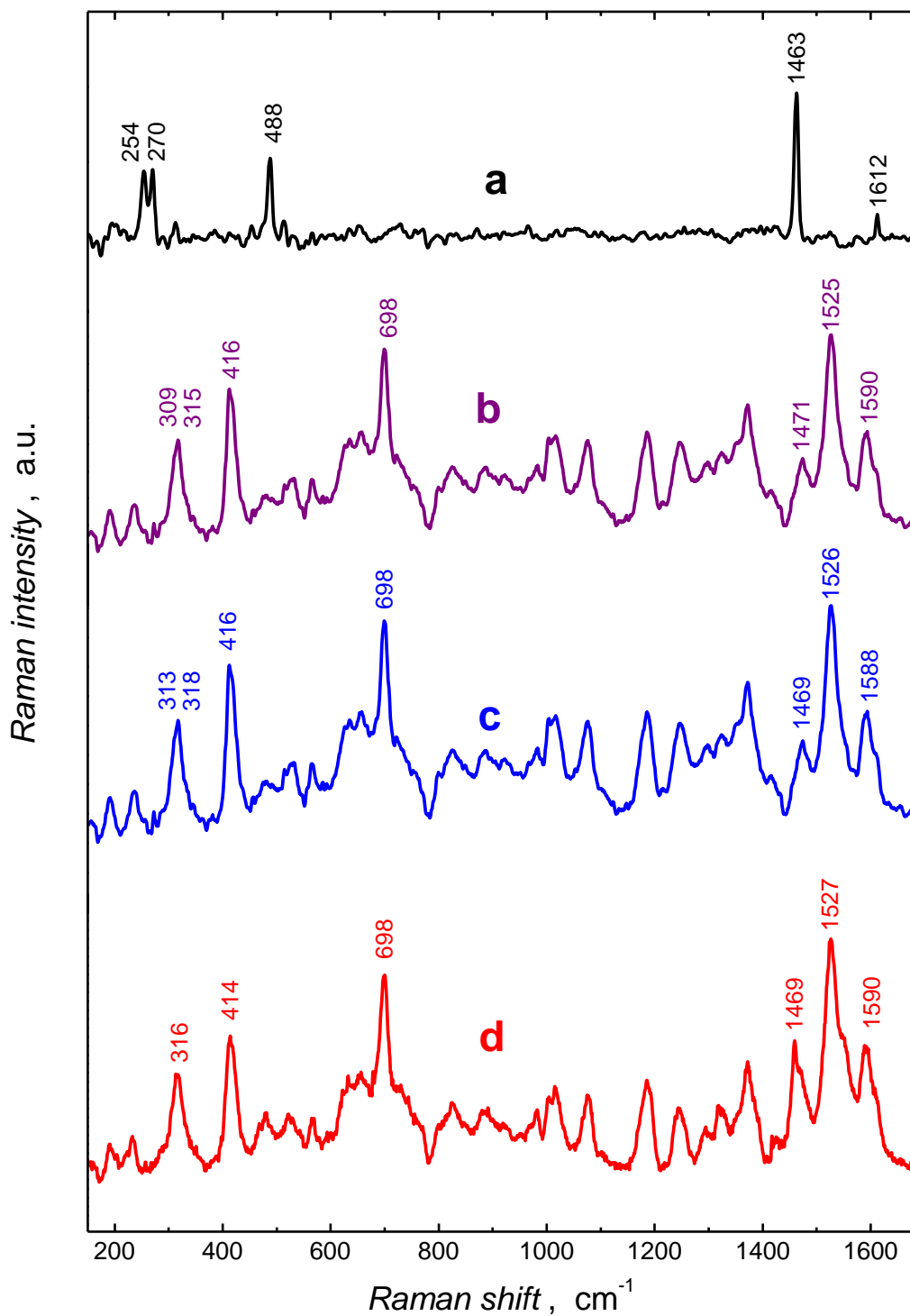
Figure 4.1.3-9. The Raman spectra for (a) the drop-coated C_{60}im film, (b) the $(Ph_3N)_4ZnP$ polymer film, (c) the $[(Ph_3N)_4ZnP$ polymer]-C_{60}im prepared by binding of the C_{60}im ligand by the $[(Ph_3N)_4ZnP$ polymer film in the FIA experiment, and (d) the film of the $[(Ph_3N)_4ZnP$ polymer]-C_{60}im, $1:1$ (mole : mole) dyad deposited by potentiodynamic electropolymerization on the 5-mm diameter Au-over-Ti electrode of 10-MHz QCR using the EQCM.

117

There were no any remarkable changes in the spectra of the $(Ph_3N)_4ZnP$ polymer after its ligation with $C_{60}im$ to produce the $[(Ph_3N)_4ZnP$ polymer]-$C_{60}im$ dyad. However, the ratio of the peak height at ~1525 to that at ~1470 cm^{-1} qualitatively corresponded to the amount of the $C_{60}im$ ligand in the film. That is, for the pristine $(Ph_3N)_4ZnP$ polymer, the dyad prepared in the FIA experiment, and for the electropolymerized $[(Ph_3N)_4ZnP$ polymer]-$C_{60}im$ (1 : 1, mole : mole), prepared in solution prior electropolymerization) dyad, this value was 2.86, 2.82, and 1.88, respectively. Thus, relative quantity of $C_{60}im$ in the dyad film prepared by electropolymerization of the dyad was higher than that prepared during FIA experiment.

4.1.3.5 Spectroelectrochemical properties of the [(Ph₃N)₄ZnP polymer]-C₆₀im dyad film

The cell for the photoelectrochemical measurements was assemblied according to Scheme 4.1.3-5 illustrating as well the simplified mechanism of photocurrent generation by the $[(Ph_3N)_4ZnP$ polymer film]-fullerene modified electrode.
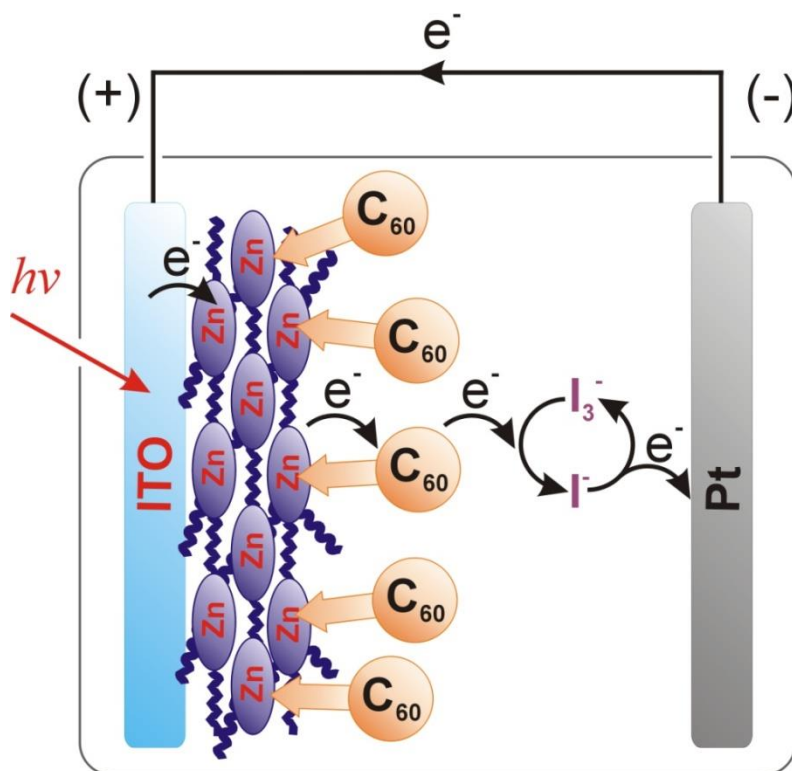
Scheme 4.1.3-5. Schematic view of the mechanism of the cathodic photocurrent generation by the $[(Ph_3N)_4ZnP$ polymer film]-fullerene modified optically transparent ITO electrode.

118

The *I-V* characteristics for the pristine $(Ph_3N)_4ZnP$ polymer film coated ITO electrode (curve *1* in Fig. 4.1.3-10) and that with the coordinated $C_{60}im$ ligand (curve *2* in Fig. 4.1.3-10) were recorded. The presence of the coordinated $C_{60}im$ significantly increased the photoelectrochemical performance of the film.
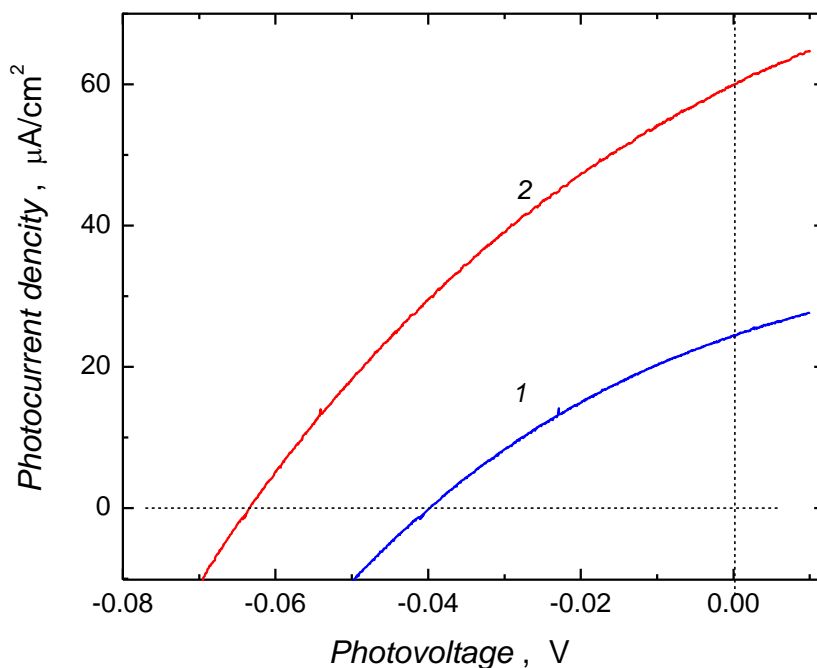
Figure 4.1.3-10. Photocurrent-photovoltage (*I-V*) characteristics for ITO electrodes coated with the $(Ph_3N)_4ZnP$ polymer film in the (*1*) absence and (*2*) presence of $C_{60}im$. The *I-V* curves were generated for the acetonitrile solution of the I_3^-/I^- (0.1 M / 0.1 M) mediating redox couple.

Both the photocurrent and photovoltage generation was examined in a light-switching on and off experiment (Fig. 4.1.3-11). The photocurrents increased as much as three times while the photovoltage increased twice in the presence of the coordinated fullerene adduct. Moreover, these modulations were reversible with respect to both the amplitude of photocurrent and photovoltage.

The I_3^-/I_2 charge mediating redox system in acetonitrile was used in the photoelectrochemical experiments. The analytical concentration of I^- and I_2 was 0.1 M and 0.119 M, respectively, resulting in the I_3^- concentration of 0.119 M. The I_3^- concentration was calculated from the stability constant of $\sim 10^7$ M^{-1} at room temperature of the I_3^- complex, whose equilibrium is described by Equation 4.1.3-1.[145]

119

$$\text{I}^- + \text{I}_2 \;\rightleftharpoons\; \text{I}_3^- \hspace{4cm} (4.1.3\text{-}1)$$

Presumably, the I_3^- electron acceptor forms a ground-state complex with the $(\text{Ph}_3\text{N})_4\text{ZnP}$ moiety and oxidatively quenches the excited state, as shown below by Equations (4.1.3-2) and (4.1.3-3).
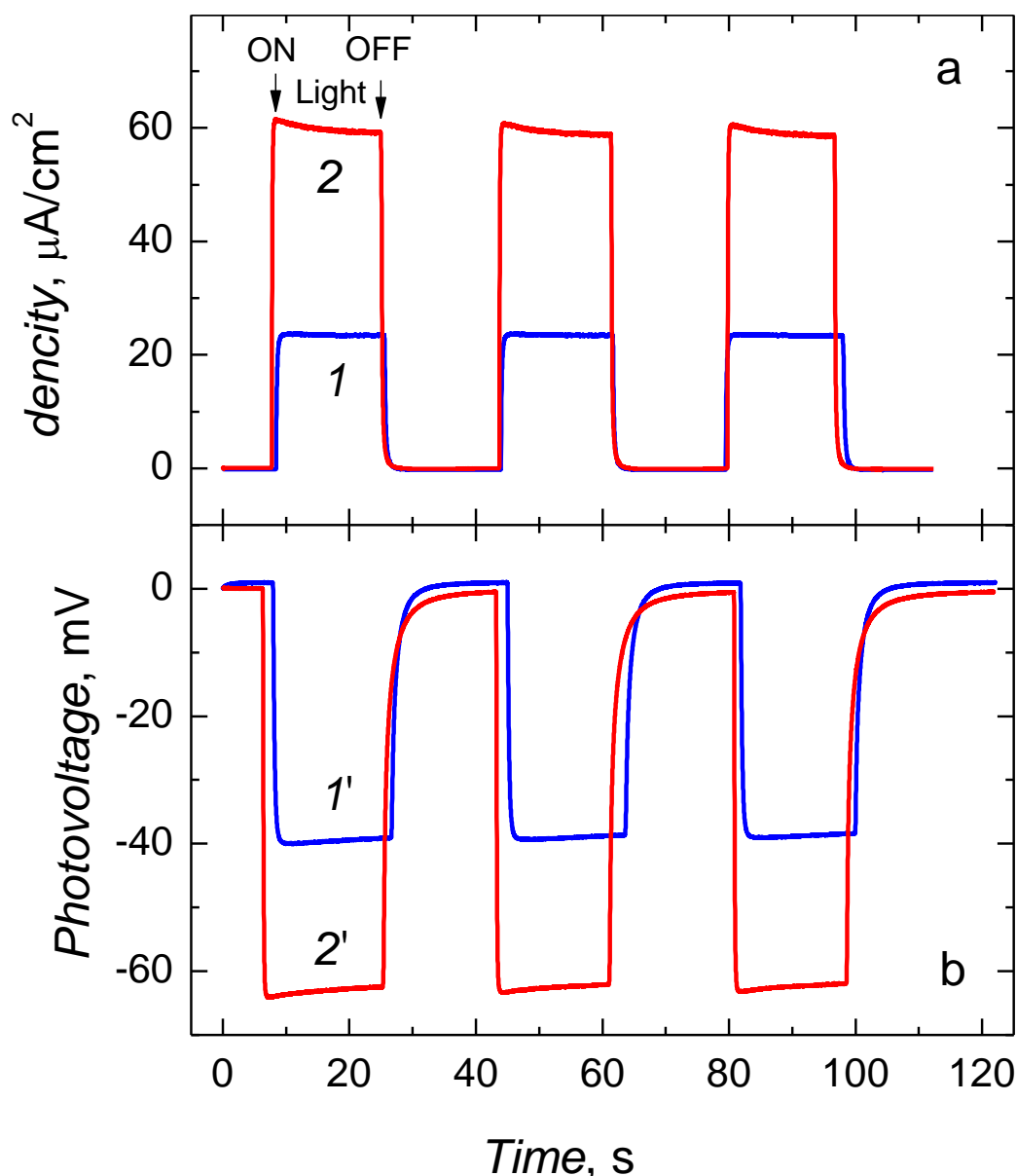
Figure 4.1.3-11. The effect of light switching on and off on (a) photocurrent and (b) photovoltage of the $(\text{Ph}_3\text{N})_4\text{ZnP}$ polymer film coated ITO electrode in the (*1* and *1'*) absence and (*2* and *2'*) presence of C_{60}im. The photocurrent and photovoltage switching were recorded for the acetonitrile solution of the 0.1 M / 0.1 M, I_3^-/ I^-, mediating redox couple.

120

$$(Ph_3N)_4ZnP + I_3^- \; \rightleftharpoons \; [(Ph_3N)_4ZnP:I_3^-] \hspace{3cm} (4.1.3\text{-}2)$$

$$[(Ph_3N)_4ZnP:I_3^-] \; \underset{}{\overset{h\nu}{\rightleftharpoons}} \; (Ph_3N)_4ZnP^{\bullet+} + I_3^{2-} \rightarrow Products \hspace{1.5cm} (4.1.3\text{-}3)$$
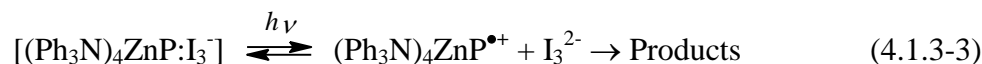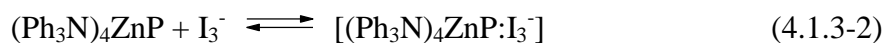
The proposed mechanism of the photoelectrochemical reaction is, as follows. Light excitation of the $(Ph_3N)_4ZnP$ moiety in the donor-acceptor dyad results in vectorial photoinduced electron transfer from the $(Ph_3N)_4ZnP$ electron donor to the $C_{60}im$ acceptor to generate a radical ion pair, $(Ph_3N)_4ZnP^{\bullet+}$-$C_{60}im^{\bullet-}$. The resulting $C_{60}im^{\bullet-}$ transfers the electron to the I_3^- oxidant to close the circuit. The $(Ph_3N)_4ZnP$-localized hole travels through the conducting dyad polymer film until it reaches the ITO photocathode while the electron abstracted from I^- at the Pt anode flows through the external circuit and when reaching the photocathode, it neutralizes $(Ph_3N)_4ZnP^{\bullet+}$ in the polymer to regenerate its light-absorbing neutral form.
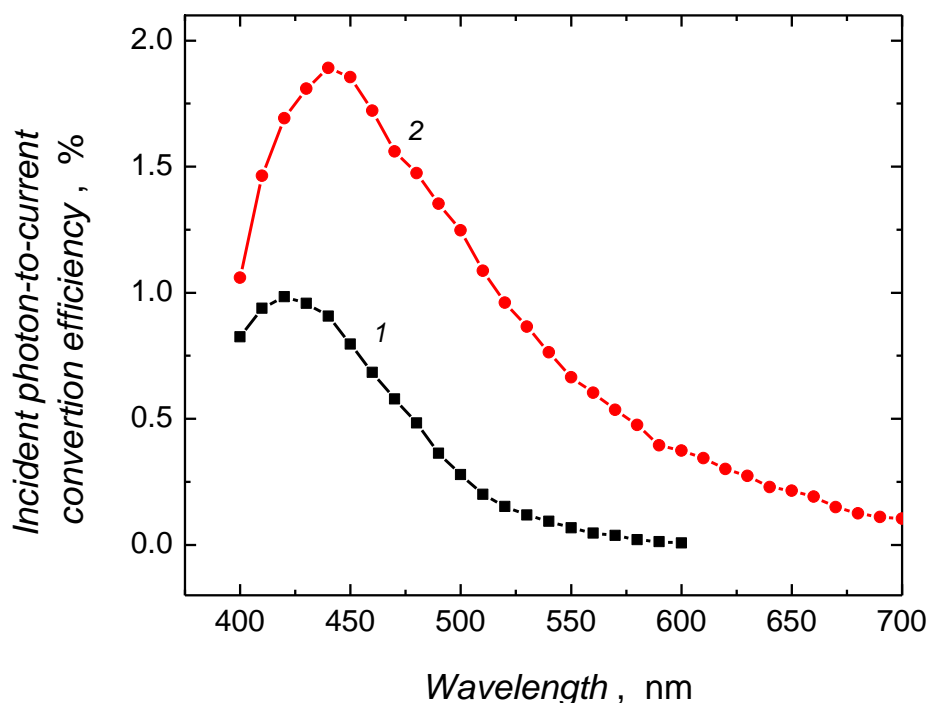
Figure 4.1.3-12. Incident photon-to-current efficiency (IPCE) of conversion for the $(Ph_3N)_4ZnP$ polymer film coated ITO electrode in the (*1*) absence and (*2*) presence of the coordinating $C_{60}im$ ligand, in acetonitrile solution of the I_3^-/ I^- (0.1 M / 0.1 M) mediating redox couple.

121

Particular steps of the letter process are: (i) the electron from $[^1(Ph_3N)_4ZnP^*:I_3^-]$ is transported by the I^- mediator through the solution to the Pt counter electrode, (ii) the $(Ph_3N)_4ZnP$-localized hole travels through the redox conducting polymer film until it reaches the ITO surface, and (iii) the electron from the counter electrode moves through the external circuit, reaches the ITO photocathode and reacts with the $(Ph_3N)_4ZnP^{\bullet+}$ at the ITO/[$(Ph_3N)_4ZnP$ polymer film] interface

The IPCE of conversion for the best performing film of the [$(Ph_3N)_4ZnP$ polymer film]-C_{60}im and for the pristine $(Ph_3N)_4ZnP$ polymer film was determined. The photocurrent action spectrum for the $(Ph_3N)_4ZnP$ polymer film coated electrode in the absence and presence of the coordinating C_{60}im ligand, in acetonitrile solution of the 0.1 M (TBA)I and 0.1 M I_2 mediator, with a Pt foil as the anode, is shown in Figure 4.1.3-12. Both these spectra resemble those of the absorption spectra of the $(Ph_3N)_4ZnP$ and the dyad (Fig 4.1.3-7). However, photocurrents in the action spectrum, recorded in the presence of the coordinated C_{60}im, are enhanced, again signifying the importance of the coordinated fullerene. At the wavelength of maximum photocurrent, the ICPE was calculated as ~2 % for the [$(Ph_3N)_4ZnP$ polymer film]-fullerene modified electrode.

4.2 Molecularly-imprinted polymer films of (Ph$_3$N)$_4$CoP for electrocatalytic dioxygen reduction

Dioxygen reduction electrocatalysis has extensively been studied for several decades now because of still unresolved problem of substitution of expensive noble metal catalysts, used in cathodes of fuel cells, with cheaper materials.[146-149] Among others, metalloporphyrin catalysts attract attention as potential alternatives for platinum. Different metalloporphyrins, viz. those of Co, Fe, Ir, Ru, etc., were reported as promising catalysts for electroreduction of dioxygen.[150,151]
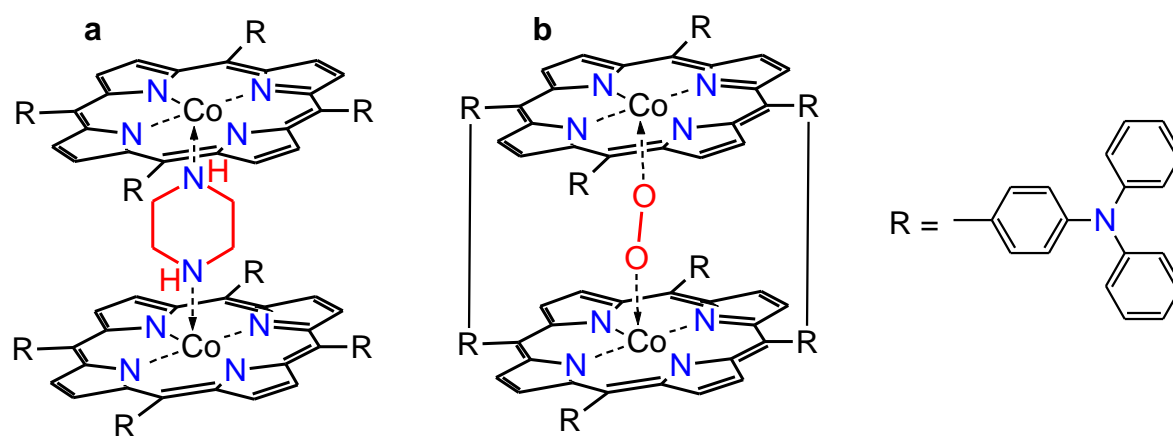
Scheme 4.2-1. Simplified structural formulas of the 2 : 1 complex of (a) *tetrakis*[4-(*N,N*-diphenylamino)phenyl]porphyrinatocobalt(II), (Ph$_3$N)$_4$CoP, with the piperazine (PPZ) templating ligand and (b) the dioxygen molecule coordinated by the template-free cavity of the (Ph$_3$N)$_4$CoP polymer.

Apparently, the electrocatalytic cathode efficiency towards dioxygen electroreduction is increased when co-facially stacked Co porphyrin dimers are used.[69,71] These dimers with the Co-to-Co atom distance of ~0.3-0.4 nm catalyze dioxygen electroreduction to water according to the one-step four-electron mechanism.[70,72,152]

The present research involves preparation and study of electrocatalytic performance of a bidentate ligand molecularly imprinted polymer (MIP) of Co porphyrin bearing four peripheral triphenylamine substituents in the *meso* positions (Scheme 4.2-1). The role of the templating ligand is to pre-arrange in solution the monomers of the Co porphyrin macrocycles into an axially coordinated dimer with the bidentate ligand linking Co atoms of two macrocycles. The triphenylamine substituents served electropolymerization of the (Ph$_3$N)$_4$CoP, thus leading to formation of an electrocatalytically active polymer.

123

In the present research, piperazine (PPZ) was selected as the template for molecular imprinting because with its two nitrogen atoms it can axially coordinate two cobalt porphyrin macrocycles forming co-facial "double decker" stacks (Scheme 4.2-1) with the cobalt-to-cobalt distance of ~0.68 nm, as calculated herein from the complex structure optimized with the Gaussian 09 software.[130] This value is close to those of the Co-to-Co distances in co-facial metalloporphyrin covalent dimers, reported to be effective in the dioxygen electrocatalytic reduction. Moreover, the pK_a values of PPZ in an aqueous solution are, advantageously, high, i.e., $pK_{a,1} = 5.33$ and $pK_{a,2} = 9.73$ (Scheme 4.2.-2). Therefore, PPZ can serve as a bidentate ligand in protic solvent solutions of pH > $pK_{a,2}$. At pH < $pK_{a,1}$, however, PPZ is doubly protonated and, therefore, the complex cannot be formed.
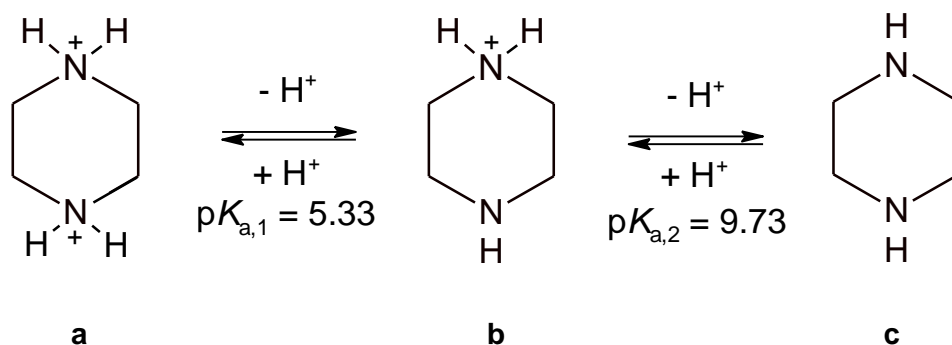
Scheme 4.2-2. Acid-base equilibria of PPZ in an aqueous solution.

These two opposite features allow to use PPZ as a templating ligand for complex formation in solution before electropolymerization on the one hand, and to remove this template from the polymer film after electropolymerization at elevated solution acidity (pH < $pK_{a,1}$) on the other.

4.2.1 UV-vis spectroscopic study of interaction of (Ph$_3$N)$_4$CoP with piperazine

In order to confirm formation of the axial complex of the $(Ph_3N)_4CoP$ with the PPZ ligand, a series of UV-vis absorption spectra of the pristine $(Ph_3N)_4CoP$ as well as those of a mixture of this monomer and the PPZ ligand in the ODCB solution were recorded (Fig. 4.2-1a).

The spectrum for the pristine $(Ph_3N)_4CoP$ solution (curve *1* in Fig. 4.2-1a) exhibits a strong Soret band at 434 nm and two weak Q bands at ~536 nm and ~577 nm, all typical for porphyrins. The Soret band of the spectrum recorded for the freshly prepared solution containing both $(Ph_3N)_4CoP$ and PPZ at the 1 : 1 mole ratio (curve *2* in Fig. 4.2-1a) is blue

124

shifted by 4 nm and both Q bands are broadened with respect to those seen in the spectrum for the solution of the $(Ph_3N)_4CoP$. However, the spectrum recorded for the same solution of the $(Ph_3N)_4CoP$: PPZ, at the mole : mole ratio of 1 : 1, after two-week aging (curve *3* in Fig. 4.2-1a) is different than that for the freshly prepared solution. That is, the Soret band is substantially decreased and broadened as if testifying the coexistence of different complex types with H- and J-type mutual orientation of porphyrin macrocycles. This slow complex rearrangement may indicate organization of bigger complex aggregates of general stoichiometry of 1 : 1, e.g., $[-(Ph_3N)_4CoP-PPZ-(Ph_3N)_4CoP-PPZ-]_n$.[153,154] The Q band of the aged complex at ~536 nm disappeared and that at ~577 nm was red shifted by 35 nm.

Moreover, the UV-vis spectra for the freshly prepared (not shown) and aged for two weeks (curve *4* in Fig. 4.2-1a) ODCB solutions of the $(Ph_3N)_4CoP$-PPZ complex of the 1 : 2 molar ratio were recorded. The spectrum for the solution of the freshly prepared $(Ph_3N)_4CoP$-PPZ complex of the 1 : 2 molar ratio was similar to that for the 1 : 1 molar ratio complex. However, the Q band of the aged 1 : 2 molar ratio complex at ~536 nm was by ~3 nm red shifted with respect to that for the 1 : 2 freshly prepared complex. The Q band of the 1 : 2 molar ratio complex at ~577 nm disappeared or red shifted to ~612 nm after two-week aging of the solution (curve *4* in Fig. 4.2-1a).

After deposition of the $(Ph_3N)_4CoP$ polymer films, the UV-vis reflectance spectra were recorded (Fig. 4.2-1b). Importantly, the Soret and Q bands, characteristic of both the non-imprinted polymer of $(Ph_3N)_4CoP$ [NIP-$(Ph_3N)_4CoP$] (curve *1* in Fig. 4.2-1a) and its molecularly imprinted polymer $(Ph_3N)_4CoP$ [MIP-$(Ph_3N)_4CoP$] of the $(Ph_3N)_4CoP$: PPZ, 1 : 1 (mole : mole) ratio (curve *3* in Fig. 4.2-1a) were seen in the spectrum of both the NIP-$(Ph_3N)_4CoP$ (curve *1'* in Fig. 4.2-1b) and MIP-$(Ph_3N)_4CoP$ (curve *2'* in Fig. 4.2-1b) films, and, moreover, after PPZ extraction with the HCl solution of pH = 3.0 (curve *3'* in Fig. 4.2-1b). These spectral features confirm that the porphyrin macrocycle was not ruptured during the electropolymerization, similarly as in the case of electropolymerization of the analogous Zn porphyrin (Section 4.1.3.1, above). The $(Ph_3N)_4CoP$ electropolymerization is discussed in Section 4.2.3, below.
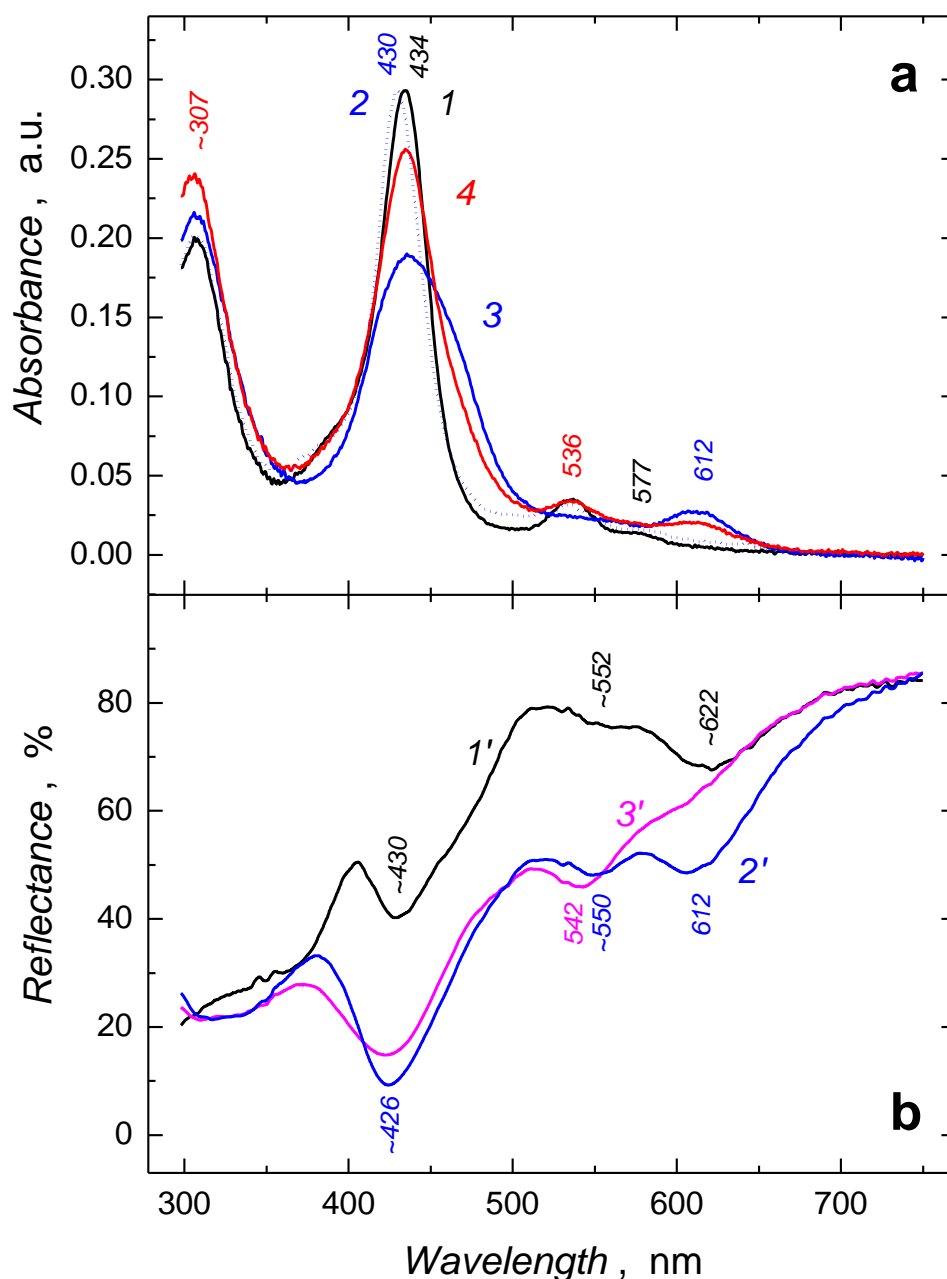
Figure 4.2-1. The UV-vis (a) absorption spectra for the ODCB solution of (*1*) the (Ph$_3$N)$_4$CoP monomer, (*2*) the newly prepared (Ph$_3$N)$_4$CoP : PPZ, 1 : 1 (mole : mole) mixture, (*3*) the (Ph$_3$N)$_4$CoP : PPZ, 1 : 1 (mole : mole) mixture after two-week aging, and (*4*) the (Ph$_3$N)$_4$CoP : PPZ, 1 : 2 (mole : mole) mixture after two-week aging, and (b) the UV-vis reflectance spectra for the film of (*1'*) NIP-(Ph$_3$N)$_4$CoP, (*2'*) the MIP-(Ph$_3$N)$_4$CoP of the (Ph$_3$N)$_4$CoP : PPZ, 1 : 1 (mole : mole) ratio, and (*3'*) the latter film after extraction of the PPZ ligand with the HCl solution (pH = 3.0). The films were deposited by electrochemical polymerization under potentiodynamic conditions on the Au electrode of QCR from 0.107 mM (Ph$_3$N)$_4$CoP in 0.1 M (TBA)ClO$_4$, in the ODCB solutions; the potential scan rate was 0.1 V/s.

126

Apparently, peripheral aminophenyl substituents were solely responsible for the electropolymerization, most likely governed by the benzidine rearrangement mechanism (Section 4.1.3.1, above).[155] In the MIP-$(Ph_3N)_4CoP$ film before ligand extraction, the Soret band at 426 nm was by ~9 nm blue shifted with respect to that at ~435 nm for the 1 : 1, mole : mole, complex in solution (curve *2'* in Fig. 4.2-1b and curve *3* in Fig. 4.2-1a) while the Q band at ~550 nm disappeared in the spectrum for the aged complex in solution. Interesting changes in spectral features were observed in the spectra recorded before and after extraction of the PPZ ligand (curve *2'* and *3'*, respectively, in Fig. 4.2-1b). That is, the Soret band was slightly (by 1.5 nm) blue shifted and almost negligibly broadened (by 1 nm) after this extraction. Similarly, the Q bands at 550 and 612 nm were blue shifted by ~8 and ~5 nm, respectively, compared to those recorded before the PPZ extraction. Moreover, the ratio of the Q band intensity at ~612 nm to that at ~550 nm was largely decreased for the ligand-extracted polymer, compared to that for the polymer before extraction. These spectral changes can be ascribed to dissociation of the $(Ph_3N)_4CoP$ polymer-PPZ complex and removal of the PPZ ligand from the film because these changes were opposite to those typical for formation of such a complex in solution. That is, both the Soret and Q band were red shifted and the absorbance of the band at ~612 nm increased, as compared to the bands for the non-complexed $(Ph_3N)_4CoP$.

Two additional overlapped bands at 310 to 350 nm, present in all the polymer reflectance spectra, can be assigned to the diphenylamine moieties forming a benzidine-type link in the $(Ph_3N)_4CoP$ polymer during electrochemical polymerization.[144]

4.2.2 Electrochemical properties of the $(Ph_3N)_4CoP$ monomer

The DPV curves for the $(Ph_3N)_4CoP$ monomer in solution were recorded to ensure the absence of redox signals of the polymer in the potential range of the dioxygen electroreduction and exact determination of formal redox potential for the monomer (Fig. 4.2-2). The $(Ph_3N)_4CoP$ monomer showed reversible Peaks *1*, *2*, *3*, and *1'* (Fig. 4.2-2). The DPV curves for the monomer in the range of -1.40 to +1.60 V revealed anodic Peaks *1*, *2*, and *3* of the formal potential of $E_1^{0\prime}= +0.81$, $E_2^{0\prime}= +1.13$, and $E_3^{0\prime}= +1.46$ V, respectively, and the cathodic Peak *1'* of the formal potential of $E_{1'}^{0\prime}= -0.94$ V. Advantageously, the monomer showed no redox activity in the potential range of -0.80 to +0.60 V of the redox activity of dioxygen.

127
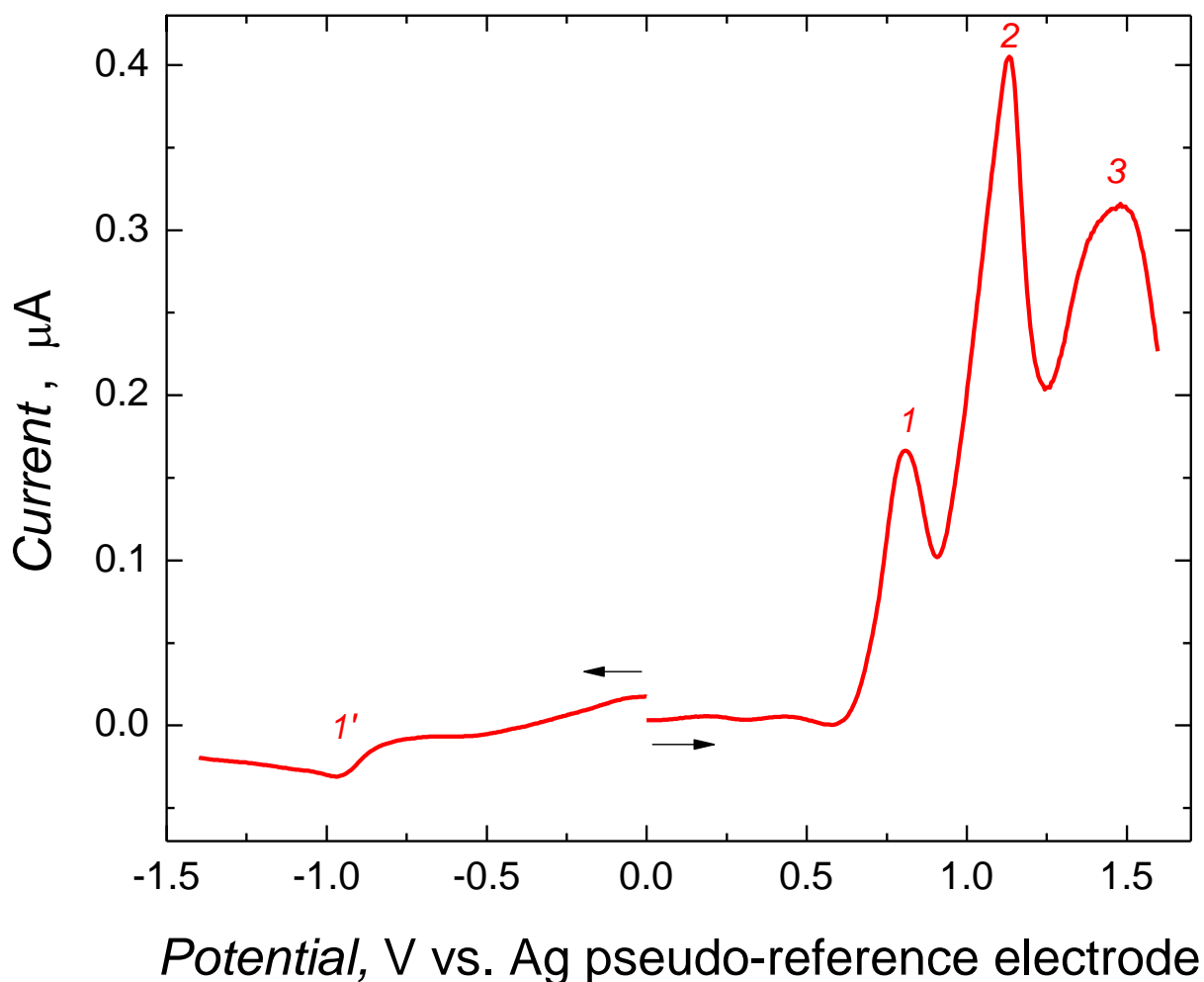
Figure 4.2-2 The DPV curves at the 0.02-cm^2 area Pt disk electrode, for the 0.1 mM (Ph$_3$N)$_4$CoP monomer in 0.1 M (TBA)ClO$_4$, in ODCB. Solutions were deaerated with Ar before measurements.

The Co(II)/(III) oxidation potential for Co(II) complexed by porphyrins strongly depends on the solvent used. For non-binding solvents, such as ODCB, it is observed in the range of +0.75 to +0.78 V.[156] The $E_1^{0\prime}$ of Peak *1* is very close to this range and potential cycling between 0.0 and 1.0 V, i.e., over this peak, does not result in formation of a polymer film on the electrode surface (not shown). Peaks *2* and *3* correspond to electro-oxidation of peripheral triphenylamine substituents.[157] The cathodic Peak *1'* may indicate one-electron reduction of the porphyrin macrocycle.[156]

128

4.2.3 Electrochemical polymerization of NIP-(Ph₃N)₄CoP and (Ph₃N)₄CoP complexed by the piperazine ligand

The pristine $(Ph_3N)_4CoP$ and the $(Ph_3N)_4CoP$ complexed by the PPZ ligand were electrochemically polymerized under the potentiodynamic or pulsed potentiostatic conditions, and properties of the resulting polymer films with respect to dioxygen electrocatalytic reduction were compared.
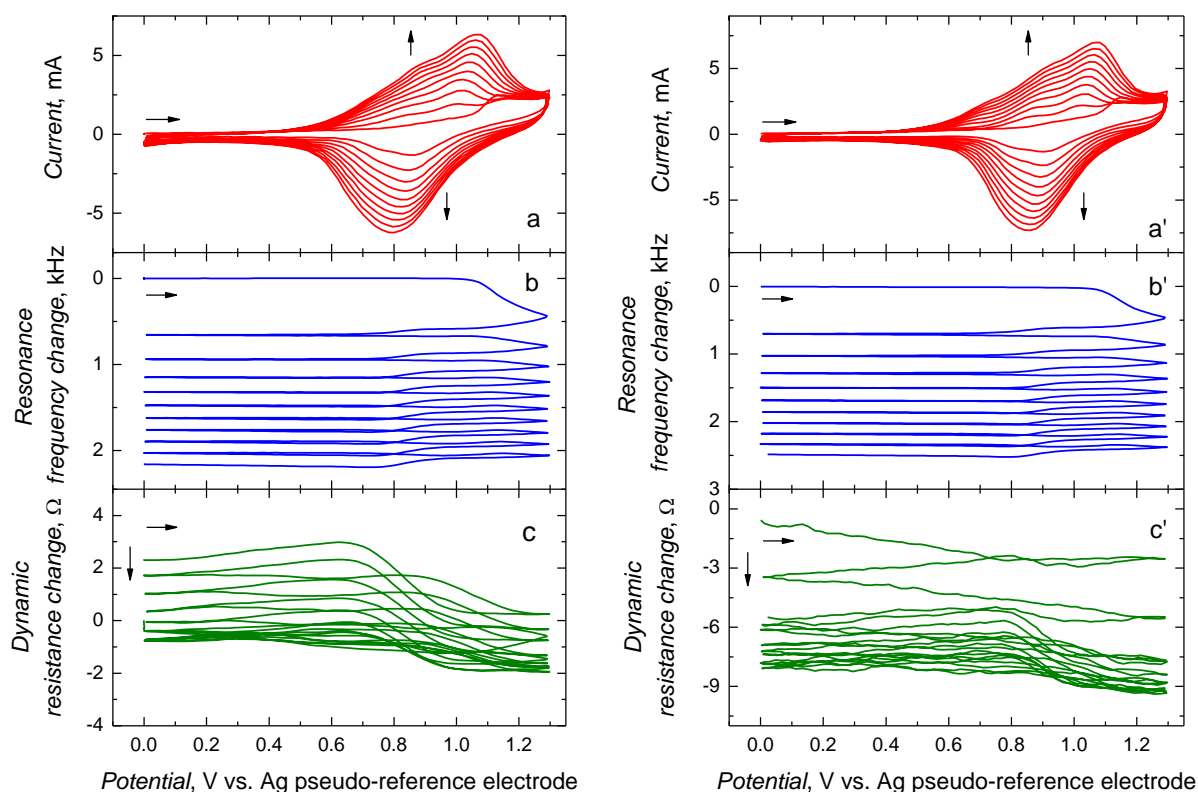
Figure 4.2-3 Curves of (a and a') the multi-cyclic current-potential dependence as well as the potential dependence of (b and b') the resonance frequency change, and (c and c') the dynamic resistance change for deposition by potentiodynamic electropolymerization of the (a, b, and c) the NIP-$(Ph_3N)_4CoP$ as well as (a', b', and c') the MIP-$(Ph_3N)_4CoP$ of the $(Ph_3N)_4CoP$: PPZ ratio of 2 : 1 (mole : mole), from a deaerated ODCB solution of 0.107 mM $(Ph_3N)_4CoP$ and 0.1 M (TBA)ClO₄. The potential sweep rate was 100 mV/s. The 5-mm diameter gold-film electrodes of the 10-MHz Au/Ti quartz crystal resonators served as the working electrodes.

Typical curves of potentiodynamic electropolymerization with the simultaneously recorded change of resonance frequency, Δf, and that of dynamic resistance, ΔR_d, of the Au-

129

QCR as a function of potential, during polymer film deposition, are shown in Figure 4.2-2. The current vs. potential curves, in the presence (Fig. 4.2-2a, 4.2-2b, and 4.2-2c) and absence (Fig. 4.2-2a', 4.2-2b', and 4.2-2c') of the PPZ ligand are very much alike.

In the first potential cycle for NIP-$(Ph_3N)_4CoP$, a broad anodic peak, centered at ~0.92 V, and a well-developed anodic peak at ~1.14 V as well as two overlapping cathodic peaks at ~0.86 and ~0.75 V were developed. In the potential range of the second anodic peak, the Δf decreased during the positive potential excursion pointing to concomitant deposition of the polymer film on the electrode. Moreover, the ΔR_d accompanying film deposition decreased in this potential range. However, the ΔR_d change was merely equal to a few ohms indicating that rigidity of the film remained virtually unchanged in this process. In each subsequent potential cycle, Δf decreased and all the current-potential peaks increased manifesting both the film growth and its pronounced electroactivity, respectively. The overall Δf decrease during ten potential cycles was larger for the solution containing both $(Ph_3N)_4CoP$ and PPZ (Fig. 4.2-3b'), being equal to 2.48 kHz, than that for the PPZ-free solution (Fig. 4.2-3b) equaling 2.16 kHz. The frequency difference of 320 Hz between the two films may approximately correspond to the mass of the PPZ ligand hosted by the templated polymer. Then, the ligand-to-porphyrin molar ratio was estimated as 2.47 : 1, which is fairly close to the 2 : 1 ratio, expected. Moreover, the difference of the anodic-to-cathodic peak potential, measured for the curve of the tenth cycle, was lower for the PPZ containing film like if resistance of this film to ion transfer was lower. These results are consistent with those expected for deposition by electropolymerization of a PPZ-templated $(Ph_3N)_4CoP$ and, hence, more loosely packed metalloporphyrin macrocycles.

The electrochemical equivalent calculated for the $(Ph_3N)_4CoP$ is 84.2 while that determined from the first current-potential cycle (Fig. 4.2-3a) was 76.6 ± 2.5. Presumably, the discrepancy found is due to some ingress of counter ions into the film and, hence, a mass change of the film.

The second approach to prepare the MIP-$(Ph_3N)_4CoP$ involved electropolymerization of the $(Ph_3N)_4CoP$ monomer or the $(Ph_3N)_4CoP$: PPZ complex by applying 1-ms potential pulses of the amplitude of 1.30 V vs. the Ag pseudo-reference electrode (Fig. 4.2-4). The number of pulses was adjusted to pass the charge required for oxidation of the $(Ph_3N)_4CoP$ monomer necessary to deposit a 20-monolayer polymer film on the working electrode assuming parallel orientation of the porphyrin macrocycles with respect to the electrode

surface plane (800 potential pulses). Compared to the polymer films deposited under potentiodynamic conditions, the resulting polymer films should be more uniform with smaller aggregates formed because of a thinner diffusion layer developed.
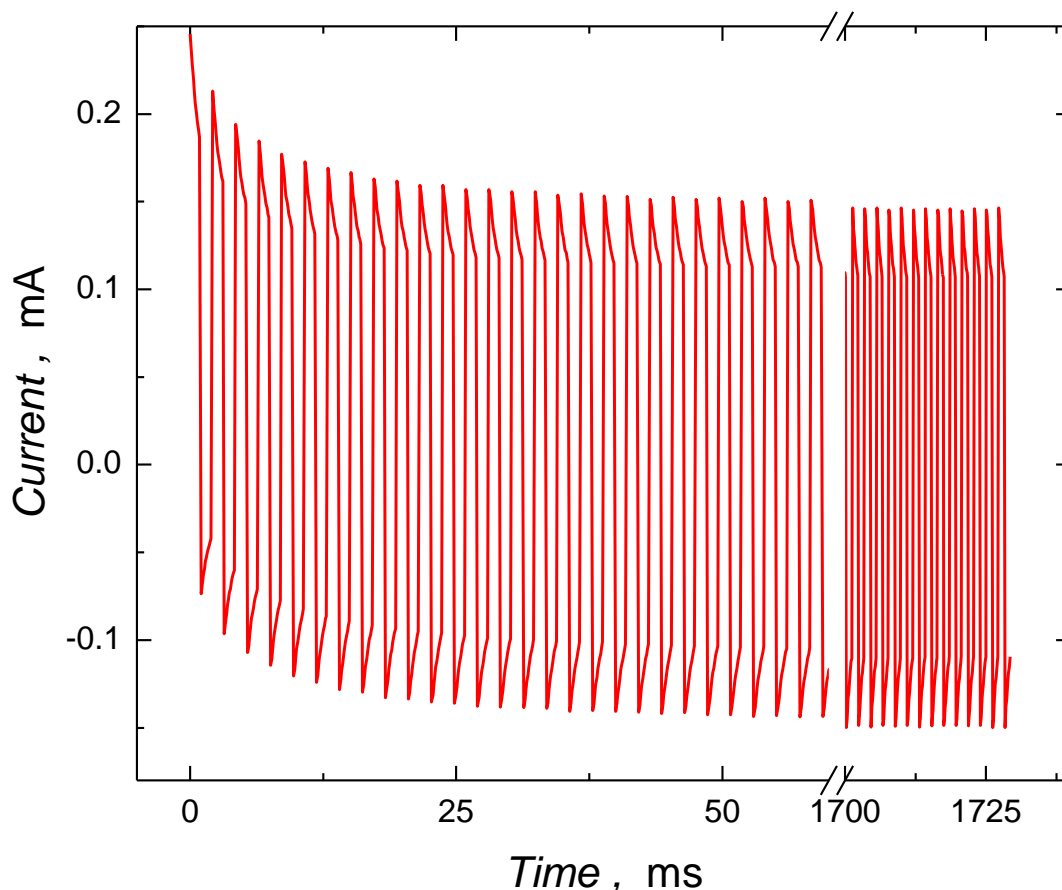
Figure 4.2-4. The current-potential transient for the NIP-(Ph$_3$N)$_4$CoP film deposition on the 3-mm diameter disk GCE by consecutive 1.30-V potentiostatic pulses vs. Ag wire pseudo-reference electrode. The pulse time, initial and final potential were $t = 1$ ms, $E_i = 1.3$ V, $E_f = 0.0$ V, respectively.

The calculated diffusion layer thickness ratio for electropolymerization of the (Ph$_3$N)$_4$CoP under potentiodynamic conditions (Eqn. 2.5-7a) with the potential sweep rate of 0.1 V s^{-1} to that for electropolymerization by 1-ms potentiostatic pulses (Eqn. 2.5-7b) was ~12.5 assuming that the electropolymerization requires transfer of four electrons. That is, the potential sweep rate would have to be ~15.8 V s^{-1} in order to obtain similar morphology of the film. Further decreasing of the diffusion layer thickness by using the pulse duration of electropolymerization of 1.6 μs did not affect electrocatalytic properties of the polymer films (not shown).

131

4.2.4 Characterization of the (Ph₃N)₄CoP polymer films by AFM

Topography of the polymer films deposited under potentiodynamic conditions was examined by AFM (Fig. 4.2-5).
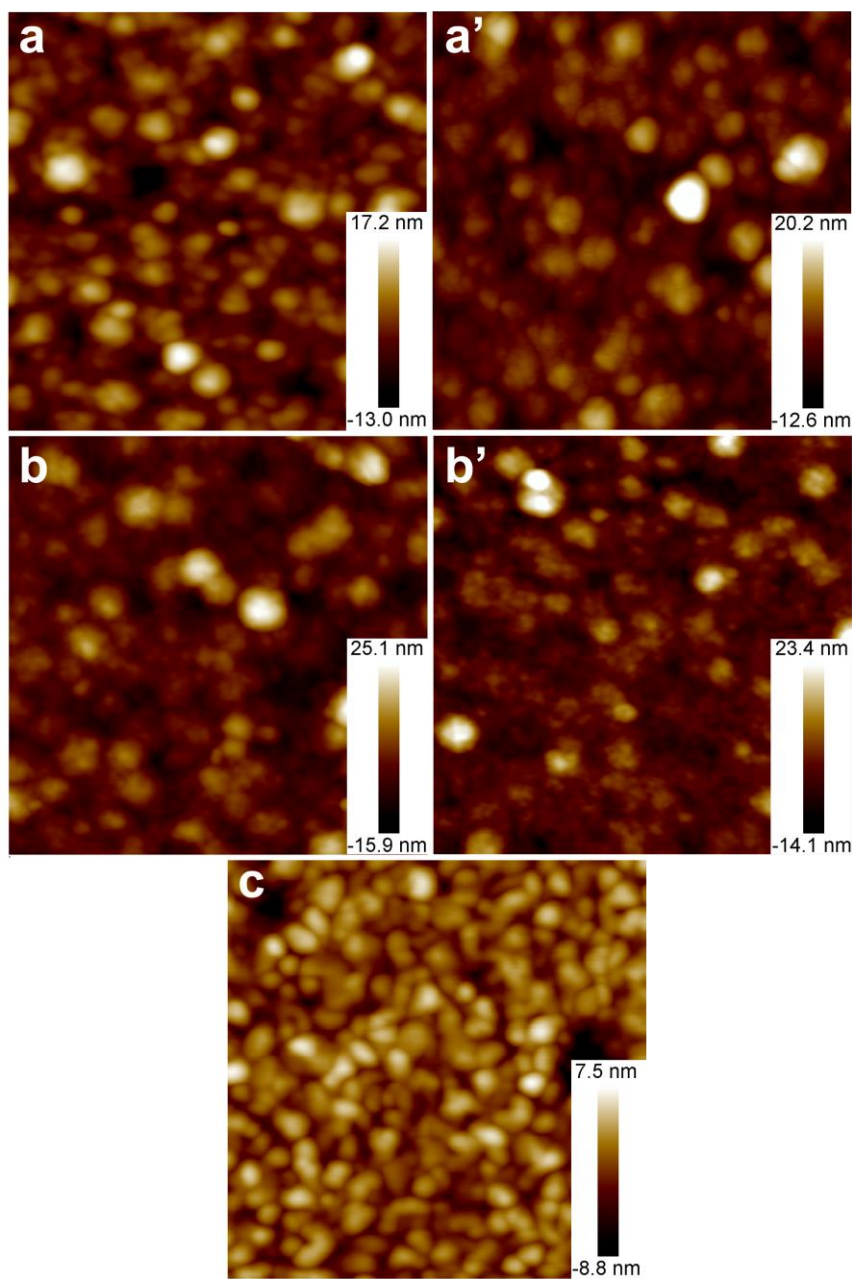
Figure 4.2-5 The tapping mode (1×1) μm^2 AFM images of (a and a') the NIP-(Ph₃N)₄CoP and (b and b') MIP-(Ph₃N)₄CoP film before and after treating with the HCl (pH = 3.0) for 1 h, respectively, and (c) the bare Au-over-Ti-coated glass slide.

132

For that, the films were deposited on the Au-over-Ti coated glass slides from the 0.107 mM $(Ph_3N)_4CoP$, 0.1 M $(TBA)ClO_4$ solution of ODCB, in the course of ten potential cycles, at the sweep rate of 0.1 V s^{-1}. The NIP-$(Ph_3N)_4CoP$ film (Fig. 4.2-5a) was composed of 40-to-80 nm diameter spherical aggregates with thickness of ~100 nm. The surface of these aggregates was relatively smooth (R_{sa} = 1.024). The surface macrostructure of the MIP-$(Ph_3N)_4CoP$ film (Fig. 4.2-5b) was similar to that of the NIP-$(Ph_3N)_4CoP$ film. However, its surface was slightly more rough (R_{sa} = 1.048).

Extraction of the PPZ templating ligand with HCl (pH = 3.0) for 1 h slightly developed the MIP film surface (R_{sa} = 1.052). That is, small aggregates became hardly distinguishable and the surface revealed a nonporous topography. The NIP-$(Ph_3N)_4CoP$ polymer film was treated with the template extracting solution the same way as the MIP film was in order to evaluate the extraction influence on the polymer film morphology (Fig. 4.2-5a'). In effect, roughness of the NIP-$(Ph_3N)_4CoP$ film slightly increased (R_{sa} = 1.024). Nevertheless, it was still lower than that of the MIP film with the PPZ template inside. The $(Ph_3N)_4CoP$ polymer films deposited on the Au-over-Ti coated glass slides under pulse potentiostatic conditions appeared to be too thin to be visualized by AFM.

The R_{sa} value for the blank Au-over-Ti coated glass slide was 1.004. In order to determine precise values of R_{sa}, (10×10) μm^2 area AFM images were recorded (not shown).

4.2.5 Dioxygen electrocatalytic reduction at the $(Ph_3N)_4CoP$ polymer film-coated electrodes

For comparison of the electrocatalytic effects, half-peak potentials rather than peak potentials were used. That was because the former was determined much more precisely. Electrocatalytic activity of the NIP-$(Ph_3N)_4CoP$ and MIP-$(Ph_3N)_4CoP$ film coated GCEs with respect to dioxygen electroreduction was compared. The LSV curves for the GCE, coated with the NIP-$(Ph_3N)_4CoP$ or MIP-$(Ph_3N)_4CoP$ film, deposited by electropolymerization under potentiodynamic conditions, in the oxygen-saturated buffer solution were recorded (Fig. 4.2-6).

Only one peak for the dioxygen reduction was seen for the bare GCE. However, the $(Ph_3N)_4CoP$ polymer film coated GCEs revealed two peaks (curves *2*, *3* and *4* in Fig. 4.2-6, Table 4.2-1). Peak *1* for the GCE coated with the NIP-$(Ph_3N)_4CoP$ film vanished, while Peak *2* was very well-developed (curve *2* in Fig. 4.2-6). The $E'_{1/2, 1}$ and $E'_{1/2, 2}$ of the peaks for the

133

MIP-(Ph$_3$N)$_4$CoP film of the (Ph$_3$N)$_4$CoP : PPZ, 1 : 1 (mole : mole) ratio, after PPZ extraction, were slightly positively shifted with respect to those for the NIP-(Ph$_3$N)$_4$CoP (curves *3* and *4* in Fig. 4.2-6). The peaks for the GCE coated with the MIP-(Ph$_3$N)$_4$CoP film of the (Ph$_3$N)$_4$CoP : PPZ, 1 : 2 (mole : mole) ratio, were less positively shifted (curve *4* in Fig. 4.2-6).
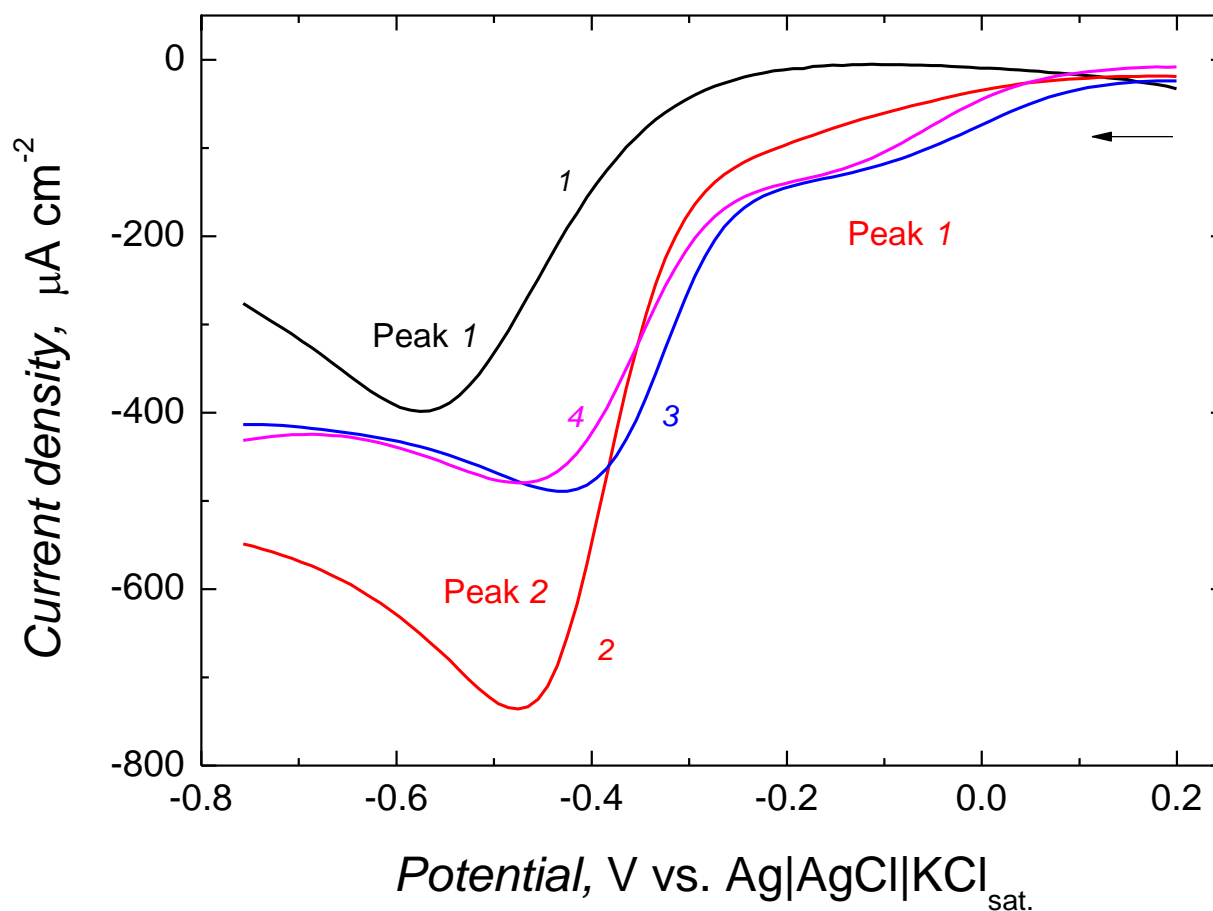
Figure 4.2-6. The LSV curves for (*1*) the bare 3-mm diameter disk GCE, and that coated with the film of (*2*) the NIP-(Ph$_3$N)$_4$CoP as well as that of (*3*) the MIP-(Ph$_3$N)$_4$CoP, of (Ph$_3$N)$_4$CoP : PPZ 1 : 1 ratio, after extraction of the PPZ template, and (*4*) the MIP-(Ph$_3$N)$_4$CoP, of the (Ph$_3$N)$_4$CoP 1 : 2 ratio, after extraction of the PPZ template using the working buffer solution (pH = 3.0) for 30 min. The dioxygen-saturated 0.04 M Britton-Robinson buffer (pH = 3.0) solution used was 0.3 M in Na$_2$SO$_4$. The potential scan rate was 0.1 V s^{-1}. The polymer films were deposited under potentiodynamic conditions, in the course of 10 potential cycles, in the range of 0 to 1.30 V with the potential scan rate of 0.1 V s^{-1} using the 0.1 mM (Ph$_3$N)$_4$CoP ODCB solution, which was 0.1 M (TBA)ClO$_4$.

134
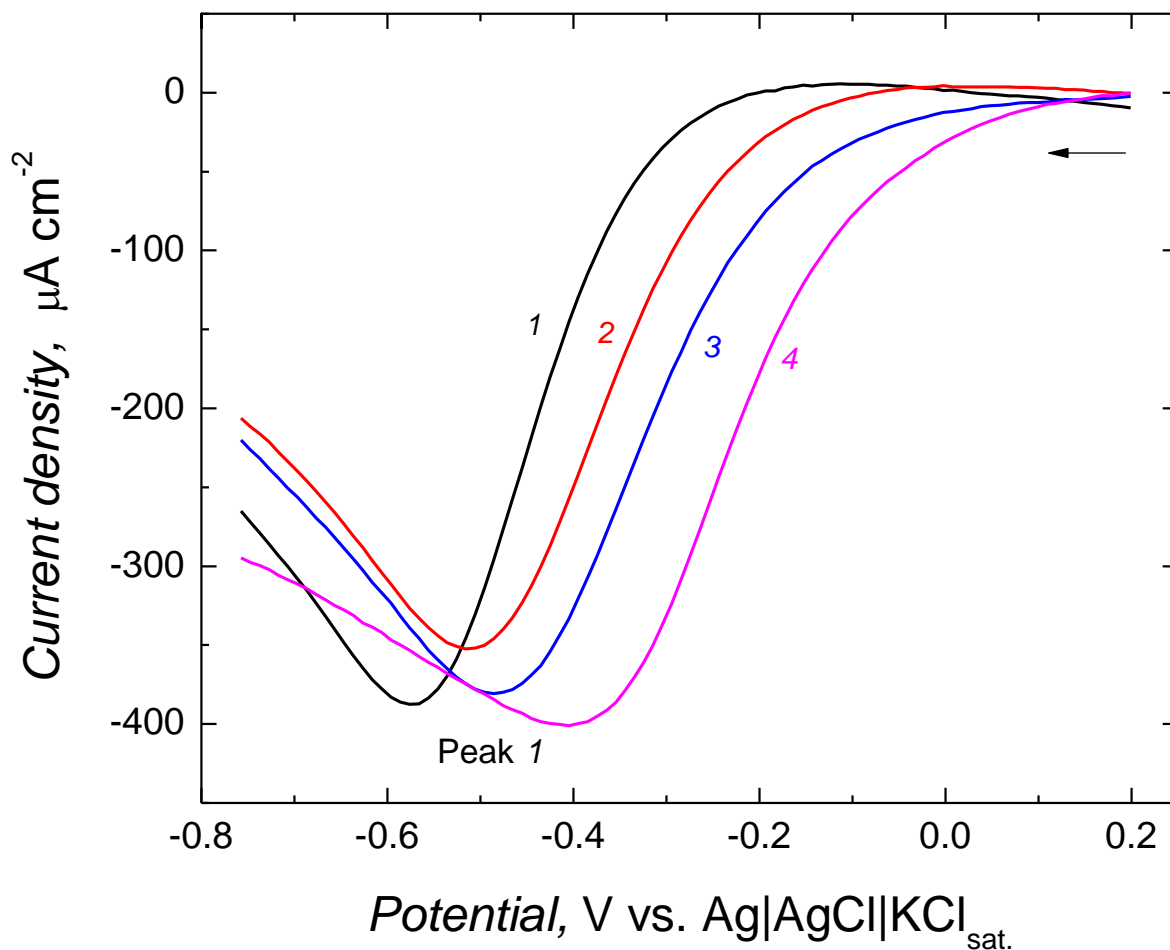
Figure 4.2-7. The LSV curves for (*1*) the bare 3-mm diameter disk GCE, and that coated with the film of (*2*) the NIP-(Ph₃N)₄CoP, (*3*) the MIP-(Ph₃N)₄CoP film of the (Ph₃N)₄CoP : PPZ, 1 : 1 (mole : mole) ratio after extraction of the PPZ and (*5*) the MIP-(Ph₃N)₄CoP of the (Ph₃N)₄CoP : PPZ, 1 : 2 (mole : mole) ratio after extraction of the PPZ template using the working solution (pH = 3.0) for 30 min. The dioxygen saturated 0.04 M Britton-Robinson buffer (pH = 3.0) used was 0.3 M in Na₂SO₄. The potential scan rate was 0.1 V s⁻¹. The polymer films were deposited by consecutive potentiostatic 1-ms pulses between the initial and final potential of $E_i = 0.0$ V and $E_f = 1.30$ V, respectively, for the 0.1 mM (Ph₃N)₄CoP ODCB solution, which was 0.3 M in (TBA)ClO₄.

Apparently, both the NIP and MIP films of (Ph₃N)₄CoP, deposited by electropolymerization under potentiodynamic conditions, catalyzed electroreduction of dioxygen to hydrogen peroxide, and then to water. However, cathodic peaks for the NIP-(Ph₃N)₄CoP and high current density of Peak *2* may indicate dioxygen electroreduction via two different mechanisms, simultaneously, that is, one involving one-step four-electron

135

electroreduction to water and the other involving two-step two-electron electroreduction with production of the H_2O_2 intermediate (curve *2* in Fig. 4.2-6). The most pronounced electrocatalytic effect towards dioxygen electroreduction to hydrogen peroxide was manifested by the positive shift of the $E'_{1/2,\,1}$ value by ~430 mV for the GCE coated with the $(Ph_3N)_4CoP$: PPZ, 1 : 1 (mole : mole) polymer film after extraction of the PPZ template.

The LSV curves of dioxygen reduction at the GCE coated with the $(Ph_3N)_4CoP$ polymer film, deposited by pulsed potentiostatic electropolymerization, with the background currents subtracted, are shown in Figure 4.2-7. Interestingly, only one cathodic peak was clearly developed, in contrast to the corresponding LSV curves for the polymer films deposited under the potentiodynamic electropolymerization conditions.

Table 4.2-1. Values of the dioxygen electroreduction half-peak potentials for the bare and $(Ph_3N)_4CoP$ polymer film coated GC electrodes.

Electrode	Cathodic half-peak potential, V vs. Ag/AgCl/KCl$_{sat.}$	
	$E'_{1/2,\,1}$	$E'_{1/2,\,2}$
Bare GCE	-0.43	-
Polymer films electropolymerized under potentiodynamic conditions		
GCE/[NIP-$(Ph_3N)_4CoP$ film]	-0.39	-
GCE/[MIP-$(Ph_3N)_4CoP$], $(Ph_3N)_4CoP$: PPZ, 1 : 1, after extraction of PPZ	+0.01	-0.32
GCE/[(MIP-$Ph_3N)_4CoP$], $(Ph_3N)_4CoP$: PPZ, 1 : 2, after extraction of PPZ	-0.05	-0.35
Polymer films electropolymerized by potentiostatic pulsing		
GCE/[NIP-$(Ph_3N)_4CoP$]	-0.35	-
GCE/[MIP-$(Ph_3N)_4CoP$], $(Ph_3N)_4CoP$: PPZ, 1 : 1,after extraction of PPZ	-0.26	-
GCE/[MIP-$(Ph_3N)_4CoP$], $(Ph_3N)_4CoP$: PPZ, 1 : 2, after extraction of PPZ	-0.22	-

The $E'_{1/2}$ value for the GCE coated with the NIP-(Ph$_3$N)$_4$CoP film deposited under pulsed potentiostatic conditions was ~ 20 mV less positively shifted than that deposited under potentiodynamic conditions (curve *2* in Fig. 4.2-7 and Table 4.2-1). The half-peak potentials for the MIP-(Ph$_3$N)$_4$CoP films were more positively shifted with respect to those for the MIP-(Ph$_3$N)$_4$CoP film deposited under potentiodynamic conditions, assuming that they corresponded to Peak *2* for the NIP and MIPs in Fig. 4.2-6. The GCE coated with the MIP-(Ph$_3$N)$_4$CoP film deposited under pulsed potentiostatic conditions revealed catalytic effect of dioxygen electroreduction manifested by the $E'_{1/2}$ positive shift with respect to that of the bare GCE. It was 170 and 210 mV for the (Ph$_3$N)$_4$CoP : PPZ film of the 1 : 1 and 1 : 2 (mole : mole) ratio, respectively (curves *3* and *4* in Fig. 4.2-7). That is, the MIP-(Ph$_3$N)$_4$CoP film of the (Ph$_3$N)$_4$CoP : PPZ, 1 : 2, (mole : mole) ratio revealed higher electrocatalytic activity than that for the MIP film with the 1 : 1 ratio.

4.2.6 Dioxygen electrocatalytic reduction at the (Ph$_3$N)$_4$CoP polymer film coated RRDE

In order to get closer insight into the mechanism of the dioxygen electroreduction, the LSV measurements at the RRDE were performed with either the NIP- or MIP-(Ph$_3$N)$_4$CoP film coated GCE disk and the bare Pt ring electrode using the Britton-Robinson buffer solution of pH = 3.0, which was 0.3 M in Na$_2$SO$_4$ (Fig. 4.2-8). The disk potential was negatively scanned while that of the ring was kept constant at 1.0 V.

The ring current for the NIP-(Ph$_3$N)$_4$CoP film reached maximum at the potential close to that of Peak *1* in the corresponding LSV curve at the GCE disk (curves *2* and *2'* in Fig. 4.2-8). Moreover, the ring current increased and reached plateau, which slowly decayed at lower potentials. This behavior indicates simultaneous dioxygen electroreduction via at least two different mechanisms. That is, dioxygen is electroreduced mostly via one-step four-electron mechanism to water at lower overpotentials. The H$_2$O$_2$ yield was 66.7 % at the first ring current maximum at $E' \approx$ -0.16. Then, this yield dropped to the value as low as 4.7% for potentials of the current plateau at the ring. The corresponding disk current was nearly twice that for the bare GCE. The major fraction of dioxygen was electroreduced via one-step for-electron mechanism.

137
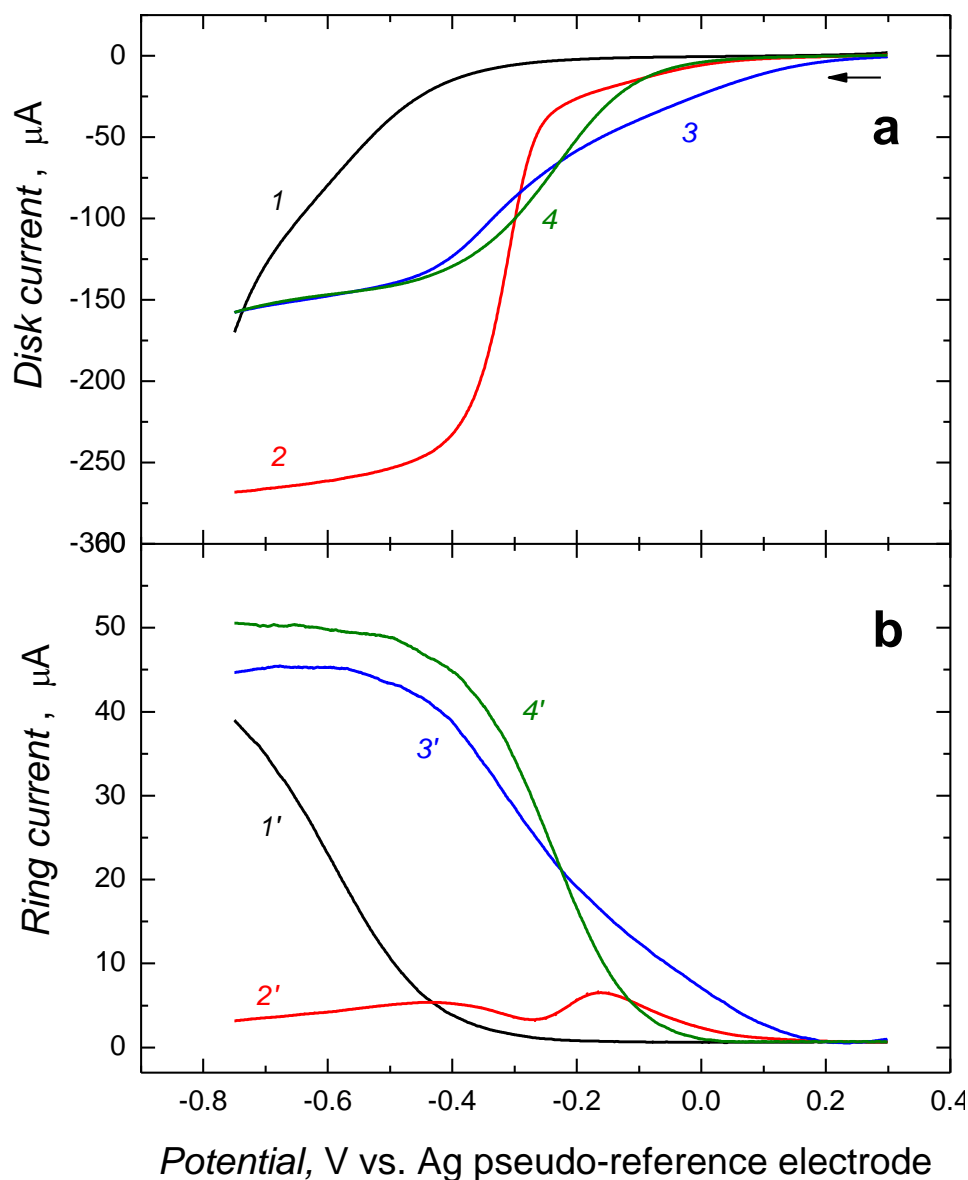
Figure 4.2-8 The LSV curves at the 4-mm diameter disk GCE and the Pt ring of the RRDE for the dioxygen electroreduction (*1* and *1'*) at the bare GCE, and that at the coated with (2 and 2') the NIP-$(Ph_3N)_4CoP$ film, the MIP-$(Ph_3N)_4CoP$ film of the $(Ph_3N)_4CoP$: PPZ, 1 : 1 (mole : mole) ratio, deposited under (*3* and *3'*) potentiodynamic and (*4* and *4'*) potentiodynamic conditions. The ring potential was 1.0 V. The 0.04 M Britton-Robinson buffer (pH = 3.0), 0.3 M in Na_2SO_4, was used. The potential scan rate was 10 mV s^{-1}. The rotation rate was 400 r.p.m.

The MIP-$(Ph_3N)_4CoP$ films of the 1 : 1 ratio, electropolymerized both under potentiodynamic (curves *3* and *3'* in Fig. 4.2-8) and pulsed potentiostatic (curves *4* and *4'* in

138

Fig. 4.2-8) conditions generated H_2O_2 on the disk electrode. The potential at which H_2O_2 was generated for both MIP-$(Ph_3N)_4CoP$ films was much more positive than that for the NIP-$(Ph_3N)_4CoP$ film. That is, these films electrocatalized dioxygen reduction to H_2O_2. Moreover, the ring current for the MIP-$(Ph_3N)_4CoP$ film deposited under potentiodynamic conditions revealed two slopes before reaching plateau. This behavior indicates two competing mechanisms for this electrocatalysis. Furthermore, there was no maximum in the ring currents for these MIPs. That is, the H_2O_2 generated was not reduced to water in this potential range.

4.2.6 Dioxygen electrocatalytic reduction at the NIP- and MIP-$(Ph_3N)_4CoP$ film coated GCEs in solutions of different pH

The mechanism of the dioxygen electroreduction at the $(Ph_3N)_4CoP$ polymer film-coated electrode depends on the solution acidity. That is, this electroreduction involves equal number of protons and electrons exchanged in acidic solutions while protons are not involved in this mechanism in neutral and alkaline solutions.

In order to understand this mechanism better, dependence of the cathodic half-peak potential of dioxygen electroreduction on pH was examined in a broad, $3.0 \leq pH \leq 10.0$, range using both the NIP- and MIP-$(Ph_3N)_4CoP$ films (Figure 4.2-9). The $E_{1/2}$ for the dioxygen electroreduction on the bare GCE is pH independent in the entire pH range.[158] Here, the $E'_{1/2}$ was ~ -0.49 V for the uncoated GCE. The electroreduction at the GCE coated with the NIP-$(Ph_3N)_4CoP$ film, deposited by electropolymerization under potentiodynamic conditions, revealed a single cathodic peak, with the $E'_{1/2}$ value of ~ -0.30 V. This $E'_{1/2}$ value was virtually independent of the solution pH (curve *1* in Fig. 4.2-9).

The film of MIP-$(Ph_3N)_4CoP$ of the $(Ph_3N)_4CoP : PPZ$, $1 : 1$ (mole : mole) ratio, deposited by electropolymerization under potentiodynamic conditions, showed two peaks in the whole pH range. That is, Peak *1*, was observed in the range of $3.0 \leq pH \leq 7.0$ with the negative slope of -46 mV/pH unit (curve *2* in Fig. 4.2-9). Peak *2* was observed in the entire pH range selected (curve *2'* in Fig. 4.2-9). The slope of the dependence of $E'_{1/2}$ on pH was +37 mV/pH unit, in the range of $3.0 \leq pH \leq 8.0$. At $pH \leq 8.0$, the $E'_{1/2}$ of Peak *2* did not change being -0.23 V. The film of the MIP-$(Ph_3N)_4CoP$ of the $(Ph_3N)_4CoP : PPZ$, $1 : 1$ (mole : mole) ratio, deposited by electropolymerization under pulsed potentiostatic conditions, revealed two peaks in the range of $4.0 \leq pH \leq 10.0$. The slope of the $E'_{1/2}$ for

139

Peak *1* dependence on pH was ~ -9 mV (curve *3* in Fig. 4.2-9), while that for Peak *2* merely changed (curve *3'* in Fig. 4.2-9).

Finally, the GCE coated with the MIP-(Ph₃N)₄CoP of the (Ph₃N)₄CoP : PPZ, 1 : 2 (mole : mole) ratio, deposited by electropolymerization under potentiodynamic conditions, revealed two peaks for the whole pH range with the exception of pH = 5.0 where, surprisingly, three peaks were observed.
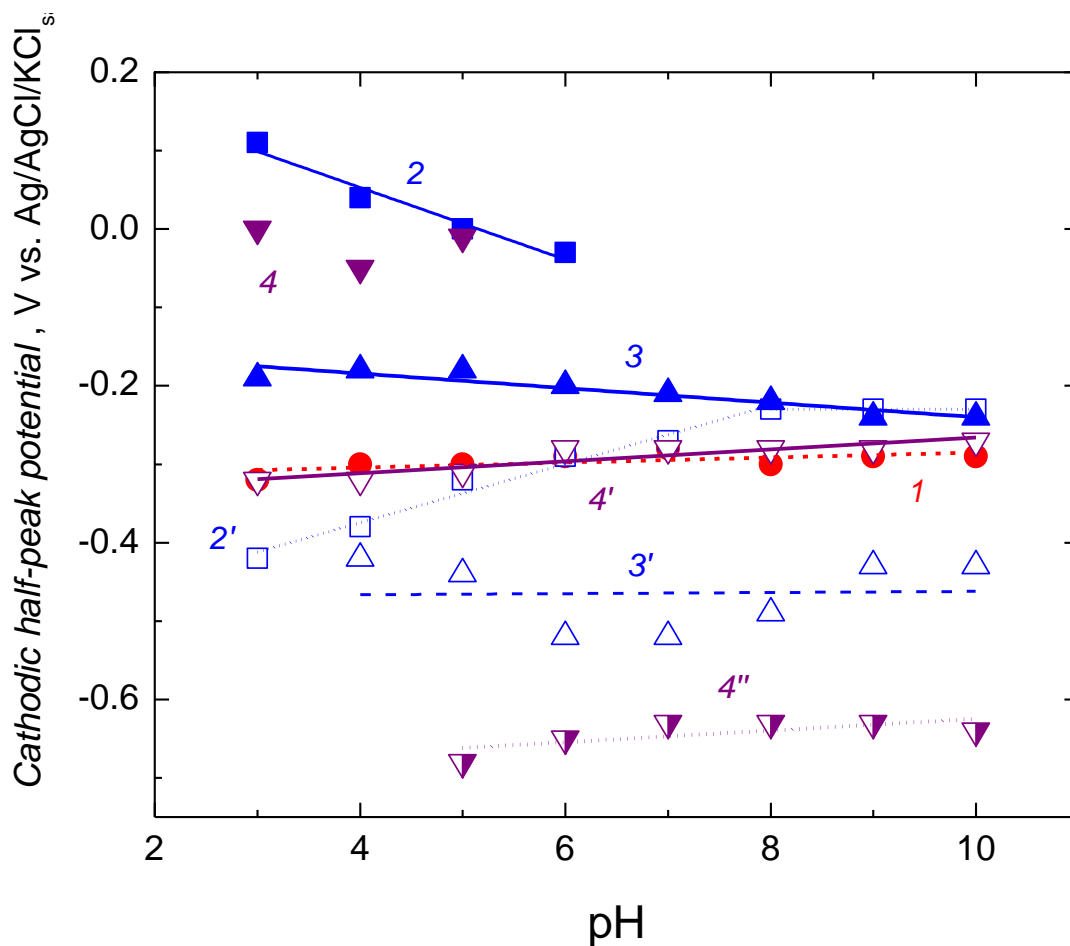
Figure 4.2-9 The pH dependence of the LSV cathodic half-peak potential of the dioxygen electroreduction at the GCE coated with (*1*) the NIP-(Ph₃N)₄CoP or with the MIP-(Ph₃N)₄CoP film of the (Ph₃N)₄CoP : PPZ, 1 : 1 (mole : mole) ratio, deposited by electropolymerization under potentiodynamic conditions (*2*) Peak *1* and (*2'*) Peak *2*, and that, deposited by electropolymerization under pulsed potentiostatic conditions, (*3*) Peak *1*, and (*3'*) Peak *2*; the MIP-(Ph₃N)₄CoP film, of the (Ph₃N)₄CoP : PPZ, 1 : 2 (mole : mole) ratio, deposited by electropolymerization under potentiodynamic conditions, (*4*) Peak *1*, (*4'*) Peak *2*, and (*4''*) Peak *3*. The solution used was 0.04 M Britton-Robinson buffer, which was 0.3 M in Na₂SO₄.

140

Peak *1* was observed for the range of $3.0 \leq pH \leq 5.0$. It decreased with the pH increase (curve *4* in Fig. 4.2-9). Peak *2* was observed for the $3.0 \leq pH \leq 10.0$ range with its $E'_{1/2}$ hardly changed, being ~ -0.3 V (curve *4'* in Fig. 4.2-9). Peak *3* was seen for the $5.0 \leq pH \leq 10.0$ range. It increased with the pH increase (curve *4''* in Fig. 4.2-9).

Considering all the results, one can conclude that the mechanism of the dioxygen electrocatalytic reduction depends on the type of the $(Ph_3N)_4CoP$ polymer. Clearly, this mechanism was different for the NIP-$(Ph_3N)_4CoP$, which revealed a pH independent single cathodic peak. Apparently, this peak corresponded to electrocatalytic reduction of dioxygen to hydrogen peroxide. The MIP-$(Ph_3N)_4CoP$ film of the $(Ph_3N)_4CoP$: PPZ, 1 : 1 (mole : mole) ratio, deposited by electropolymerization under potentiodynamic conditions, revealed the electrocatalytic effect both for the dioxygen and hydrogen peroxide reduction; the first being depressed but the second enhanced with the pH increase. The MIP-$(Ph_3N)_4CoP$ film of the $(Ph_3N)_4CoP$: PPZ, 1 : 1 (mole : mole) ratio, deposited under pulsed potentiostatic conditions, catalyzed both the dioxygen and hydrogen peroxide electroreduction with the $E'_{1/2}$ only slightly depending on the solution pH. Finally, the MIP-$(Ph_3N)_4CoP$ of the $(Ph_3N)_4CoP$: PPZ, 1 : 2 (mole : mole) ratio, deposited under potentiodynamic conditions, electrocatalized dioxygen and hydrogen peroxide reduction in acidic media. However, the catalytic effect was lower in solutions of lower acidity. Unexpectedly, the NIP-$(Ph_3N)_4CoP$ revealed more pronounced electrocatalytic effect than MIP-$(Ph_3N)_4CoP$, however, the latter electrocatalized dioxygen electroreduction to H_2O_2 at higher potentials.

4.3 Conducting composites of carbon nanotubes and a redox polymer

CNTs and C_{60} are often used for preparation of composites serving as functional materials for supercapacitors. Among them, a (conducting polymer)-(CNTs) composite is used because of high specific capacitance of the resulting electrode material.[85,159,160] We addressed several aspects of this way of composite preparation in the present research. First, SWCNTs were non-covalently modified with 1-pyrenebutyric acid via π-π stacking. This modification allowed for electrophoretic deposition of a uniform pyr-SWCNTs film on an electrode surface. Redox species, like pristine C_{60}, cannot be much attractive for the Type III symmetric supercapacitors because it is not conducting at positive potentials. Therefore, some another redox material must be additionally used for that (Scheme 4.3-1). This point is addressed herein by selecting a monomer, which is electroactive in both the positive and negative potential range (Fig. 4.3-1).

a   **b**
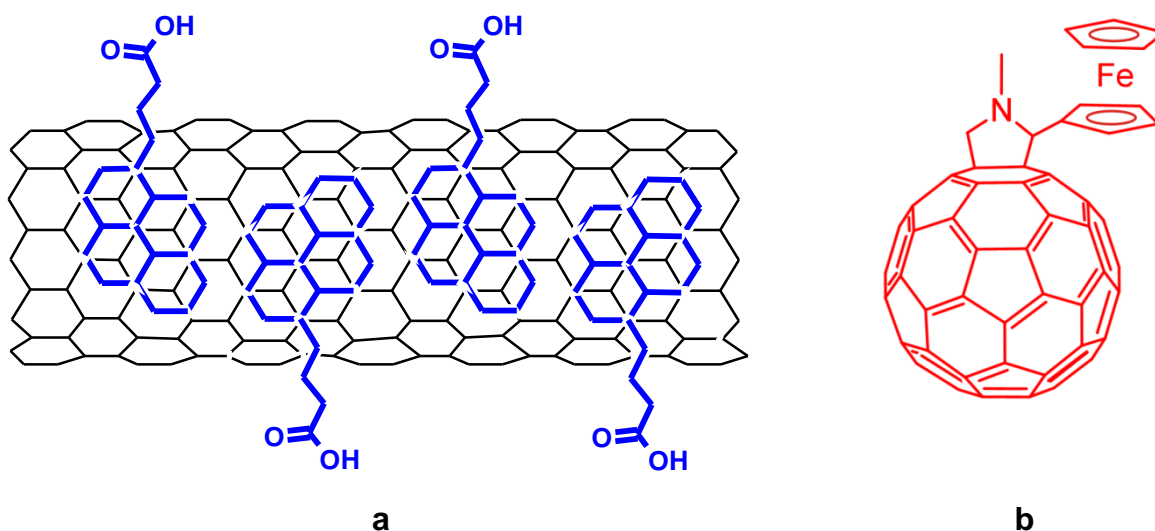
Scheme 4.3-1. The simplified structural formula of (a) metallic single-wall carbon nanotube non-covalently surface modified with 1-pyrenebutyric acid (pyr-SWCNTs) and (b) C_{60}Fc.

     This C_{60}Fc monomer was electropolymerized on top of the deposited pyr-SWCNTs film. Electropolymerization as well as electrochemical and capacitive properties of the resulting electrode material were examined elsewhere.[161]

142
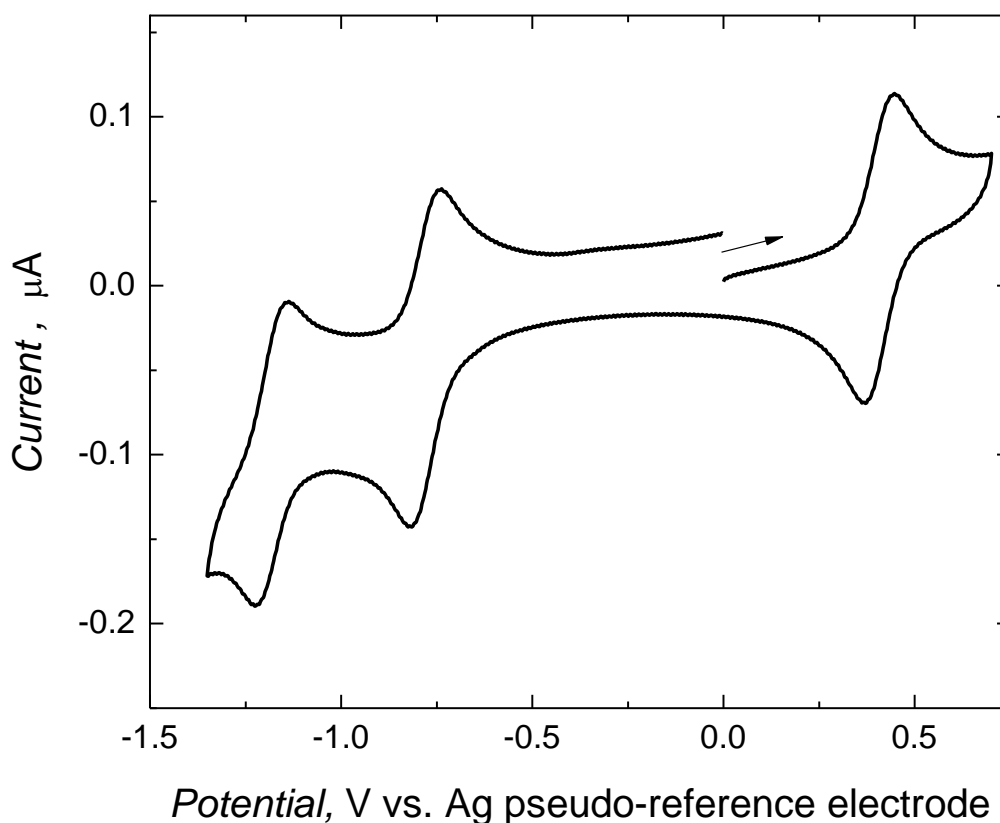
Figure 4.3-1. The CV curve for 0.1 mM $C_{60}Fc$ in the deaerated 0.1 M $(TBA)ClO_4$ ODCB solution recorded at the 1-mm diameter Pt disk working electrode. The potential scan rate was 100 mV s^{-1}.

Our research was focused on optimization of electrophoretic deposition of the pyr-SWCNTs film as well as on the power and electrochemical stability determination of the composite, in a two-electrode system, by galvanostatic charging and discharging. The cell power was determined by discharging of the capacitor through different resistors.

First, the pyr-SWCNTs film was electrophoretically deposited using different procedures until the optimized electrophoretic deposition procedure was reached. Then, $C_{60}Fc$ was electropolymerized in the presence of $Pd(Ac)_2$ and the resulting polymer deposited on top of the pyr-SWCNTs film. Next, a device composed of two identical Au disk electrodes coated with pyr-SWCNTs/($C_{60}Fc$-Pd) films was assembled (Fig. 2.3-16). Electrochemical stability of the pyr-SWCNTs/($C_{60}Fc$-Pd) films in galvanostatic charge-discharge experiments was evaluated for different operation modes of the device. Finally, power of the fully or partially charged device was determined.

143

4.3.1 Electrophoretic deposition of pyr-SWCNTs

There are several procedures for preparation of the CNT-modified electrodes. One of the simplest consists in dropcasting of a fine suspension of CNTs in a volatile solvent, and then evaporating the solvent. The disadvantages of this procedure include non-uniformity of the resulting film, aggregation of CNTs, and a challenging need of a precise control of the CNTs mass deposited on the electrode. Therefore, other deposition procedures, which are free of these disadvantages, are desired. The electrophoretic CNTs deposition is one of them. It involves preliminary surface functionalization of CNTs with charged molecules. This procedure allows for energy-efficient reusing the solvent after deposition of SWCNTs instead of its evaporating.

Herein, two apparatus setups were used for electrophoretic deposition of SWCNTs. One, involving EQCM, appeared to be challenging because of low adherence of the resulting pyr-SWCNTs film to the Au-over-Ti or Pt electrode of QCR. In order to measure the resonance frequency changes accompanying the deposition, the film must be relatively rigid. For that, the film must be deposited very thoroughly. Moreover, mass of the deposited SWCNTs film may not accurately be determined because the film is swollen with the solvent. Therefore, another procedure was developed herein for precise weighing of the deposited pyr-SWCNTs film.

The other setup allowed for a long-lasting measurement of the resonance frequency, f, and dynamic resistance, R. A general idea behind the experiment was to determine changes with time of real mass of the deposited film by continuous f measurement starting from the bare and dry, and finishing with the rinsed, and then well-dried film-coated electrode. Accordingly, the measurement was initiated with a dry Pt electrode of QCR in air (time point *0* and *0'* in Fig. 4.3-3). Then, a sample of 0.25 ml of the fine ~0.4 mg ml^{-1} pyr-SWCNTs suspension in CHP was dispensed onto the horizontally oriented QCR (time point *1* and *1'* in Fig. 4.3-3) resulting in the $\Delta f \cong$ -10.3 kHz drop due to viscosity and/or density change of the medium. Then, the pyr-SWCNTs film was electrophoretically deposited on the electrode from this suspension (time points *2*, *2'* and *3*, *3'* in Fig. 4.3-3). In the presence of excess of (TBA)OH $\times$ 20 H$_2$O in the suspension, the film deposition was drastically faster due to deprotonation of carboxy groups of 1-pyrenebutyric acid π-π stacked on SWCNTs surface at pH > 7.0 and the increase of the negative surface charge of pyr-SWCNTs. A non-transparent black solid was deposited on the electrode (Fig. 4.3-4) while the initially cloudy suspension

144

became transparent. During film formation, the frequency change, $\Delta f \cong$ -683 Hz, was unexpectedly low. The reason for that might arise from soaking with viscous CHP of the resulting film and forming a solvent layer between the electrode substrate and the film, thus deteriorating mechanical contact between the electrode and the film. Next, the CHP solvent was carefully aspirated with a pipette from above the film (time point *4* and *4'* in Fig. 4.3-3). Then, the film was several times thoroughly rinsed with ACN (time point *5* and *5'* in Fig. 4.3-3). Each time, the solvent was aspirated, and then replaced with that fresh. The CHP solvent used for preparation of the suspension was miscible with ACN. Finally, the film was exposed to a mild Ar stream overnight (time points *6* and *6'* in Fig. 4.3-3).
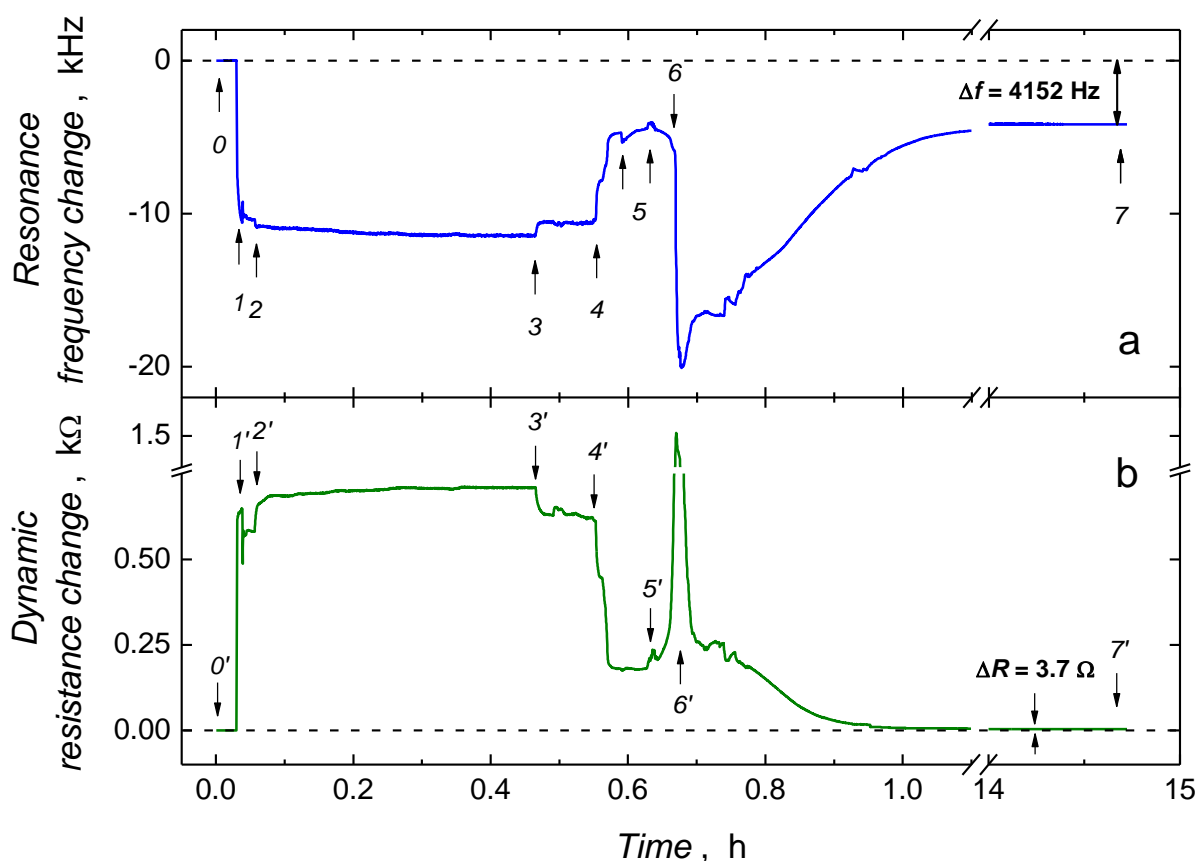
Figure 4.3-2. The simultaneously recorded change with time of (a) resonance frequency and (b) dynamic resistance for (*0* and *0'*) the dry electrode in air, (*1* and *1'*) after dispensing the ~0.4 mg ml^{-1} suspension of pyr-SWCNTs in CHP, (*2* and *2'*) after initiating electrophoretic deposition of pyr-SWCNTs; for that, the Pt/QCR working electrode was positively polarized with the 24 V dc voltage, (*3* and *3'*) after finishing electrophoretic deposition of pyr-SWCNTs, (*4* and *4'*) after solvent aspiration, (*5* and *5'*) after rinsing the pyr-SWCNTs film with ACN, (*6* and *6'*) after a gentle argon purge over the film, and (*7* and *7'*) the final measurement.

145

The initial frequency decrease at this step was most likely due to pressing the electrode with the Ar stream. Over the first 45 min of this step, the resonance frequency rapidly increased by ~12 kHz due to solvent evaporation. Moreover, the frequency increased by ~430 Hz for subsequent ~13.5 h because of that. The total frequency change for the initial stage of the bare dry electrode and that for the final stage of the electrode preparation was $\Delta f = 4152$ Hz resulting in a well-dried pyr-SWCNTs film.

The dynamic resistance change (Fig. 4.3-3b) mirrored the resonance frequency change (Fig. 4.3-3a) over the entire measurement. At the end of the experiment, its total change was merely 3.5 Ω, indicating formation of a quite rigid film.
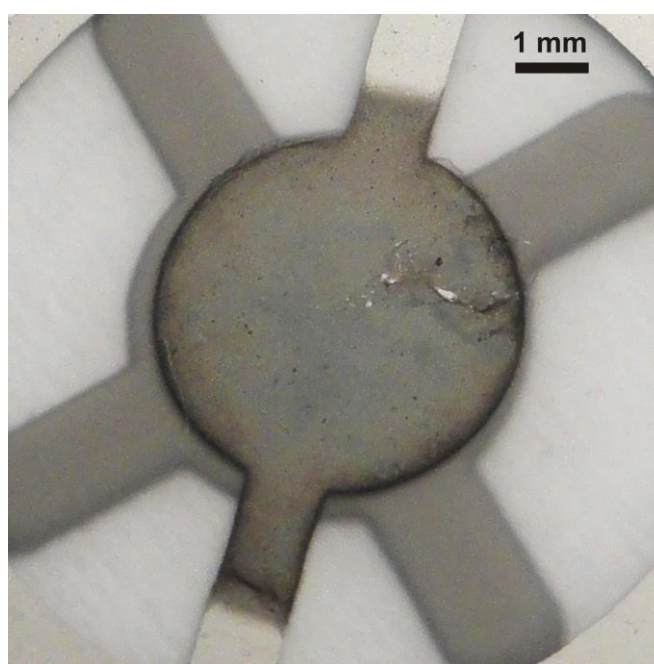
Figure 4.3-3. The photo of a pyr-SWCNTs film electrophoretically deposited on the Pt/QCR. (This film was not used for the measurement discussed above.)

The resulting mass was determined precisely because only traces of solvent were left in the film. Assuming that deposition of the pyr-SWCNTs from the suspension during electrophoresis was complete, one can determine concentration of the suspension and use this value for quantitation of mass of the films deposited onto regular disk electrodes. The time stability of the 0.4 mg ml^{-1} pyr-SWCNTs suspension in CHP exceeds one year.

146

4.3.2 Galvanostatic charging and discharging of the energy storage device featuring two identical pyr-SWCNTs/C$_{60}$Fc-Pd composite electrodes

The use of the pyr-SWCNTs/(C$_{60}$Fc-Pd) composite electroactive in both the positive and negative potential range allowed us to change the electrode polarity in the assembled charge storage device by alternate charging it with current of opposite direction. This ability was studied in the galvanostatic charge-discharge regime of the assembled device, according to the procedure outlined in Fig. 3.2-15.

WE1 pyr-SWCNTs – charged positively, C$_{60}$Fc$^+$-Pd

WE2 pyr-SWCNTs – charged negatively, C$_{60}$$^-$Fc-Pd

Charging-discharging cycle

WE1 and WE2: (4-mm Au disk)/pyr-SWCNTs/ C$_{60}$Fc-Pd
Deaerated 0.1 M (TBA)ClO$_4$ in CH$_3$CN

At zero charge:
WE1 pyr-SWCNTs – no charge, C$_{60}$Fc-Pd
WE2 pyr-SWCNTs – no charge, C$_{60}$Fc-Pd

Opposite polarity charging-discharging cycle

WE1 pyr-SWCNTs – charged negatively, C$_{60}$$^-$Fc-Pd

WE2 pyr-SWCNTs – charged positively, C$_{60}$Fc$^+$-Pd

Scheme 4.3-3. The voltage-time galvanostatic (40 μA cm^{-2}) plot for two identical pyr-SWCNTs/C$_{60}$Fc-Pd working electrodes WE1 and WE2, arranged as shown in Scheme 3.2-2, demonstrating oxidation states of each electrode under different polarization conditions.

147

The repetitive alternate galvanostatic +0.72- and -0.72-mA cm^{-2} polarization was applied to the cell until it reached the predefined voltage limit where the current direction was turned back. The resulting voltage-time transients were recorded for different voltage limits (Fig. 4.3-4). Two sets of the voltage limit were selected. The "narrow" limit was set between +0.6 and -0.6 V allowing for only double-layer charging and discharging in the absence of any faradaic process. The resulting voltage-time transients were nearly linear and repeatable (curves *1* and *1′* in Fig. 4.3-4).
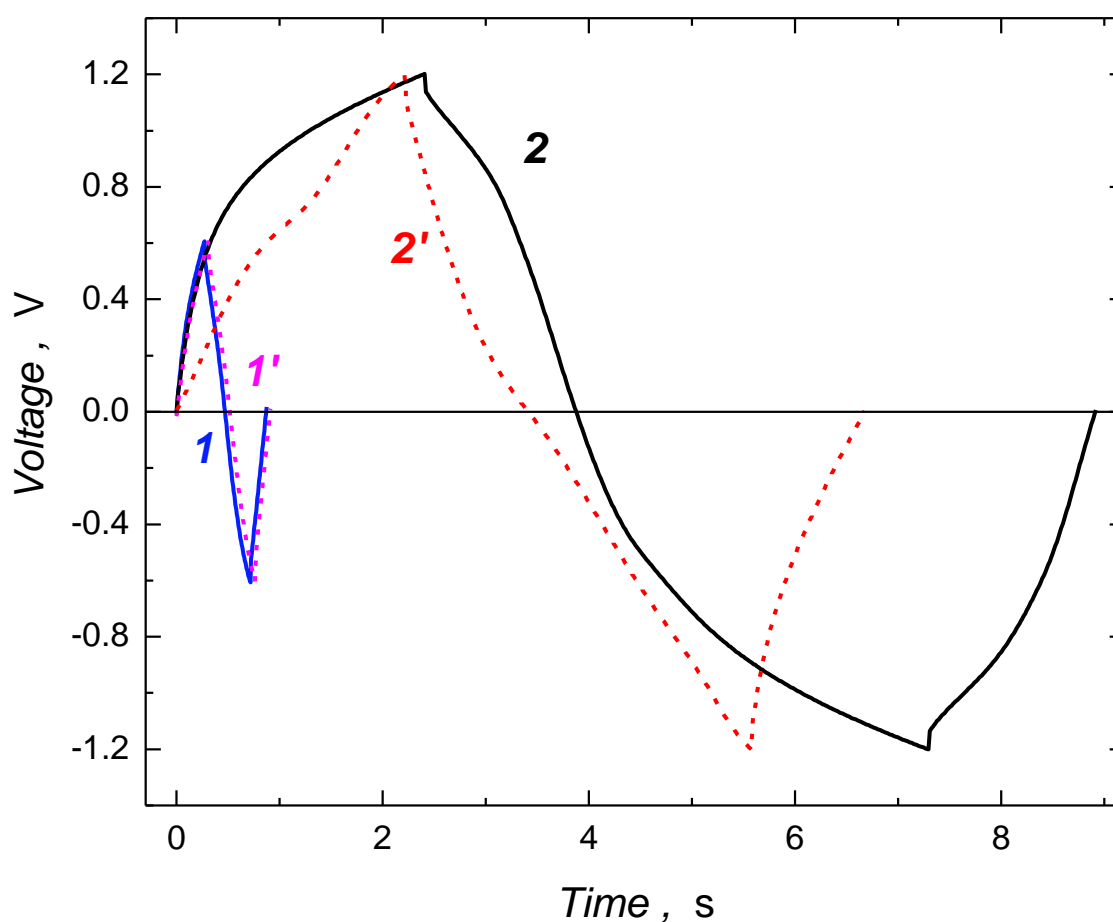
Figure 4.3-4. Voltage-time transients for alternate galvanostatic +0.72-mA cm^{-2}, and then -0.72-mA cm^{-2} polarization followed by +0.72-mA cm^{-2} polarization for (*1* and *2*) the first and (*1′* and *2′*) the 1000th charge-discharge cycle (see Scheme 4.3-3) for two identical (4-mm diameter Au disk)/pyr-SWCNTs/C$_{60}$Fc-Pd working electrodes WE1 and WE2 (Scheme 3.2-2) for the voltage range between (*1* and *1′*) +0.60 and -0.60 V as well as (*2* and *2′*) +1.2 and -1.2 V. A deaerated 0.1 M (TBA)ClO$_4$ acetonitrile solution served as the working solution.

148

The "wide" voltage range was set between +1.2 and -1.2 V. It allowed for both double layer charging and discharging as well as for the C_{60}^0/C_{60}^- and Fc^0/Fc^+ redox processes occuring. The initial part of the charging curve overlapped that for the "narrow" voltage range. The slope of the former curve decreased, however, with the voltage increase due to the redox processes manifested. For positive charging, the Fc/Fc^+ and C_{60}/C_{60}^- electrode processes proceeded on WE1 and WE2, respectively. The opposite charging resulted in the C_{60}/C_{60}^- and Fc/Fc^+ processes on WE1 and WE2, respectively (Scheme 4.3-3). For the "wide" voltage range, the capacity repeatability in the charge-discharge cycling was not as high as that for the "narrow" range. Some irreversible polymer changes might be responsible for that. The resulting initial voltage-time transient (curve *2* in Fig. 4.3-4) substantially changed after 1000 charge-discharge cycles (curve *2'* in Fig. 4.3-4).
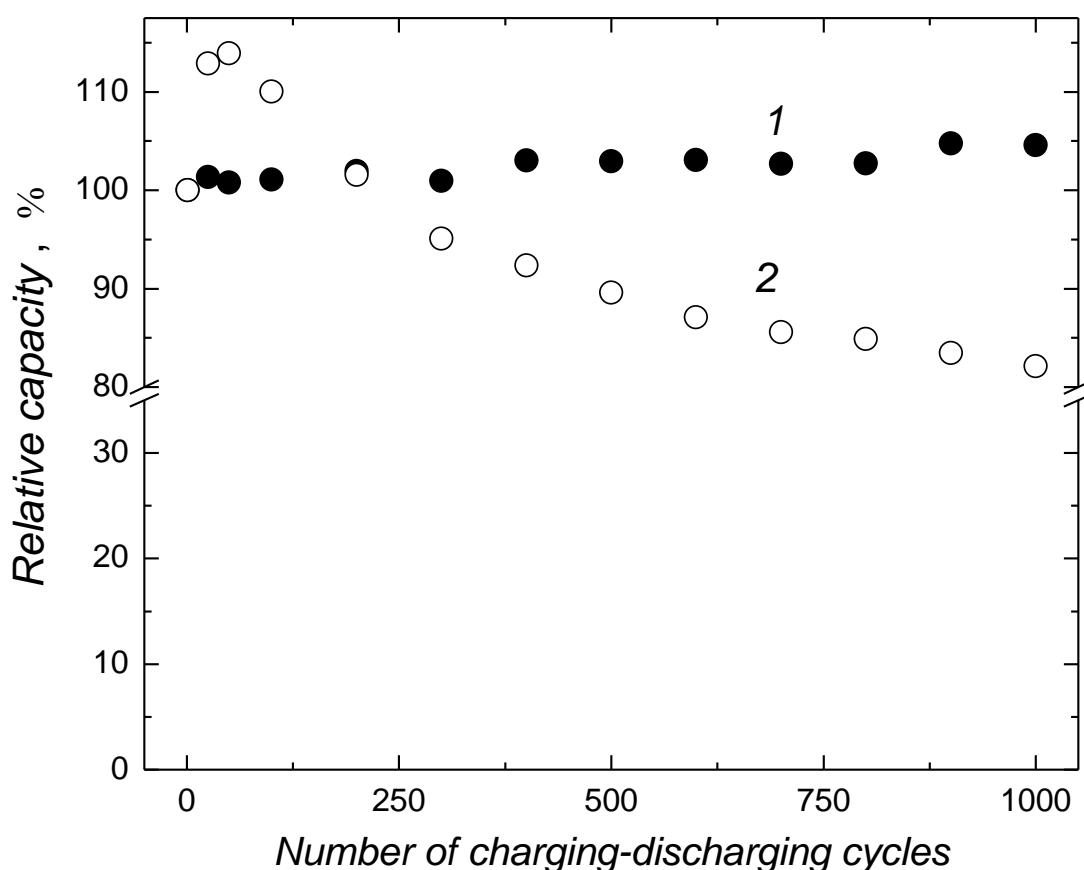
Figure 4.3-5. The dependence of relative capacity on the number of charging-discharging cycles for two identical (4-mm diameter Au disk)/pyr-SWCNTs/C_{60}Fc-Pd working electrodes WE1 and WE2 (Scheme 4.3-2) under repeated galvanostatic alternate +0.72-mA cm^{-2} and -0.72-mA cm^{-2} polarization within the voltage limits of (*1*) +0.60 and -0.6 V as well as (*2*) +1.2 and -1.2 V. A deaerated 0.1 M (TBA)ClO$_4$ acetonitrile solution served as the working solution.

149

The relative capacity of the device exposed to repetitive alternate galvanostatic charging and discharging in the "narrow" voltage range between +0.6 and -0.6 V was nearly constant. Moreover, it evenly increased by ~5% after 1000 cycles (curve *1* in Fig. 4.3-5). The "wide" voltage range, set between +1.2 and -1.2 V, allowed for the occurrence of both the capacitive and faradaic behavior of the composite. After initial increase by ~15%, the relative capacity decreased by ~18% after 1000 cycles (curve *2* in Fig. 4.3-5). The apparent reason for this decrease may arise from incomplete reversibility of the redox processes.

4.3.3 Measurements of power of the two-electrode energy storage device with identical pyr-SWCNTs/C_{60}Fc-Pd composite electrodes

In order to evaluate power capabilities for two different states of the device, i.e., "fully charged" and "partially charged", the average power of the device was determined for different discharge currents (Fig. 4.3-6).
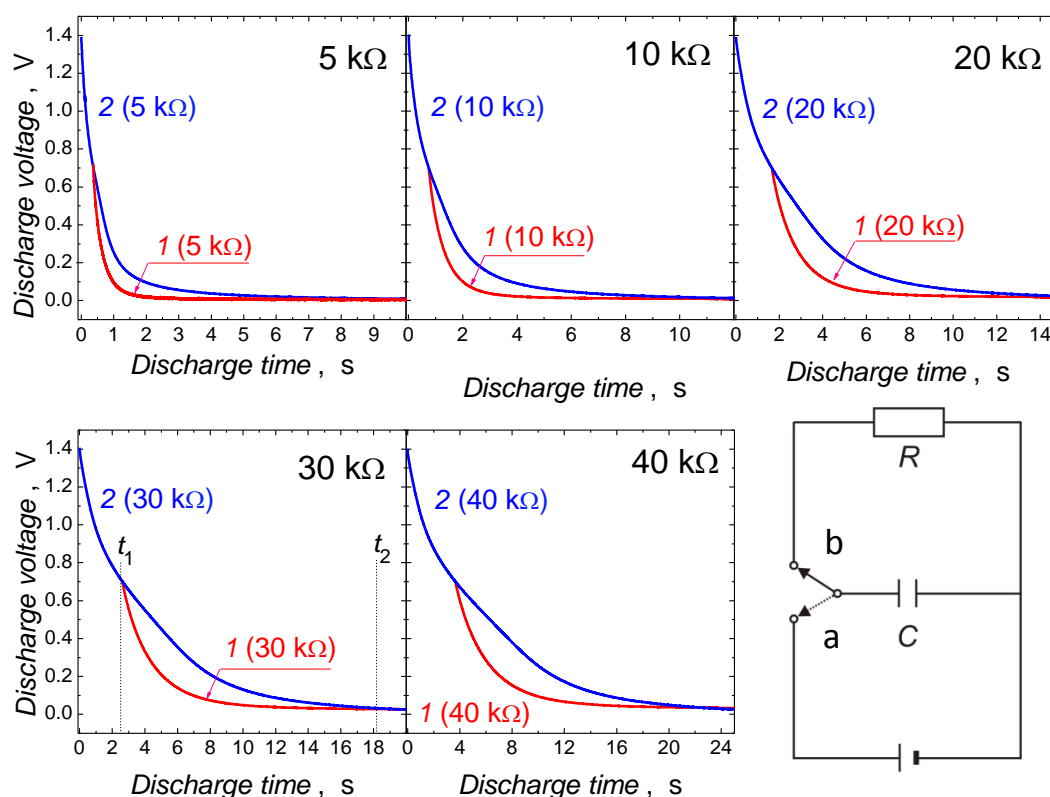
Figure 4.3-6. Voltage decay with time for discharging, through different resistors indicated with numbers at curves, of the two-electrode charge storage device (see Scheme 3.2-2), which was charged with the current density of 40 μA cm^{-2} to either (curve *1*) 0.7 V or (curve *2*) 1.4 V and the electric circuit scheme used for switching between (a) charging and (b) discharging of the device.

150

This evaluation provided information on power characteristics of an electric storage device in closer approximation to a real life situation. Our device was charged with the current density of 40 μA cm^{-2} to reach either "partially charged" (0.70 V) or "fully charged" (1.40 V) state.
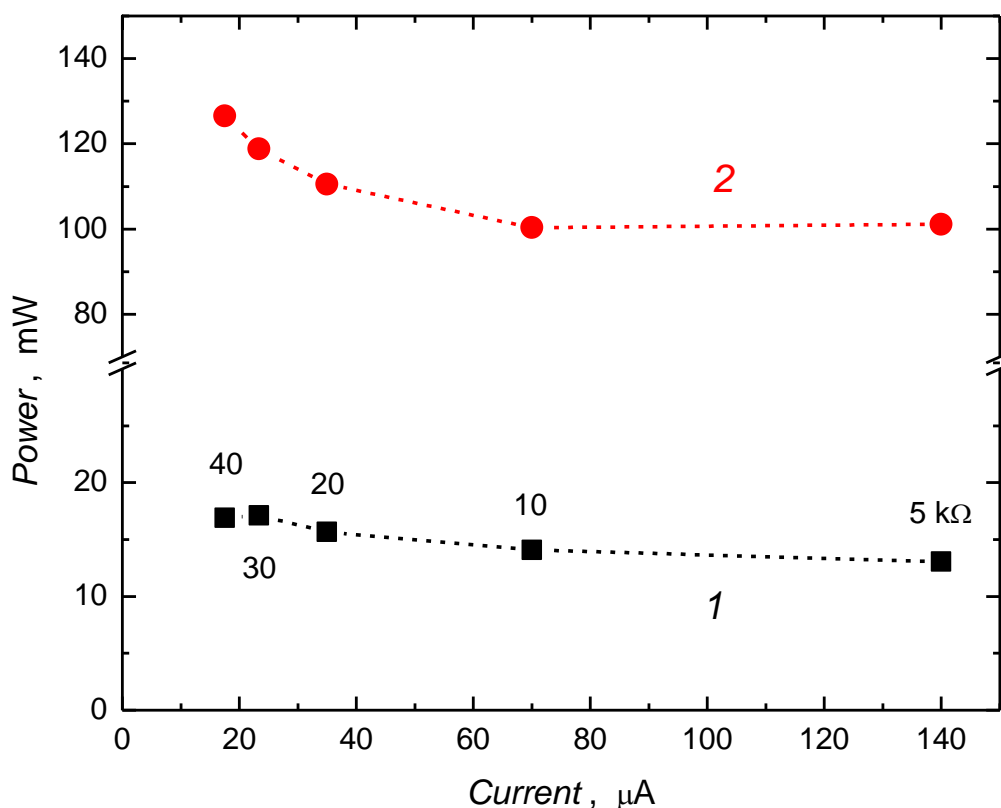
Figure 4.3-7. The power vs. discharge current curves for two identical (4-mm diameter Au disk)/pyr-SWCNTs/(C$_{60}$Fc-Pd) working electrodes WE1 and WE2 (Scheme 4.3-2), charged with the current density of 40 μA cm^{-2} to reach the voltage of (*1*) 0.70 and (*2*) 1.40 V. A deaerated 0.1 M (TBA)ClO$_4$ acetonitrile solution served as the working solution. Resistances of the resistors used for electrode discharging are indicated with numbers at each current value.

Next, the device was discharged through the resistor of the 5, 10, 20, 30, or 40 kΩ resistance and the voltage vs. time curves were recorded. Finally, the average power was determined using Eqn. 2.4-6.

Device charging, which involved faradaic Fc/Fc$^+$ and C$_{60}$$^-$/C$_{60}$ processes occurring in the pyr-SWCNTs/(C$_{60}$Fc-Pd) film, significantly increased average power because of the increase of the charge stored in the composite. Moreover, higher voltage increased the

151

average power even more. The average power of the "fully charged" device was by ~7.3 times higher than that "partially charged" despite that the voltage was just twice higher (Fig. 4.3-7). Unfortunately, charging of the composite to the higher voltage decreased its operation lifetime.

The average power at the lower discharge rate was slightly higher for both the "fully charged" and "partially charged" device (curves *1* and *2* in Fig. 4.3-7, respectively). A limiting effect of the counter ion diffusion in the film might be a plausible reason for that.

5. Conclusions

5.1 Organic electron donor-acceptor systems for photovoltaic solar energy conversion

❖ Three different approaches to supramolecular assembling of electron donor-acceptor dyads were explored, including (i) Watson-Crick nucleobase paring in a Langmuir film, (ii) metal-ligand coordination of monomer molecules in solution, and (iii) metal-ligand coordination of the polymer donor and the monomer acceptor molecules. Metal-ligand coordination of moieties in solution or in a polymer film was the most promising for that purpose while hydrogen bonding of the donor and acceptor moiety in a Langmuir film was weak.

❖ Two photoactive materials were examined. One involved separation of dyad molecules in the Langmuir and Langmuir-Blodgett films by flexible peripheral substituents of donor moieties while the other involved, first, linking donor moieties by electropolymerization, and then coordinating acceptor molecules by the donor polymer film. The latter approach, with the $[(Ph_3N)_4ZnP$ polymer electron donor]-$(C_{60}im$ acceptor) dyad, was more efficient with respect to solar energy conversion.

❖ The constructed dyads were non-stoichiometric. That is, the LB transferred dyads partially dissociated during the LB transfer while in the $(Ph_3N)_4ZnP$ polymer not all Zn atoms were accessible for $C_{60}im$ binding.

5.2 Template-imprinted polymer films of $(Ph_3N)_4CoP$ for electrocatalytic dioxygen reduction

❖ The NIP-$(Ph_3N)_4CoP$ film catalyzed dioxygen electroreduction via two competing mechanisms. One resulted in production of H_2O_2, while the second, dominating at lower potentials, was mostly one-step four-electron electroreduction dioxygen to water. The LSV half-peak potential of that process was pH independent.

❖ Presumably, this unexpected behavior was due to presence of bulky triphenylamine peripheral substituents, which allowed to assume the Co-to-Co distance optimal for one-step four-electron dioxygen electroreduction. The face-to-face arrangement of the Co porphyrin macrocycles in the working solution for polymerization could be due to π-π interactions of perpendicular orientation of peripheral triphenylamine substituents to the porphyrin macrocycle plane.

153

❖ The MIP-$(Ph_3N)_4CoP$ film catalyzed electroreduction of dioxygen to water. Most likely, the piperazine templating ligand used was too big for proper distancing Co atoms in the film.

❖ The mechanism of dioxygen electrocatalytic reduction by MIP-$(Ph_3N)_4CoP$ films was dependent not only on pH and the $(Ph_3N)_4CoP$: PPZ ratio but on the polymer preparation procedure and, hence, the film morphology as well.

5.3 Conducting composites of carbon nanotubes and the C_{60}Fc-Pd redox polymer for energy storage devices

❖ The herein developed procedure of electrophoretic deposition of carbon nanotubes was, advantageously, more precise and easier to use than that applied earlier.

❖ Stability of the pyr-SWCNTs/$(C_{60}$Fc-Pd) composite in the multi(charging-discharging) experiment was evaluated for two different voltage ranges. One, narrow (0.60 V), covered only the double-layer capacity range while the other, broader (1.20 V), included the pseudocapacity range of the polymer redox processes. Relative capacity of the energy storage device increased by 5% after 1000 cycles of charging and discharging for the double-layer capacity range.   The wide voltage range encompassed both the C_{60}/C_{60}^- and Fc/Fc$^+$ faradaic process.   Because of that, advantageously, the voltage-time transients were nonlinear. Advantageously, the relative capacity decreased merely by 18% after 1000 cycles.

❖ Power of the fully and partially charged energy storage device, composed of two identical electrodes coated with the pyr-SWCNTs/$(C_{60}$Fc-Pd) films, was measured. For that, the electrodes were polarized to 1.4 V, and 0.70 V, respectively. The average power of the device polarized to the higher voltage was $\sim$7.3 times that polarized to the lower voltage.

154

6. Proposed further research

6.1 Organic photovoltaics

In order to increase performance of the OPV materials and bring them closer to a possible commercial application, I propose the following topics of further research, which will target the overall efficiency increase of the PVC by enhancing all steps of solar light conversion mechanism, extending the lifetime of the PVC, and withstanding real outdoor temperatures. These will require the following studies.

- ❖ Devising and preparing photoactive donor-acceptor materials of increased efficiency.
- ❖ Devising and preparing macro-structure organized photoactive materials of increased area contacting an electrolyte.
- ❖ Employing low volatility solvents with a broad range of operating temperature.
- ❖ Using efficient charge mediators capable of surviving billions redox cycles.

6.2 Metalloporphyrins for electrocatalytic dioxygen reduction

In order to increase electrocatalytic activity of metalloporphyrins towards dioxygen electroreduction, the dimers should be more strongly coordinated to maintain their structure during surface immobilization and subsequent operation. Functional properties of the polymer can be improved by depositing the polymer on a structured conducting substrate or preparing linear polymer wires. Towards that, the following activity is needed.

- ❖ Increasing control over formation of cofacial metalloporphyrin dimers through syntheses of new dedicated monomers.
- ❖ Depositing films of catalysts on surface-developed conducting substrates or producing such structures by synthesizing appropriate polymers.

6.3 Functional (conducting polymer)-(carbon material) composites for energy storage devices

Further increase of electric capacity of these composites is connected with improvement of morphology of carbon materials and their organization in films. Synthesis of new polymers with suitably adjusted redox potentials may result in composites of increased pseudocapacity. Electrolyte solutions capable of withstanding real operating conditions of a supercapacitor will help introducing supercapacitors to industry. Here, the following studies are envisioned.

- ❖ Using carbon materials with a higher surface-to-mass ratio.

155

❖ Higher extent of material organization.

❖ Using carbon materials of a pore size adjusted to the size of the electrolyte ions.

❖ Applying non-volatile solvent electrolytes with a high temperature operating range.

❖ Developing a standard for evaluation of capacitive properties of an energy storage material.

References

(1)   Armaroli, N.; Balzani, V. The Future of Energy Supply: Challenges and Opportunities. *Angew. Chem. Int. Ed.* **2007**, *46*, 52-66.

(2)   Renewable Energy: a Major Player in the European Energy Market, European Comission, 2012.

(3)   Key World Energy Statistics 2012, International Energy Agency, 2012.

(4)   Conti, J.; Holtberg, P. *International Energy Outlook 2011*, U.S. Energy Information Administration, 2011.

(5)   Chu, S.; Majumdar, A. Opportunities and Challenges for a Sustainable Energy Future. *Nature* **2012**, *488*, 294-303.

(6)   Omer, A. M. Energy, Environment and Sustainable Development. *Renewable Sustainable Energy Rev.* **2008**, *12*, 2265-2300.

(7)   Vesborg, P. C. K.; Jaramillo, T. F. Addressing the Terawatt Challenge: Scalability in the Supply of Chemical Elements for Renewable Energy. *RSC Adv.* **2012**, *2*, 7933-7947.

(8)   Coletti, G.; Bronsveld, P. C. P.; Hahn, G.; Warta, W.; Macdonald, D.; Ceccaroli, B.; Wambach, K.; Le Quang, N.; Fernandez, J. M. Impact of Metal Contamination in Silicon Solar Cells. *Adv. Funct. Mater.* **2011**, *21*, 879-890.

(9)   Kippelen, B.; Bredas, J.-L. Organic Photovoltaics. *Energy Environ. Sci.* **2009**, *2*, 251-261.

(10)   Su, Y.-W.; Lan, S.-C.; Wei, K.-H. Organic Photovoltaics. *Mater. Today* **2012**, *15*, 554-562.

(11)   Li, C.; Liu, M.; Pschirer, N. G.; Baumgarten, M.; Müllen, K. Polyphenylene-Based Materials for Organic Photovoltaics. *Chem. Rev.* **2012**, *110*, 6817-6855.

(12)   Osedach, T. P.; Andrew, T. L.; Bulovic, V. Effect of Synthetic Accessibility on the Commercial Viability of Organic Photovoltaics. *Energy Environ. Sci.* **2013**, *6*, 711-718.

(13)   Kaltenbrunner, M.; White, M. S.; Głowacki, E. D.; Sekitani, T.; Someya, T.; Sariciftci, N. S.; Bauer, S. Ultrathin and Lightweight Organic Solar Cells with High Flexibility. *Nat. Commun.* **2012**, *3*, 770.

(14)   Grossiord, N.; Kroon, J. M.; Andriessen, R.; Blom, P. W. M. Degradation Mechanisms in Organic Photovoltaic Devices. *Org. Electron.* **2012**, *13*, 432-456.

157

(15) Hecht, D. S.; Hu, L.; Irvin, G. Emerging Transparent Electrodes Based on Thin Films of Carbon Nanotubes, Graphene, and Metallic Nanostructures. *Adv. Mater.* **2011**, *23*, 1482-1513.

(16) Pang, S.; Hernandez, Y.; Feng, X.; Müllen, K. Graphene as Transparent Electrode Material for Organic Electronics. *Adv. Mater.* **2011**, *23*, 2779-2795.

(17) Li, H.; Pan, W.; Zhang, W.; Huang, S.; Wu, H. TiN Nanofibers: A New Material with High Conductivity and Transmittance for Transparent Conductive Electrodes. *Adv. Funct. Mater.* **2013**, *23*, 209-214.

(18) King, R. R.; Bhusari, D.; Larrabee, D.; Liu, X. Q.; Rehder, E.; Edmondson, K.; Cotal, H.; Jones, R. K.; Ermer, J. H.; Fetzer, C. M.; Law, D. C.; Karam, N. H. Solar Cell Generations Over 40% Efficiency. *Prog. Photovolt: Res. Appl.* **2012**, *20*, 801-815.

(19) Tang, C. W. Two-layer organic photovoltaic cell. *Appl. Phys. Lett.* **1986**, *48*, 183-185.

(20) O'Regan, B.; Gratzel, M. A Low-Cost, High-Efficiency Solar Cell Based on Dye-Sensitized Colloidal TiO_2 Films. *Nature* **1991**, *353*, 737-740.

(21) Chidichimo, G.; Filippelli, L. Organic Solar Cells: Problems and Perspectives. *Int. J. Photoenergy* **2010**, *Article ID 123534*, 11 pages.

(22) Lin, Y.; Li, Y.; Zhan, X. Small Molecule Semiconductors for High-Efficiency Organic Photovoltaics. *Chem. Soc. Rev.* **2012**, *41*, 4245-4272.

(23) Topham, P. D.; Parnell, A. J.; Hiorns, R. C. Block Copolymer Strategies for Solar Cell Technology. *J. Polym. Sci., Part B: Polym. Phys.* **2011**, *49*, 1131-1156.

(24) Elliott, C. M. Dye-Sensitized Solar Cells: Out With Both Baby and Bathwater. *Nat. Chem.* **2011**, *3*, 188-189.

(25) Gregg, B. A.; Hanna, M. C. Comparing Organic to Inorganic Photovoltaic Cells: Theory, Experiment, and Simulation. *J. Appl. Phys.* **2003**, *93*, 3605-3614.

(26) Walter, M. G.; Rudine, A. B.; Wamser, C. C. Porphyrins and Phthalocyanines in Solar Photovoltaic Cells. *J. Porphyrins Phthalocyanines* **2010**, *14*, 759-792.

(27) Nelson, J. In *The Physics of Solar Cells*; Imperial College Press: London, 2002, pp 17-39.

(28) Balzani, V.; Credi, A.; Venturi, M. Photochemical Conversion of Solar Energy. *ChemSusChem* **2008**, *1*, 26-58.

(29) Tkachenko, N. V.; Lemmetyinen, H. In *Handbook of Carbon Nano Materials*; D'Souza, F., Kadish, K. M., Eds.; World Scientific: Singapore, 2011; Vol. 2, pp 405-440.

158

(30) Koo, H.-J.; Chang, S. T.; Slocik, J. M.; Naik, R. R.; Velev, O. D. Aqueous Soft Matter Based Photovoltaic Devices. *J. Mater. Chem.* **2011**, *21*, 72-79.

(31) Ruban, A. V.; Johnson, M. P.; Duffy, C. D. P. Natural Light Harvesting: Principles and Environmental Trends. *Energy Environ. Sci.* **2011**, *4*, 1643-1650.

(32) Martinez-Diaz, M. V.; de la Torre, G.; Torres, T. Lighting Porphyrins and Phthalocyanines for Molecular Photovoltaics. *Chem. Commun.* **2010**, 7090-7108.

(33) D'Souza, F.; Ito, O. Photosensitized Electron Transfer Processes of Nanocarbons Applicable to Solar Cells. *Chem. Soc. Rev.* **2012**, *41*, 86-96.

(34) Steed, J. W.; Atwood, J. L. In *Supramolecular Chemistry*; 2, Ed.; John Wiley & Sons, Ltd: Chichester, 2009, pp 62-68.

(35) Steed, J. W.; Atwood, J. L. In *Supramolecular Chemistry*; 2, Ed.; John Wiley & Sons, Ltd: Chichester, 2009, pp 172.

(36) Bikram, C. K. C.; Subbaiyan, N. K.; D'Souza, F. Supramolecular Donor-Acceptor Assembly Derived from Tetracarbazole-Zinc Phthalocyanine Coordinated to Fullerene: Design, Synthesis, Photochemical, and Photoelectrochemical Studies. *J. Phys. Chem. C* **2012**, *116*, 11964-11972.

(37) Chandra, B., KC.; Stranius, K.; D'Souza, P.; Subbaiyan, N. K.; Lemmetyinen, H.; Tkachenko, N. V.; D'Souza, F. Sequential Photoinduced Energy and Electron Transfer Directed Improved Performance of the Supramolecular Solar Cell of a Zinc Porphyrin-Zinc Phthalocyanine Conjugate Modified TiO2 Surface. *J. Phys. Chem. C* **2013**, *117*, 763-773.

(38) El-Khouly, M. E.; Ju, D. K.; Kay, K.-Y.; D'Souza, F.; Fukuzumi, S. Supramolecular Tetrad of Subphthalocyanine-Triphenylamine-Zinc Porphyrin Coordinated to Fullerene as an "Antenna-Reaction-Center" Mimic: Formation of a Long-Lived Charge-Separated State in Nonpolar Solvent. *Chem. Eur. J.* **2010**, *16*, 6193-6202.

(39) Pfuetzner, S.; Meiss, J.; Petrich, A.; Riede, M.; Leo, K. Thick C_{60}:ZnPc Bulk Heterojunction Solar Cells With Improved Performance by Film Deposition on Heated Substrates. *Appl. Phys. Lett.* **2009**, *94*, 253303.

(40) Bottari, G.; de la Torre, G.; Guldi, D. M.; Torres, T. Covalent and Noncovalent Phthalocyanine-Carbon Nanostructure Systems: Synthesis, Photoinduced Electron Transfer, and Application to Molecular Photovoltaics. *Chem. Rev.* **2010**, *110*, 6768-6816.

(41) Ince, M.; Hausmann, A.; Martinez-Diaz, M. V.; Guldi, D. M.; Torres, T. Non-Covalent Versus Covalent Donor-Acceptor Systems Based on Near-Infrared Absorbing Azulenocyanines and C_{60} Fullerene Derivatives. *Chem. Commun.* **2012**, 4058-4060.

159

(42) Guldi, D. M.; Gouloumis, A.; Vázquez, P.; Torres, T.; Georgakilas, V.; Prato, M. Nanoscale Organization of a Phthalocyanine-Fullerene System: Remarkable Stabilization of Charges in Photoactive 1-D Nanotubules. *J. Am. Chem. Soc.* **2005**, *127*, 5811-5813.

(43) Isosomppi, M.; Tkachenko, N. V.; A., E.; Kaunisto, K.; Hosomizu, K.; Imahori, H.; Lemmetyinen, H. J. Photoinduced Electron Transfer in Multilayer Self-Assembled Structures of Porphyrins and Porphyrin–Fullerene Dyads on ITO *J. Mater. Chem.* **2005**, *15*, 4546-4554.

(44) Steed, J. W.; Atwood, J. L. *Supramolecular Chemistry*; John Wiley & Sons, Ltd: Chichester, 2009.

(45) Boyd, P. D. W.; Reed, C. A. Fullerene-Porphyrin Constructs. *Acc. Chem. Res.* **2004**, *38*, 235-242.

(46) Imahori, H.; Umeyama, T.; Kurotobi, K.; Takano, Y. Self-Assembling Porphyrins and Phthalocyanines for Photoinduced Charge Separation and Charge Transport. *Chem. Commun.* **2012**, 4032-4045.

(47) Marczak, R.; Sgobba, V.; Kutner, W.; Gadde, S.; D'Souza, F.; Guldi, D. M. Langmuir-Blodgett Films of a Cationic Zinc Porphyrin-Imidazole-Functionalized Fullerene Dyad: Formation and Photoelectrochemical Studies. *Langmuir* **2007**, *23*, 1917-1923.

(48) D'Souza, F.; Maligaspe, E.; Ohkubo, K.; Zandler, M. E.; Subbaiyan, N. K.; Fukuzumi, S. Photosynthetic Reaction Center Mimicry: Low Reorganization Energy Driven Charge Stabilization in Self-Assembled Cofacial Zinc Phthalocyanine Dimer−Fullerene Conjugate. *J. Am. Chem. Soc.* **2009**, *131*, 8787-8797.

(49) Torres, T.; Gouloumis, A.; Sanchez-Garcia, D.; Jayawickramarajah, J.; Seitz, W.; Guldi, D. M.; Sessler, J. L. Photophysical Characterization of a Cytidine-Guanosine Tethered Phthalocyanine-Fullerene Dyad. *Chem. Commun.* **2007**, 292-294.

(50) Damaskin, B. B.; Petrij, O. A. In *Introduction to electrochemical kinetics*; High School: Moscow, 1975, pp 354.

(51) Ramaswamy, N.; Mukerjee, S. Fundamental Mechanistic Understanding of Electrocatalysis of Oxygen Reduction on Pt and Non-Pt Surfaces: Acid versus Alkaline Media. *Adv. Phys. Chem.* **2011**, *2012*, Article ID 491604.

(52) Dong-Hee Lim; Wilcox, J. Mechanisms of the Oxygen Reduction Reaction on Defective Graphene-Supported Pt Nanoparticles from First-Principles. *J. Phys. Chem. C* **2012**, 3653-3660.

(53) Bard, A. J.; Faulkner, L. R.; 2nd ed.; John Wiley & Sons, Inc: New York, 2001.

160

(54) Jose H. Zagal; Maritza A. Paez; Silva, J. F. In *N4-Macrocyclic Metal Complexes*; Jose H. Zagal, Fethi Bedioui, Dodelet, J.-P., Eds.; Springer Science: New York, 2006, pp 41-82.

(55) Abe, T.; Kaneko, M. Reduction Catalysis by Metal Complexes Confined in a Polymer Matrix. *Progr. Polym. Sci.* **2003**, *28*, 1441-1488.

(56) Peng, Z. M.; Yang, H. Designer Platinum Nanoparticles: Control of Shape, Composition in Alloy, Nanostructure and Electrocatalytic Property. *Nano Today* **2009**, *4*, 143-164.

(57) Li, W. Z.; Sun, G. Q.; Yan, Y. S.; Qin, X. Supported Noble Metal Electrocatalysts in Low Temperature Fuel Cells. *Progr. Chem.* **2005**, *17*, 761-772.

(58) Larminie, J.; Dicks, A. *Fuel Cell Systems Explained*; 2nd ed.; John Wiley & Sons Ltd: Chichester, 2003.

(59) Song, C.; Zhang, J. In *PEM Fuel Cell Electrocatalysts and Catalyst Layers*; Zhang, J., Ed.; Springer: London, 2008, pp 89-134.

(60) N.A. Karim; Kamarudin, S. K. An Overview on Non-Platinum Cathode Catalysts for Direct Methanol Fuel Cell. *Appl. Energy* **2013**, 212-220.

(61) Karim, N. A.; Kamarudin, S. K. An overview on non-platinum cathode catalysts for direct methanol fuel cell. *Appl. Energy* **2013**, *103*, 212-220.

(62) Gewirth, A. A.; Thorum, M. S. Electroreduction of dioxygen for fuel-cell applications: Materials and challenges. *Inorg. Chem.* **2010**, *49*, 3557-3566.

(63) Ren, Y.; Chia, G. H.; Gao, Z. Metal-organic frameworks in fuel cell technologies. *Nano Today* **2013**, *8*, 577-597.

(64) Serov, A.; Kwak, C. Review of Non-Platinum Anode Catalysts for DMFC and PEMFC Application. *Appl. Catal. B* **2009**, *90*, 313-320.

(65) Zhang, L.; Zhang, J. J.; Wilkinson, D. P.; Wang, H. J. Progress in Preparation of Non-Noble Electrocatalysts for PEM Fuel Cell Reactions. *J. Power Sources* **2006**, *156*, 171-182.

(66) Wang, B. Recent Development of Non-Platinum Catalysts for Oxygen Reduction Reaction. *J. Power Sources* **2005**, *152*, 1-15.

(67) Feng, Y. J.; Alonso-Vante, N. Nonprecious Metal Catalysts for the Molecular Oxygen-Reduction Reaction. *Phys. Status Solidi B* **2008**, *245*, 1792-1806.

(68) Dodelet, J.-P. In *N4-Macrocyclic Metal Complexes*; Jose H. Zagal, Fethi Bedioui, Dodelet, J.-P., Eds.; Springer Science: New York, 2006, pp 82-147.

(69) Collman, J. P.; Denisevich, P.; Konai, Y.; Marrocco, M.; Koval, C.; Anson, F. C. Electrode Catalysis of the Four-Electron Reduction of Oxygen to Water by Dicobalt Face-to-Face Porphyrins. *J. Am. Chem. Soc.* **1980**, *102*, 6027-6036.

(70) Collman, J. P.; Wagenknecht, P. S.; Hutchison, J. E. Molecular Catalysts for Multielectron Redox Reactions of Small Molecules: The "Cofacial Metallodiporphyrin" Approach. *Angew. Chem. Int. Ed.* **1994**, *33*, 1537-1554.

(71) Chang, C. J.; Deng, Y.; Shi, C.; Chang, C. K.; Anson, F. C.; Nocera, D. G. Electrocatalytic Four-Electron Reduction of Oxygen to Water by a Highly Flexible Cofacial Cobalt Bisporphyrin. *Chem. Commun.* **2000**, 1355-1356.

(72) Durand, R. R.; Bencosme, C. S.; Collman, J. P.; Anson, F. C. Mechanistic Aspects of the Catalytic Reduction of Dioxygen by Cofacial Metalloporphyrins. *J. Am. Chem. Soc.* **1983**, *105*, 2710-2718.

(73) D'Souza, F.; Hsieh, Y.-Y.; R. Deviprasad, G. Four-Electron Electrocatalytic Reduction of Dioxygen to Water by an Ion-Pair Cobalt Porphyrin Dimer Adsorbed on a Glassy Carbon Electrode. *Chem. Commun.* **1998**, 1027-1028.

(74) Rosenthal, J.; Nocera, D. G. Role of Proton-Coupled Electron Transfer in O–O Bond Activation. *Acc. Chem. Res.* **2007**, *40*, 543–553.

(75) Shino Satoh; Kei Murakoshi; Ikeda, K. In *PRiME*; The Electrochemical Society: Honolulu, 2012.

(76) Armaroli, N.; Balzani, V. The Hydrogen Issue. *ChemSusChem* **2011**, *4*, 21-36.

(77) Cheng, F.; Chen, J. Metal-Air Batteries: From Oxygen Reduction Electrochemistry to Cathode Catalysts. *Chem. Soc. Rev.* **2012**, *41*, 2172-2192.

(78) De Leon, C. P.; Pletcher, D. Removal of formaldehyde from aqueous solutions via oxygen reduction using a reticulated vitreous carbon cathode cell. *J Appl Electrochem* **1995**, *25*, 307-314.

(79) Panizza, M.; Bocca, C.; Cerisola, G. Electrochemical Treatment of Wastewater Containing Polyaromatic Organic Pollutants. *Water Res.* **2000**, *34*, 2601-2605.

(80) Tai, H.; Yang, Y.; Liu, S.; Li, D. In *Computer and Computing Technologies in Agriculture V*; Li, D., Chen, Y., Eds.; Springer Berlin Heidelberg: 2012; Vol. 369, pp 569-576.

(81) Béguin, F.; Frąckowiak, E. *Supercapacitors : materials, systems, and applications*; Wiley-VCH: Weinheim, 2013.

(82) Snook, G. A.; Kao, P.; Best, A. S. Conducting-polymer-based supercapacitor devices and electrodes. *J. Power Sources* **2011**, *196*, 1-12.

162

(83) Simon, P.; Gogotsi, Y. Materials for electrochemical capacitors. *Nat. Mater.* **2008**, 845-854.

(84) Reddy, A. L. M.; Gowda, S. R.; Shaijumon, M. M.; Ajayan, P. M. Hybrid Nanostructures for Energy Storage Applications. *Adv. Mater.* **2012**, *24*, 5045-5064.

(85) Pieta, P.; Obraztsov, I.; D'Souza, F.; Kutner, W. Composites of Conducting Polymers and Various Carbon Nanostructures for Electrochemical Supercapacitors. *ECS J. Solid State Sci. Technol.* **2013**, *2*, M3120-M3134.

(86) Simon, P.; Gogotsi, Y. Charge storage mechanism in nanoporous carbons and its consequence for electrical double layer capacitors. *Phil. Trans. R. Soc. A* **2010**, 3457-3467.

(87) Reddy, A. L. M.; Shaijumon, M. M.; Gowda, S. R.; Ajayan, P. M. Multisegmented Au-MnO2/Carbon Nanotube Hybrid Coaxial Arrays for High-Power Supercapacitor Applications. *J. Phys. Chem. C* **2010**, 658-663.

(88) Skotheim, T. A.; Reynolds, J. *Conjugated Polymers: Processing and Applications*; CRC Press: New York, 2006.

(89) Pell, W. G.; Conway, B. E.; Adams, W. A.; de Oliveira, J. Electrochemical efficiency in multiple discharge recharge cycling of supercapacitors in hybrid EV applications. *Journal of Power Sources* **1999**, *80*, 134-141.

(90) Peng, C.; Zhang, S.; Zhou, X.; Chen, G. Z. Unequalisation of electrode capacitances for enhanced energy capacity in asymmetrical supercapacitors. *Energy and Environmental Science* **2010**, *3*, 1499-1502.

(91) Pieta, P.; Zukowska, G. Z.; Das, S. K.; D'Souza, F.; Petr, A.; Dunsch, L.; Kutner, W. Mechanism of Reductive C_{60} Electropolymerization in the Presence of Dioxygen and Application of the Resulting Fullerene Polymer for Preparation of a Conducting Composite with Single-Wall Carbon Nanotubes. *J. Phys. Chem. C* **2010**, *114*, 8150-8160.

(92) Grądzka, E.; Winkler, K.; Borowska, M.; Plonska-Brzezinska, M. E.; Echegoyen, L. Comparison of the electrochemical properties of thin films of MWCNTs/C_{60}-Pd, SWCNTs/C_{60}-Pd and ox-CNOs/C_{60}-Pd. *Electrochim. Acta* **2013**, *96*, 274-284.

(93) Brancewicz, E.; Grądzka, E.; Winkler, K. Comparison of electrochemical properties of two-component C_{60}-Pd polymers formed under electrochemical conditions and by chemical synthesis. *J. Solid State Electrochem.* **2012**, *17*, 1233-1245.

(94) Winkler, K.; Grodzka, E.; D'Souza, F.; Balch, A. L. Two-Component Films of Fullerene and Palladium as Materials for Electrochemical Capacitors. *J. Electrochem. Soc.* **2007**, *154*, K1-K10.

163

(95) Wysocka-Żołopa, M.; Winkler, K.; Thorn, A. A.; Chancellor, C. J.; Balch, A. L. Electrochemical properties of two-component polymers of palladium and pyrrolidine and piperazine derivatives of C60. *Electrochim. Acta* **2010**, *55*, 2010-2021.

(96) Xiong, S.; Yang, F.; Ding, G.; Mya, K. Y.; Ma, J.; Lu, X. Covalent bonding of polyaniline on fullerene: Enhanced electrical, ionic conductivities and electrochromic performances. *Electrochim. Acta* **2012**, *67*, 194-200.

(97) Xiong, S.; Yang, F.; Jiang, H.; Ma, J.; Lu, X. Covalently bonded polyaniline/fullerene hybrids with coral-like morphology for high-performance supercapacitor. *Electrochim. Acta* **2012**, *85*, 235-242.

(98) Walter, M. G.; Wamser, C. C. Synthesis and Characterization of Electropolymerized Nanostructured Aminophenylporphyrin Films. *J. Phys. Chem. C* **2010**, *114*, 7563-7574.

(99) Funes, M. a. D.; Caminos, D. A.; Alvarez, M. G.; Fungo, F.; Otero, L. A.; Durantini, E. N. Photodynamic Properties and Photoantimicrobial Action of Electrochemically Generated Porphyrin Polymeric Films. *Environ. Sci. Technol.* **2009**, *43*, 902-908.

(100) Schaming, D.; Ahmed, I.; Hao, J.; Alain-Rizzo, V.; Farha, R.; Goldmann, M.; Xu, H.; Giraudeau, A.; Audebert, P.; Ruhlmann, L. Easy Methods for the Electropolymerization of Porphyrins Based on the Oxidation of the Macrocycles. *Electrochim. Acta* **2011**, *56*, 10454-10463.

(101) Delphine Schaming; Alain Giraudeau; Laurent Ruhlmann; Clémence Allain; Jian Hao; Yun Xia; Rana Farha; Michel Goldmann; Yann Leroux; Hapiot, P. In *Electropolymeryzation*; Schab-Balcerzak, E., Ed.; InTech: Rijeka, Croatia, 2011.

(102) Xia, Y.; Schaming, D.; Farha, R.; Goldmann, M.; Ruhlmann, L. Bis-Porphyrin Copolymers Covalently Linked by Pyridinium Spacers Obtained by Electropolymerization From b-Octaethylporphyrins and Pyridyl-Substituted Porphyrins. *New J. Chem.* **2012**, *36*, 588-596.

(103) Winkler, K.; Balch, A.; Kutner, W. Electrochemically formed fullerene-based polymeric films. *J. Solid State Electrochem.* **2006**, *10*, 761-784.

(104) Winkler, K.; Noworyta, K.; Kutner, W.; Balch, A. L. A study of redox active C60/Pd films by simultaneous cyclic voltammetry and piezoelectric microgravimetry at an electrochemical quartz crystal microbalance. *J. Electrochem. Soc.* **2000**, 2597-2603.

(105) Winkler, K.; Balch, A. L.; Kutner, W. Electrochemically formed fullerene-based polymeric films. *J. Solid State Electrochem.* **2006**, 761-784.

(106) Ulman, A. In *An Introduction to Ultrathin Organic Films: From Langmuir-Blodgett to Self-Assembly*; Academic Press: New York, 1991, pp 117-127.

(107) Hann, R. A. In *Langmuir-Blodgett Films*; Plenum Press: New York, 1990, pp 17-92.

164

(108) Davies, J. T.; Rideal, E. K. In *Interfacial Phenomena*; Academic Press: London, 1961, pp 217-281.

(109) Wilhelmy, L. Ueber die abhangigkeit der capillaritats-constanten des alkohol con substanz und gestalt des benetzten festen korpers. *Ann. Phys. Chem.* **1863**, 177-217.

(110) Dresselhaus, M. S.; Dresselhaus, G.; Eklund, P. C. In *Science of Fullerenes and Carbon Nanotubes*; Academic Press, Inc.: San Diago, CA, 1996, pp 329.

(111) Ulman, A. In *An Introduction to Ultrathin Organic Films: From Langmuir-Blodgett to Self-Assembly*; Academic Press: New York, 1991, pp 127-130.

(112) Petty, M. C.; Barlow, W. A. In *Langmuir-Blodgett Films*; Plenum Press: New York, 1990, pp 120-123.

(113) Bard, A. J.; Faulkner, L. R. In *Electrochemical Methods: Fundamentals and Applications*; 2nd ed.; John Wiley & Sons, Inc: New York, 2001, pp 226-260.

(114) Galus, Z. In *Fundamentals of Electrochemical Analysis*; 2nd, Ed.; Ellis Horwood Limited: Chichester, England, 1994, pp 371-386.

(115) Bard, A. J.; Faulkner, L. R. In *Electrochemical Methods: Fundamentals and Applications*; 2nd ed.; John Wiley & Sons, Inc: New York, 2001, pp 275-304.

(116) Bard, A. J.; Faulkner, L. R. In *Electrochemical Methods: Fundamentals and Applications*; 2nd ed.; John Wiley & Sons, Inc: New York, 2001, pp 331-367.

(117) Hillman, A. R. In *Encyclopedia of Electrochemistry*; Wiley-VCH: Weinheim, 2003; Vol. 3, p 230-289.

(118) Benesi, H. A.; Hildebrand, J. H. Ultraviolet Absorption of Iodine in Aromatic Hydrocarbons. *J. Am. Chem. Soc.* **1948**, *70*, 2832-2833.

(119) Young, V. Y.; Hoflund, G. B. In *Handbook of Surface and Interface Analysis: Methods for Problem-Solving*; Riviere, J. C., Myhra, S., Eds.; CRC Press: New York, 2009, pp 20-62.

(120) Frey, B. L.; Corn, R. M.; Weibel, S. C. In *Handbook of Vibrational Spectroscopy*; John Wiley & Sons, Ltd: 2006, pp 1042-1056.

(121) Guilhaus, M. Special feature: Tutorial. Principles and instrumentation in time-of-flight mass spectrometry. Physical and instrumental concepts. *J. Mass Spectrom.* **1995**, *30*, 1519-1532.

(122) Binnig, G.; Quate, C. F.; Gerber, C. Atomic Force Microscope. *Phys. Rev. Lett.* **1986**, *56*, 930-933.

(123) Hénon, S.; Meunier, J. Microscope at the Brewster angle: Direct observation of first-order phase transitions in monolayers. *Rev. Sci. Instrum.* **1991**, *62*, 936-939.

(124) Hoenig, D.; Moebius, D. Direct Visualization of Monolayers at the Air-Water Interface by Brewster Angle Microscopy. *J. Phys. Chem.* **1991**, *95*, 4590-4592.

(125) Prato, M.; Maggini, M.; Giacometti, C.; Scorrano, G.; Sandona, G.; Farnia, G. Synthesis and Electrochemical Properties of Substituted Fulleropyrrolidines. *Tetrahedron* **1996**, *52*, 5221-5234.

(126) Marczak, R.; Hoang, V. T.; Noworyta, K.; Zandler, M. E.; Kutner, W.; D'Souza, F. Molecular Recognition of Adenine, Adenosine and ATP at the Air-Water Interface by a Uracil Appended Fullerene. *J. Mater. Chem.* **2002**, *12*, 2123-2129.

(127) D'Souza, F.; Deviprasad, G. R.; Zandler, M. E.; Hoang, V. T.; Klykov, A.; VanStipdonk, M.; Perera, A.; El-Khouly, M. E.; Fujitsuka, M.; Ito, O. Spectroscopic, Electrochemical, and Photochemical Studies of Self-Assembled via Axial Coordination Zinc Porphyrin−Fulleropyrrolidine Dyads. *J. Phys. Chem. A* **2002**, *106*, 3243-3252.

(128) D'Souza, F.; Zandler, M. E.; Smith, P. M.; Deviprasad, G. R.; Arkady, K.; Fujitsuka, M.; Ito, O. A Ferroceneв-C_{60}-Dinitrobenzene Triad: Synthesis and Computational, Electrochemical, and Photochemical Studies. *J. Phys. Chem. A* **2002**, *106*, 649-656.

(129) Huang, C.-W.; Chiu, K. Y.; Cheng, S.-H. Novel Spectral and Electrochemical Characteristics of Triphenylamine-Bound Zinc Porphyrins and Their Intramolecular Energy and Electron Transfer. *Dalton Trans.* **2005**, 2417-2422.

(130) Frisch, M. J.; Trucks, G. W.; Schlegel, H. B.; Scuseria, G. E.; Robb, M. A.; Cheeseman, J. R.; Scalman, G.; Barone, V.; Mennucci, B.; Petersson, G. A.; Nakatsuji, H.; Caricato, M.; Li, X.; Hratchian, H. P.; Izmaylov, A. F.; Bloino, J.; Zheng, G.; Sonnenberg, J. L.; Hada, M.; Ehara, M.; Toyota, K.; Fukuda, R.; Hasegawa, J.; Ishida, M.; Nakajima, T.; Honda, Y.; Kitao, O.; Nakai, H.; Vreven, T.; Montgomery, J. A.; Peralta, J. E.; Ogliaro, F.; Bearpark, M.; Heyd, J. J.; Brothers, E.; Kudin, K. N.; Staroverov, V. N.; Kobayashi, R.; Normand, J.; Raghavachari, K.; Rendell, A.; Burant, J. C.; Iyengar, S. S.; Tomasi, J.; Cossi, M.; Rega, N.; Millam, J. M.; Klene, M.; Knox, J. E.; Cross, J. B.; Bakken, V.; Adamo, C.; Jaramillo, J.; Gomperts, R.; Stratmann, R. E.; Yazyev, O.; Austin, A. J.; Cammi, R.; Pomelli, C.; Ochterski, J. W.; Martin, R. L.; Morokuma, K.; Zakrzewski, V. G.; Voth, G. A.; Salvador, P.; Dannenberg, J. J.; Dapprich, S.; Daniels, A. D.; Farkas, Ö.; Foresman, J. B.; Ortiz, J. V.; Cioslowski, J.; Fox, D. J.; Gaussian, Inc.: Wallingford CT, 2009.

(131) Pieta, P.; Venukadasula, G. M.; D'Souza, F.; Kutner, W. Preparation and Selected Properties of an Improved Composite of the Electrophoretically Deposited Single-Wall Carbon Nanotubes, Electrochemically Coated With a C_{60}-Pd and Polybisthiophene Mixed Polymer Film. *J. Phys. Chem. C* **2009**, *113*, 14046-14058.

(132) D'Souza, F.; Gadde, S.; Islam, D. M. S.; Pang, S.-C.; Schumacher, A. L.; Zandler, M. E.; Horie, R.; Araki, Y.; Ito, O. Photoinduced electron transfer in a Watson-Crick
166

base-paired, (2-aminopurine):(uracil-C60) hydrogen bonding conjugate. *Chem. Commun.* **2007**, 480-482.

(133) Huynh, T.-P.; Pietrzyk-Le, A.; Bikram K.C, C.; Noworyta, K. R.; Sobczak, J. W.; Sharma, P. S.; D'Souza, F.; Kutner, W. Electrochemically synthesized molecularly imprinted polymer of thiophene derivatives for flow-injection analysis determination of adenosine-5вЂІ-triphosphate (ATP). *Biosens. Bioelectron.* **2013**, *41*, 634-641.

(134) In *CRC Handbook of Chemistry and Physics*; 74th ed.; Lide, D. R., Ed.; CRC Press: Boca Raton, 1993-1994, p 7-3.

(135) Scholes, G. D.; Fleming, G. R.; Olaya-Castro, A.; van Grondelle, R. Lessons From Nature About Solar Light Harvesting. *Nat. Chem.* **2011**, *3*, 763-774.

(136) Barber, J. Photosynthetic Energy Conversion: Natural and Artificial. *Chem. Soc. Rev.* **2009**, *38*, 185-196.

(137) Concepcion, J. J.; House, R. L.; Papanikolas, J. M.; Meyer, T. J. Chemical Approaches to Artificial Photosynthesis. *Proc. Natl. Acad. Sci. USA* **2012**, *109*, 15560-15564.

(138) Marczak, R.; Noworyta, K.; Nowakowski, R.; Kutner, W.; Desbat, B.; Araki, Y.; Ito, O.; Gadde, S.; Zandler, M. E.; D'Souza, F. Self-Assembling of Porphyrin-Fullerene Dyads in the Langmuir and Langmuir-Blodgett Films: Formation as well as Spectral, Electrochemical and Vectorial Electron Transfer Studies. *J. Nanosci. Nanotechnol.* **2007**, *7*, 1455-1471.

(139) Pereira, A. M. V. M.; Hausmann, A.; Tome, J. P. C.; Trukhina, O.; Urbani, M.; Neves, M. G. P. M. S.; Cavaleiro, J. A. S.; Guldi, D. M.; Torres, T. Porphyrin-Phthalocyanine/Pyridylfullerene Supramolecular Assemblies. *Chem. Eur. J.* **2012**, *18*, 3210-3219.

(140) Das, S. K.; Mahler, A.; K., W. A.; D'Souza, F. High Potential Perfluorinated Phthalocyanine-Fullerene Dyads for Generation of High Energy Charge Separated States: Formation and Photoinduced Electron Transfer Studies. *ChemPhysChem* **2014**.

(141) D'Souza, F.; Ito, O. Photoinduced Electron Transfer Processes of Functionalized Nanocarbons; Fullerenes, Nanotubes and Graphene. *Sci. Prog.* **2013**, *96*, 369-397.

(142) Njus, D.; Jalukar, V.; Zu, J. A.; Kelley, P. M. Concerted Proton-Electron Transfer Between Ascorbic Acid and Cytochrome b561. *Am. J. Clin. Nutr.* **1991**, *54*, 1179S-1183S.

(143) Mortimer, R. J. Electrochromic Materials. *Chem. Soc. Rev.* **1997**, *26*, 147-156.

(144) Seo, E. T.; Nelson, R. F.; Fritsch, J. M.; Marcoux, L. S.; Leedy, D. W.; Adams, R. N. Ternary Amine Electrochemistry. *J. Am. Chem. Soc.* **1966**, *88*, 3498-3503.

167

(145) Macagno, V. A.; Giordano, M. C.; Arvía, A. J. *Electrochim. Acta* **1969**, 335-357.

(146) Morozan, A.; Jousselme, B.; Palacin, S. Low-Platinum and Platinum-Free Catalysts for the Oxygen Reduction Reaction at Fuel Cell Cathodes. *Energy Environ. Sci.* **2011**, *4*, 1238-1254.

(147) Jaouen, F.; Proietti, E.; Lefevre, M.; Chenitz, R.; Dodelet, J.-P.; Wu, G.; Chung, H. T.; Johnston, C. M.; Zelenay, P. Recent Advances in Non-Precious Metal Catalysis for Oxygen-Reduction Reaction in Polymer Electrolyte Fuel Cells. *Energy Environ. Sci.* **2011**, *4*, 114-130.

(148) Debe, M. K. Electrocatalyst approaches and challenges for automotive fuel cells. *Nature* **2012**, *486*, 43-51.

(149) Hung, T.-F.; Chen, S.-H.; Tu, M.-H.; Lu, Z.-H.; Chen, C. K.; Liu, R.-S.; Greer, H. F.; Zhou, W.; Lo, M.-Y. Advances in Carbon-Incorporated Non-Noble Transition Metal Catalysts for Oxygen Reduction Reaction in Polymer Electrolyte Fuel Cells. *J. Chin. Chem. Soc.* **2014**, *61*, 93-100.

(150) Cheng, N.; Kemna, C.; Goubert-Renaudin, S.; Wieckowski, A. Reduction Reaction by Porphyrin-Based Catalysts for Fuel Cells. *Electrocatalysis* **2012**, *3*, 238-251.

(151) Kiros, Y. Metal porphyrins for oxygen reduction in PEMFC. *Int. J. Electrochem. Sci.* **2007**, *2*, 285-300.

(152) Barbe, J.-M.; Guilard, R. In *The Porphyrin Handbook, Inorganic, Organometallic and Coordination Chemistry*; Kadish, K. M., Smith, K. M., Guilard, R., Eds.; Academic Press: London, 2000; Vol. 3, pp 235-237.

(153) Diskin-Posner, Y.; Patra, G. K.; Goldberg, I. Crystal engineering of metalloporphyrin assemblies. New supramolecular architectures mediated by bipyridyl ligands. *Chem. Commun.* **2002**, 1420-1421.

(154) Noworyta, K.; Marczak, R.; Tylenda, R.; Sobczak, J. W.; Chitta, R.; Kutner, W.; D'Souza, F. "Two-Point" Assembling of Zn(II) and Co(II) Metalloporphyrins Derivatized with a Crown Ether Substituent in Langmuir and Langmuir−Blodgett Films. *Langmuir* **2007**, *23*, 2555-2568.

(155) Gervaldo, M.; Funes, M.; Durantini, J.; Fernandez, L.; Fungo, F.; Otero, L. Electrochemical polymerization of palladium (II) and free base 5,10,15,20-tetrakis(4-N,N-diphenylaminophenyl)porphyrins: Its applications as electrochromic and photoelectric materials. *Electrochim. Acta* **2010**, *55*, 1948-1957.

(156) Kadish, K. M.; Caemelbecke, E.; Guy, R. In *The Porphyrin Handbook, Electron transfer*; Kadish, K. M., Smith, K. M., Guilard, R., Eds.; Academic Press: London, 2000; Vol. 3, pp 59-65.

(157) Lana-Villarreal, T.; Campina, J. M.; Guijarro, N.; Gomez, R. Solid-state electropolymerization and doping of triphenylamine as a route for electroactive thin films. *Phys. Chem. Chem. Phys.* **2011**, *13*, 4013-4021.

(158) Nagaoka, T.; Yoshino, T. Surface properties of electrochemically pretreated glassy carbon. *Anal. Chem.* **1986**, *58*, 1037-1042.

(159) Zhang, L. L.; Zhao, X. S. Carbon-Based Materials as Supercapacitor Electrodes. *Chem. Soc. Rev.* **2009**, *38*, 2520-2531.

(160) Nyholm, L.; Nyström, G.; Mihranyan, A.; Strømme, M. Toward Flexible Polymer and Paper-Based Energy Storage Devices. *Adv. Mater.* **2011**, *23*, 3751-3769.

(161) Pięta, P., Doctoral dissertation, The Institute of Physical Chemistry of the Polish Academy of Sciences, 2009.

169